

UC Berkeley

UC Berkeley Electronic Theses and Dissertations

Title

Disorders and Dynamics of Reticular Materials Studied by Single-Crystal X-ray Diffraction

Permalink

<https://escholarship.org/uc/item/6rb3k9q7>

Author

Pei, Xiaokun

Publication Date

2021

Peer reviewed|Thesis/dissertation

Disorders and Dynamics of Reticular Materials Studied by Single-Crystal X-ray Diffraction

By

Xiaokun Pei

A dissertation submitted in partial satisfaction of the
requirements of a doctoral degree of

Doctor of Philosophy

in

Chemistry

in the

Graduate Division

of the

University of California, Berkeley

Committee in charge:

Professor Omar M. Yaghi, Chair

Professor Kenneth N. Raymond

Professor Jeffery A. Reimer

Fall 2021

Abstract

Disorders and Dynamics of Reticular Materials Studied by Single-Crystal X-ray Diffraction

by

Xiaokun Pei

Doctor of Philosophy in Chemistry

University of California, Berkeley

Professor Omar M. Yaghi, Chair

The work presented here focuses on understanding the complex structural phenomena inside metal–organic frameworks (MOFs), zeolitic imidazolate frameworks (ZIFs), and covalent organic frameworks (COFs) by single-crystal X-ray diffraction (SXRD). These materials feature high porosity inside crystal structures, making spaces for the displacements and motions of the framework that are rarely observed in conventional crystals formed by close packing of molecules. While most studies solely rely on SXRD to obtain the skeleton of the structures, recent advances in the crystallographic analyses of reticular materials highlight the importance of rigorous interpretation of the disorders and how the observed static disorders might be associated with dynamics.

Chapters 2 and 3 describe a framework-assisted crystal structure determination method for complex small molecules, the coordinative alignment method. Guests were incorporated and covalently attached into MOF-520, providing a platform to understand the behaviors of the guests when residing in a void space. Chapter 2 analyzes the stereoselectivity of the method originated from asymmetric coordination bond, which explains why the method can prevent a primary source of disorder that often interferes structural determination of guests. The thorough look at the solvent-induced guest disorder in Chapter 3 provides an insight into solvent-guest interactions that generally exist in porous crystals, and additionally introduces a method for improving the quality of structural solutions by solvent removal. Chapter 4 reports a correction to a previously reported ZIF structure (ZIF-90) after considering merohedral twinning. Rigorous crystallographic studies revealed the origin of merohedral twinning and associated it with a displacive phase transition at elevated temperatures, introducing a new facet to the forms of disorders in ZIFs and an unprecedented cause of displacive phase transition among any other materials. Finally, Chapter 5 describes the design and synthesis of a woven COF, which by design will transfer to a structure of interlocking 2D rings upon post-synthetic demetallation. It aims at a material at the boundary of crystalline and non-crystalline and thus challenging the boundary of crystallographic characterizations.

Table of Contents

Chapter 1. Introduction to the Disorders and Dynamics of Reticular Materials.....	1
1.1. Reticular Materials	2
1.2. Interpretation of complex structural phenomena.....	3
1.3. Structural Dynamics of Reticular Materials	8
1.4. Conclusion	9
1.5. Bibliography	10
Chapter 2. Structures and Disorders of Small Molecules Binding onto MOF-520... 14	14
2.1. Introduction.....	15
2.2. Experimental	15
2.2.1. Materials	15
2.2.2. Synthesis of MOF-520 Single Crystals	16
2.2.3. Procedure for Incorporation of Target Molecules	16
2.2.4. Single-Crystal X-ray Diffraction.....	18
2.2.5. Computational Methods	18
2.3. Results and Discussions	20
2.3.1. Incorporation of Target Molecules with N-, S-, P-containing Functionalities.....	20
2.3.2. Single-Crystal X-ray Diffraction Studies of Sulfur-Oxoacids-Incorporated MOF-520.....	21
2.3.3. Single-Crystal X-ray Diffraction Studies of Phosphorous-Oxoacids-Incorporated MOF-520	26
2.3.4. Diastereoselective Incorporation on Prochiral Target Molecules	27
2.4. Conclusion	32
2.5. Appendices and Notes.....	33
2.5.1. Acknowledgments	33
2.5.2. Summary of SXRD Results.....	33
2.5.3. Refinement details of SXRD datasets	35
2.5.4. Structure Models for Hirshfeld Analyses.....	69
2.6. Bibliography	71
Chapter 3. Reducing the Disorder of Incorporated Large Biomolecules in MOF-520	74
.....	74
3.1. Introduction.....	75
3.2. Experimental	75
3.2.1. Materials	75
3.2.2. Syntheses	76
3.3. Results and Discussions	78
3.3.1. Enantiomeric Discrimination of a Racemic Mixture by Incorporation into MOF-520.....	78
3.3.2. Incorporated MOF-520 Crystals with and without Solvent	79
3.4. Conclusion	81

3.5. Appendices and Notes.....	82
3.5.1. Terms for Describing Stereoselectivity of MOF-520.....	82
3.5.2. Single-crystal X-ray diffraction results	83
3.6. Bibliography	99
Chapter 4. Accurate Structure Determination and Displacive Phase Transition of ZIF-90	101
4.1. Introduction.....	102
4.2. Experimental	102
4.2.1. Materials	102
4.2.2. Syntheses of ZIF-90 crystals	102
4.2.3. Instrumentations and Methods	103
4.3. Results and Discussions	103
4.3.1. The Correct Structure of ZIF-90 Considering Merohedral Twinning.....	103
4.3.2. Structure Variation of Solvated ZIF-90 Crystals Measured at 100 K.....	105
4.3.3. Continuous Structure Change of ZIF-90 vs. Temperature	106
4.4. Conclusion	109
4.5. Appendices and Notes.....	110
4.5.1. SXRDR Results of Solvated ZIF-90 Crystals Measured at 100 K	110
4.5.2. Variable Temperature SXRDR Results of Solvated ZIF-90 Crystals.....	117
4.5.3. SXRDR Results of Variable Temperature Series of Activated ZIF-90	121
4.6. Bibliography	134
Chapter 5. Synthesis and Characterization Toward a Woven Covalent Organic Framework.....	136
5.1. Introduction.....	137
5.2. Experimental	138
5.2.1. Materials and Methods	138
5.2.2. Syntheses and Characterizations	138
5.3. Results and Discussions	141
5.4. Conclusion	145
5.5. Appendices and Notes.....	146
5.5.1. Acknowledgments	146
5.5.2. Mass Spectrometry	146
5.5.3. Single-crystal X-ray diffraction results	151
5.5.4. Structural Model of the Proposed Woven COFs.....	153
5.6. Bibliography	157
Chapter 6. Conclusion and Outlook	159

Acknowledgments

Looking back to the course of my Ph.D., I was fortunate to have received tremendous support from mentors, colleagues, friends, and families that accompanied me through this exciting while challenging five-year journey. I am grateful for having them all in my life.

I would like to thank my advisor, Professor Omar Yaghi. He has taught me the vision and ambition of research that shape me to focus on the most challenging questions. I learned from him the standards of the best research, which constantly drives me to achieve excellence. The experience of working with a world-leading scientist has had a life-long influence on me, and I am determined to carry the great qualities I learned to the future. I also want to thank Prof. Yaghi for encouraging me to working on the interdisciplinary area between crystallography and reticular materials. Without his endless support, I won't have had the chance and courage to pursue this challenging research direction.

I would like to thank Professor Hans-Beat Bürgi, my crystallography mentor. He guided me through the numbers and statistics in crystal structures with his clear mind and showed me how math turned into elegant chemical information. Working with him always reminds me of the history of the golden era in modern physics that had greatly influenced me as a kid. It is a fortune to reacquaint the charm of mathematical analysis outside of books and its vitality in 21-century materials research. I also want to thank my collaborators, Dr. Stefano Canossa and Dr. Ruggero Frison. It was incredible to have a chance to work with a vibrant team formed by materials chemists and computational crystallographers, which broadened my vision as a young Ph. D. student.

I'd like to thank my colleagues in the Yaghi group. From practical experiments to pioneering sciences, day-to-day discussions with them have become invaluable memories. I have learned a lot from the senior group members, Markus, Philipp, Farhad, Jayeon, Roc, Mathieu, Nobuya, Chenfei, Cornelius, Yuzhong, Yingbo, Jingjing, Bunyarat, Chris, Christian, Eugene, SK, Robinson, Peter, Steven, Zhe, Lei, Xiang, Philjun, and Bing. They mentored me on all aspects, from syntheses and characterizations to scientific presentation and writing. They are my role models on how to become a better researcher. In addition, I want to sincerely thank my peers, Hao and Wentao. My success of Ph.D. is greatly owed to my fantastic friendship with them. I would also like to thank the current group members, Lac Ha, Tianqiong, Xing, Daria, Nikita, Haoze, Fangying, Zach, Oscar, Ephraim, Matt, Zichao, Zihui, Haozhe, Kaiyu, Ali, and Kelvin. It is always a joy to collaborate with them on new sciences and the lab's daily operations.

I want to thank Professor Bo Wang at Beijing Institute of Technology, my undergraduate advisor. I would not have had a chance to study in a top chemistry program in the United States without his support. His dedication to providing the best opportunities for students has inspired me to pursue a career in academia in the future as he does, passing on knowledge and thoughts to the younger generations.

I won't have made it now without my parents, Yirong Pei and Ailing Wang. The pandemic and my visa issue didn't make an easy life in the past five years, but the unsettled feelings are always smoothed by their constant love and support. They make me determined always to do the best work and live the best life regardless of real-world difficulties. Likewise, I deeply appreciate the support from my friends, Mengmeng Zhang, Chang Xiong, Ning Ai, Shuyan Wang, and Ning Ge. They are ambitious young people in their early careers working diligently toward great goals. It is my fortune to be a part of such wonderful fellows and support each other through difficult times. I sincerely wish them to achieve themselves in the future.

Chapter 1.
Introduction to the Disorders and Dynamics of Reticular Materials

1.1. Reticular Materials

Reticular chemistry discovers the materials connected through covalent or coordination bonds throughout 2-dimensional or 3-dimensional space in an ordered fashion.¹ The thus far discovered reticular materials contain three major categories: metal–organic frameworks (MOFs)², zeolitic imidazolate frameworks (ZIFs)³, and covalent organic frameworks (COFs)⁴. MOFs are composed of metal–oxo clusters (secondary building unit, SBU)⁵ and typically carboxylate-based linkers. ZIFs, sometimes considered a subcategory of MOFs, are composed of tetrahedral-coordinated single metal ions and imidazolate linkers. COFs are formed by pure organic building units via reactions such as imine condensation. All reticular materials feature high intrinsic structural rigidity that allows permanent porosity and well-defined pore shapes, which becomes the center of their developed applications.

The formation of well-defined pore structures requires a high level of order, which means that they are always crystalline materials. Starting from the day that the first reticular material is synthesized, their characterizations rely on crystallographic techniques, including both single-crystal X-ray diffraction (SXRD) and powder X-ray diffraction (PXRD), joined by the emerging technique electron diffraction (ED) in recent years. Since then, the unique feature of porosity has brought unprecedented phenomena, questions, and challenges to traditional small-molecule crystallography.

The first feature of the crystals of reticular materials is that they exhibit larger unit cells than molecular crystals. The first discovered 3-dimensional MOF in 1999, MOF-5, has a cubic lattice and a unit cell parameter of 25.6572(5) Å.⁶ One of the first 3D COFs, COF-105, lies in cubic I lattice with a unit cell parameter of 44.886(5) Å.⁷ One of the largest reported ZIFs to date, ZIF-100, has a unit cell parameter of 71.9797(4) Å and contains 7524 atoms in one unit cell.⁸ A number of larger MOFs have been developed over the years, expanding the record of dimensions to what are usually observed from protein crystals.⁹ For example, the unit cell size and volume of NU-1301, a uranium MOF, are 173.26 Å and 5,201,096 Å³, respectively.¹⁰ Such large unit cells usually form the first challenge of crystal structure determination: for many times, longer wavelengths or longer detector distances are required to clearly distinguish the diffraction peaks from compact reciprocal spaces. Sometimes, detectors with the better spatial resolutions are preferred, which is mostly only equipped at protein crystallography beamlines at synchrotron sources.

Accompanied by the large unit cells is a significant portion of void space in the crystal structures, which is the second important feature of the crystals of reticular materials. MOF-5 was reported with more than 55% of its volume occupied by guest molecules.⁶ MOF-210, a zinc MOF reported in 2010, has a void space of 89% in its crystal structure.¹¹ Such extraordinary porosities leave plenty of space for the displacements and motions of the framework, therefore lowering the diffraction limits of the crystals. In addition, the giant void space accompanies ultralow densities, further decreasing the diffraction ability of the crystals. MOF-210 is a typical example: even though the data collection was conducted at a synchrotron source with reasonable crystal size (300 μm in diameter), the crystal was only able to diffract to 1.9 Å. The low resolution of information contained in diffractions and data-to-parameter ratio limited by diffraction ability place challenges on obtaining a high-quality structural solution. Thus, only part of the SBU (Zn₄O) were anisotropically refined but not any other atoms on linkers or SBUs. The observed structure factor (F_o) electron density plot of resolved MOF-210 well demonstrated the challenge of modeling electron densities (**Figure 1.1**), that sphere-shaped atomic electron densities were not in the plot, but only the skeleton of the framework was able to be distinguished. Such common challenges for

large-pore reticular materials bring a new requirement to small-molecule crystal structure refinement algorithms on providing criteria to evaluate the reliability of refinement at uncommonly low resolutions. Further beyond, it requests the development in phasing algorithms for datasets at such resolution ranges. It is fortunate for MOFs and ZIFs that the heavy atoms in the structures help the initial phasing during structure determination, while difficulties can appear in the structure determination of COFs as they are primarily composed of light atoms.

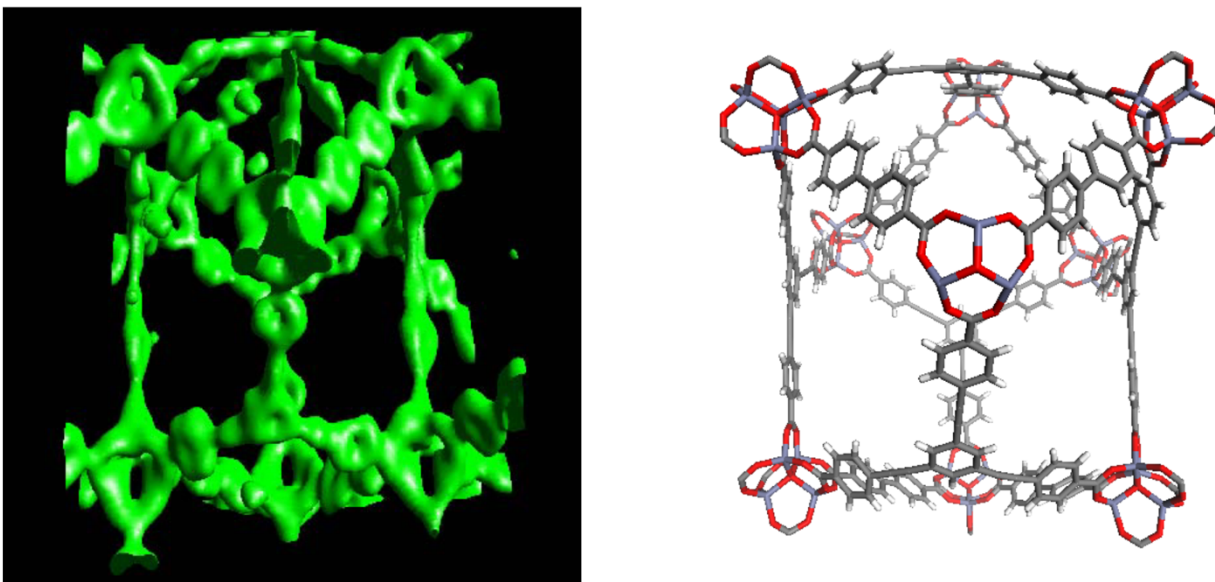


Figure 1.1. Observed structure factor (F_o) electron density plot of MOF-210. From Furukawa, et al., *Science* **2010**, 329 (5990), 424–428.¹¹ Reprinted with permission from AAAS.

Void space in crystals is rarely observed before the discovery of reticular materials. The exponential growth of MOFs, ZIFs, and COFs in the past twenty years greatly promotes methods and instrumentations for observing framework-guest chemistry. The earliest attempt was based on glass capillaries to keep crystals in vacuum or specific gaseous environment. With this technique, the gas adsorption site in MOF-5 was first determined.¹² Later, a liquid flow setup on crystal mounts was developed, which enabled the first direct observation of imine condensation reaction happening in the pore of a coordination polymer.¹³ Almost ten years ago, *in situ* gas crystallography was developed, which relies on a modified goniometer head (named “environmental gas cell”) with a glass cap over the crystal-mounting pin.^{14–17} The environment inside the glass cap is connected to gas inlet and outlet, thus allowing the crystal to be activated and dosed gas on the goniometer. This relatively convenient setup boosted the fundamental chemistry discoveries on gas-framework interactions, which contributes to the development of gas sorption materials. As an example, a cooperative chemical adsorption mechanism of CO₂ into a diamine-appended Mg₂(dobpdc) was revealed step-by-step using the gas cell.¹⁸

1.2. Interpretation of complex structural phenomena

Though the SXRD structure determination has been used for years, the focus has only been on confirming structures; many hints of complex structural phenomena were buried in reported data but not thoroughly discussed and studied. The abovementioned unit cell dimension and resolution problems are critical issues; however, they are only the tip of the iceberg of the complexity in the

crystals of reticular materials. A tutorial review was published by Lillerud *et al.* in 2017 covering the pitfalls in MOF crystallography, which included brilliant discussions on the treatment of disordered solvent and pseudo-merohedral twinning.¹⁹ Herein, the discussion is expanded to more basic aspects of crystal structure determinations of reticular materials, where many problems and interesting findings also reside.

The fundamental requirement is to report correct crystal structures. Unfortunately, it is not an easy achievement. For a correct crystal structure refinement, it is not only important to rigorously look at R factors and residual densities. More essentially, one needs to critically check the atomic displacement parameters (ADPs) and understand whether the structural information behind matches with the chemical information, which are important physical information in addition to chemical information such as bond length and bond angle. The reason is that although the idea of ADP started from thermal displacement of atoms, it is unable to distinguish disorders from thermal displacements.²⁰ The famous “moving atom” in the crystallography textbooks is an example.²¹ When the PLATON checkCIF routine²² raises alerts on significantly distorted atomic ADPs, one should diligently research and explain the physical nature that results in it.

A good example in the crystallography of reticular materials is the clear distinction of positional disorder in $Zr_6O_4(OH)_4(-COO)_x[(OH)(H_2O)]_{12-x}$ SBUs, which is the only reported type of SBU existing in zirconium MOFs.^{23,24} The two works utilized two zirconium MOFs, UiO-66 and UiO-67, but concluded with the same interpretation on the disorders of the Zr SBU. It firstly features the residual density next to the carboxylate oxygens, which indicates the position of coordinating water/hydroxyl group when there are missing carboxylate linkers (**Figure 1.2b, c**). Secondly, it pointed out the long ADP of μ_3 -oxygen could be split into two positions (**Figure 1.2a**), and they meant by half occupation of μ_3 -oxo (O^{2-}) and half occupation of μ_3 -hydroxy (OH^-). The disorder model is consistent with the chemical information that an equal population of O^{2-} and OH^- is needed to attain the charge balance of the Zr SBU. The establishment of the correct structural model makes a good basis for further detailed studies of the properties of Zr MOFs.

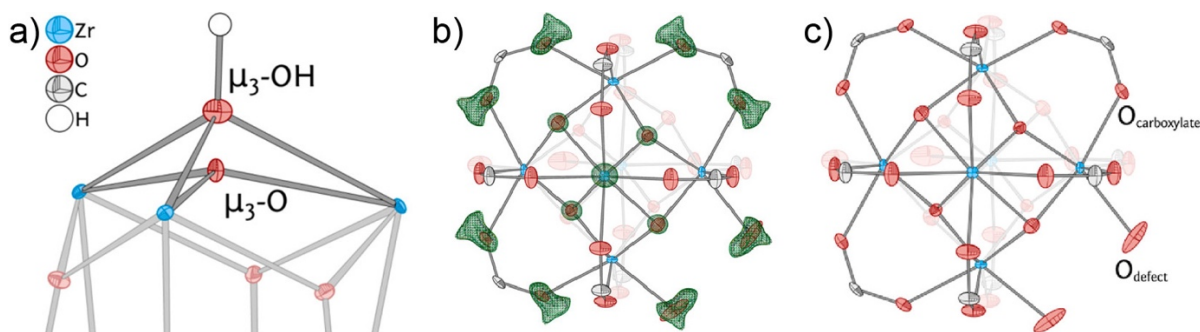


Figure 1.2. a) Disorder of μ_3 -oxygen in a Zr_6 cluster. b) Observed electron density plot next to the carboxylate oxygens, indicating c) the position of hydroxy/water when there is missing carboxylate linker. Adapted with permission from Øien *et al.*, *Cryst. Growth Des.* **2014**, *14* (11), 5370–5372. Copyright 2014 American Chemical Society.

On the contrary, ignoring the abnormal ADPs can lead to a completely wrong structure. For example, PCN-221 was reported to be a Zr MOF with Zr_8 SBUs, which didn't exist in any previous or later studies.²⁵ It was until 2021 that the structure of PCN-221 was re-investigated. It was found that the structure doesn't contain Zr_8 SBUs.²⁶ Instead, the MOF was composed of a complex disorder that the average four Zr_6 SBUs in different orientations result in a Zr_8 -like structure (**Figure 1.3a**). Such variation of the orientations of Zr_6 SBUs was ensured by a combination of two factors: partial coordination of Zr_6 clusters, and random missing linkers throughout the crystal.

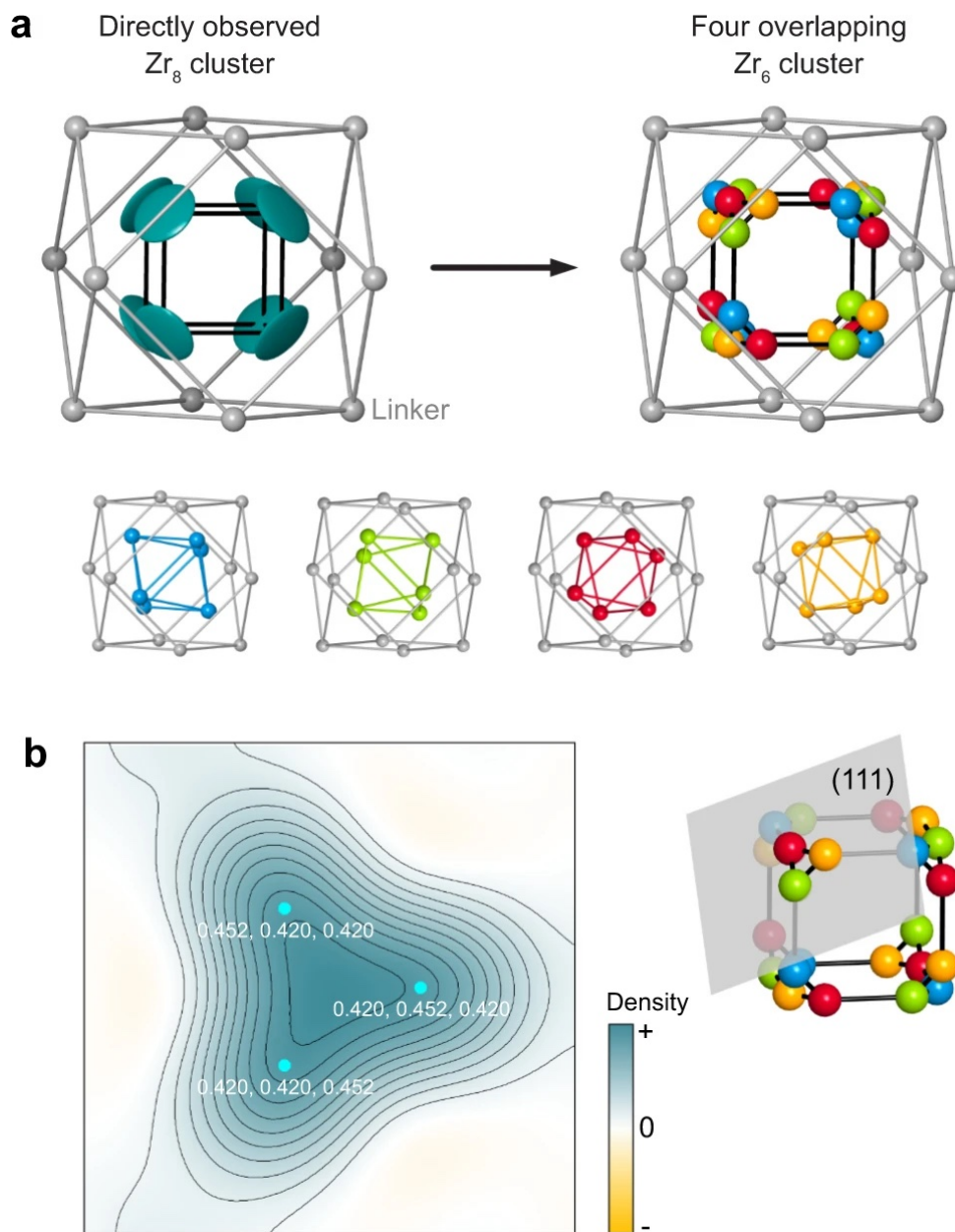


Figure 1.3. a) Illustration on how the four disorder Zr_6 clusters contributing to the average structure of “ Zr_8 SBU” in PCN-221. b). Electron density plot across the plane of three close located Zr disordered positions. Reprinted²⁶ under open access Creative Commons CC BY license.

This is unlikely to happen in molecular crystals. Molecular crystals are difficult to tolerate a significant degree of random disorders while not changing its crystalline packing mode. Interestingly, the clue for a wrong structure assignment could be found in the first place: the Zr atoms showed clearly larger-sized plate-shape ADPs (**Figure 1.3a**) while all other atoms on SBU had relatively spherical ellipsoids, and this is impossible if only thermal displacement is involved because the whole SBU must displace simultaneously as a rigid unit. The correction of the structure of PCN-221 is educational toward the crystal structure determination of reticular materials, that they need to be more than rigorously treated because of a higher level of complexity than molecular crystals.

Traditional small-molecule crystallography requires the students to split atoms when there is an abnormally long ADP; however, such interpretation is only reasonable when the disorder indeed contains a countable number of energy-minimized configurations. In other words, it is the proper treatment of disorder when the electron densities can be represented by the sum of a countable number of closely located spherical electron densities, and in this circumstance, splitting atoms will yield distinct atoms with sphere-like ADPs. For example, in the case of PCN-221 three maxima in the electron density distribution were observed at the Zr location in the “Zr₈” SBU (**Figure 1.3b**) corresponding to three distinct disordered positions. However, what is common in reticular materials are disorders caused by vibrations and rotations. As crystals are normally measured at 100 K, the vibrational and rotational states are frozen at the low temperature, resulting in Gaussian distributions of disordered positions and thus the electron density distribution. In such cases, splitting the atoms into two positions is not a model representing its physical nature: it is suggested to leave the ADP as it is, and meanwhile, describing it in the refinement details embedded in CIF files.

The deviation in the shape of atomic ADPs from spheres generally exists in almost all the crystal structures of reticular materials. The imidazole linkers in all the reported ZIF structures share a

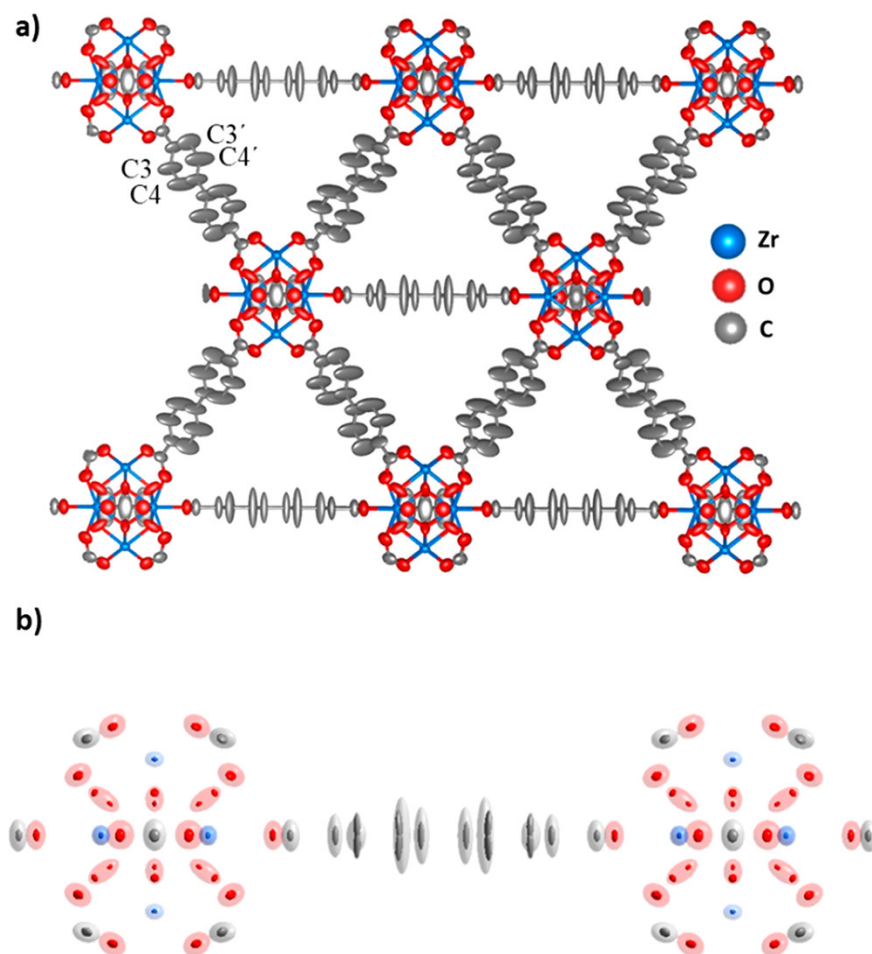


Figure 1.4. a) ADP plot and b) electron density plot of the structure of UiO-67 measured by electron diffraction. Reprinted with permission from Huang *et al.*, *J. Am. Chem. Soc.* **2021**, *143* (43), 17947–17952. Copyright 2021 American Chemical Society.

common character that the atomic ADP becomes larger as the atom gets further from the ligand-metal coordination bond.^{27,28} It is attributed to a gate-opening model proposed based on experimental observations that ZIFs allow gaseous molecules smaller than their pore openings to diffuse across the crystal.^{29,30} The trend of ADP shapes indeed follows a positional disorder distribution resulting from linker vibrations and is thus taken as a correct explanation toward the disorder. Similar linker motions are also observed in MOFs. Huang *et al.* used electron diffraction to analyze two MOFs with the same organic linker (4,4'-biphenylcarboxylate, bpdc), UiO-67 and MIL-140C.³¹ Larger ADPs of the phenyl carbons were observed in UiO-67 (**Figure 1.4a**) compared to in MIL-140C, while the bpdc linkers are π - π stacked in MIL-140C but not in UiO-67. Analyses indicated that the deviation of ADP shapes is ascribed to the liberation of bpdc linkers in UiO-67 (**Figure 1.4b**). As always, it is dangerous to hide the information behind constrained or restrained beautiful ADP shapes. In the crystal structure of PCN-136 containing hexabenzocoronene (HBC),³² it was noticed that extensive SHELXL constrains (ISOR, EADP) and restraints (DFIX, SADI, FLAT)³³ were used for all HBC carbons. After removing the constrains/restraints and refining the structure based on the embedded reflections in the CIF file, the carbons showed much longer ellipsoids (**Figure 1.5**). In addition, the bond lengths further deviated from ideal C-C bond lengths of HBC.³⁴ As the HBC unit was reported to transform from a hexaphenylbenzene unit inside a formed MOF single crystal, it is therefore of greater importance to examine the origin of elongated ADPs and understand its relationship with chemical transformation and linker disorder.

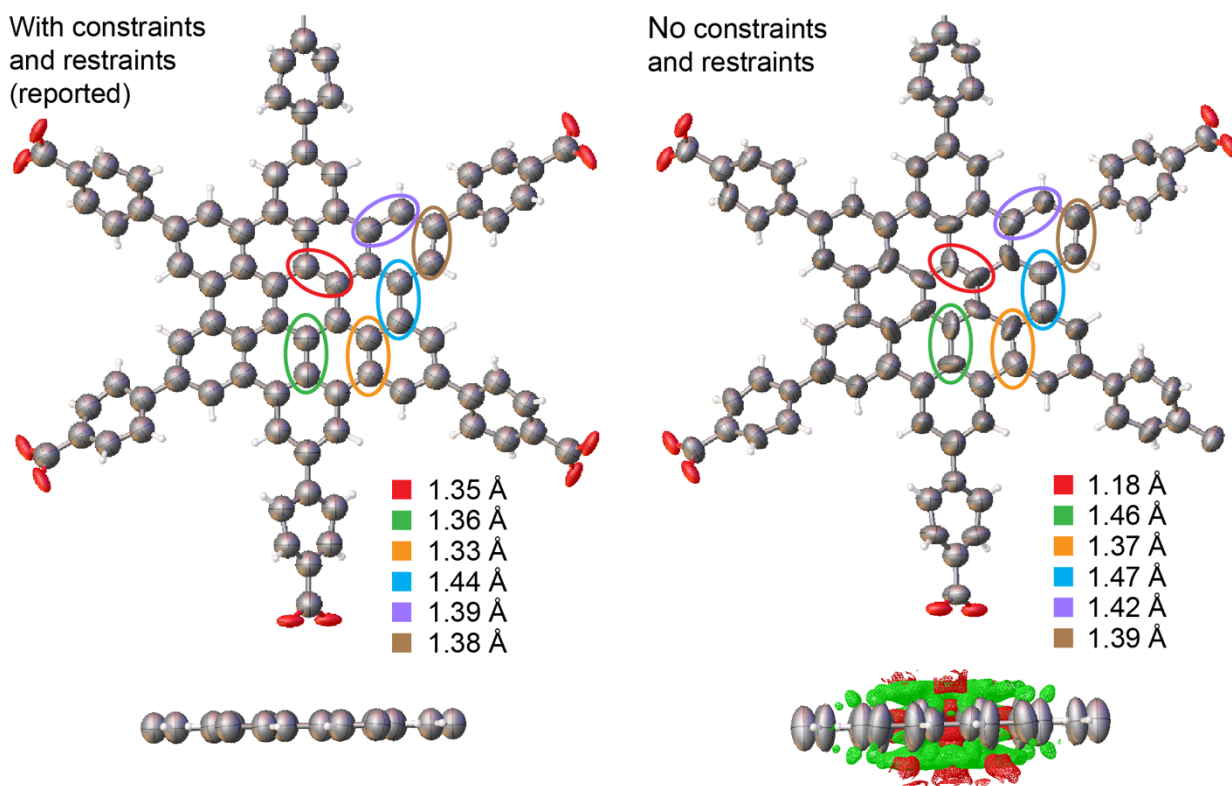


Figure 1.5. Comparison of linker geometries in the reported structure of PCN-136 and refined structure after removing restraints and constraints. The bottom figures are the horizontal look across the hexabenzocoronene ring. Residual electron density wire plot (isosurface level $0.6 e/\text{\AA}^3$) around the coronene rings overlays with the structure on the right. Green mesh indicates the positive residual density, and red mesh indicates the negative residual density.

Besides the disorders and motions of the framework themselves, the solvent inside the pores of reticular materials can additionally contribute by interacting with the frameworks. It is unclear yet whether the solvent can induce the motions as there is no direct experimental evidence. Nevertheless, it is known that the solvent can indeed induce the framework change. For example, COF-118 demonstrates distinct unit cells when dropping different solvents onto the COF.³⁵ The solvent-induced structure expansion or contraction is not a rare case. In addition, when the contained solvent is cooled to cryostream temperature (typically 100 K), the flash-frozen solvent further introduces disorder by impinging on the structure, and sometimes can seriously downgrade the material's crystallinity.³⁶ To reduce such disorders, some of them MOFs, especially large-pore MOFs, were reported to be measured at non-cryo temperatures.^{11,37} Because of the influence of solvent on the framework, it is therefore suggested to use solvent-removed (termed "activated") crystals to study the disorders and motions of reticular materials when possible.

When the influence of solvent is excluded or properly considered, the quality of the collected data provides a qualitative understanding toward the intrinsic crystallinity of the material, or in other words, reveals the level of order inside the structure. Single crystals of COFs, which were first reported in 2018, are an exemplar case.³⁸ COFs are known to be challenging to crystallize, and it was only after 13 years of COF's discovery an 80-day crystallization method was found. Among the first reported COF single crystals, COF-300 is of the best crystallinity and its reported resolution was 0.85 Å. What forms a clear contrast is LZU-111: although the reported crystal sizes used for SXRD measurement was similar to COF-300, it only diffracts around 1.8 Å under synchrotron radiation. Besides, the long ellipsoid of silicon atom at the center of LZU-111's linker indicates that the framework might has a significant translational disorder, although the failure of anisotropic refinement on other carbon atoms prevents further information to be derived from whether there is a combination of different disorders. What can be speculated is that the disorder is of a length scale matching with the diffraction limit (~ 1.8 Å). A general notion on crystallinity and disorder is important for a critical look at the properties and applications of materials, especially when "atomic precision" is featured or required in some scenarios.

1.3. Structural Dynamics of Reticular Materials

While the simple forms of dynamics such as vibrations and rotations are described in the previous section, the central interest of the community more lies in the large-scale, correlated dynamic motion throughout the framework. Correlated dynamic changes throughout the crystal mostly exist in compounds connected by strong bonds at least in one dimension. Molecular materials have weak interactions between the molecules inside crystals, which is not enough to drive correlated motions (the motion of one molecule propagates to the next one through strong interactions), or the formation of molecular crystals heavily relies on stacking that doesn't contain enough space for motions.³⁹ Minerals have strong interactions between the composing ions and are thus well-known for dynamical motions such as lattice distortion, but the scale of motions are limited by the space inside crystals.⁴⁰ Reticular materials are formed by strong correlations (covalent/coordination bonds) that potentially allow such dynamics. Moreover, the void spaces leave freedom to the motions of structural units. As a result, many reticular materials are able to undergo large-scale motions while retaining order (*i.e.*, crystallinity) throughout the structure.

MIL-53 is the earliest dynamic MOF that was discovered.⁴¹ It performed a signature pore opening-contracting motion named "breathing effect" that was confirmed by PXRD analysis. The breath of the pores was later found to determine the shape of various gas sorption isotherms of

MIL-53, and enabled its applications such as drug release. The breathing effect was later identified in several isostructural MOFs,⁴² including MOF-303, which demonstrated excellent water harvesting ability from air. *In situ* variable temperature SXRD study of a MOF-303 crystal fully loaded with water found that the breath the pore synchronizes with water desorption: the pore changes from open to almost-close form upon the desorption of first ~70% of waters, then slowly retains original open form upon the complete desorption of water.⁴³ Additional forms of large-scale motions include what led to negative gas adsorption: DUT-49 could undergo a 3-dimensional shrinking/expansion of 50% of its crystallographic volume during the sorption of methane at or above 91 K, and the evidence was provided by *in situ* serial PXRD upon methane dosing.⁴⁴ *In situ* characterizations provide an accurate correlation between structural change and guest loading. Thus, an interesting future research topic arises on how to interpret the function of structural dynamics on specific guest uptakes.

Furthermore, in 2015, our lab introduced molecular weaving, a type of COF showing high flexibility that almost diminishes crystallinity.^{45,46} Although the exact structures and motions of molecular weaving is difficult to characterize by diffraction or scattering methods, it opens up future possibilities of reticular materials: ordered materials ranging distinct flexibilities can be developed by reticular chemistry, which will push future development of crystallography from perfect crystalline solids from a junction between crystalline and non-crystalline compounds.

1.4. Conclusion

Based on the discussions above, it is concluded that crystallographic methods are able to provide enormous information on disorders and dynamics. Although crystallography produces average, static structures, information on dynamics can be extracted by ADP analyses and *in situ* serial crystallography. In addition, among the crystallographic methods, single-crystal-based experiments produce 3-dimensional real space electron density distributions from 3-dimensional information of reciprocal space, which provides the best spatial resolution and the richest information.

In this thesis, the author focuses on understanding the disorders and dynamics in reticular materials using single-crystal X-ray diffraction. In Chapters 2 and 3, guest molecules were incorporated into an aluminum MOF (MOF-520), providing a platform to understand the behaviors of the guests when residing in a void space with no influence of close-packing. Chapter 4 describes a correction to a previously reported ZIF structure (ZIF-90) after considering merohedral twinning. Rigorous crystallographic studies revealed the origin of merohedral twinning and associated it with an order-disorder transition at elevated temperatures, introducing a new facet to the forms of disorders in ZIFs. Finally, Chapter 5 aims at challenging the limit of crystallographic characterizations, and a material at the boundary of crystalline and non-crystalline, woven COF, was designed and synthesized.

1.5. Bibliography

- (1) Yaghi, O. M.; Kalmutzki, M. J.; Diercks, C. S. Introduction to Reticular Chemistry. **2019**.
- (2) Stock, N.; Biswas, S. Synthesis of Metal-Organic Frameworks (MOFs): Routes to Various MOF Topologies, Morphologies, and Composites. *Chem. Rev.* **2012**, *112* (2), 933–969.
- (3) Phan, A.; Doonan, C. J.; Uribe-Romo, F. J.; Knobler, C. B.; O’Keeffe, M.; Yaghi, O. M. Synthesis, Structure, and Carbon Dioxide Capture Properties of Zeolitic Imidazolate Frameworks. *Acc. Chem. Res.* **2010**, *43* (1), 58–67.
- (4) Geng, K.; He, T.; Liu, R.; Dalapati, S.; Tan, K. T.; Li, Z.; Tao, S.; Gong, Y.; Jiang, Q.; Jiang, D. Covalent Organic Frameworks: Design, Synthesis, and Functions. *Chem. Rev.* **2020**, *120* (16), 8814–8933.
- (5) Kalmutzki, M. J.; Hanikel, N.; Yaghi, O. M. Secondary Building Units as the Turning Point in the Development of the Reticular Chemistry of MOFs. *Sci. Adv.* **2018**, *4* (10), eaat9180.
- (6) Li, H.; Eddaoudi, M.; O’Keeffe, M.; Yaghi, O. M. Design and Synthesis of an Exceptionally Stable and Highly Porous Metal-Organic Framework. *Nature* **1999**, *402* (6759), 276–279.
- (7) El-Kaderi, H. M.; Hunt, J. R.; Mendoza-Cortés, J. L.; Côté, A. P.; Taylor, R. E.; O’Keeffe, M.; Yaghi, O. M. Designed Synthesis of 3D Covalent Organic Frameworks. *Science* **2007**, *316* (5822), 268–272.
- (8) Wang, B.; Côté, A. P.; Furukawa, H.; O’Keeffe, M.; Yaghi, O. M. Colossal Cages in Zeolitic Imidazolate Frameworks as Selective Carbon Dioxide Reservoirs. *Nature* **2008**, *453* (7192), 207–211.
- (9) Férey, G.; Mellot-Draznieks, C.; Serre, C.; Millange, F.; Dutour, J.; Surblé, S.; Margiolaki, I. A Chromium Terephthalate-Based Solid with Unusually Large Pore Volumes and Surface Area. *Science* **2005**, *309* (5743), 2040–2042.
- (10) Li, P.; Vermeulen, N. A.; Malliakas, C. D.; Gómez-Gualdrón, D. A.; Howarth, A. J.; Mehdi, B. L.; Dohnalkova, A.; Browning, N. D.; O’Keeffe, M.; Farha, O. K. Bottom-up Construction of a Superstructure in a Porous Uranium-Organic Crystal. *Science* **2017**, *356* (6338), 624–627.
- (11) Furukawa, H.; Ko, N.; Go, Y. B.; Aratani, N.; Choi, S. B.; Choi, E.; Yazaydin, A. Ö.; Snurr, R. Q.; O’Keeffe, M.; Kim, J.; Yaghi, O. M. Ultrahigh Porosity in Metal-Organic Frameworks. *Science* **2010**, *329* (5990), 424–428.
- (12) Rowsell, J. L. C.; Spencer, E. C.; Eckert, J.; Howard, J. A. K.; Yaghi, O. M. Gas Adsorption Sites in a Large-Pore Metal-Organic Framework. *Science* **2005**, *309* (5739), 1350–1354.
- (13) Kawamichi, T.; Haneda, T.; Kawano, M.; Fujita, M. X-Ray Observation of a Transient Hemiaminal Trapped in a Porous Network. *Nature* **2009**, *461* (7264), 633–635.
- (14) Warren, J. E.; Pritchard, R. G.; Abram, D.; Davies, H. M.; Savarese, T. L.; Cash, R. J.; Raithby, P. R.; Morris, R.; Jones, R. H.; Teat, S. J. A Prototype Environmental Gas Cell for in Situ Small-Molecule X-Ray Diffraction. *J. Appl. Crystallogr.* **2009**, *42* (3), 457–460.
- (15) Cox, J. M.; Walton, I. M.; Benson, C. A.; Chen, Y.-S.; Benedict, J. B. A Versatile Environmental Control Cell for in Situ Guest Exchange Single-Crystal Diffraction. *J. Appl. Crystallogr.* **2015**, *48* (2), 578–581.

- (16) Gonzalez, M. I.; Mason, J. A.; Bloch, E. D.; Teat, S. J.; Gagnon, K. J.; Morrison, G. Y.; Queen, W. L.; Long, J. R. Structural Characterization of Framework-Gas Interactions in the Metal-Organic Framework Co₂(Dobdc) by in Situ Single-Crystal X-Ray Diffraction. *Chem. Sci.* **2017**, *8* (6), 4387–4398.
- (17) McCormick, L. J.; Giordano, N.; Teat, S. J.; Beavers, C. M. Chemical Crystallography at the Advanced Light Source. *Crystals* **2017**, *7* (12), 382.
- (18) McDonald, T. M.; Mason, J. A.; Kong, X.; Bloch, E. D.; Gygi, D.; Dani, A.; Crocellà, V.; Giordanino, F.; Odoh, S. O.; Drisdell, W. S.; Vlasisavljević, B.; Dzubak, A. L.; Poloni, R.; Schnell, S. K.; Planas, N.; Lee, K.; Pascal, T.; Wan, L. F.; Prendergast, D.; Neaton, J. B.; Smit, B.; Kortright, J. B.; Gagliardi, L.; Bordiga, S.; Reimer, J. A.; Long, J. R. Cooperative Insertion of CO₂ in Diamine-Appended Metal-Organic Frameworks. *Nature* **2015**, *519* (7543), 303–308.
- (19) Øien-Ødegaard, S.; Shearer, G. C.; Wragg, D. S.; Lillerud, K. P. Pitfalls in Metal–Organic Framework Crystallography: Towards More Accurate Crystal Structures. *Chem. Soc. Rev.* **2017**, *46* (16), 4867–4876.
- (20) Trueblood, K. N.; Bürgi, H.-B.; Burzlaff, H.; Dunitz, J. D.; Gramaccioli, C. M.; Schulz, H. H.; Shmueli, U.; Abrahams, S. C. Atomic Displacement Parameter Nomenclature. Report of a Subcommittee on Atomic Displacement Parameter Nomenclature. *Acta Crystallogr., Sect. A: Found. Crystallogr.* **1996**, *52* (5), 770–781.
- (21) Girolami, G. S. Chapter 36. Modeling the Electron Density. In *X-ray Crystallography*; University Science Books: Mill Valley, California, USA, **2015**; p 387.
- (22) Spek, A. L. PLATON SQUEEZE: A Tool for the Calculation of the Disordered Solvent Contribution to the Calculated Structure Factors. *Acta Crystallographica Section C: Structural Chemistry* **2015**, *71* (1), 9–18.
- (23) Øien, S.; Wragg, D.; Reinsch, H.; Svelle, S.; Bordiga, S.; Lamberti, C.; Lillerud, K. P. Detailed Structure Analysis of Atomic Positions and Defects in Zirconium Metal–Organic Frameworks. *Cryst. Growth Des.* **2014**, *14* (11), 5370–5372.
- (24) Trickett, C. A.; Gagnon, K. J.; Lee, S.; Gándara, F.; Bürgi, H.; Yaghi, O. M. Definitive Molecular Level Characterization of Defects in UiO-66 Crystals. *Angew. Chem. Int. Ed.* **2015**, *54* (38), 11162–11167.
- (25) Feng, D.; Jiang, H.-L.; Chen, Y.-P.; Gu, Z.-Y.; Wei, Z.; Zhou, H.-C. Metal–Organic Frameworks Based on Previously Unknown Zr₈/Hf₈ Cubic Clusters. *Inorg. Chem.* **2013**, *52* (21), 12661–12667.
- (26) Koschnick, C.; Stäglich, R.; Scholz, T.; Terban, M. W.; Mankowski, A. von; Savasci, G.; Binder, F.; Schökel, A.; Etter, M.; Nuss, J.; Siegel, R.; Germann, L. S.; Ochsenfeld, C.; Dinnebier, R. E.; Senker, J.; Lotsch, B. V. Understanding Disorder and Linker Deficiency in Porphyrinic Zirconium-Based Metal–Organic Frameworks by Resolving the Zr₈O₆ Cluster Conundrum in PCN-221. *Nat. Commun.* **2021**, *12* (1), 3099.
- (27) Banerjee, R.; Phan, A.; Wang, B.; Knobler, C.; Furukawa, H.; O’Keeffe, M.; Yaghi, O. M. High-Throughput Synthesis of Zeolitic Imidazolate Frameworks and Application to CO₂ Capture. *Science* **2008**, *319* (5865), 939–943.

- (28) Yang, J.; Zhang, Y.-B.; Liu, Q.; Trickett, C. A.; Gutiérrez-Puebla, E.; Monge, M. A.; Cong, H.; Aldossary, A.; Deng, H.; Yaghi, O. M. Principles of Designing Extra-Large Pore Openings and Cages in Zeolitic Imidazolate Frameworks. *J. Am. Chem. Soc.* **2017**, *139* (18), 6448–6455.
- (29) Hayashi, H.; Côté, A. P.; Furukawa, H.; O’Keeffe, M.; Yaghi, O. M. Zeolite A Imidazolate Frameworks. *Nat. Mater.* **2007**, *6* (7), 501–506.
- (30) Casco, M. E.; Cheng, Y. Q.; Daemen, L. L.; Fairen-Jimenez, D.; Ramos-Fernández, E. V.; Ramirez-Cuesta, A. J.; Silvestre-Albero, J. Gate-Opening Effect in ZIF-8: The First Experimental Proof Using Inelastic Neutron Scattering. *Chem. Commun.* **2016**, *52* (18), 3639–3642.
- (31) Samperisi, L.; Jaworski, A.; Kaur, G.; Lillerud, K. P.; Zou, X.; Huang, Z. Probing Molecular Motions in Metal–Organic Frameworks by Three-Dimensional Electron Diffraction. *J. Am. Chem. Soc.* **2021**, *143* (43), 17947–17952.
- (32) Qin, J.-S.; Yuan, S.; Zhang, L.; Li, B.; Du, D.-Y.; Huang, N.; Guan, W.; Drake, H. F.; Pang, J.; Lan, Y.-Q.; Alsalme, A.; Zhou, H.-C. Creating Well-Defined Hexabenzocoronene in Zirconium Metal–Organic Framework by Postsynthetic Annulation. *J. Am. Chem. Soc.* **2019**, *141* (5), 2054–2060.
- (33) Sheldrick, G. M. SHELXL instructions https://shelx.uni-goettingen.de/shelxl_html.php (accessed 2021/11/23).
- (34) Goddard, R.; Haenel, M. W.; Herndon, W. C.; Krueger, C.; Zander, M. Crystallization of Large Planar Polycyclic Aromatic Hydrocarbons: The Molecular and Crystal Structures of Hexabenzobenzocoronene and Benzo[1,2,3-Bc:4,5,6-b’c’]Dibenzocoronene. *J. Am. Chem. Soc.* **1995**, *117* (1), 30–41.
- (35) Zhao, C.; Diercks, C. S.; Zhu, C.; Hanikel, N.; Pei, X.; Yaghi, O. M. Urea-Linked Covalent Organic Frameworks. *J. Am. Chem. Soc.* **2018**, *140* (48), 16438–16441.
- (36) Lee, S.; Bürgi, H.-B.; Alshimmri, S. A.; Yaghi, O. M. Impact of Disordered Guest–Framework Interactions on the Crystallography of Metal–Organic Frameworks. *J. Am. Chem. Soc.* **2018**, *140* (28), 8958–8964.
- (37) Farha, O. K.; Eryazici, I.; Jeong, N. C.; Hauser, B. G.; Wilmer, C. E.; Sarjeant, A. A.; Snurr, R. Q.; Nguyen, S. T.; Yazaydin, A. O.; Hupp, J. T. Metal–Organic Framework Materials with Ultrahigh Surface Areas: Is the Sky the Limit? *J. Am. Chem. Soc.* **2012**, *134* (36), 15016–15021.
- (38) Ma, T.; Kapustin, E. A.; Yin, S. X.; Liang, L.; Zhou, Z.; Niu, J.; Li, L.-H.; Wang, Y.; Su, J.; Li, J.; Wang, X.; Wang, W. D.; Wang, W.; Sun, J.; Yaghi, O. M. Single-Crystal X-Ray Diffraction Structures of Covalent Organic Frameworks. *Science* **2018**, *361* (6397), 48–52.
- (39) Briels, W. J.; Jansen, A. P. J.; Avoird, A. V. D. Dynamics of Molecular Crystals. *Adv. Quantum Chem.* **1986**, *18*, 131–206.
- (40) Salje, E. K. H. Crystallography and Structural Phase Transitions, an Introduction. *Acta Crystallogr., Sect. A: Found. Crystallogr.* **1991**, *47* (5), 453–469.
- (41) Millange, F.; Serre, C.; Férey, G. Synthesis, Structure Determination and Properties of MIL-53as and MIL-53ht: The First Cr III Hybrid Inorganic–Organic Microporous Solids: Cr III (OH)·{O₂C–C₆H₄–CO₂}·{HO₂C–C₆H₄–CO₂H} x. *Chem. Commun.* **2002**, *0* (8), 822–823.

- (42) Férey, G.; Serre, C. Large Breathing Effects in Three-Dimensional Porous Hybrid Matter: Facts, Analyses, Rules and Consequences. *Chem. Soc. Rev.* **2009**, *38* (5), 1380–1399.
- (43) Hanikel, N.; Pei, X.; Chheda, S.; Lyu, H.; Jeong, W.; Sauer, J.; Gagliardi, L.; Yaghi, O. M. Evolution of Water Structures in Metal-Organic Frameworks for Improved Atmospheric Water Harvesting. *Science* **2021**, *374* (6566), 454–459.
- (44) Krause, S.; Bon, V.; Senkowska, I.; Stoeck, U.; Wallacher, D.; Többers, D. M.; Zander, S.; Pillai, R. S.; Maurin, G.; Coudert, F.-X.; Kaskel, S. A Pressure-Amplifying Framework Material with Negative Gas Adsorption Transitions. *Nature* **2016**, *532* (7599), 348–352.
- (45) Liu, Y.; Ma, Y.; Zhao, Y.; Sun, X.; Gándara, F.; Furukawa, H.; Liu, Z.; Zhu, H.; Zhu, C.; Suenaga, K.; Oleynikov, P.; Alshammari, A. S.; Zhang, X.; Terasaki, O.; Yaghi, O. M. Weaving of Organic Threads into a Crystalline Covalent Organic Framework. *Science* **2016**, *351* (6271), 365–369.
- (46) Liu, Y.; Diercks, C. S.; Ma, Y.; Lyu, H.; Zhu, C.; Alshimmri, S. A.; Alshihri, S.; Yaghi, O. M. 3D Covalent Organic Frameworks of Interlocking 1D Square Ribbons. *J. Am. Chem. Soc.* **2019**, *141* (1), 677–683.

Chapter 2.

Structures and Disorders of Small Molecules Binding onto MOF-520

The research in this chapter was published as a part of:

Pei, X.; Bürgi, H.-B.; Kapustin, E. A.; Liu, Y.; Yaghi, O. M. Coordinative Alignment in the Pores of MOFs for the Structural Determination of N-, S-, and P-Containing Organic Compounds Including Complex Chiral Molecules. *J. Am. Chem. Soc.* **2019**, *141* (47), 18862–18869. <https://doi.org/10.1021/jacs.9b10501>.

2.1. Introduction

Single-crystal X-ray diffraction (SXRD) analysis is a powerful technique to determine the spatial arrangement of molecules with atomic precision. While single crystals for most common molecules can be obtained, it remains a problem when the amount of material is limited, the crystal quality is poor, and the target molecule is complex and of irregular geometry. In 2016, our group reported the coordinative alignment (CAL) method: It involves the coordinative attachment of the molecule of interest to the backbone of a chiral metal-organic framework (MOF), MOF-520.^{1,2} In this way the crystallinity of the MOF allows determination of the single-crystal X-ray structure and absolute configuration of the bound molecule. This method provides a number of advantages: (1) The coordinative attachment of target molecules to the framework backbone decreases their motional degrees of freedom and aligns them into an ordered pattern within the MOF, thus facilitating their structural determination; and (2) each of the two enantiomorphs of chiral MOF-520 (Δ and Λ) can selectively crystallize one of the enantiomers from a racemic mixture of target molecules. In contrast to previously reported methods,³⁻⁵ the CAL method is enabled by strong bonding that anchors the functional groups of the target molecule onto the framework, in addition, weak interactions between the molecule and the framework help in steadying the former. To be suitable for structure solution using the CAL method, target molecules need to bear functional groups that can coordinate to metal sites of the framework's secondary building units (SBUs, Al^{3+} in the case of MOF-520). As such, expanding the scope of suitable coordinating functionalities is paramount to gaining access to structural data of a library of chiral and complex organic molecules that are difficult to crystallize on their own.

In this work, molecules containing three new categories of functionalities; namely, nitrogen-containing azolates, sulfur-containing oxoacids, and phosphorous-containing oxoacids (**Scheme 1a**) were successfully crystallized in MOF-520. The precise structures of seventeen molecules with these functionalities were unambiguously determined, four of which are complex molecules being crystallized for the first time. The high robustness of MOF-520 allows solvent in the pores to be evacuated and ensure better definition of the structures of the target molecule at low occupancy. Compared to solvated structures, these molecules were better aligned and the electron density background due to solvent molecules was significantly reduced. The stereoselectivity induced by the chirality of MOF-520 was further studied. The chiral host not only enables high selectivity towards one enantiomer of a racemic mixture, but also imposes diastereoselective incorporation of achiral molecules to crystallize in specific orientations. Indeed, the stereoselectivity of MOF-520 stems from asymmetric chemical bonding in addition to previously observed steric and intermolecular interactions of the chiral pore environment.¹

2.2. Experimental

2.2.1. Materials

$Al(NO_3)_3 \cdot 9H_2O$, *N,N*-dimethylformamide (DMF) (98%, HPLC) were purchased from Sigma-Aldrich. 1,3,5-benzenetricarboxylic acid (H_3BTB) was purchased from TCI America. Formic acid (99.8 %) was obtained from EMD Millipore. Anhydrous acetone was purchased from Acros Organics. Molecule **1**, **8** were purchased from Alfa Aesar. Molecule **2**, **4** were purchased from TCI America. Molecule **3**, **5**, **6**, **9**, **10**, **12**, were purchased from Sigma-Aldrich. Molecule **7** was purchased from EMD Millipore. Molecule **13** was purchased from Enamine LLC. Sodium benzenesulfonate was purchased from Fluka Chemie AG. Tetrabutylammonium chloride was purchased from Chem Impex Intl Inc. *N,N*-dimethylformamide (DMF) (98%, HPLC) was

purchased from Sigma-Aldrich and was purified in an Inert[®] solvent purification system PureSolv MD7 before use. All other chemicals were used without further purification. Scintillation vials (20 mL) and polypropylene cabs with foil liner were purchased from VWR International, LLC.

2.2.2. Synthesis of MOF-520 Single Crystals

90 mg $\text{Al}(\text{NO}_3)_3 \cdot 9\text{H}_2\text{O}$ was dissolved in 2 mL anhydrous DMF and 75 mg H_3BTB was dissolved in 2 mL anhydrous DMF. Two solutions were mixed and additional 13 mL anhydrous DMF was added, followed by 1.75 mL formic acid and 40 μL deionized water. The amount of formic acid and deionized water needs to be adjusted carefully if different brands of chemicals are selected, or the bottles have been opened for long time, because the moisture contents of anhydrous DMF and formic acid can change over time. The mixture was sealed in a 20 mL scintillation vial then heated at 140 °C for 3 to 5 days. Colorless block crystals were obtained, washed with DMF (9×20 mL) for 3 days and soaked in CH_2Cl_2 before further use.

2.2.3. Procedure for Incorporation of Target Molecules

General Procedure: Nitrogen-containing azolates were incorporated into MOF-520 by immersion of pristine MOF-520 in 0.1 to 1 mol L^{-1} *N,N*-dimethylformamide (DMF) solutions at 85–100 °C for 2 or 3 days. Sulfur oxoacids were incorporated by immersion in 0.3–0.6 mol L^{-1} solutions at 85–100 °C for 1 or 2 days. Phosphorous oxoacids were incorporated by immersion in 0.005–0.015 mol L^{-1} solutions at –20 to 0 °C for 2 or 3 days.

Detail Procedures:

MOF-520-1: 1 mg of MOF-520 were immersed in 1 mL of 1 mol L^{-1} DMF solution of **1** and the reaction mixture was heated at 85 °C for 2 days. The crystals were washed with DMF for 3 times in one day before SXRD measurement.

MOF-520-2: 1 mg of MOF-520 were immersed in 1 mL of 0.5 mol L^{-1} DMF solution of **2** and the reaction mixture was heated at 75 °C for 3 days. The crystals were washed with DMF for 3 times in one day before SXRD measurement.

MOF-520-3: 1 mg of MOF-520 were immersed in 1 mL of 0.75 mol L^{-1} DMF solution of **3** and the reaction mixture was heated at 70 °C for 3 days. The crystals were washed with DMF for 3 times in one day before further treatment.

MOF-520-4: 1 mg of MOF-520 were immersed in 1 mL of 1 mol L^{-1} DMF solution of **20** and the reaction mixture was heated at 70 °C for 3 days. The crystals were washed with DMF for 3 times in one day before SXRD measurement.

MOF-520-5: 1 mg of MOF-520 were immersed in 1 mL of 0.5 mol L^{-1} DMF solution of **5** and the reaction mixture was heated at 85 °C for 2 days. The crystals were washed with DMF for 3 times in one day before further treatment.

MOF-520-6: To a 0.03 mol L^{-1} solution of H_2SO_4 in DMF, 2 equivalents of triethylamine was added. The solution was heated at 50 °C overnight before use to make sure the deprotonation of **6** is completed. 1 mg of MOF-520 were immersed in 1 mL the solution, and the reaction mixture was heated at 85 °C for 2 days. After that, the crystals were washed with DMF for 3 times in one day before SXRD measurement.

MOF-520-7: To a 0.015 mol L^{-1} solution of **7** in DMF, 1 equivalent of triethylamine was added. The solution was heated at 50 °C overnight before use to make sure the deprotonation of **7** is completed. 1 mg of MOF-520 were immersed in 1 mL of the solution and the reaction mixture

was kept at 0 °C for 3 days. After that, the crystals were immediately washed with DMF for 3 times then soaked in DMF before SXRD measurement.

MOF-520-8: To a 0.015 mol L⁻¹ solution of **8** in DMF, 1 equivalent of triethylamine was added. The solution was heated at 50 °C overnight before use to make sure the deprotonation of **8** is completed. 1 mg of MOF-520 were immersed in 1 mL the solution, and the reaction mixture was kept at 0 °C for 3 days. After that, the crystals were immediately washed with DMF for 3 times then soaked in DMF before SXRD measurement.

MOF-520-9: To a 0.015 mol L⁻¹ solution of **9** in DMF, 1 equivalent of triethylamine was added. The solution was heated at 50 °C overnight before use to make sure the deprotonation of **9** is completed. 1 mg of MOF-520 were immersed in 1 mL of the solution, and the reaction mixture was kept at 0 °C for 3 days. After that, the crystals were immediately washed with DMF for 3 times then soaked in DMF before further treatment.

MOF-520-10: To a 0.005 mol L⁻¹ solution of **10** in DMF, 1 equivalent of triethylamine was added. The solution was heated at 50 °C overnight before use to make sure the deprotonation of **10** is completed. 1 mg of MOF-520 were immersed in 1 mL of the solution, and the reaction mixture was kept at -20 °C for 2 days. After that, the crystals were immediately washed with DMF for 3 times then soaked in DMF before further treatment.

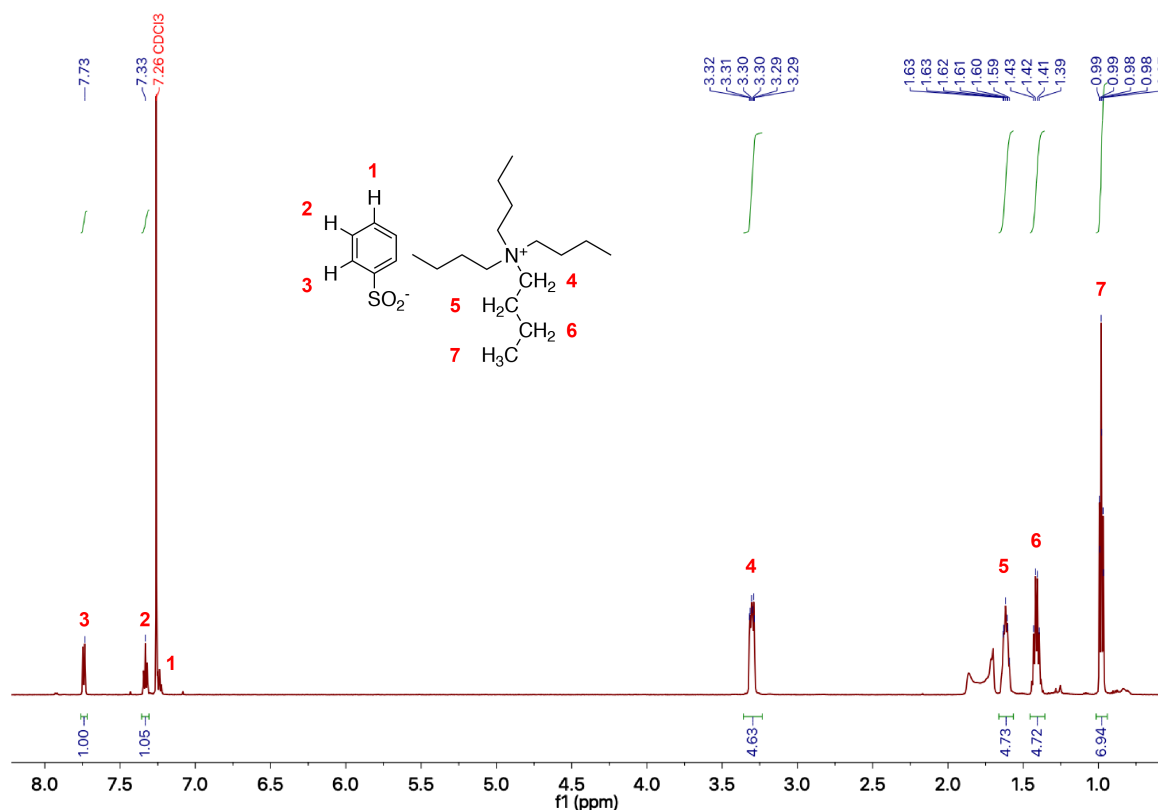


Figure 2.1. ¹H NMR spectra of tetrabutylammonium benzenesulfinate (**11**).

MOF-520-11: 1.27g sodium benzenesulfinate and 0.27g tetrabutylammonium chloride was dissolved in 20 mL water and the solution was extracted with chloroform for one time. The extraction was dried with MgSO₄ and the solvent was removed under vacuum to obtain tetrabutylammonium benzenesulfinate with purity of ~85% (determined by ¹H NMR Spectroscopy,

Figure S1). The impurity was determined to be tetrabutylammonium chloride based on ^1H NMR Spectrum, besides that sodium benzenesulfinate doesn't dissolve in chloroform. The mixture was dissolved in anhydrous acetone to form a solution of 0.06 mol L^{-1} concentration of tetrabutylammonium benzenesulfinate. 1 mg of MOF-520 were immersed in 1 mL of the solution and the reaction mixture was degassed before sealed in a glass tube then heated at $100\text{ }^\circ\text{C}$ for 1 day. The crystals were washed with anhydrous acetone for 3 times before SXRD measurement.

MOF-520-12: 1 mg of MOF-520 were immersed in 1 mL of 0.25 mol L^{-1} DMF solution of **12** and the reaction mixture was heated at $85\text{ }^\circ\text{C}$ for 2 days. The crystals were immediately washed with DMF for 3 times before further treatment.

MOF-520-13: To a 0.033 mol L^{-1} solution of **13** in DMF, 1 equivalent of triethylamine was added. The solution was degassed and heated at $50\text{ }^\circ\text{C}$ overnight before use to make sure the deprotonation of the acid is completed. Crystals of MOF-520 were immersed in 1 mL the solution and the reaction mixture was heated at $85\text{ }^\circ\text{C}$ for 1 day. The crystals were immediately washed with DMF for 3 times then soaked in DMF until further use.

2.2.4. Single-Crystal X-ray Diffraction

Because the chirality of a single crystal could not be distinguished by inspection of the shape of the crystal or by polarized light, the choice of the chirality of the inclusion crystal from the batch was random. Three single crystals from each batch of incorporated samples were analyzed by SXRD. The dataset with best R_{int} and resolution was chosen and is reported here. Single crystal data were collected at beamlines 11.3.1/12.2.1 at the Advanced Light Source, and a Bruker D8 Venture diffractometer. Single crystals were mounted in a 100(2) K nitrogen cold stream. The data up to $\sin(\theta)/\lambda = 2/3$ were collected with combined phi and omega scans to ensure a data multiplicity of at least 8. The raw data were processed with the Bruker APEX3 V8.38 software package.⁶ The data were first integrated using SAINT and then corrected for absorption with SADABS.⁷ The structures were solved by direct methods (*SHELXS*) and the refinements done by full-matrix least squares on F^2 (*SHELXL*),^{8,9} using the Olex² software package.¹⁰ Solvent masking was applied to non-activated structures.^{11,12} Parameters indicating data quality fall into the following ranges: resolution, $0.75\text{--}0.90\text{ \AA}$; R_{int} , $4.72\%\text{--}11.82\%$; R , $3.21\%\text{--}8.14\%$; Flack parameter, $-0.01(5)$ to $0.16(5)$; standard uncertainties of C–C bond lengths, $0.0020\text{--}0.0076\text{ \AA}$. Details for each structure determination are described in Section 2.5.

2.2.5. Computational Methods

Density functional theory (DFT) calculations on the total energy of the molecular models of the secondary building unit (SBU) were performed using spin-unrestricted dispersion-corrected PBE0-D3(BJ) functional (except one that used PBE0) implemented in Gaussian 16 (revision A03).^{13–15} Def2-SVPD basis sets were used for all N, O atoms, as well as all carboxylates and α -C of carboxylates, while def2-SVP basis sets were employed for all other C atoms. Def2-SV(P) was used for all H atoms. Def2-TZVP was used for Al atoms.^{16,17} The structures were not optimized before total energy calculation because the geometric optimization will make the model deviated a lot from crystal structure, which will not be able to resemble the energy of the experimental structure from SXRD result.

Solvent effects were accounted by polarizable continuum model (PCM)¹⁸ using the integral equation formalism variant (IEF-PCM). Default solvent surface models in the PCM is van der Waals (vdW) surface, and when ionic solution environment is applied, solvent-excluded surface

Table 2.1. Summary of parameters from the reported crystallographic data.

Name	<i>a</i> /Å	<i>c</i> /Å	Molecule occupancy	Resolution /Å	Solvent evacuation	<i>R</i> _{int}	<i>R</i> (all data)	Flack parameter	s.u. of C-C bond length /Å	Weighting parameters*	
										<i>a</i>	<i>b</i>
Δ-MOF-520	18.5778(6)	37.2977(13)	-	0.78	No	5.79%	8.14%	-0.01(5)	0.0058	0.1702	0.6465
Δ-MOF-520-1	19.4481(6)	35.7074(13)	0.936(5)	0.85	No	4.72%	7.16%	0.039(13)	0.0053	0.0763	0
Δ-MOF-520-2	18.9000(10)	36.682(2)	0.680(4)	0.75	No	6.17%	2.74%	0.06(2)	0.0020	0.0495	0
Δ-MOF-520-2	18.9155(9)	36.6951(19)	0.632(4)	0.85	No	5.91%	3.21%	0.15(4)	0.0024	0.0289	0
Δ-MOF-520-3	19.5339(5)	35.7057(10)	0.8624	0.80	Yes	7.14%	4.73%	-0.02(2)	0.0031	0.0909	1.6816
Δ-MOF-520-4	18.8135(11)	36.797(2)	0.5180	0.90	No	11.82%	4.22%	0.08(7)	0.0047	0.0548	0
Δ-MOF-520-5	19.4353(6)	35.7957(11)	1	0.75	Yes	7.27%	7.77%	-0.003(3)	0.0052	0.1385	4.1029
Δ-MOF-520-6	18.1729(8)	37.6737(17)	0.8602(15)	0.83	No	4.72%	3.50%	0.053(11)	0.0025	0.0332	0
Δ-MOF-520-7	18.1702(6)	37.8430(14)	0.5479	0.83	No	5.90%	3.30%	0.08(2)	0.0030	0.0689	0
Δ-MOF-520-8	18.7104(5)	37.1528(11)	0.506(4)	0.80	No	6.81%	5.23%	0.10(5)	0.0032	0.0493	0
Δ-MOF-520-8	18.6051(8)	37.3840(18)	0.514(4)	0.80	No	7.52%	3.69%	0.16(5)	0.0024	0.0319	0
Δ-MOF-520-9	18.9892(8)	36.9796(15)	0.7264	0.85	Yes	6.04%	5.13%	-0.01(2)	0.0046	0.1027	1.4516
Δ-MOF-520-10	19.1935(11)	36.602(2)	0.349(8)	0.85	Yes	5.29%	7.31%	0.01(2)	0.0076	0.1374	3.9533
Δ-MOF-520-11	18.4641(6)	37.4193(12)	0.3594	0.80	No	6.08%	5.26%	0.05(2)	0.0039	0.1194	0
Δ-MOF-520-12	19.3331(6)	36.2317(12)	0.3821	0.85	Yes	7.32%	6.82%	0.03(4)	0.0057	0.1191	1.6967
Δ-MOF-520-13	18.6986(11)	37.201(3)	0.5219	0.90	No	9.93%	6.46%	0.14(6)	0.0074	0.1123	0

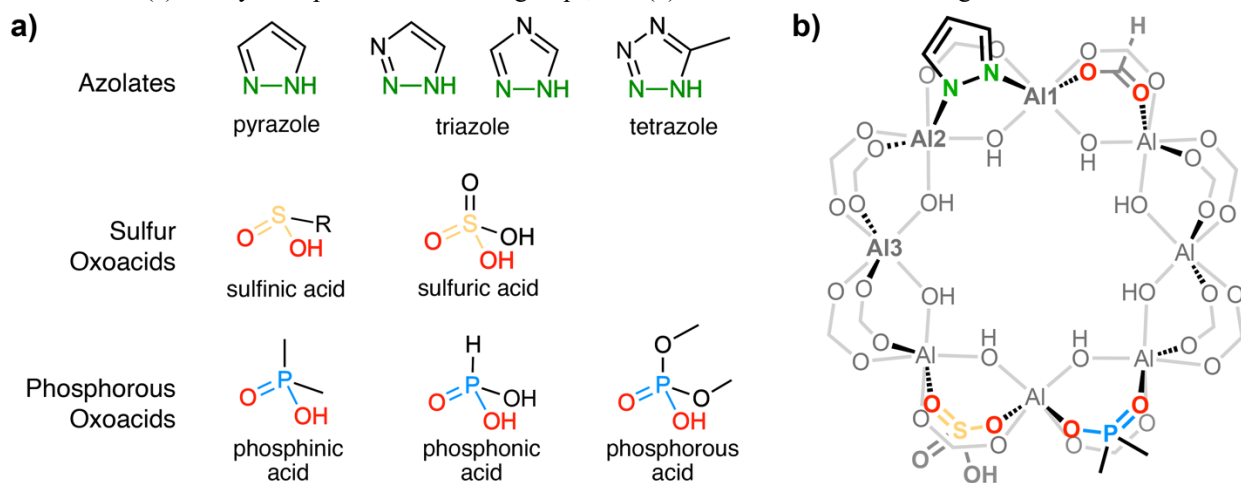
(SES). To control the variables in the calculation, the surface generation methods were unified to SES in all cases, as it's a more realistic description of the surface that solvent forms compared to vdW surface. The Gaussian keyword IONIC DISM was used to specify ionic strength in the system.

Hirshfeld surface of the bounded **2** were computed by CrystalExplorer17¹⁹ using a local implementation of B3LYP-D2/6-31G(d,p).

2.3. Results and Discussions

MOF-520 crystallizes in the Sohncke space group $P4_22_12$. Each MOF-520 crystal is enantiopure (labelled as Δ or Λ) but the batch is a racemic mixture of both enantiomorphs of MOF-520. The SBUs of the framework are composed of eight aluminum octahedra in a circular arrangement with 222 point symmetry.²⁰ Each pair of adjacent aluminum atoms is bridged by one μ_2 -OH and two carboxylate groups (Scheme 2.1b). Out of the sixteen μ_2 -COO at each SBU, twelve are contributed by the organic linker 1,3,5-benzotribenzoate (BTB), and four are formate ligands that can be exchanged by incoming target molecules with coordinating functionalities. The different carboxylates provide the aluminum atoms with three different chemical environments: Al1 is coordinated to two formates and two BTBs, Al2 is coordinated to one formate and three BTBs, while Al3 is coordinated to four BTBs.

Scheme 2.1. (a) Newly incorporated functional groups, and (b) illustration of their binding modes.

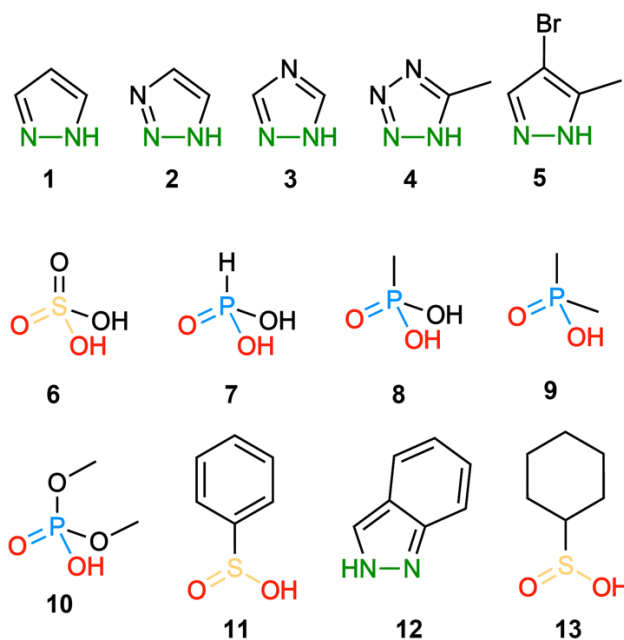


2.3.1. Incorporation of Target Molecules with N-, S-, P-containing Functionalities.

In this work, molecules of eight new classes of coordination moieties were introduced into MOF-520, including pyrazole, triazole, tetrazole, sulfuric acid, sulfinic acid, phosphinic acid, phosphonic acid, and phosphoric acid (Scheme 2.1a). As a result, 17 molecules were incorporated into MOF-520: 1*H*-pyrazole **1**, 1*H*-1,2,3-triazole **2**, 1*H*-1,2,4-triazole **3**, 5-methyl-1*H*-tetrazole **4**, 4-bromo-3-methyl-1*H*-pyrazole **5**, sulfuric acid **6**, phosphonic acid **7**, methylphosphonic acid **8**, dimethylphosphonic acid **9**, dimethyl phosphate **10**, phenylsulfinic acid **11**, 1*H*-indazole **12**, cyclohexanesulfinic acid **13** (Scheme 2.2).

The incorporation temperatures, concentrations, and reaction times were similar within each respective group of N-, S-, and P-containing molecules. Molecules with nitrogen containing azolates were introduced into MOF-520 as 0.15–1 mol L⁻¹ solutions at 85 °C, while sulfur oxoacids were incorporated at lower concentrations (0.033–0.06 mol L⁻¹) and phosphorous oxoacids were introduced at lower temperatures of 0 °C or –20 °C due to different ligand binding strength. Lower

Scheme 2.2. Target molecules of incorporation.



temperatures and concentrations decrease the diffusion rate of molecules within the pores of the MOF. Therefore, the loading of phosphorous oxoacids is approximately 25–70%, while the azolate-bonded molecules generally show higher loadings (50–100%) (Table 2.1).

The high structural and chemical stability of MOF-520 facilitates ligand substitution while preserving crystallinity of the backbone. Both the space group and enantiomorph of MOF-520 remain unchanged since the incoming ligands bind to the MOF in the same μ_2 -bridging fashion as the replaced formates (Scheme 2.1b). The changes of the unit cell parameters of MOF-520 upon binding of the molecules serve as a first indicator of incorporation. In pristine MOF-520, the unit cell parameters are approximately $18.58 \text{ \AA} \times 18.58 \text{ \AA} \times 37.30 \text{ \AA}$. On substituting the formates by azolates, the c axis of azolate-incorporated MOF-520 is shortened to $\sim 35.7 \text{ \AA}$, while the a and b axes elongate to $\sim 19.5 \text{ \AA}$ (Table 2.1). This can be traced to the change of distance between the coordinating atoms (*i.e.* $\sim 2.3 \text{ \AA}$ between the oxygen atoms of formates, but $\sim 1.4 \text{ \AA}$ between nitrogen atoms of azolates, Figure 2.2a-f, m), which leads to a distortion of the SBU and consequently of the entire unit cell. For similar reasons, the a and b axes are slightly longer in sulfur and phosphorous oxoacids, whereas the c axis is slightly shorter: the unit cell parameters of Λ -MOF-520-13 are $a = 18.7011(9) \text{ \AA}$ and $c = 37.206(2) \text{ \AA}$, and of Δ -MOF-520-9, $a = 18.9892(8) \text{ \AA}$ and $c = 36.9796(15) \text{ \AA}$ (Table 2.1). The connectivity and conformations of incorporated molecules were determined with atomic precision (Figure 2.2).

2.3.2. Single-Crystal X-ray Diffraction Studies of Sulfur-Oxoacids-Incorporated MOF-520

Sulfuric acid (**6**) retains its tetrahedral geometry when coordinates to MOF-520 through one double-bonded oxygen and one deprotonated hydroxyl oxygen, as corroborated by the observed bond lengths [$1.4625(12) \text{ \AA}$ and $1.5018(11) \text{ \AA}$; Figure 2.2g].^{21–23} The presence of an oxygen atom from a solvent molecule inside of the MOF's pore was also observed, and its distance to the closest oxygen atom of **6** is $\sim 2.73 \text{ \AA}$, suggesting hydrogen bonding might exist between **6** and solvent which energetically stabilizes the position of the target molecule. However, the structure of Λ -MOF-520-**6** was resolved with DMF presenting in the pores, which is an aprotic solvent. In addition, the solution used for incorporating sulfate into DMF is sulfuric acid and 2 equivalents of

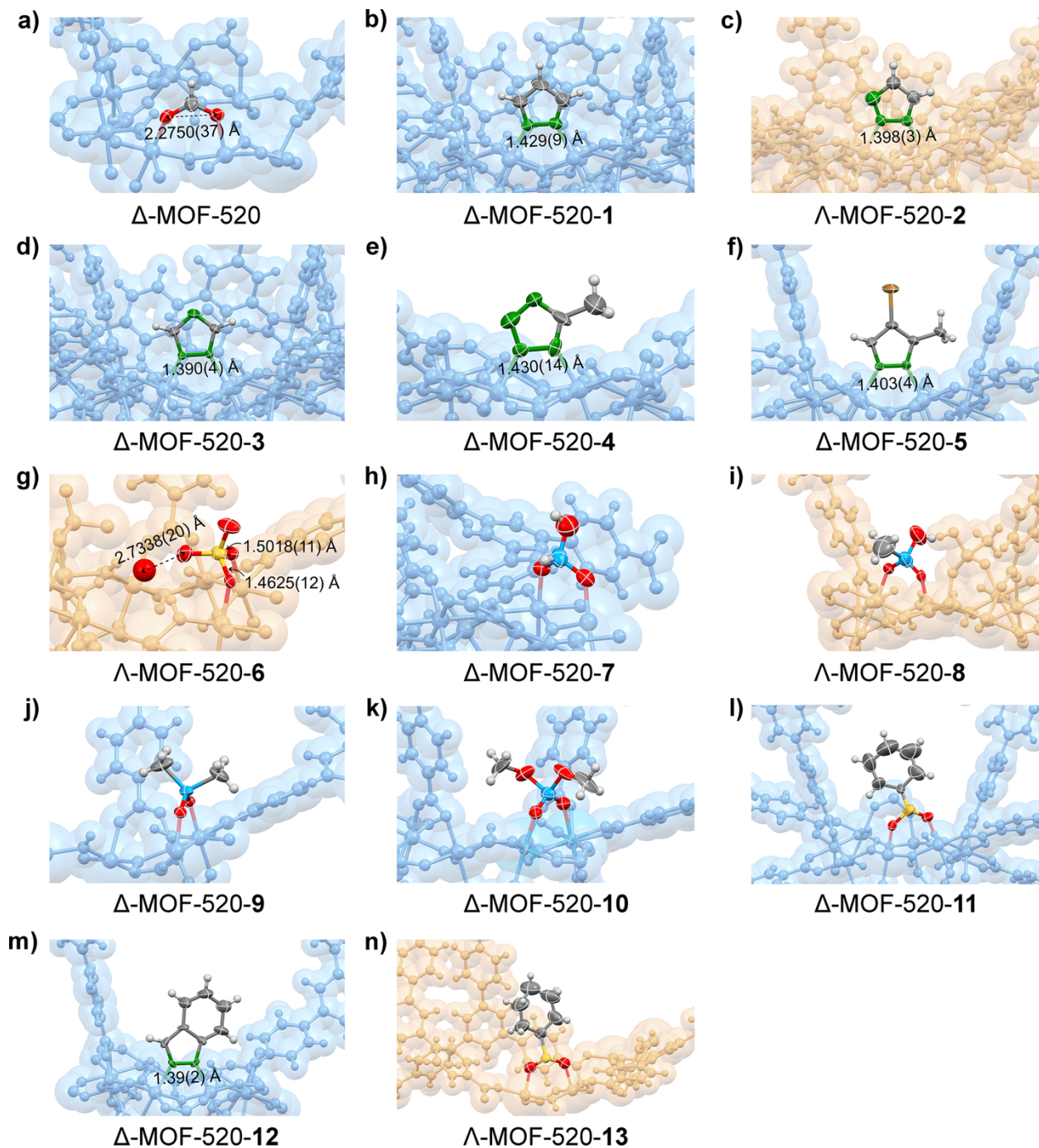


Figure 2.2. (a) Structure of Δ -MOF-520 showing the formate group to be replaced by target molecules. (b–n) Refined structures of **1** to **13** crystallized in Δ - or Λ -MOF-520. The refined structures of the molecules obtained from SXRD data are illustrated with 50% probability thermal ellipsoids. The distances between coordinating atoms are marked in (a–f) and (m). Bond lengths and possible hydrogen bonding is indicated in (g). In the case of positional disorder, only one conformation of the bound molecules is shown for clarity (c, h, n). Color code: blue, Al; orange, P; yellow, S; red, O; green, N; dark gray, C; pink, B; gray, H. The MOF backbone in the figures was drawn as blue (for Δ -MOF-520) or orange (for Λ -MOF-520) space-filling model.

triethylamine in DMF (Section 2.2.3). Theoretically, triethylamine would fully deprotonate sulfuric acid, and it would be sulfate incorporate into MOF-520, while 1 equivalent of protonated triethylamine floating in the channels of MOF, which is also not able to provide proton or polarized hydrogen for forming hydrogen bond.

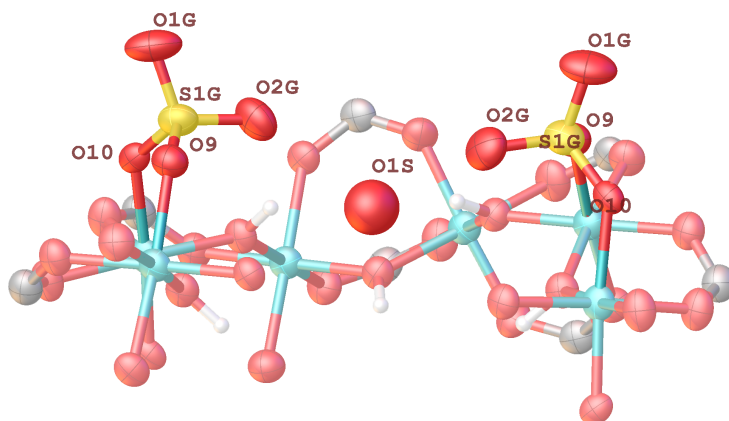


Figure 2.3. Close-up of the two SO_4^{2-} ions on opposite sides of the SBU and flanking a solvent oxygen atom in the single crystal structure of Λ -MOF-520-6. Thermal ellipsoids are drawn with 50% probability.

Table 2.2. Selected bond length for Λ -MOF-520-6.

Atom	Atom	Length/Å
S1G	O9	1.5018(11)
S1G	O2G	1.4661(14)
S1G	O1G	1.4215(15)
S1G	O10	1.4625(12)

To elucidate how the crystallographically observed hydrogen bond was formed, digestion ¹H NMR spectrum measurement was performed: Crystals of MOF-520-6 were washed with DMF for 9 times in 3 days, and 6 times with CH₂Cl₂ in 2 days. The resulting crystals were activated at room temperature for 3 hours, then digested with 20 μL of D₂O solution of 1M NaOH, and 600 μL *d*₆-DMSO. The resulting ¹H NMR spectrum of the dissolved MOF (Figure 2.4) indicates that there are no peaks corresponding to triethylamine [$\delta = 0.93(\text{t}, 3\text{H}), 2.43(\text{q}, 2\text{H})$]. Since there is no triethylamine in the structure to be protonated, it should be proton itself that exist in the structure to balance the charge, *i.e.*, the incorporated species is HSO₄⁻. If there is a proton in the structure, it should prefer the site that has strongest proton affinity. DMF can act as hydrogen-bond donors, however, these interactions shouldn't be stronger than a hydrogen bond with sulfate, as the sulfate is the only charged species that is not fully coordinated yet.

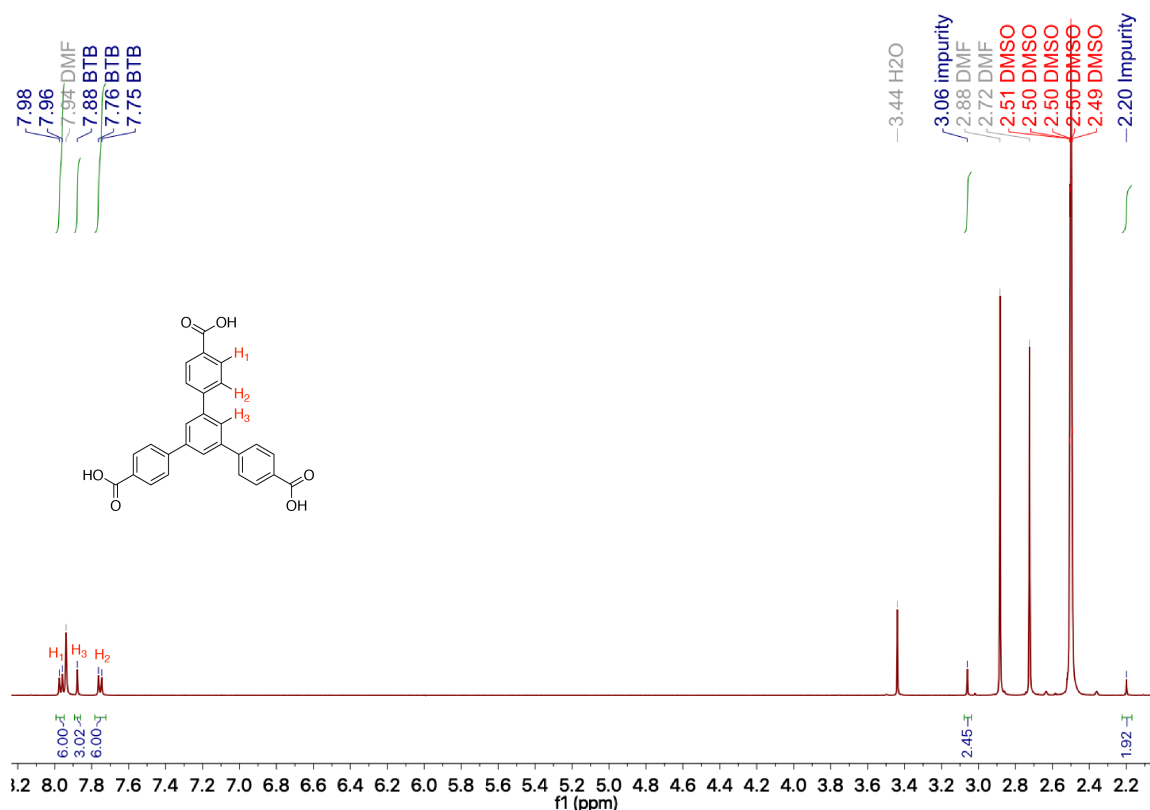


Figure 2.4. Digestion ¹H NMR spectra of MOF-520-6.

Analysis on atomic distances also suggest that proton may participate in the hydrogen bonding with sulfate. **6** is bonded to the framework with only one orientation; the O9–S1G–O10 plane is bent toward the solvent oxygen atom O1S near the center of the SBU rather than towards the other side (Figure 2.3). The distance between O1S and O2G (~2.73 Å) indicates that these atoms are involved in a hydrogen bond (Table 2.3, 2.4). Besides, the S1G–O2G distance is significantly longer than S1G–O1G distance (Table 2.2), indicating a difference in the bond order for the two. The S1G–O2G distance in **6** was also compared with those in reported structures in order to understand whether the sulfate oxygen is a hydrogen bond donor or acceptor. The O1S and O2G distance in Λ-MOF-520-**6** falls in the both ranges of the both the D...A and the A...D cases which overlap (Table 2.3, 2.4). Thus, the hydrogen atom in the hydrogen bonding cannot be assigned ambiguously to O1S or O2G.

Table 2.3. Reported S–O bond length in A...H–O–S. The structures in this table are from (powder/single crystal) neutron diffraction data.

CCDC Ref Code	A...H–O–S (Å)	O–S bond length (Å)	A–O distance (Å)	Ref.
ZATLAJ	O12...H1–O19–S5	1.531	2.565	24
ZATLAJ02	O20...H19–O27–S5	1.495	2.624	24
	O40...H20–O47–S10	1.476	2.655	
	Mean	1.501	2.615	
	s.t.d	0.028	0.046	
	Minimum	1.476	2.565	
	Maximum	1.531	2.655	

Table 2.4. Reported S-O bond length in D-H...O-S. The structures in this table are from (powder/single crystal) neutron diffraction data.

CCDC Ref Code	D-H...O-S (Å)	O-S bond length (Å)	D-O distance (Å)	Ref.
AGLYSL01	O5-H7...O2-S1	1.499	2.599	25
	N2-H9...O4-S1	1.456	2.839	
AYETHS01	O2-H3...O3-S1	1.450	2.736	26
EZULAM02	N2-H4...O1-S1	1.471	3.056	27
	N3-H2...O6-S2	1.479	3.008	
EZULAM05	N2-H4...O1-S1	1.477	2.981	27
	N3-H3...O6-S2	1.476	3.038	
HBPCUS01	O1-H1...O5-S1	1.625	2.813	28
	O11-H27...O6-S1	1.499	2.640	
	O9-H23...O4-S1	1.504	2.711	
HOESUL	O5-H1...O3-S1	1.460	2.807	29
RAYRAM03	O11-H15...O1-S1	1.474	2.750	30
	O9-H11...O2-S1	1.483	2.811	
	N1-H66...O1-S1	1.481	2.877	
TAPBOB06	O1-H2...O9-S1	1.484	2.593	31
	O2-H3...O7-S1	1.492	2.642	
	N1-H14...O10-S1	1.473	2.817	
TGLYSU11	N3-H16...O7-S1	1.520	2.785	32
	N2-H10...O6-S1	1.466	2.769	
THURZN	N1-H1...O4-S1	1.468	2.959	33
	Mean	1.487	2.812	
	s.t.d	0.037	0.141	
	Minimum	1.450	2.593	
	Maximum	1.625	3.056	

Since O1S sits on a 2-fold axis, each O1S forms two hydrogen bonds with two sulfate O2G atoms on opposite sides of the SBU. Consequently, there would be three possible kinds of hydrogen bond arrangements around O2G:

- 1) Both sulfate O2G atoms act as hydrogen donors, such that O1S is hydrogen acceptor for two protons.
- 2) One sulfate O2G atom acts as a hydrogen donor, while the other one is a hydrogen bond acceptor.
- 3) Both sulfate O2G act as hydrogen acceptors.

Distinguishing between these three cases is difficult: on the one hand, pK_{a2} of H_2SO_4 is 1.99, but the one of HSO_4^- coordinated to two Al^{3+} is probably considerably lower; on the other hand, the nature of the solvent oxygen and thus its pK_b are unknown. Since no more information is available to determine the exact circumstance, so that the proton is not assigned between O2G and O1S.

Sulfinic acids are known to have a trigonal pyramidal sulfur configuration. Correspondingly, in molecules **11** and **13**, the cyclohexyl and phenyl groups were observed to bend out of the O-S-O plane (Figure 2.21, n). Alternating positions were observed for the molecule **13**, in which the

cyclohexyl group bends to both sides of the O–S–O plane (Figure 2.5). However, such positional disorder was not observed for **11**, although the phenyl ring was found to be vibrating strongly as indicated by the large atomic displacement parameters (ADPs) along the vibration trajectory. It is hypothesized that the unfavored position of **11** was not observed because of steric hindrance, as in this orientation the molecule points into the center of the SBU and interferes with another incorporated molecule on the same SBU from the opposite side. Compared to a rather flexible cyclohexyl unit, a rigid phenyl ring is less tolerant toward conformation changes for accommodating steric hindrance.

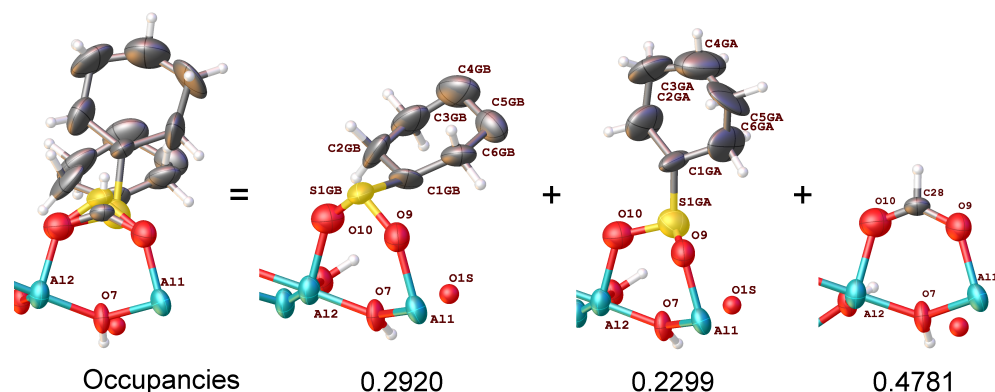


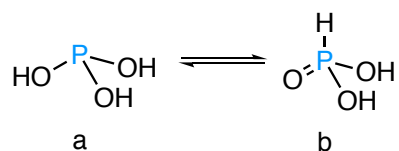
Figure 2.5. Illustration of the disorder at the incorporation site in the single crystal structure of Δ -MOF-520-13. Thermal ellipsoids are drawn with 50% probability. In the structures of both **11** and **13**, the formate group originally on SBUs were partially substituted. The details of two-part or three-part refinement are described in **Appendix XX**.

2.3.3. Single-Crystal X-ray Diffraction Studies of Phosphorous-Oxoacids-Incorporated MOF-520

Phosphorous oxoacids **8**, **9**, and **10** also display the common tetrahedral geometry of the phosphorous atom. As **9** is charge-neutral after incorporation, the crystals of Δ -MOF-520-**9** were able to be examined after solvent removal. The structure of **9** exhibits negligible disorder with a clear tetrahedron geometry of phosphorous, and only slight scissor-like vibration of the CH₃–P–CH₃ unit suggested by the elongated ADPs of two methyl carbons (Figure 2.2j). In the case of Δ -MOF-520-**8**, a tetrahedral phosphorous atom was also definitively identified, with a significant distinction between the P–OH (non-coordinating hydroxyl) and P–C bond lengths [1.527(4) Å and 1.987(8) Å, respectively].

In contrast, the atomic displacement parameters (ADPs) of the atoms in **7** are relatively large and a nearly planar geometry of the central phosphorous atom is observed. According to literature report,^{34,35} **7** may occur in two tautomeric forms, a trigonal (form **a**) and a tetrahedral one (form **b**):

Scheme 2.3. Tautomerization of **7**, phosphonic acid.



Theoretically, if we can see the trigonal/tetrahedral geometry of phosphorous, we will be able to know which is exactly the tautomer that binds to the MOF-520. However, because the common

problem that X-ray diffraction can't locate hydrogen atom (unless very good structure/data quality), these two forms will both look like trigonal pyramidal in the X-ray structures.

Seeking for other methods to understand the binding form, we turned to basic reaction analysis. **7** must deprotonate before binding to MOF-520 (as the substituted formate group has one negative charge). If form **a** deprotonates, it will have one O^- and one OH to bind to MOF-520; apparently, the OH-Al^{3+} won't be a very favored binding mode. In contrast if form **b** deprotonates, it will contain one O^- , and one double-bonded oxygen ($=\text{O}$). The double-bonded oxygen is favored over OH when coordinating to Al^{3+} , thus, we suggest that form **b** is dominating upon coordination to the MOF-520. Accordingly, in the SXR D refinement, hydrogen atoms are placed geometrically on the phosphorous atoms. In such case, a nearly planar geometry of the central phosphorous atom suggests that **7** aligns in mixed orientations, that the molecules with opposite $\text{P}=\text{O}$ and $\text{P}-\text{H}$ orientations overlap with each other.

2.3.4. Diastereoselective Incorporation on Prochiral Target Molecules

The chirality of the host framework imposes diastereoselective coordination on prochiral molecules. Here, prochiral molecules are aligned in a specific asymmetric orientation, leading to just one of the two possible diastereomers for each enantiomorph of host MOF-520. The binding

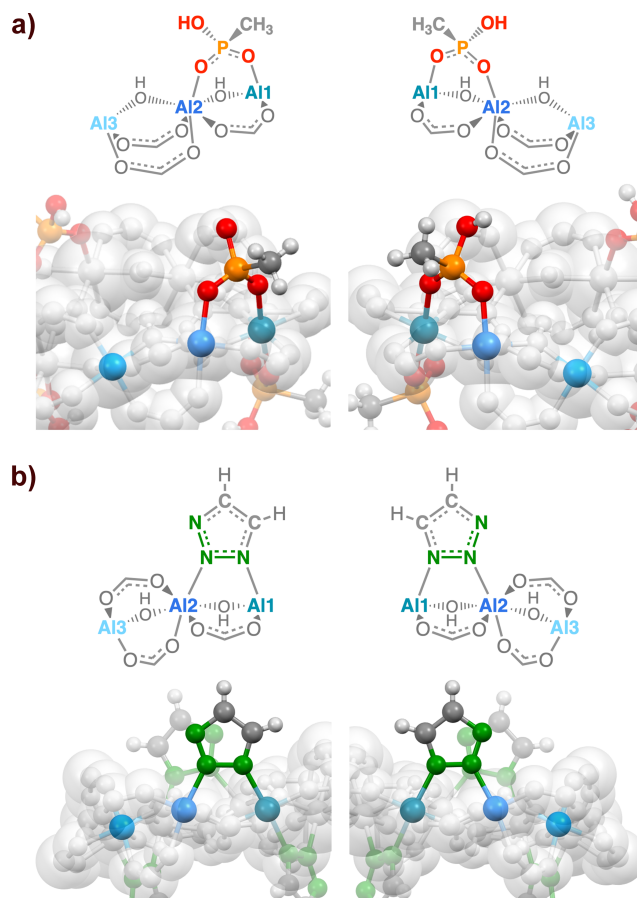


Figure 2.6. (a) Local structure of the coordination site of methylphosphonic acid in Δ -MOF-520-**8** and Λ -MOF-520-**8**. (b) Local structure of the coordination site of *1H*-1,2,3-triazole in Δ -MOF-520-**2** and Λ -MOF-520-**2**. The blue colors at different level are used to illustrate the Al atoms of different environment: Al1, turquoise; Al2, aqua blue; and Al3, violet blue. The SBUs except for bound molecules are represented by gray space-filling models. Color code: P, orange; O, red; N, green; C, gray; H, light gray.

of the spatially bulkier azoles **4**, **5**, **12**, can be attributed to steric selectivity, however, the selectivity was also observed in smaller molecules that are minimally influenced by steric hindrance.

Methylphosphonic acid (**8**) and 1*H*-1,2,3-triazole (**2**) can potentially adopt two different configurations upon coordination to one enantiomorph of MOF-520 and form two diastereomers of the molecule-incorporated framework. However, only one preferred orientation is consistently observed in a given enantiomorph. The non-coordinating hydroxyl group in **8** always points to the center of the SBU, while the methyl group points in the opposite direction (Figure 2.6a). Similarly, one specific orientation is observed to be much more preferred than the other in both Δ -MOF-520-**2** and Λ -MOF-520-**2** (Figure 2.6b). The results are supported by refining the occupancies of the two overlapping positions through free variables. The occupancies of the two possible orientations converged to 0.680(4) and 0.038(4) for Δ -MOF-520-**2**, and to 0.632(4) and 0.025(4) for Λ -MOF-520-**2**.

Hirshfeld Analyses Toward van der Waals Interactions

In order to understand the driving force that leads to the preferred orientation, possible van der Waals interactions between **2** and the host framework were examined by Hirshfeld surface analysis.³⁶

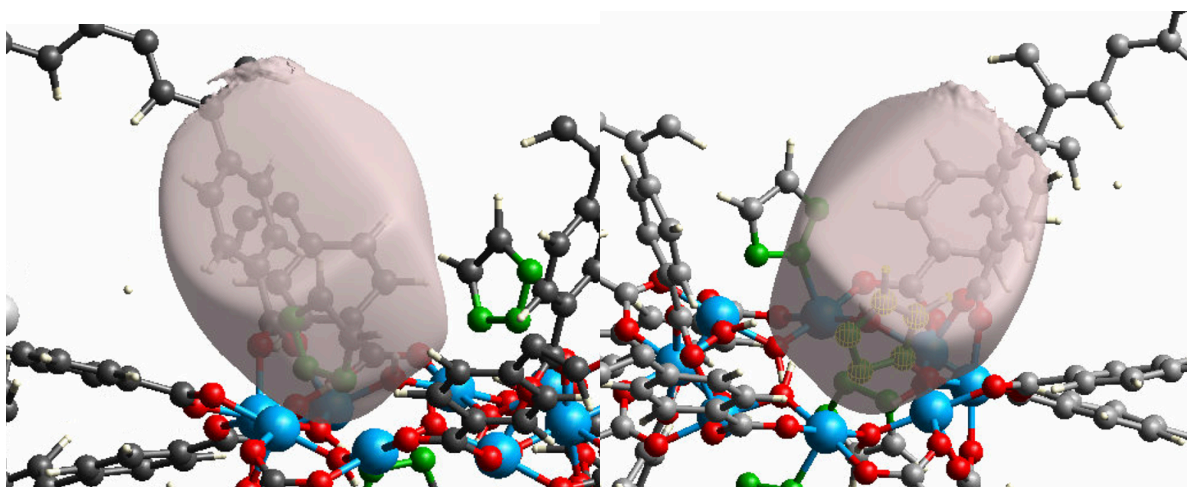


Figure 2.7. Hirshfeld surface calculated for the bounded 1,2,3-triazole in Λ -MOF-520-**2** and *inverse*- Λ -MOF-520-**2**. Surface is only plotted for one of the four molecules on the SBU for clarity. Color code: Al, blue; O, red; N, green; C, dark grey; H, white.

The single-crystal structure of Λ -MOF-520-**2** was directly used in the Hirshfeld surface analysis. For comparison, a structure with inversed orientation of 1,2,3-triazolate (noted as *inverse*- Λ -MOF-520-**2**) was modeled in Materials Studio.³⁷ The MOF framework was remained unedited, the 1,2,3-triazolate was flipped. The flipped position is in the same plane as the original position, and the nitrogen atoms bonded to Al overlap before and after flipping. The resulting Hirshfeld surface is plotted in Figure 2.7 with no surface property plotted on the surface. On the bases of that, the d_i - d_e two-dimensional fingerprint figure³⁸ was generated for Λ -MOF-520-**2** and *inverse*- Λ -MOF-520-**2** (Figure 2.8, 2.9). The whole dotted area (grey, and colored) in each figure includes the d_i - d_e plot for all atoms in the surface and out of the surface. The colored part of the full plot represents the d_i - d_e plot for all atoms in the surface, and the selected type of elements outside the surface. The criteria of having van der Waals interaction is a d_i - d_e distance shorter than 2.5 Å.³⁸

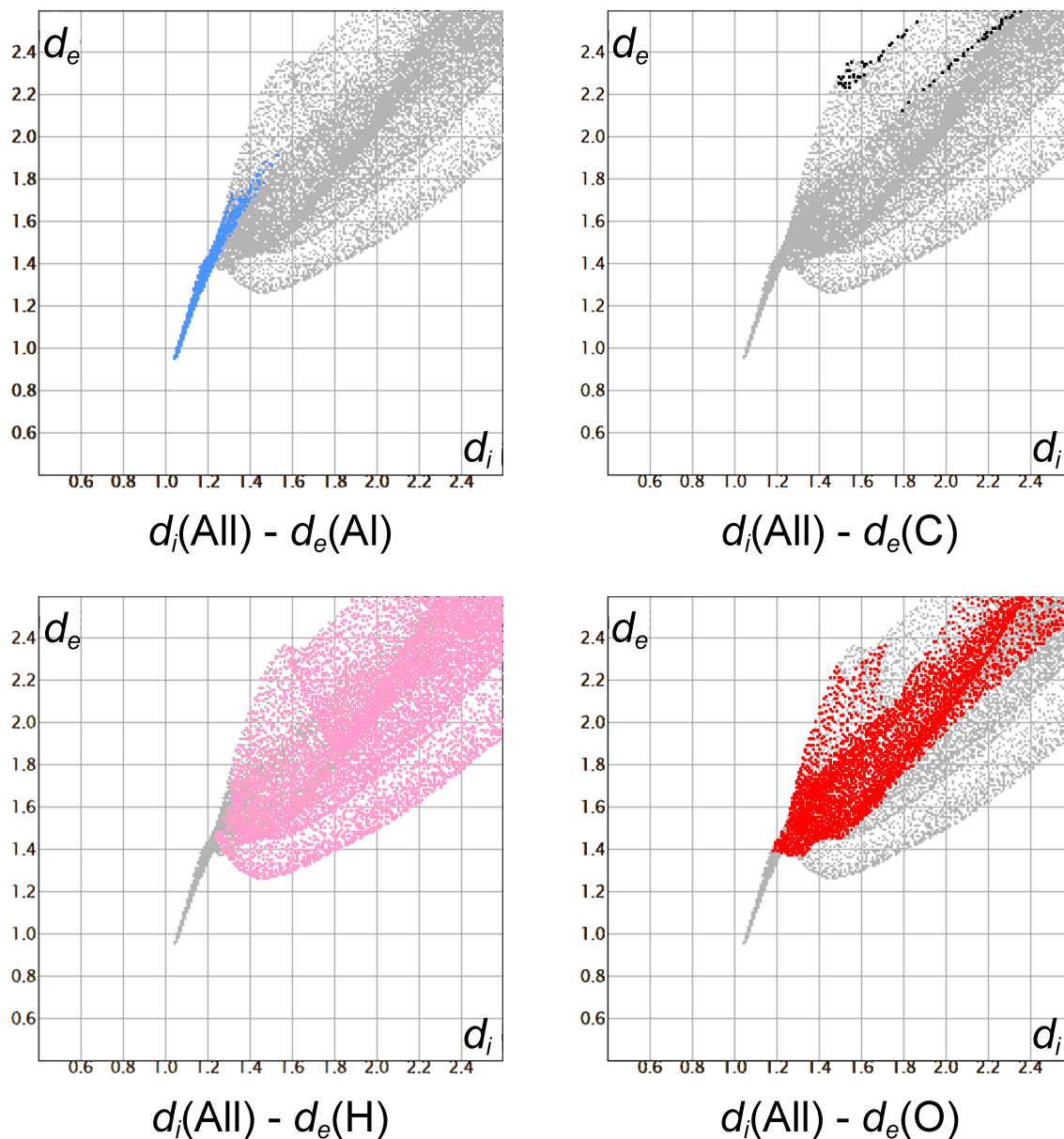


Figure 2.8. d_i - d_e two-dimensional fingerprint figure of Λ -MOF-520-2.

$d_i(\text{Al})$ - $d_e(\text{Al})$ plots for both structures indicate that the closest contact between **2** and MOF-520 is the contact between **2** and Al, which is the coordination bond. Although $d_i(\text{Al})$ - $d_e(\text{O})$ shows the closest guest-host contact distance of ~ 2.6 Å, the oxygen atoms that have this distance are the oxygens that coordinate to the same Al as **2**, which shouldn't be able to form steric hindrance to **2**. The $d_i(\text{Al})$ - $d_e(\text{O})$ plot of the both structures also support the conclusion: the distributions of red dots in the small d_i/d_e region are similar in the two plots, suggesting that they are originated from same part of the host structure (*i.e.* the fixed geometry of the SBU). Similar conclusion can be drawn from the analyses on $d_i(\text{Al})$ - $d_e(\text{H})$ plot: the closest $d_i(\text{Al})$ - $d_e(\text{H})$ contact in both structures is ~ 2.6 Å which is not unusually short,²⁴ indicating that there's no strong van der Waals attraction that helps to orientate the structure, and no very close contact that becomes steric hindrance.

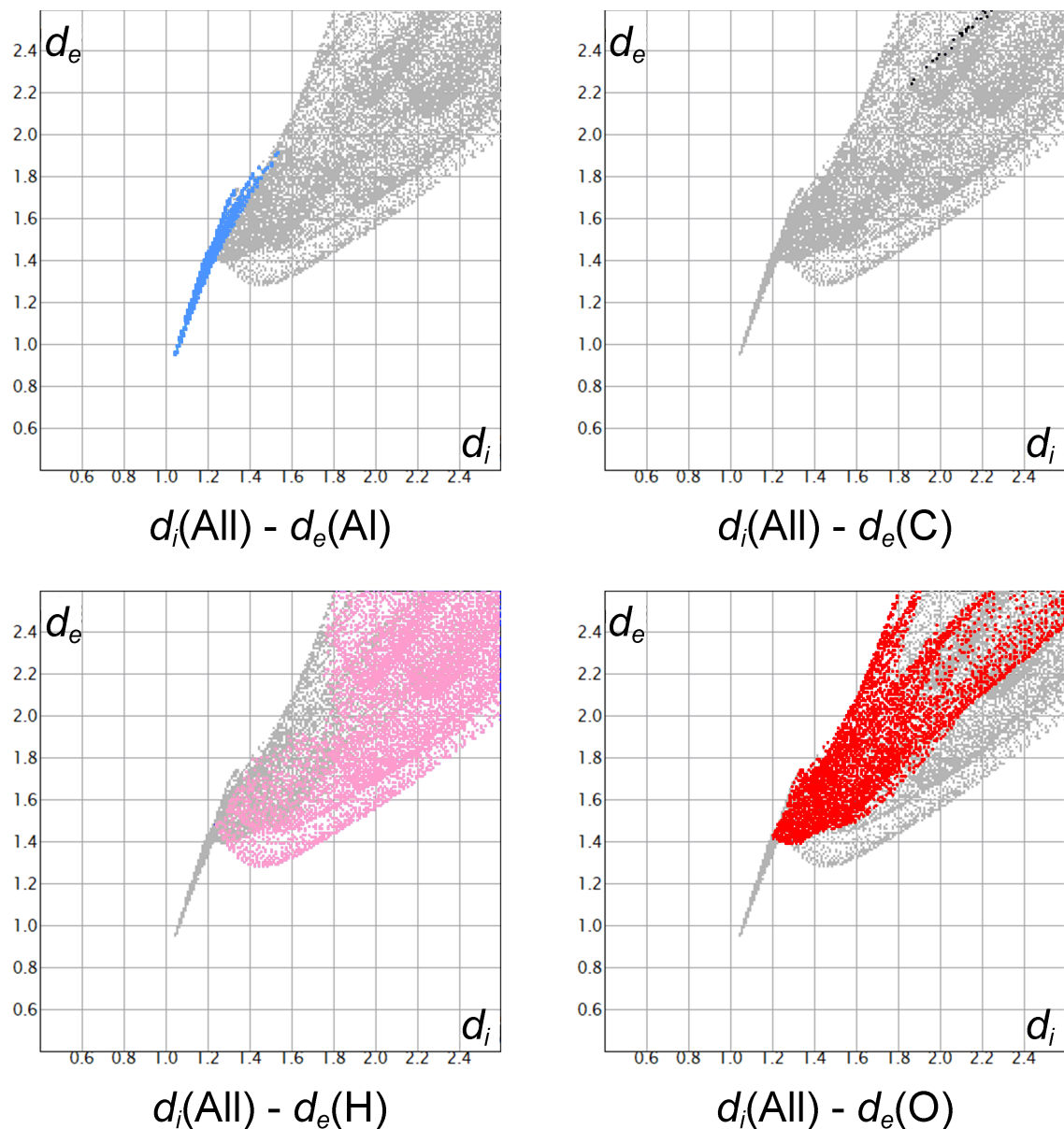


Figure 2.9. d_i - d_e two-dimensional fingerprint figure of *inverse*- Λ -MOF-520-2.

Therefore, it is concluded that no significant intermolecular repulsion or attraction was observed between molecule **2** and the MOF.

DFT Calculations Toward Coordinative Interactions

The lack of the above-mentioned factors leads us to think about the difference in the Al-N coordination bonds. When the two different N atoms of **2** bind to MOF-520, they bridge two aluminum ions in different chemical environments (Al1 and Al2). The two different sets of Al-N bonds resulting from the two different azole orientations may have different bond strengths.

Calculations were performed on the molecular models of the incorporation site, with favored and unfavored orientation of coordinated **2**. The periodic structures, Λ -MOF-520-**2** and *inverse*- Λ -MOF-520-**2** were simplified into isolated molecular units for the ease of performing energy calculations (Figure 2.10). Each unit contains a full SBU, and each BTB connected to the SBU

was simplified into benzoates. The units for calculations are denoted as Triazole_SBU (from Λ -MOF-520-2) and *inverse_Triazole_SBU* from (*inverse*- Λ -MOF-520-2).

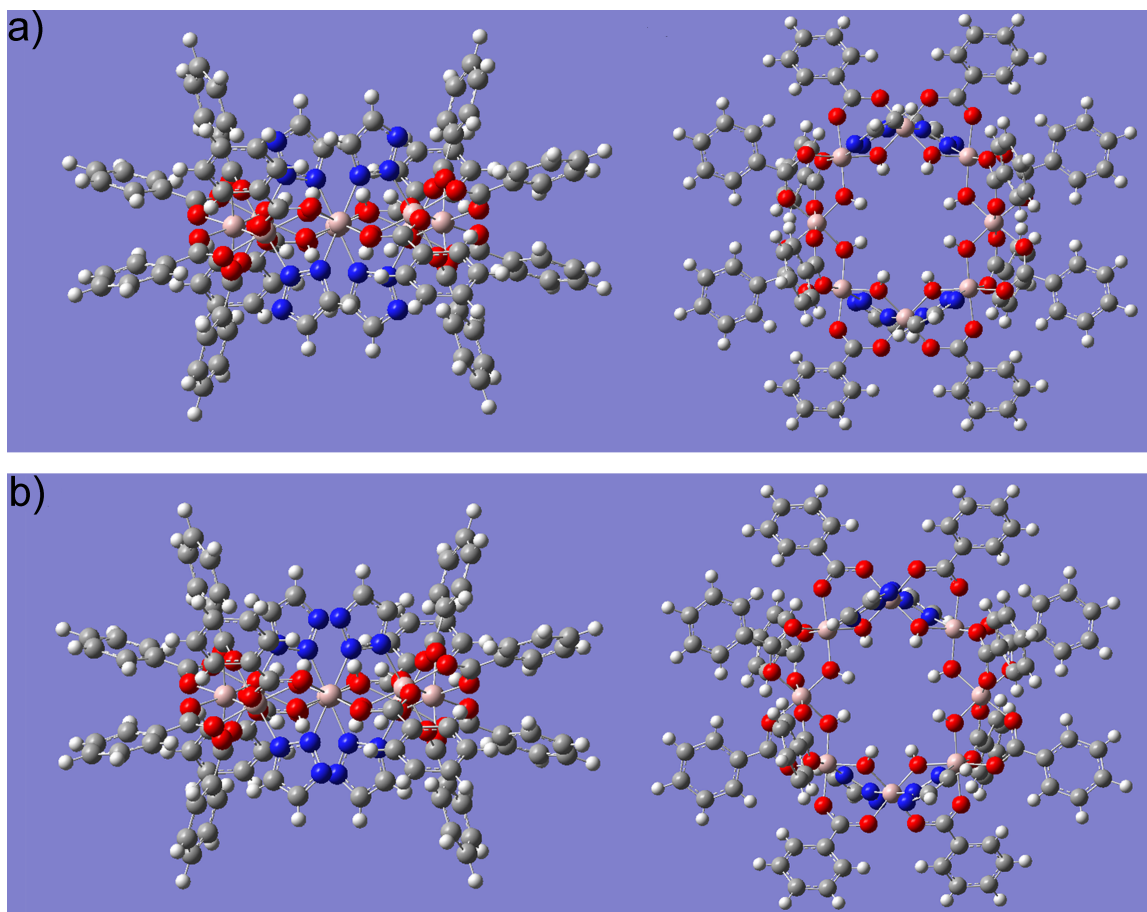


Figure 2.10. Ball-and-stick model of (a) Triazole_SBU and (b) *inverse_Triazole_SBU*.

Total energies of the models were obtained from DFT calculations with polarized continuum model (PCM) accounting for solvent effects. The energy calculation results are summarized in Table 2.5. First calculation was conducted without considering solvent or van der Waals interaction in the model (i.e., no solvent and no empirical dispersion). The energy difference of two molecular models (ΔE_{SBU}) is 9.87 kJ per mole of SBU. Because there are four triazole site on one SBU, so that for each site, the favored orientation of 1,2,3-triazole is 2.47 kJ mol⁻¹ lower in energy than the unfavored orientation (noted as ΔE_{site}). In the next calculation, solvent was not included, but empirical dispersion was considered to test the contribution of weak van der Waals interactions. The ΔE_{site} in this situation is 3.05 kJ mol⁻¹, 0.58 kJ mol⁻¹ higher than the previous one. It indicates that the major contribution comes from asymmetric covalent bonding, while the van der Waals interactions only contribute minor, which is consistent with the Hirshfeld surface analysis results. When it goes to solvated models, acetone and DMSO were chosen as two solvents that mostly representing the common incorporation conditions. ΔE_{site} was increased to ~ 8 kJ mol⁻¹ after considering solvation effects, which shows that the solvent helps to stabilize the local charges in the coordination system. The energy differences were slightly higher for the solvents with larger dielectric constant ($\epsilon_{\text{acetone}} = 20.493$, $\epsilon_{\text{DMSO}} = 46.826$). Ionic solution model was also tested for possibly stronger stabilization in a more polarized system. The ionic strength was

calculated based on the assumption that the maximum ionic strength will be reached when all the formates on MOF-520 are substituted by **2**, which is 0.0015 M. However, calculation results didn't show a significant influence after accounting ionic strength, possibly due to the low ion concentration. The calculation for Triazole_SBU in DMSO under ionic strength 0.0015 M did not converge, so that comparison wasn't made in this case.

Table 2.5. Summary of the results of energy calculation.

Solvent	$E_{\text{Triazole_SBU}}$ /hartree	$E_{\text{inverse_Triazole_SBU}}$ /hartree	ΔE_{SBU} /(kJ mol ⁻¹)	ΔE_{site} /(kJ mol ⁻¹)
No D3 correction, no solvent	-8543.42501217	-8543.42125419	9.87	2.47
None	-8543.78644306	-8543.78179171	12.21	3.05
Acetone	-8543.83609983	-8543.82440279	30.71	7.68
DMSO	-8543.83739726	-8543.82518291	32.07	8.02
0.0015 M in acetone	-8543.84576080	-8543.83324904	32.85	8.21

It should be noted that the ΔE_{site} can be strongly influenced by the calculation parameters (e.g., solvent surface type), nevertheless, the trend still exists that ΔE_{site} would increase as dielectric constant of solvent increases. Also, the difference is more significant when solvent is considered than not. Overall, it should be recognized that the difference is majorly contributed by asymmetric covalent bonding after solvent stabilization.

To conclude, the energy difference in favor of the observed orientation is *ca.* 8 kJ mol⁻¹ for DMSO and acetone, and is primarily attributed to the asymmetric coordinative bonding after solvent stabilization. Accordingly, the stereoselectivity of MOF-520 is not exclusively due to steric effects and weak van der Waals interactions, but also because of asymmetric coordination bonding which causes a sufficient energy difference between the two alternative orientations of the bound molecules.

2.4. Conclusion

In this chapter of work, model compounds of eight kinds of functionalities were successfully incorporated into MOF-520 and had their single-crystal structure determined. The geometries and conformations of the incorporated guest molecules were rigorously analyzed. The results indicate that the coordinative alignment method on additional functionalities can provide information on bond length and bond angles as much as conventional analyses on recrystallized molecules, despite the information sometimes was confused by positional disorder. Importantly, the incorporation of 1,2,3-triazole demonstrated the contribution of asymmetric coordination bond on stereoselective incorporation, which is rarely observed in other host-assisted crystal structure determination method. The broadened scope of coordinative alignment method with the promising stereoselectivity make it a better method to be adapted into real-world applications resolving the structures of natural products and drug molecules.

2.5. Appendices and Notes

2.5.1. Acknowledgments

The crystal structures are available from the Cambridge Crystallographic Data Centre under the reference number CCDC-1938269 to 1938290. Synthesis in this work is supported by King Abdulaziz City for Science and Technology (Center of Excellence for Nanomaterials and Clean Energy Applications). This research used resources of beamline 11.3.1/12.2.1 at the Advanced Light Source, which is a DOE Office of Science User Facility under contract no. DE-AC02-05CH11231. Computational works were conducted at Molecular Graphics and Computation Facility at UC Berkeley with funding number NIH S10OD023532. NMR facility in College of Chemistry are supported in part by NIH S10OD024998. We would like to acknowledge Dr. Dave Small and Mr. Jie Li for their helpful discussions on computation, and Mr. Hao Lyu, Mr. Wentao Xu, Mr. Nikita Hanikel, Dr. Cornelius Gropp, and Dr. Christian Diercks for their helpful suggestions.

2.5.2. Summary of SXRD Results

Besides the unit cell change after incorporation, MOF-520 also demonstrates dynamics toward the change of solvent in the pore, or solvent evacuation. The trend of unit cell changes upon activation (see main article) is only applicable when the compared crystals have the same solvent in the pore (or have no solvent). For example, for azolate incorporated MOF-520, the *a* and *b* axes will be elongated, and the *c* axis will be shortened after solvent evacuation: Δ -MOF-520-**4**, solvated, has the unit cell of 18.8135(11) Å \times 36.797(2) Å. While Δ -MOF-520-**12**, activated, has the unit cell of 19.3331(6) Å \times 36.2317(12) Å.

The loading of the target molecule will also influence the extent of the unit cell change. Usually, the higher the loading (target molecule occupancy), the more significant the unit cell changes. For example, comparing to the aforementioned Δ -MOF-520-**12** (occupancy of **12** is 0.3821), Δ -MOF-520-**3**, with the occupancy of **3** as 0.8624, has unit cell parameters of *a* = 19.5339(5) Å and *c* = 35.7057(10) Å, which is longer in *a* & *b* axes and shorter in *c* axis. However, the trend of molecule loading vs. unit cell change is not quite consistent when the target molecules are bigger. A possible explanation to this is that when the molecules are large in space that fills a high percent of the pore volume of MOFs, they actually act as additional struts in the pore that support the framework, thus preventing the framework from further contraction.

In most of the reported MOF-520 structures (with or without target molecules), solvent contribution can be observed at the center of the SBU. Depending on how disordered the solvent molecule is in each specific crystal, varying numbers of atoms of this disordered solvent molecule can be assigned vary from structure to structure:

- 1) A full DMF molecule can be assigned in Δ -MOF-520, Λ -MOF-520-**8**.
- 2) More than one atom can be assigned, but not a full molecule: Δ -MOF-520-**3**, Δ -MOF-520-**4**, Δ -MOF-520-**8**, Δ -MOF-520-**10**, Δ -MOF-520-**11**.
- 3) Only one atom: Λ -MOF-520-**6**, Δ -MOF-520-**7**, Δ -MOF-520-**9**, Δ -MOF-520-**12**, Λ -MOF-520-**13**.

In the first case (Δ -MOF-520, for example, Section 2.5.3), complete DMF molecules can be found at the center of the SBUs. The ellipsoid plot in Figure 2.11 shows that the aldehyde side (closer to the center of SBU) is quite ordered, while the dimethyl amine side (further in distance from the framework) is more disordered. This can be explained by the 8 hydroxyl groups (strong

hydrogen bond donors) in the SBU that lock the aldehyde group as the hydrogen bond acceptor in place. In contrast, in the third case, only a hydrogen bond acceptor atom of the solvent molecule can be located *via* difference Fourier maps (F_{diff}), showing up as one or two strong electron density peaks at (0, 0, 0) or two peaks on the two-fold axis (0, 0, z), respectively, on the two-fold axis. In the intermediate case, electron density peaks (larger than $1 \text{ e } \text{\AA}^{-3}$) can also be found near the 8 - OH groups of the SBU; they represent the not-yet-fully disordered part of a solvent molecule, and they are usually assigned as an oxygen atom, or a carbon atom, or several atoms. The assignment of these relatively strong electron densities is to better account for the observed electron densities in the model and improve the difference Fourier synthesis after later refinements of the incorporated molecules. In the solvent-evacuated structures, these relatively strong electron densities at the center of SBUs can still occur, possibly because the hydrogen bonds are so strong making it hard to remove “locked” solvents. These electron density peaks in activated structures are treated in the same way as the non-activated structures.

Table 2.6. Summary of the solvent masking result for solvated structures.

Name	Masked volume V (\AA^3)	# of e^- being masked out	$e \text{\AA}^{-3}$
Δ -MOF-520-1	9424.4	1720.5	0.1826
Δ -MOF-520-2	9121.3	2794.6	0.3064
Λ -MOF-520-2	9108.5	1352.9	0.1485
Δ -MOF-520-4	8707.5	3543.8	0.4070
Λ -MOF-520-6	8297.7	2230.4	0.2688
Δ -MOF-520-7	8289.9	3126.9	0.3772
Δ -MOF-520-8	8523.3	959.4	0.1126
Λ -MOF-520-8	8006.7	1939.7	0.2423
Δ -MOF-520-11	8015.9	2141.0	0.2671
Λ -MOF-520-13	7634.7	2946.8	0.3860

2.5.3. Refinement details of SXR D datasets

Refinement Details of Δ -MOF-520

A colorless crystal of Δ -MOF-520 was measured at beamline 12.2.1 at Advanced Light Source with radiation of $\lambda = 0.7288 \text{ \AA}$. Based on intensity statistics for the whole dataset (PRP file), the resolution was cut off to 0.78 \AA ($R_{\text{merge}} \leq 40\%$ or average $I/\sigma > 2.5$ for the highest resolution shell). All non-hydrogen atoms were refined anisotropically and hydrogen atoms were placed in calculated positions. The occupancy of *N,N*-dimethylformamide (DMF) molecule was found via a free variable and later fixed at the converged occupancy. RIGU was applied to the disordered solvent molecule. Reflections that are affected by the beamstop or having $(I_{\text{obs}} - I_{\text{calc}})/\sigma > 7$ were omitted. Solvent masking was not applied to the structure. The weighting scheme was refined to convergence and the *a*, *b* parameters are 0.1702 and 0.6454, respectively.

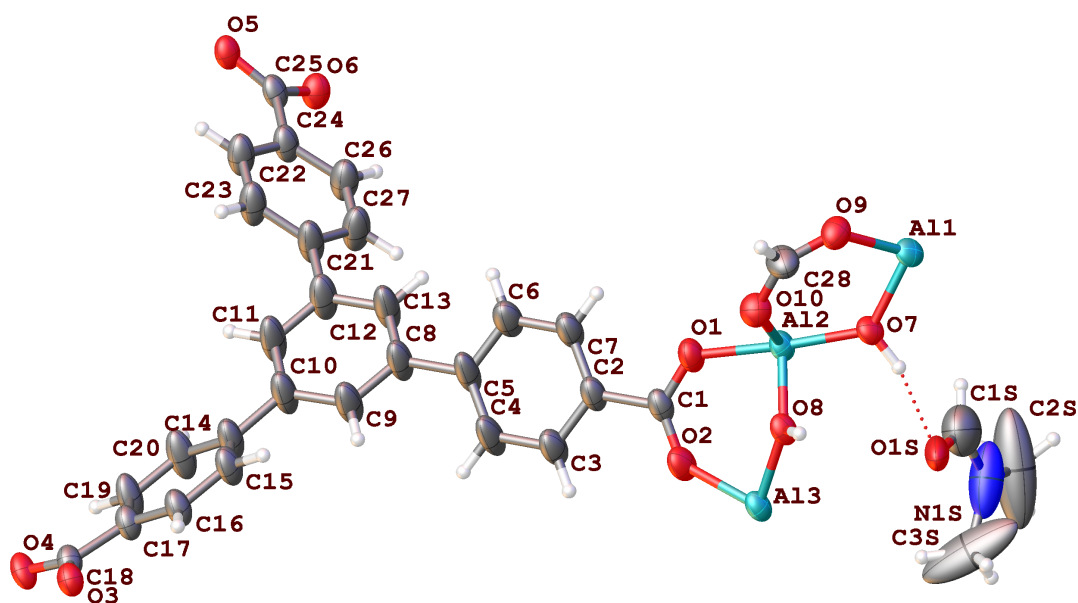


Figure 2.11. Asymmetric unit in the single crystal structure of Δ -MOF-520. Thermal ellipsoids are drawn with 50% probability.

Table 2.7. Crystal data, data collection, and structure refinement parameters for Δ -MOF-520.

Name	Δ -MOF-520
Empirical formula	$C_{30.05}H_{17}Al_2N_{0.56}O_{10.56}$
Formula weight	608.72
Temperature/K	100
Crystal system	tetragonal
Space group	$P4_22_12$
$a/\text{\AA}$	18.5778(6)
$b/\text{\AA}$	18.5778(6)
$c/\text{\AA}$	37.2977(13)
$\alpha/^\circ$	90
$\beta/^\circ$	90
$\gamma/^\circ$	90
Volume/ \AA^3	12872.7(9)
Z	8
$\rho_{\text{calc}} (\text{g}/\text{cm}^3)$	0.628
μ/mm^{-1}	0.077
F(000)	2493.0
Crystal size/ mm^3	$0.073 \times 0.068 \times 0.059$
Radiation	Synchrotron ($\lambda = 0.7288 \text{\AA}$)
2Θ range for data collection/ $^\circ$	7.112 to 55.7
Index ranges	$-20 \leq h \leq 20, -23 \leq k \leq 23, -45 \leq l \leq 46$
Reflections collected	65395
Independent reflections	13771 [$R_{\text{int}} = 0.0579, R_{\text{sigma}} = 0.0448$]
Data/restraints/parameters	13771/24/407
Goodness-of-fit on F^2	1.041
Final R indexes [$I \geq 2\sigma(I)$]	$R_1 = 0.0682, wR_2 = 0.2051$
Final R indexes [all data]	$R_1 = 0.0814, wR_2 = 0.2206$
Largest diff. peak/hole / $e \text{\AA}^{-3}$	0.78/-0.24
Flack parameter	-0.01(5)

Refinement Details of Δ -MOF-520-1

A colorless crystal of Δ -MOF-520-1 was measured with Bruker D8 Venture Diffractometer with Cu K α radiation. Based on intensity statistics for the whole dataset (PRP file), the resolution was cut off to 0.85 Å ($R_{\text{merge}} \leq 40\%$ or average $I/\sigma > 2.5$ for the highest resolution shell). The MOF framework was first assigned and refined anisotropically. Hydrogen atoms were placed in calculate positions. The occupancy of pyrazole molecule was refined with a free variable and was found to be 0.936(5). Solvent masking was applied to the structure. The void volume was estimated to be 9424.4 Å³ with 1720.5 electrons removed during masking. Reflections that are affected by the beamstop or having $(I_{\text{obs}} - I_{\text{calc}})/\sigma > 7$ were omitted. The weighting scheme was refined to convergence and the a, b parameters are 0.0763 and 0, respectively.

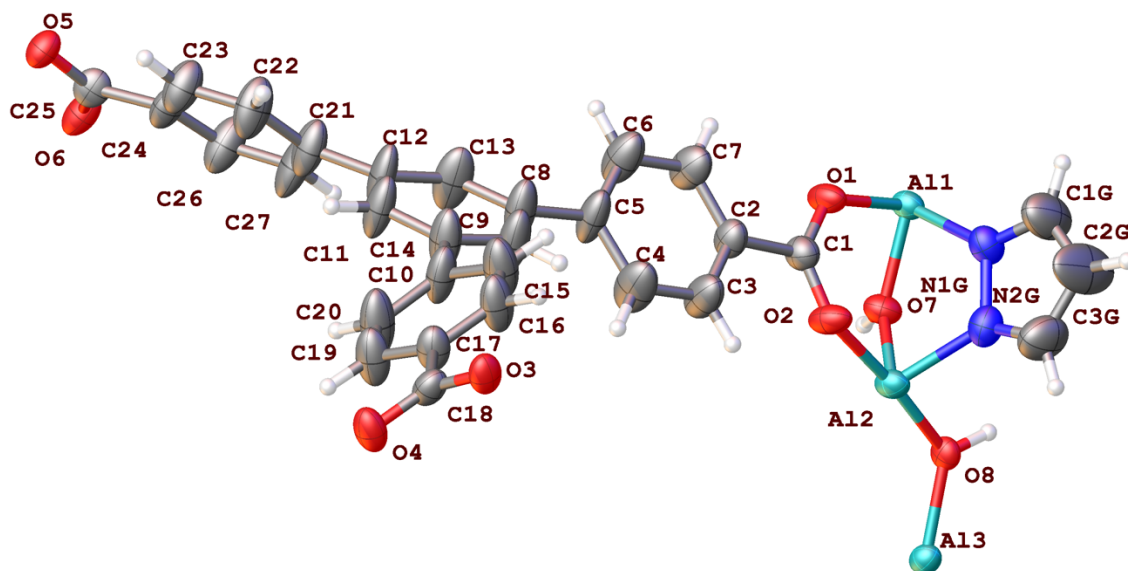


Figure 2.12. Asymmetric unit in the single crystal structure of Δ -MOF-520-1. Thermal ellipsoids are drawn with 50% probability.

Table 2.8. Crystal data, data collection, and structure refinement parameters for Δ -MOF-520-1.

	Before Solvent Masking	After Solvent Masking
Empirical formula	$C_{29.81}H_{19.81}Al_2N_{1.87}O_8$	$C_{29.81}H_{19.81}Al_2N_{1.87}O_8$
Formula weight	586.16	586.16
Temperature/K	100	100
Crystal system	tetragonal	tetragonal
Space group	$P4_22_12$	$P4_22_12$
$a/\text{\AA}$	19.4481(6)	19.4481(6)
$b/\text{\AA}$	19.4481(6)	19.4481(6)
$c/\text{\AA}$	35.7074(13)	35.7074(13)
$\alpha/^\circ$	90	90
$\beta/^\circ$	90	90
$\gamma/^\circ$	90	90
Volume/ \AA^3	13505.6(10)	13505.6(10)
Z	8	8
ρ_{calc} (g/cm^3)	0.577	0.577
μ/mm^{-1}	0.586	0.586
F(000)	2418.0	2418.0
Crystal size/ mm^3	$0.085 \times 0.06 \times 0.05$	$0.085 \times 0.06 \times 0.05$
Radiation	$\text{CuK}\alpha$ ($\lambda = 1.54178 \text{ \AA}$)	$\text{CuK}\alpha$ ($\lambda = 1.54178 \text{ \AA}$)
2θ range for data collection/ $^\circ$	9.094 to 129.716	8.71 to 129.716
Index ranges	$-9 \leq h \leq 20,$ $-20 \leq k \leq 22,$ $-35 \leq l \leq 41$	$-9 \leq h \leq 20,$ $-20 \leq k \leq 22,$ $-35 \leq l \leq 41$
Reflections collected	37696	37839
Independent reflections	11160 [$R_{\text{int}} = 0.0474,$ $R_{\text{sigma}} = 0.0648$]	11181 [$R_{\text{int}} = 0.0472,$ $R_{\text{sigma}} = 0.0644$]
Data/restraints/parameters	11160/0/381	11181/0/381
Goodness-of-fit on F^2	1.103	0.991
Final R indexes [$I \geq 2\sigma(I)$]	$R_1 = 0.0877,$ $wR_2 = 0.2290$	$R_1 = 0.0494,$ $wR_2 = 0.1214$
Final R indexes [all data]	$R_1 = 0.1182,$ $wR_2 = 0.2522$	$R_1 = 0.0716,$ $wR_2 = 0.1310$
Largest diff. peak/hole / $e \text{ \AA}^{-3}$	1.41/-0.33	0.19/-0.22
Flack parameter	0.023(13)	0.039(13)

Refinement Details of Δ -MOF-520-2

A colorless crystal of Δ -MOF-520-2 was measured at beamline 12.2.1 at ALS with radiation of $\lambda = 0.7288 \text{ \AA}$. Based on intensity statistics for the whole dataset (PRP file), the resolution was cut off to 0.75 \AA ($R_{\text{merge}} \leq 40\%$ or average $I/\sigma > 2.5$ for the highest resolution shell). The two different orientations of **2** were modeled as overlapped positions with EXYZ and EADP. The occupancies of the unsubstituted formate and the two orientations of **2**, were refined with SUMP (= 1.0000(1)). All non-hydrogen atoms were refined anisotropically and hydrogen atoms were placed in calculated positions. SIMU and DELU were applied to O9, C28, O10 to stabilize anisotropic refinement of closely overlapping atoms. Solvent masking was applied and the void volume was estimated to be 9121.3 \AA^3 with 2794.6 electrons removed during masking. Reflections that are affected by the beamstop or having $(I_{\text{obs}} - I_{\text{calc}})/\sigma > 7$ were omitted. The weighting scheme was refined to convergence and the a, b parameters are 0.0495 and 0, respectively. The occupancies of the two orientations of triazole converged to 0.680(4) and 0.038(4) and the end of the refinement.

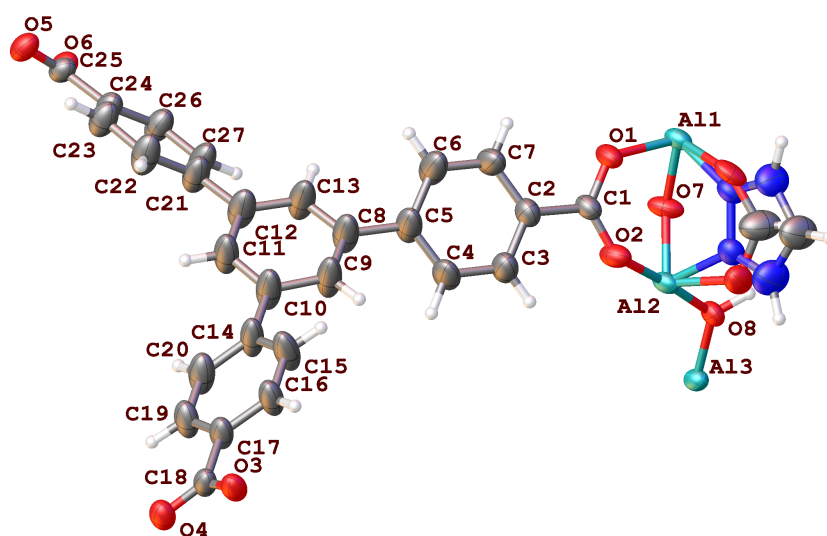


Figure 2.13. Asymmetric unit in the single crystal structure of Δ -MOF-520-2. Thermal ellipsoids are drawn with 50% probability.

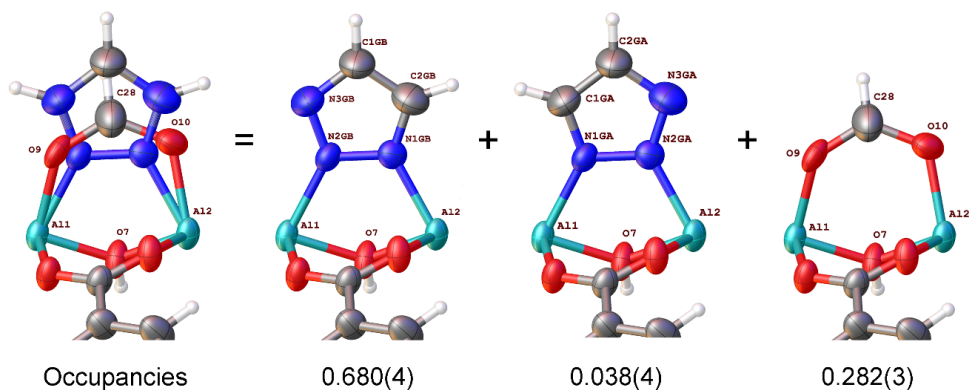


Figure 2.14. Illustration of the disorder at the incorporation site in the single crystal structure of Δ -MOF-520-2. Thermal ellipsoids are drawn with 50% probability.

Table 2.9. Crystal data, data collection, and structure refinement parameters for Δ -MOF-520-2.

	Before Solvent Masking	After Solvent Masking
Empirical formula	C _{28.72} H _{18.69} Al ₂ N _{2.15} O _{8.57}	C _{28.72} H _{18.69} Al ₂ N _{2.15} O _{8.57}
Formula weight	584.89	584.89
Temperature/K	100(2)	100(2)
Crystal system	tetragonal	tetragonal
Space group	<i>P4</i> ₂ <i>2</i> ₁ <i>2</i>	<i>P4</i> ₂ <i>2</i> ₁ <i>2</i>
<i>a</i> /Å	18.9000(10)	18.9000(10)
<i>b</i> /Å	18.9000(10)	18.9000(10)
<i>c</i> /Å	36.682(2)	36.682(2)
<i>α</i> /°	90	90
<i>β</i> /°	90	90
<i>γ</i> /°	90	90
Volume/Å ³	13103.0(16)	13103.0(16)
<i>Z</i>	8	8
ρ_{calc} (g/cm ³)	0.593	0.593
μ /mm ⁻¹	0.072	0.072
F(000)	2405.0	2405.0
Crystal size/mm ³	0.082 × 0.073 × 0.051	0.082 × 0.073 × 0.051
Radiation	Synchrotron ($\lambda = 0.7288$ Å)	Synchrotron ($\lambda = 0.7288$ Å)
2 Θ range for data collection/°	3.124 to 58.138	3.172 to 58.138
Index ranges	-25 ≤ <i>h</i> ≤ 25 -25 ≤ <i>k</i> ≤ 25 -48 ≤ <i>l</i> ≤ 48	-25 ≤ <i>h</i> ≤ 25 -25 ≤ <i>k</i> ≤ 25 -48 ≤ <i>l</i> ≤ 48
Reflections collected	215995	216133
Independent reflections	16240 [<i>R</i> _{int} = 0.0613, <i>R</i> _{sigma} = 0.0272]	16251 [<i>R</i> _{int} = 0.0617, <i>R</i> _{sigma} = 0.0272]
Data/restraints/parameters	16240/16/410	16251/16/410
Goodness-of-fit on <i>F</i> ²	1.377	0.984
Final <i>R</i> indexes [<i>I</i> ≥ 2 σ (<i>I</i>)]	<i>R</i> ₁ = 0.1167 w <i>R</i> ₂ = 0.2976	<i>R</i> ₁ = 0.0274 w <i>R</i> ₂ = 0.0711
Final <i>R</i> indexes [all data]	<i>R</i> ₁ = 0.1295 w <i>R</i> ₂ = 0.3126	<i>R</i> ₁ = 0.0344 w <i>R</i> ₂ = 0.0741
Largest diff. peak/hole / e Å ⁻³	1.69/-0.65	0.14/-0.33
Flack parameter	0.02(2)	0.06(2)

Refinement Details of Λ -MOF-520-2

A colorless crystal of Λ -MOF-520-2 was measured at beamline 12.2.1 at ALS with radiation of $\lambda = 0.7288 \text{ \AA}$. Based on intensity statistics for the whole dataset (PRP file), the resolution was cut off to 0.85 \AA ($R_{\text{merge}} \leq 40\%$ or average $I/\sigma > 2.5$ for the highest resolution shell). The two different orientations of **2** were modeled as overlapped positions with EXYZ and EADP. The occupancies of the unsubstituted formate and the two orientations of **2**, were refined with SUMP ($= 1.0000(1)$). All non-hydrogen atoms were refined anisotropically and hydrogen atoms were placed in calculated positions. SIMU and DELU were applied to O9, C28, O10 to stabilize anisotropic refinement of closely overlapping atoms. Solvent masking was applied and the void volume was estimated to be 9108.5 \AA^3 with 1352.9 electrons removed during masking. Reflections that are affected by the beamstop or having $(I_{\text{obs}} - I_{\text{calc}})/\sigma > 7$ were omitted. The weighting scheme was refined to convergence and the a, b parameters are 0.0289 and 0, respectively. The occupancies of the two orientations of triazole converged to 0.632(4) and 0.025(4) and the end of the refinement.

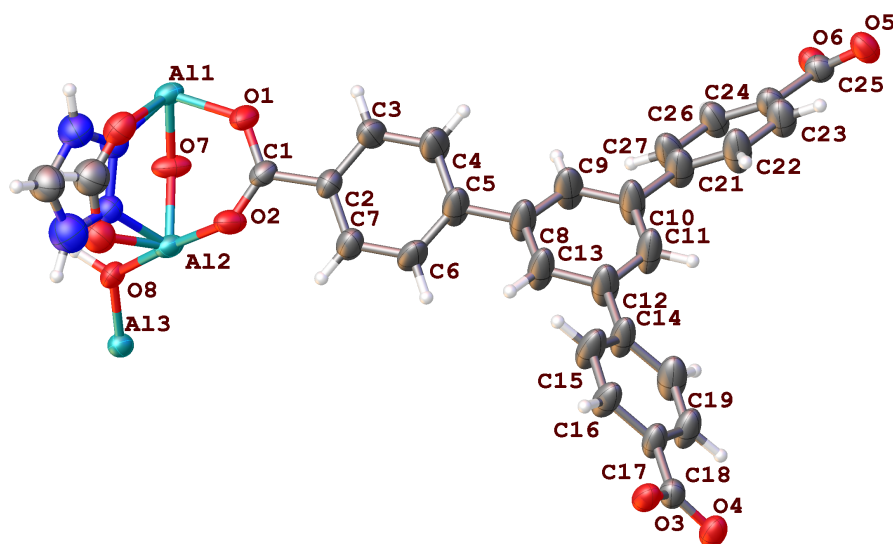


Figure 2.15. Asymmetric unit in the single crystal structure of Λ -MOF-520-2. Thermal ellipsoids are drawn with 50% probability.

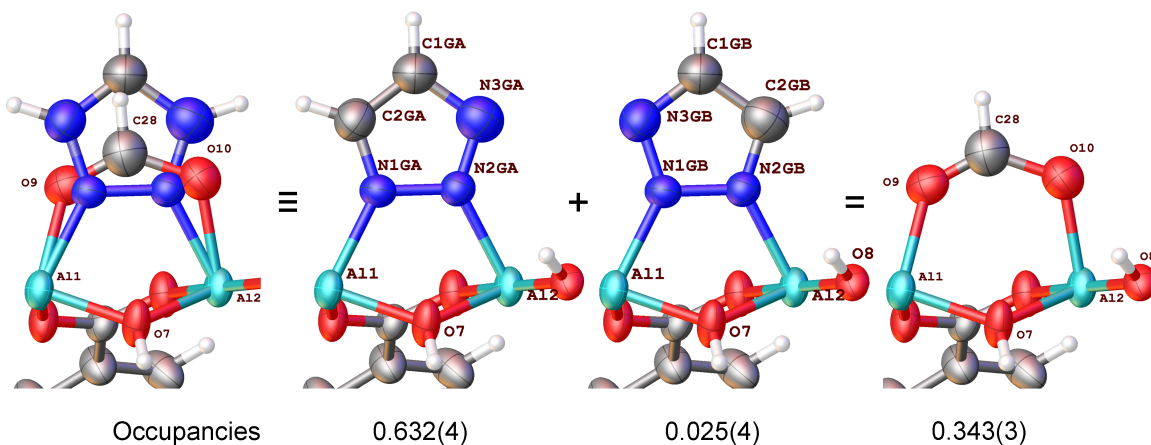


Figure 2.16. Illustration of the disorder at the incorporation site in the single crystal structure of Λ -MOF-520-2. Thermal ellipsoids are drawn with 50% probability.

Table 2.10. Crystal data, data collection, and structure refinement parameters for Λ -MOF-520-2.

	Before Solvent Masking	After Solvent Masking
Empirical formula	$C_{28.66}H_{18.66}Al_2N_{1.97}O_{8.69}$	$C_{28.66}H_{18.66}Al_2N_{1.97}O_{8.69}$
Formula weight	583.53	583.53
Temperature/K	100	100
Crystal system	tetragonal	tetragonal
Space group	$P4_22_12$	$P4_22_12$
$a/\text{\AA}$	18.9155(9)	18.9155(9)
$b/\text{\AA}$	18.9155(9)	18.9155(9)
$c/\text{\AA}$	36.6951(19)	36.6951(19)
$\alpha/^\circ$	90	90
$\beta/^\circ$	90	90
$\gamma/^\circ$	90	90
Volume/ \AA^3	13129.4(14)	13129.4(14)
Z	8	8
ρ_{calc} (g/cm^3)	0.590	0.590
μ/mm^{-1}	0.072	0.072
$F(000)$	2399.0	2399.0
Crystal size/ mm^3	$0.057 \times 0.054 \times 0.051$	$0.057 \times 0.054 \times 0.051$
Radiation	Synchrotron ($\lambda = 0.7288 \text{ \AA}$)	Synchrotron ($\lambda = 0.7288 \text{ \AA}$)
2Θ range for data collection/ $^\circ$	3.172 to 50.766	3.172 to 50.766
Index ranges	$-22 \leq h \leq 20$ $-21 \leq k \leq 22$ $-43 \leq l \leq 43$	$-22 \leq h \leq 20$ $-21 \leq k \leq 22$ $-43 \leq l \leq 43$
Reflections collected	78476	78589
Independent reflections	11123 [$R_{\text{int}} = 0.0591$, $R_{\text{sigma}} = 0.0326$]	11123 [$R_{\text{int}} = 0.0591$, $R_{\text{sigma}} = 0.0326$]
Data/restraints/parameters	11106/13/410	11123/13/410
Goodness-of-fit on F^2	1.351	0.950
Final R indexes [$I \geq 2\sigma(I)$]	$R_1 = 0.1044$ $wR_2 = 0.2947$	$R_1 = 0.0245$ $wR_2 = 0.0519$
Final R indexes [all data]	$R_1 = 0.1166$ $wR_2 = 0.3083$	$R_1 = 0.0321$ $wR_2 = 0.0538$
Largest diff. peak/hole / $e \text{ \AA}^{-3}$	1.34/-0.47	0.09/-0.13
Flack parameter	0.15(4)	0.15(4)

Refinement Details of Δ -MOF-520-3

A colorless crystal of Δ -MOF-520-3 was measured at beamline 11.2.1 at ALS with radiation of $\lambda = 0.7288 \text{ \AA}$. Based on intensity statistics for the whole dataset (PRP file), the resolution was cut off to 0.80 \AA ($R_{\text{merge}} \leq 40\%$ or average $I/\sigma > 2.5$ for the highest resolution shell). The occupancies of the guest (**3**) and the unsubstituted formate were found via a free variable, then were constrained at 0.8624 and 0.1376, respectively. All non-hydrogen atoms were refined anisotropically and hydrogen atoms were placed in calculated positions. SADI and SIMU were applied to the unsubstituted formate group to stabilize the refinement caused by closely overlapping atoms. Reflections that are affected by the beamstop or having $(I_{\text{obs}} - I_{\text{calc}})/\sigma > 7$ were omitted. The weighting scheme was refined to convergence and the a, b parameters are 0.0909 and 1.6816, respectively.

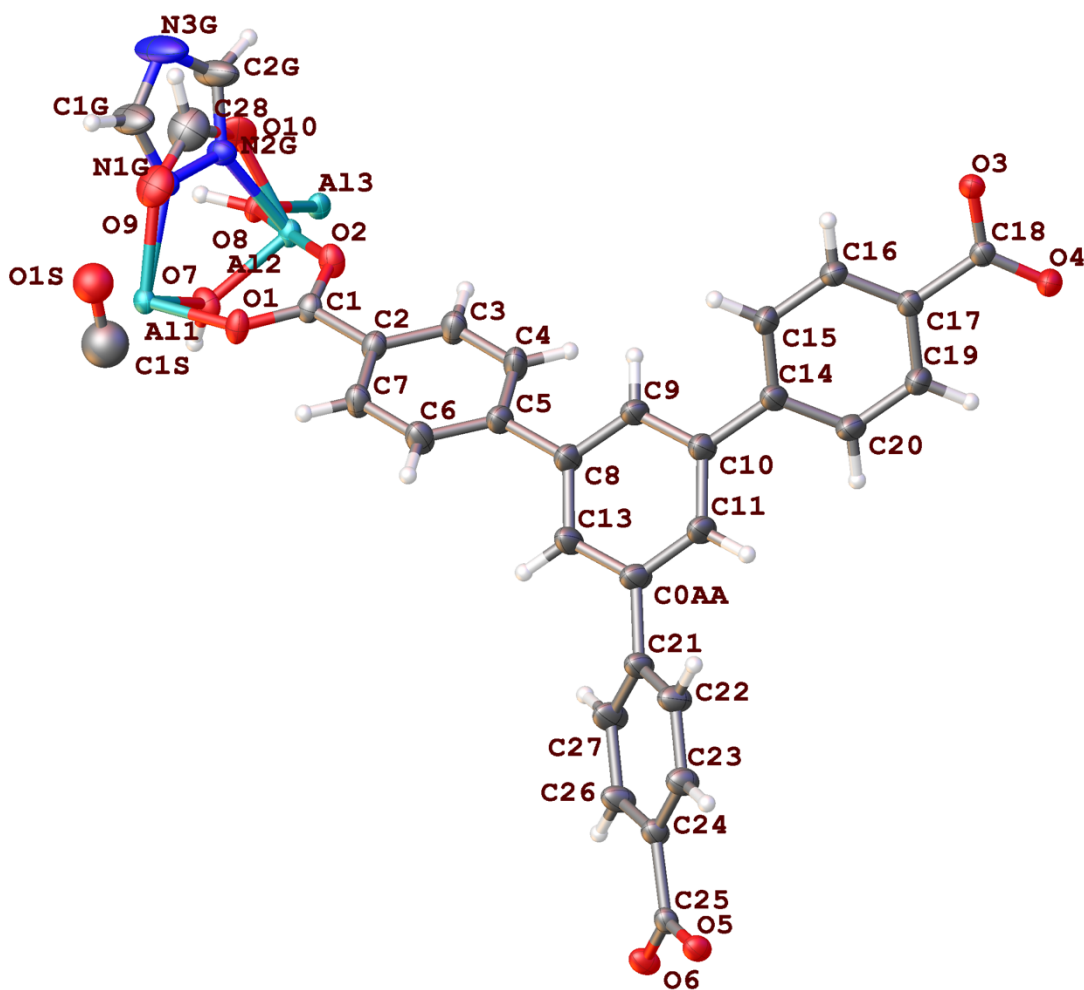


Figure 2.17. Asymmetric unit in the single crystal structure of Δ -MOF-520-3. Thermal ellipsoids are drawn with 50% probability.

Table 2.11. Crystal data, data collection, and structure refinement parameters for Δ -MOF-520-3.

Name	Δ -MOF-520-3
Empirical formula	$C_{28.98}H_{18.86}Al_2N_{2.59}O_{8.37}$
Formula weight	591.11
Temperature/K	100(2)
Crystal system	tetragonal
Space group	$P4_22_12$
$a/\text{\AA}$	19.5339(5)
$b/\text{\AA}$	19.5339(5)
$c/\text{\AA}$	35.7057(10)
$\alpha/^\circ$	90
$\beta/^\circ$	90
$\gamma/^\circ$	90
Volume/ \AA^3	13624.3(8)
Z	8
$\rho_{\text{calc}} (\text{g/cm}^3)$	0.570
μ/mm^{-1}	0.070
F(000)	2430.0
Crystal size/ mm^3	$0.05 \times 0.05 \times 0.038$
Radiation	Synchrotron ($\lambda = 0.7288 \text{ \AA}$)
2Θ range for data collection/ $^\circ$	4.276 to 54.194
Index ranges	$-24 \leq h \leq 24, -24 \leq k \leq 24, -44 \leq l \leq 44$
Reflections collected	190694
Independent reflections	13883 [$R_{\text{int}} = 0.0714, R_{\text{sigma}} = 0.0281$]
Data/restraints/parameters	13883/15/411
Goodness-of-fit on F^2	1.097
Final R indexes [$I \geq 2\sigma(I)$]	$R_1 = 0.0459, wR_2 = 0.1272$
Final R indexes [all data]	$R_1 = 0.0473, wR_2 = 0.1289$
Largest diff. peak/hole / $e \text{ \AA}^{-3}$	0.69/-0.32
Flack parameter	-0.02(2)

Refinement Details of Δ -MOF-520-4

A colorless crystal of Δ -MOF-520-4 was measured at beamline 12.2.1 at ALS with radiation of $\lambda = 0.7288 \text{ \AA}$. Based on intensity statistics for the whole dataset (PRP file), the resolution was cut off to 0.90 \AA ($R_{\text{merge}} \leq 40\%$ or average $I/\sigma > 2.5$ for the highest resolution shell). The occupancies of the unsubstituted formate and **4** were refined with a free variable. After refinement converged, the occupancy of **4** was constrained to 0.5180. All non-hydrogen atoms were refined anisotropically and hydrogen atoms were placed in calculated positions. SIMU was applied to N3G, N4G, C1G, C2G to stabilize their anisotropic refinement. Solvent masking was applied and the void volume was estimated to be 8707.5 \AA^3 with 3543.8 electrons removed during masking. Reflections that are affected by the beamstop or having $(I_{\text{obs}} - I_{\text{calc}})/\sigma > 7$ were omitted. The weighting scheme was refined to convergence and the a, b parameters are 0.0548 and 0, respectively.

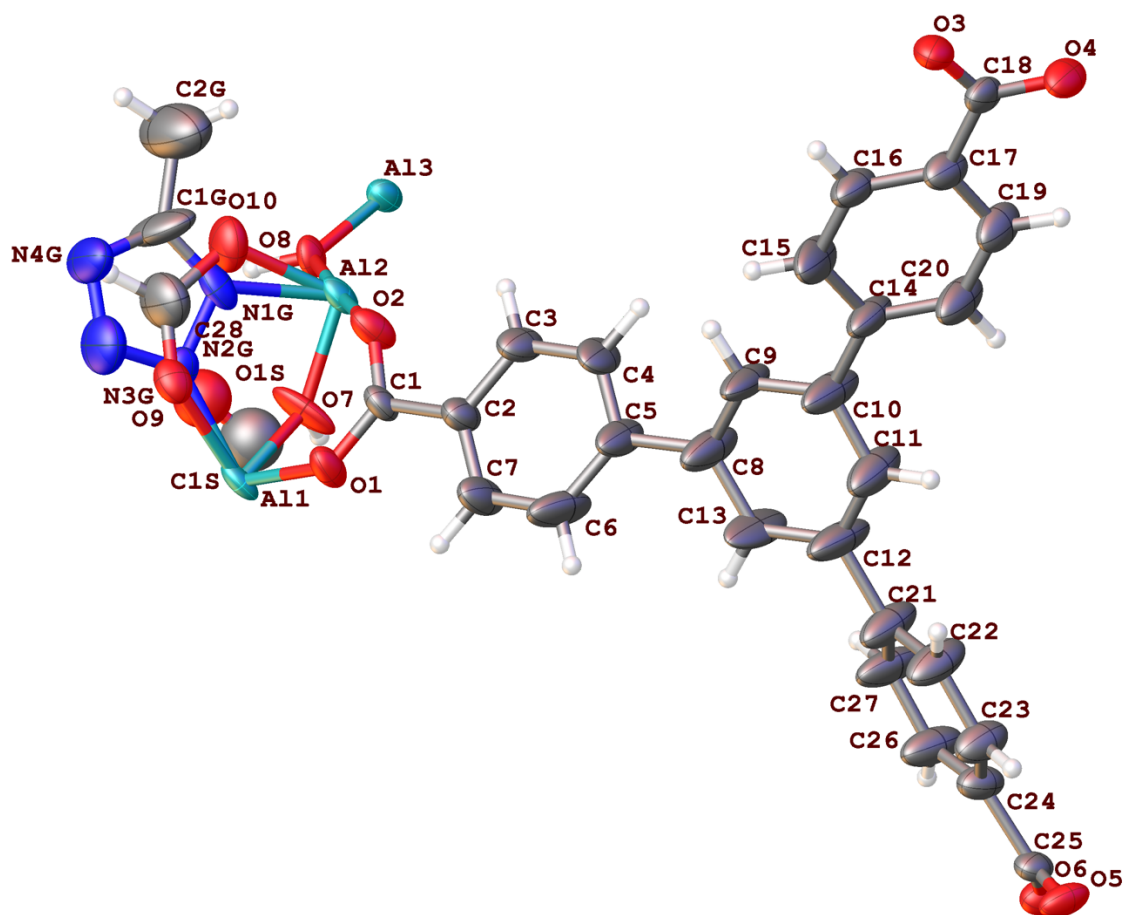


Figure 2.18. Asymmetric unit in the single crystal structure of Δ -MOF-520-4. Thermal ellipsoids are drawn with 50% probability.

Table 2.12. Crystal data, data collection, and structure refinement parameters for Δ -MOF-520-4.

	Before Solvent Masking	After Solvent Masking
Empirical formula	C _{29.02} H _{19.04} Al ₂ N _{2.07} O _{9.21}	C _{29.02} H _{19.04} Al ₂ N _{2.07} O _{9.21}
Formula weight	598.10	598.10
Temperature/K	100(2)	100(2)
Crystal system	tetragonal	tetragonal
Space group	<i>P4</i> ₂ <i>2</i> ₁ <i>2</i>	<i>P4</i> ₂ <i>2</i> ₁ <i>2</i>
<i>a</i> /Å	18.8135(11)	18.8135(11)
<i>b</i> /Å	18.8135(11)	18.8135(11)
<i>c</i> /Å	36.797(2)	36.797(2)
α /°	90	90
β /°	90	90
γ /°	90	90
Volume/Å ³	13024.1(17)	13024.1(17)
<i>Z</i>	2	2
ρ_{calc} (g/cm ³)	0.610	0.610
μ /mm ⁻¹	0.074	0.074
F(000)	2459.0	2459.0
Crystal size/mm ³	0.05 × 0.032 × 0.028	0.05 × 0.032 × 0.028
Radiation	Synchrotron ($\lambda = 0.7288$ Å)	Synchrotron ($\lambda = 0.7288$ Å)
2 θ range for data collection/°	2.494 to 47.772	3.174 to 47.772
Index ranges	-20 ≤ <i>h</i> ≤ 20 -20 ≤ <i>k</i> ≤ 20 -40 ≤ <i>l</i> ≤ 40	-20 ≤ <i>h</i> ≤ 20 -20 ≤ <i>k</i> ≤ 20 -40 ≤ <i>l</i> ≤ 40
Reflections collected	108183	108177
Independent reflections	9338 [<i>R</i> _{int} = 0.1184, <i>R</i> _{sigma} = 0.0514]	9335 [<i>R</i> _{int} = 0.1182 <i>R</i> _{sigma} = 0.0513]
Data/restraints/parameters	9338/18/419	9335/18/419
Goodness-of-fit on <i>F</i> ²	1.479	0.992
Final <i>R</i> indexes [<i>I</i> ≥ 2 σ (<i>I</i>)]	<i>R</i> ₁ = 0.1245 <i>wR</i> ₂ = 0.3204	<i>R</i> ₁ = 0.0358 <i>wR</i> ₂ = 0.0870
Final <i>R</i> indexes [all data]	<i>R</i> ₁ = 0.1368 <i>wR</i> ₂ = 0.3338	<i>R</i> ₁ = 0.0422 <i>wR</i> ₂ = 0.0900
Largest diff. peak/hole / e Å ⁻³	0.97/-0.79	0.22/-0.24
Flack parameter	0.08(7)	0.08(7)

Refinement Details of Δ -MOF-520-5

A colorless crystal of Δ -MOF-520-5 was measured at beamline 12.2.1 at ALS with radiation of $\lambda = 0.7288 \text{ \AA}$. Based on intensity statistics for the whole dataset (PRP file), the resolution was cut off to 0.75 \AA ($R_{\text{merge}} \leq 40\%$ or average $I/\sigma > 2.5$ for the highest resolution shell). The occupancy of **5** was found through adding a new variable and then constrained to 1. Non-hydrogen atoms were refined anisotropically and hydrogen atoms were placed in calculated positions. Reflections that are affected by the beamstop or having $(I_{\text{obs}} - I_{\text{calc}})/\sigma > 7$ were omitted. The weighting scheme was refined to convergence and the a, b parameters are 0.1385 and 4.1029, respectively. Solvent Masking was not applied since the solvent in the structure was evacuated before measurement.

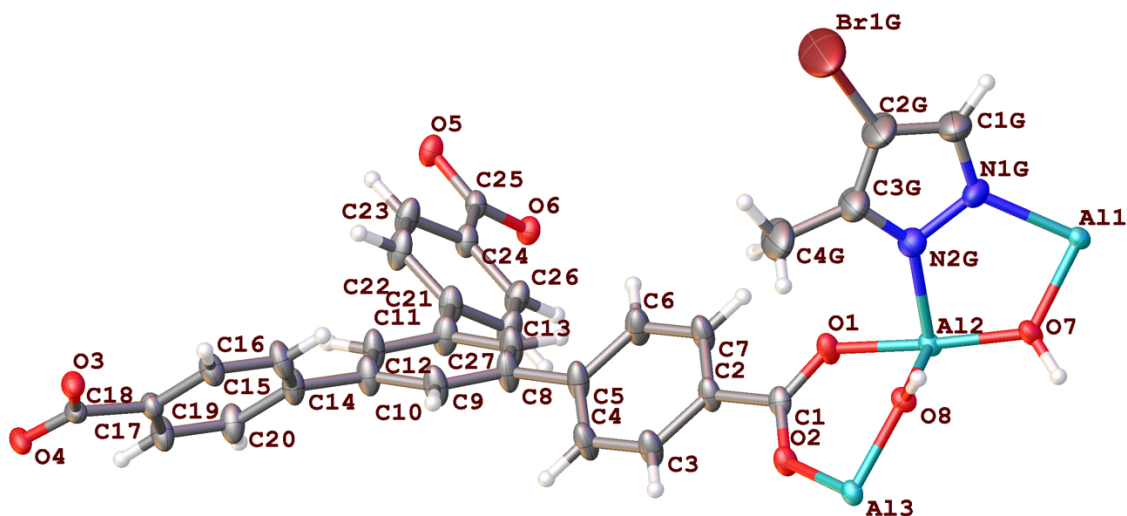


Figure 2.19. Asymmetric unit in the single crystal structure of Δ -MOF-520-5. Thermal ellipsoids are drawn with 50% probability.

Table 2.13. Crystal data, data collection, and structure refinement parameters for Δ -MOF-520-5.

Name	Δ -MOF-520-5
Empirical formula	$C_{31}H_{21}Al_2BrN_2O_8$
Formula weight	683.37
Temperature/K	100(2)
Crystal system	tetragonal
Space group	$P4_22_12$
$a/\text{\AA}$	19.4353(6)
$b/\text{\AA}$	19.4353(6)
$c/\text{\AA}$	35.7957(11)
$\alpha/^\circ$	90
$\beta/^\circ$	90
$\gamma/^\circ$	90
Volume/ \AA^3	13521.1(9)
Z	8
$\rho_{\text{calc}} (\text{g/cm}^3)$	0.671
μ/mm^{-1}	0.662
F(000)	2768.0
Crystal size/ mm^3	$0.071 \times 0.064 \times 0.054$
Radiation	Synchrotron ($\lambda = 0.7288 \text{ \AA}$)
2Θ range for data collection/ $^\circ$	4.298 to 58.382
Index ranges	$-25 \leq h \leq 21, -24 \leq k \leq 20, -39 \leq l \leq 47$
Reflections collected	100616
Independent reflections	16738 [$R_{\text{int}} = 0.0727, R_{\text{sigma}} = 0.0497$]
Data/restraints/parameters	16738/0/399
Goodness-of-fit on F^2	1.009
Final R indexes [$I \geq 2\sigma(I)$]	$R_1 = 0.0654, wR_2 = 0.1850$
Final R indexes [all data]	$R_1 = 0.0777, wR_2 = 0.1970$
Largest diff. peak/hole / $e \text{ \AA}^{-3}$	1.38/-1.76
Flack parameter	-0.003(3)

Refinement Details of Λ -MOF-520-6

A colorless crystal of Λ -MOF-520-6 was measured at beamline 11.3.1 at ALS with radiation of $\lambda = 1.0332 \text{ \AA}$. Based on intensity statistics for the whole dataset (PRP file), the resolution was cut off to 0.83 \AA ($R_{\text{merge}} \leq 40\%$ or average $I/\sigma > 2.5$ for the highest resolution shell). The occupancy of **6** was found through adding a new variable and converged at $0.8602(15)$. The unsubstituted formate has a low occupancy that couldn't be allocated from a difference electron density map (F_{diff}). A strong electron density peak was found at the center of the SBU, which is assigned as an oxygen atom (O1S; See section S3.1). The atom is not necessarily representing water, as there's only a trace amount of water in the incorporation reaction system (Section S2.2), so that hydrogens were not assigned to the O1S. Solvent masking was applied during structure refinement. The void volume was estimated to be 8297.7 \AA^3 with 2230.4 electrons removed during masking. Before solvent masking procedure, the structure was refined anisotropically and hydrogen atoms were placed at calculated positions. Reflections that are affected by the beamstop or having $(I_{\text{obs}} - I_{\text{calc}})/\sigma > 7$ were omitted. The weighting scheme was refined to convergence and the a, b parameters are 0.0332 and 0, respectively.

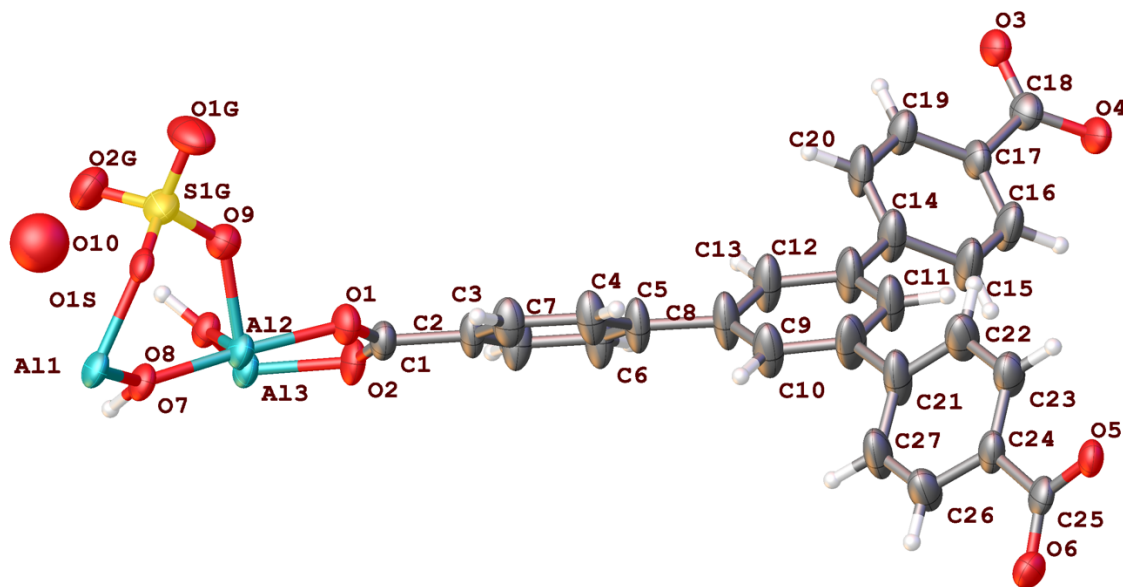


Figure 2.20. Asymmetric unit in the single crystal structure of Λ -MOF-520-6. Thermal ellipsoids are drawn with 50% probability.

Table 2.14. Crystal data, data collection, and structure refinement parameters for Λ -MOF-520-6.

	Before Solvent Masking	After Solvent Masking
Empirical formula	$C_{27}H_{17}Al_2O_{12.05}S_{0.85}$	$C_{27}H_{17}Al_2O_{12.08}S_{0.86}$
Formula weight	615.52	616.22
Temperature/K	100	100
Crystal system	tetragonal	tetragonal
Space group	$P4_22_12$	$P4_22_12$
$a/\text{\AA}$	18.1729(8)	18.1729(8)
$b/\text{\AA}$	18.1729(8)	18.1729(8)
$c/\text{\AA}$	37.6737(17)	37.6737(17)
$\alpha/^\circ$	90	90
$\beta/^\circ$	90	90
$\gamma/^\circ$	90	90
Volume/ \AA^3	12441.9(12)	12441.9(12)
Z	8	8
$\rho_{\text{calc}} (\text{g/cm}^3)$	0.657	0.658
μ/mm^{-1}	0.321	0.322
F(000)	2520.0	2523.0
Crystal size/ mm^3	$0.06 \times 0.06 \times 0.05$	$0.06 \times 0.06 \times 0.05$
Radiation	Synchrotron ($\lambda = 1.0332 \text{ \AA}$)	Synchrotron ($\lambda = 1.0332 \text{ \AA}$)
2Θ range for data collection/ $^\circ$	4.528 to 77.064	4.528 to 77.064
Index ranges	$-21 \leq h \leq 21$ $-21 \leq k \leq 21$ $-45 \leq l \leq 45$	$-21 \leq h \leq 21$ $-21 \leq k \leq 21$ $-45 \leq l \leq 45$
Reflections collected	107833	107958
Independent reflections	11370 [$R_{\text{int}} = 0.0474$, $R_{\text{sigma}} = 0.0306$]	11375 [$R_{\text{int}} = 0.0472$, $R_{\text{sigma}} = 0.0303$]
Data/restraints/parameters	11370/0/384	11375/0/383
Goodness-of-fit on F^2	1.129	0.946
Final R indexes [$I \geq 2\sigma(I)$]	$R_1 = 0.0833$, $wR_2 = 0.2281$	$R_1 = 0.0254$, $wR_2 = 0.0542$
Final R indexes [all data]	$R_1 = 0.0970$, $wR_2 = 0.2470$	$R_1 = 0.0350$, $wR_2 = 0.0570$
Largest diff. peak/hole / $e \text{ \AA}^{-3}$	0.91/-0.58	0.13/-0.18
Flack parameter	0.043(11)	0.053(11)

Refinement Details of Δ -MOF-520-7

A colorless crystal of Δ -MOF-520-7 was measured at beamline 12.2.1 at ALS with radiation of $\lambda = 0.7288 \text{ \AA}$. Based on intensity statistics for the whole dataset (PRP file), the resolution was cut off to 0.83 \AA ($R_{\text{merge}} \leq 40\%$ or average $I/\sigma > 2.5$ for the highest resolution shell). The formates were not fully substituted, so that the occupancies of formate and **7** were refined via a free variable. The initial solution of **7** provided a refined structure of the molecule with large ADPs. Examination of the P-O bond length and the orientation of the ellipsoids leads to the result that **7** should be refined as two mirrored orientations. The molecule was carefully split, and the occupancies of the formate and the two positions were constrained to sum to 1 by SUMP (=1.0000(1)). DFIX was applied to fix the bond length in the formate. SADI was applied to constrain the equivalent bonds in the two positions of **7**. RIGU and ISOR were applied to constrain the heavily overlapped atoms. All non-hydrogen atoms were refined anisotropically and hydrogen atoms were placed in calculated positions. After the refinement converged, the occupancies of two positions of **7** were constrained to 0.3163 and 0.2334, respectively. At last, solvent masking was applied during structure refinement. The void volume was estimated to be 8289.9 \AA^3 with 3126.9 electrons removed during masking. Reflections that are affected by beamstop or having $(I_{\text{obs}} - I_{\text{calc}})/\sigma > 7$ were omitted. The weighting scheme was refined to convergence and the a, b parameters are 0.0689 and 0, respectively.

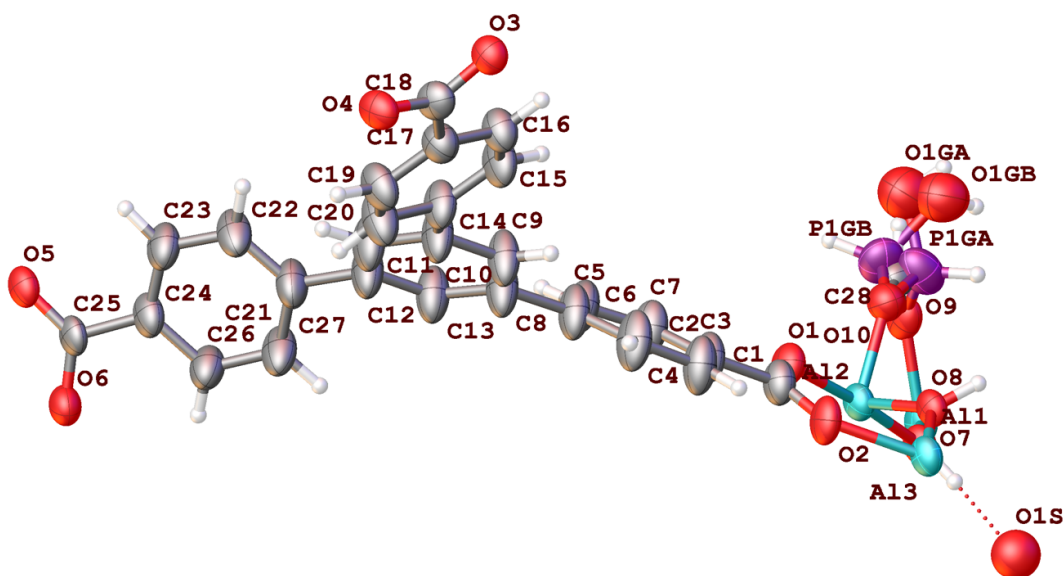


Figure 2.21. Asymmetric unit in the single crystal structure of Δ -MOF-520-7. Thermal ellipsoids are drawn with 50% probability.

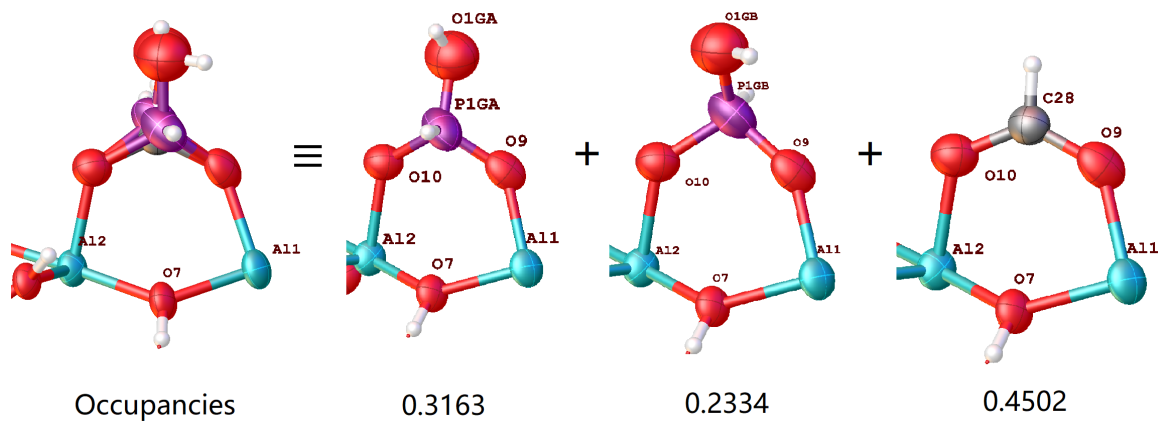


Figure 2.22. Illustration of the disorder at the incorporation site in the single crystal structure of Δ -MOF-520-7. Thermal ellipsoids are drawn with 50% probability.

Table 2.15. Crystal data, data collection, and structure refinement parameters for Δ -MOF-520-7.

	Before Solvent Masking	After Solvent Masking
Empirical formula	C _{27.45} H _{18.55} Al ₂ O _{11.03} P _{0.55}	C _{27.45} H _{18.55} Al ₂ O _{11.03} P _{0.55}
Formula weight	595.89	595.89
Temperature/K	100(2)	100(2)
Crystal system	tetragonal	tetragonal
Space group	<i>P4</i> ₂ <i>2</i> ₁ <i>2</i>	<i>P4</i> ₂ <i>2</i> ₁ <i>2</i>
<i>a</i> /Å	18.1702(6)	18.1702(6)
<i>b</i> /Å	18.1702(6)	18.1702(6)
<i>c</i> /Å	37.8430(14)	37.8430(14)
α /°	90	90
β /°	90	90
γ /°	90	90
Volume/Å ³	12494.1(9)	12494.1(9)
<i>Z</i>	8	8
ρ_{calc} (g/cm ³)	0.634	0.634
μ /mm ⁻¹	0.093	0.083
F(000)	2446.0	2446.0
Crystal size/mm ³	0.071 × 0.058 × 0.052	0.071 × 0.058 × 0.052
Radiation	Synchrotron ($\lambda = 0.7288$ Å)	Synchrotron ($\lambda = 0.7288$ Å)
2 θ range for data collection/°	3.186 to 52.216	4.64 to 52.216
Index ranges	-21 ≤ <i>h</i> ≤ 21 -21 ≤ <i>k</i> ≤ 21 -45 ≤ <i>l</i> ≤ 45	-21 ≤ <i>h</i> ≤ 21 -21 ≤ <i>k</i> ≤ 21 -45 ≤ <i>l</i> ≤ 45
Reflections collected	245737	245782
Independent reflections	11485 [R _{int} = 0.0591, R _{sigma} = 0.0195]	11482 [R _{int} = 0.0590, R _{sigma} = 0.0195]
Data/restraints/parameters	11485/32/403	11482/32/402
Goodness-of-fit on F ²	1.459	0.991
Final R indexes [<i>I</i> ≥ 2 σ (<i>I</i>)]	R ₁ = 0.1166 wR ₂ = 0.3067	R ₁ = 0.0330 wR ₂ = 0.0871
Final R indexes [all data]	R ₁ = 0.1232 wR ₂ = 0.3144	R ₁ = 0.0367 wR ₂ = 0.0890
Largest diff. peak/hole / e Å ⁻³	1.00/-0.61	0.37/-0.25
Flack parameter	0.052(19)	0.08(2)

Refinement Details of Δ -MOF-520-8

A colorless crystal of Δ -MOF-520-8 was measured at beamline 12.2.1 at ALS with radiation of $\lambda = 0.7288 \text{ \AA}$. Based on intensity statistics for the whole dataset (PRP file), the resolution was cut off to 0.80 \AA ($R_{\text{merge}} \leq 40\%$ or average $I/\sigma > 2.5$ for the highest resolution shell). The formates were not fully substituted, so that the occupancies of formate and **8** were refined via a free variable. Due to the overlap of the positions of **8** and remaining formate, the formate carbon (C28) and the phosphorous atom (P1G) were constrained by EXYZ and EADP. Solvent masking was applied during structure refinement. Before solvent masking, the structure was refined anisotropically and hydrogen atoms were placed in calculated positions. An oxygen atom and a carbon atom were assigned at the center of the SBU to represent the electron densities contributed by disordered yet hydrogen-bonding-confined solvent molecules. The void volume was estimated to be 8523.3 \AA^3 with 959.4 electrons removed during solvent masking. Reflections that are affected by the beamstop or having $(I_{\text{obs}} - I_{\text{calc}})/\sigma > 7$ were omitted. The weighting scheme was refined to convergence and the a, b parameters are 0.0493 and 0, respectively. The occupancy of **8** converged to 0.506(4) in the end.

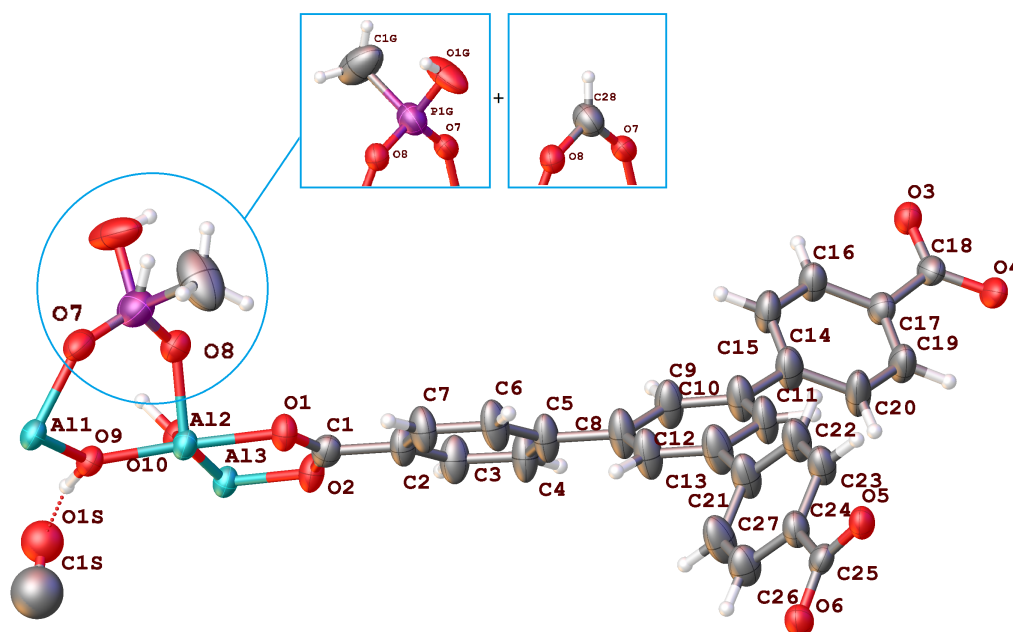


Figure 2.23. Asymmetric unit in the single crystal structure of Δ -MOF-520-8. Thermal ellipsoids are drawn with 50% probability. The positions of P1G and C28 overlap, but are illustrated in separate insets for clarity.

Table 2.16. Selected Bond Lengths.

	Atom	Atom	Length/ \AA
Before Solvent Masking	P1G	C1G	1.873(17)
	P1G	O1G	1.548(10)
After Solvent Masking	P1G	C1G	1.883(6)
	P1G	O1G	1.545(3)

The difference between P1G–O1G and P1G–C1G bond lengths clearly confirms the atomic assignment of O1G and C1G, and in addition, the orientational preference of the incorporation of this molecule.

Table 2.17. Crystal data, data collection, and structure refinement parameters for Δ -MOF-520-8.

	Before Solvent Masking	After Solvent Masking
Empirical formula	$C_{29}H_{19.5}Al_2O_{11.08}P_{0.5}$	$C_{29}H_{19.5}Al_2O_{11.08}P_{0.5}$
Formula weight	614.73	614.73
Temperature/K	100(2)	100(2)
Crystal system	tetragonal	tetragonal
Space group	$P4_22_12$	$P4_22_12$
$a/\text{\AA}$	18.7104(5)	18.7104(5)
$b/\text{\AA}$	18.7104(5)	18.7104(5)
$c/\text{\AA}$	37.1528(11)	37.1528(11)
$\alpha/^\circ$	90	90
$\beta/^\circ$	90	90
$\gamma/^\circ$	90	90
Volume/ \AA^3	13006.4(8)	13006.4(8)
Z	8	8
ρ_{calc} (g/cm^3)	0.628	0.628
μ/mm^{-1}	0.089	0.089
F(000)	2525.0	2525.0
Crystal size/ mm^3	$0.08 \times 0.05 \times 0.04$	$0.08 \times 0.05 \times 0.04$
Radiation	Synchrotron ($\lambda = 0.7288 \text{\AA}$)	Synchrotron ($\lambda = 0.7288 \text{\AA}$)
2Θ range for data collection/ $^\circ$	4.044 to 54.19	4.044 to 54.19
Index ranges	$-22 \leq h \leq 20,$ $-23 \leq k \leq 23,$ $-44 \leq l \leq 46$	$-22 \leq h \leq 20,$ $-23 \leq k \leq 23,$ $-44 \leq l \leq 46$
Reflections collected	77976	78161
Independent reflections	13192 [$R_{\text{int}} = 0.0682,$ $R_{\text{sigma}} = 0.0571$]	13211 [$R_{\text{int}} = 0.0681,$ $R_{\text{sigma}} = 0.0569$]
Data/restraints/parameters	13192/0/393	13211/0/392
Goodness-of-fit on F^2	1.070	0.905
Final R indexes [$I \geq 2\sigma(I)$]	$R_1 = 0.0923,$ $wR_2 = 0.2584$	$R_1 = 0.0354,$ $wR_2 = 0.0802$
Final R indexes [all data]	$R_1 = 0.1151,$ $wR_2 = 0.2761$	$R_1 = 0.0523,$ $wR_2 = 0.0844$
Largest diff. peak/hole / $e \text{\AA}^{-3}$	0.98/-0.38	0.30/-0.13
Flack parameter	0.08(4)	0.10(5)

Refinement Details of Λ -MOF-520-8

A colorless crystal of Λ -MOF-520-8 was measured at beamline 12.2.1 at ALS with radiation of $\lambda = 0.7288 \text{ \AA}$. Based on intensity statistics for the whole dataset (PRP file), the resolution was cut off to 0.80 \AA ($R_{\text{merge}} \leq 40\%$ or average $I/\sigma > 2.5$ for the highest resolution shell). The formates were not fully substituted, so that the occupancies of formate and **8** were refined via a free variable. Due to the overlap of the positions of **8** and remaining formate, the formate carbon (C28) and the phosphorous atom (PIG) were constrained by EXYZ and EADP. Solvent masking was applied during structure refinement. Before solvent masking, the structure was refined anisotropically and hydrogen atoms were placed in calculated positions. A DMF molecule was assigned at the center of the SBU to represent the electron densities contributed by disordered yet hydrogen-bonding confined solvent molecules, and RIGU was applied to this solvent molecule. The void volume was estimated to be 8006.7 \AA^3 with 1939.7 electrons removed during masking. Reflections that are affected by the beamstop or having $(I_{\text{obs}} - I_{\text{calc}})/\sigma > 7$ were omitted. The weighting scheme was refined to convergence and the a, b parameters are 0.019 and 0, respectively. The occupancy of **8** converged to 0.514(4) in the end.

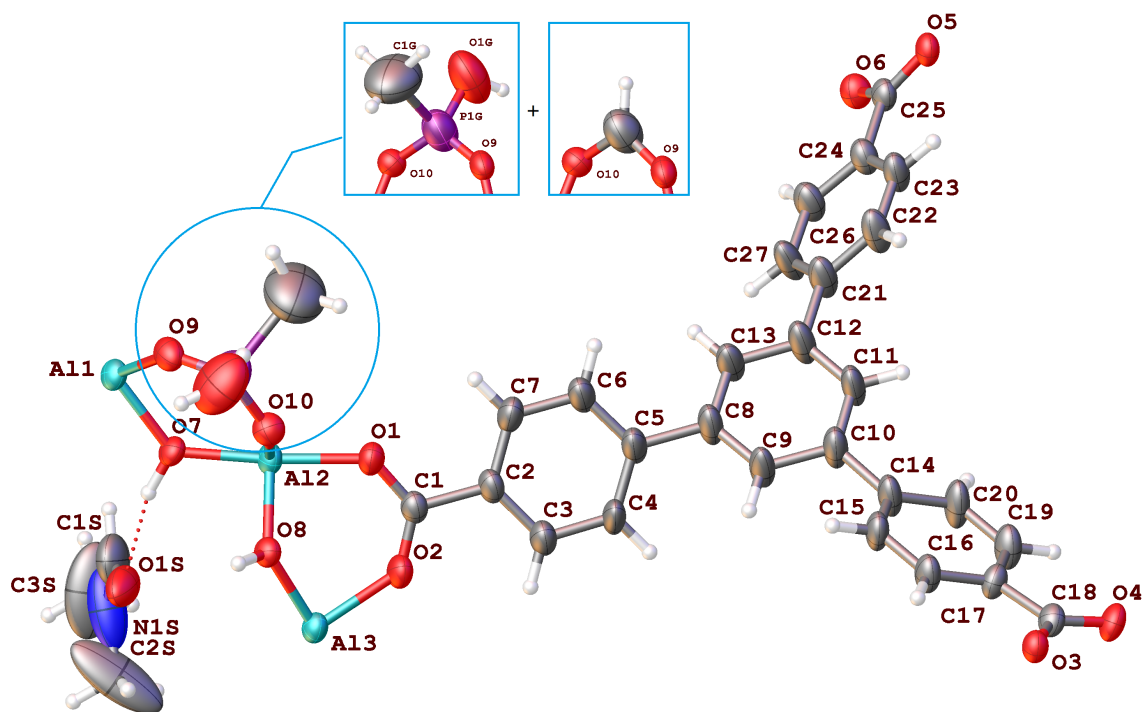


Figure 2.24. Asymmetric unit in the single crystal structure of Λ -MOF-520-8. Thermal ellipsoids are drawn with 50% probability. The positions of PIG and C28 overlap, but are illustrated in separate insets for clarity.

Table 2.18. Selected Bond Lengths.

	Atom	Atom	Length/Å
Before Solvent Masking	P1G	C1G	1.88(3)
	P1G	O1G	1.553(14)
After Solvent Masking	P1G	C1G	1.987(8)
	P1G	O1G	1.527(4)

The bond length of P1G–C1G differs a lot before and after solvent masking, possibly due to imperfection of the solvent masking process around the not-full-occupancy incoming molecule (as the bond length before solvent masking matches well with it in Δ -MOF-520-**8**). Nevertheless, the difference between P1G–O1G and P1G–C1G bond lengths clearly confirms the atomic assignment of O1G and C1G, and in addition, the orientational preference of the incorporation of this molecule.

Table 2.19. Crystal data, data collection, and structure refinement parameters for Λ -MOF-520-8.

	Before Solvent Masking	After Solvent Masking
Empirical formula	$C_{30.06}H_{24.02}Al_2N_{0.69}O_{11.09}P_{0.41}$	
Formula weight	638.75	
Temperature/K	100	
Crystal system	tetragonal	
Space group	$P4_22_12$	
$a/\text{\AA}$	18.6051(8)	
$b/\text{\AA}$	18.6051(8)	
$c/\text{\AA}$	37.3840(18)	
$\alpha/^\circ$	90	
$\beta/^\circ$	90	
$\gamma/^\circ$	90	
Volume/ \AA^3	12940.5(13)	
Z	8	
ρ_{calc} (g/cm^3)	0.656	
μ/mm^{-1}	0.089	
F(000)	2640.0	
Crystal size/ mm^3	$0.1 \times 0.1 \times 0.1$	
Radiation	Synchrotron ($\lambda = 0.7288 \text{\AA}$)	
2θ range for data collection/ $^\circ$	3.168 to 54.384	3.168 to 54.384
Index ranges	$-23 \leq h \leq 23,$ $-19 \leq k \leq 19,$ $-45 \leq l \leq 46$	$-23 \leq h \leq 23,$ $-19 \leq k \leq 19,$ $-45 \leq l \leq 46$
Reflections collected	88562	88734
Independent reflections	13291 [$R_{\text{int}} = 0.0761,$ $R_{\text{sigma}} = 0.0439$]	13310 [$R_{\text{int}} = 0.0752,$ $R_{\text{sigma}} = 0.0431$]
Data/restraints/parameters	13291/30/429	13310/30/428
Goodness-of-fit on F^2	1.102	0.909
Final R indexes [$I \geq 2\sigma(I)$]	$R_1 = 0.0916,$ $wR_2 = 0.2436$	$R_1 = 0.0282,$ $wR_2 = 0.0610$
Final R indexes [all data]	$R_1 = 0.1030,$ $wR_2 = 0.2542$	$R_1 = 0.0369,$ $wR_2 = 0.0631$
Largest diff. peak/hole / $e \text{\AA}^{-3}$	0.76/-0.45	0.23/-0.17
Flack parameter	0.13(5)	0.16(5)

Refinement Details of Δ -MOF-520-9

A colorless crystal of Δ -MOF-520-9 was measured at beamline 12.2.1 at ALS with radiation of $\lambda = 0.7288 \text{ \AA}$. Based on intensity statistics for the whole dataset (PRP file), the resolution was cut off to 0.85 \AA ($R_{\text{merge}} \leq 40\%$ or average $I/\sigma > 2.5$ for the highest resolution shell). The formates were not fully substituted, so that the occupancies of formate and **9** were found via a free variable. Because the carbon atom of formate (C28) and the phosphorous atom of **9** (P1G) were too close to be distinguished, they were constrained at same coordinate with EXYZ and EADP. After the refinement converged, the occupancy of **9** was constrained to 0.7264. All non-hydrogen atoms were refined anisotropically and hydrogen atoms were placed in calculated positions. Reflections that are affected by the beamstop or having $(I_{\text{obs}} - I_{\text{calc}})/\sigma > 7$ were omitted. The weighting scheme was refined to convergence and the a, b parameters are 0.1027 and 1.4516, respectively. Solvent masking was not applied since the solvent in the structure was evacuated before measurement.

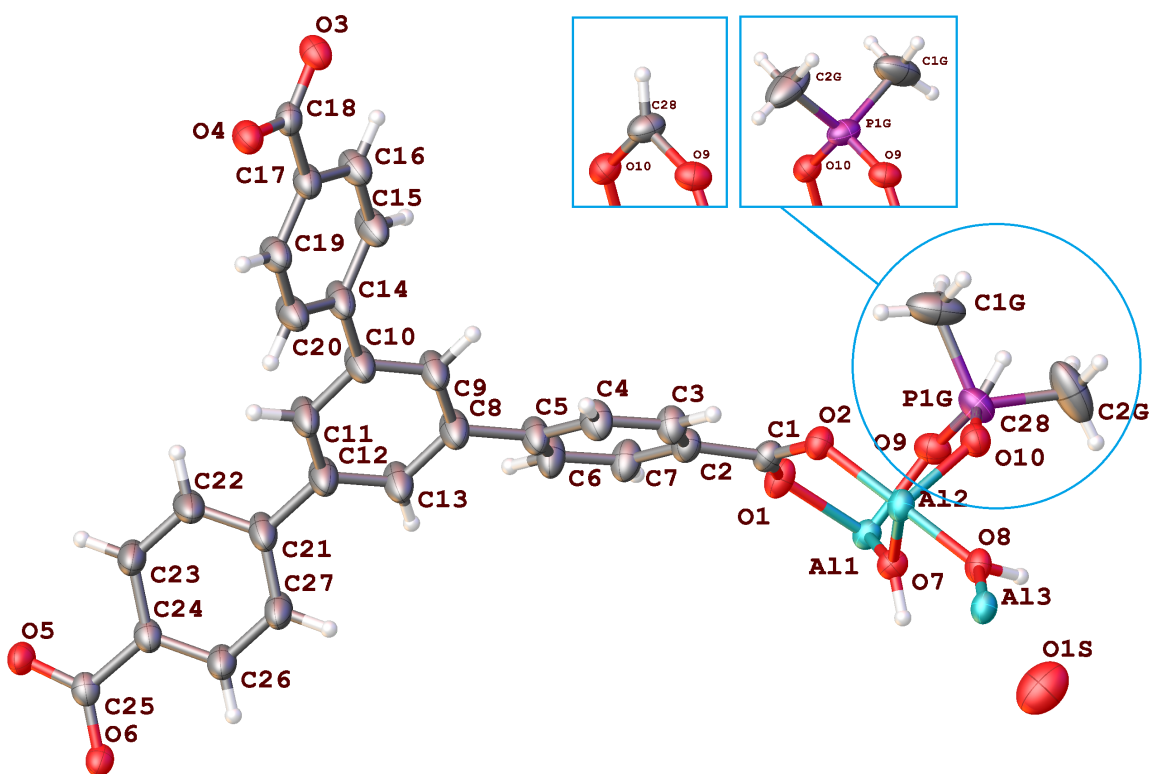


Figure 2.25. Asymmetric unit in the single crystal structure of Δ -MOF-520-9. Thermal ellipsoids are drawn with 50% probability. The positions of P1G and C28 overlap, but are illustrated in separate insets for clarity.

Table 2.20. Crystal data, data collection, and structure refinement parameters for Δ -MOF-520-9.

Name	Δ -MOF-520-9
Empirical formula	$C_{28.73}H_{21.63}Al_2O_{10.09}P_{0.73}$
Formula weight	604.64
Temperature/K	100(2)
Crystal system	tetragonal
Space group	$P4_22_12$
$a/\text{\AA}$	18.9892(8)
$b/\text{\AA}$	18.9892(8)
$c/\text{\AA}$	36.9796(15)
$\alpha/^\circ$	90
$\beta/^\circ$	90
$\gamma/^\circ$	90
Volume/ \AA^3	13334.5(12)
Z	8
$\rho_{\text{calc}} (\text{g}/\text{cm}^3)$	0.602
μ/mm^{-1}	0.091
F(000)	2493.0
Crystal size/ mm^3	$0.072 \times 0.043 \times 0.042$
Radiation	Synchrotron ($\lambda = 0.7288 \text{\AA}$)
2Θ range for data collection/ $^\circ$	4.542 to 50.77
Index ranges	$-22 \leq h \leq 22, -22 \leq k \leq 22, -43 \leq l \leq 43$
Reflections collected	159563
Independent reflections	11342 [$R_{\text{int}} = 0.0604, R_{\text{sigma}} = 0.0218$]
Data/restraints/parameters	11342/0/385
Goodness-of-fit on F^2	1.065
Final R indexes [$I \geq 2\sigma(I)$]	$R_1 = 0.0476, wR_2 = 0.1358$
Final R indexes [all data]	$R_1 = 0.0513, wR_2 = 0.1396$
Largest diff. peak/hole / $e \text{\AA}^{-3}$	0.86/-0.32
Flack parameter	-0.01(2)

Refinement Details of Δ -MOF-520-10

A colorless crystal of Δ -MOF-520-10 was measured at beamline 12.2.1 at ALS with radiation of $\lambda = 0.7288 \text{ \AA}$. Based on intensity statistics for the whole dataset (PRP file), the resolution was cut off to 0.85 \AA ($R_{\text{merge}} \leq 40\%$ or average $I/\sigma > 2.5$ for the highest resolution shell). The carbon of unsubstituted formate (C28) and the phosphorous of **10** (P1G) overlap and are constrained by EXYZ and EADP. The occupancy of **10** (together with the unsubstituted formate) was found through adding a new variable and converged at 0.349(8). Structure was refined anisotropically and hydrogen atoms were placed into calculated positions. The distance between methyl carbon and its connected oxygen was fixed at 1.43 \AA . The methyl carbon atoms (C1G, C2G) were also restrained by DELU, RIGU to solve its rotational disorder. Reflections that are affected by the beamstop or having $(I_{\text{obs}} - I_{\text{calc}})/\sigma > 7$ were omitted. The weighting scheme was refined to convergence and the a, b parameters are 0.1374 and 3.9533, respectively. Solvent masking was not applied since the solvent in the structure was evacuated before measurement.

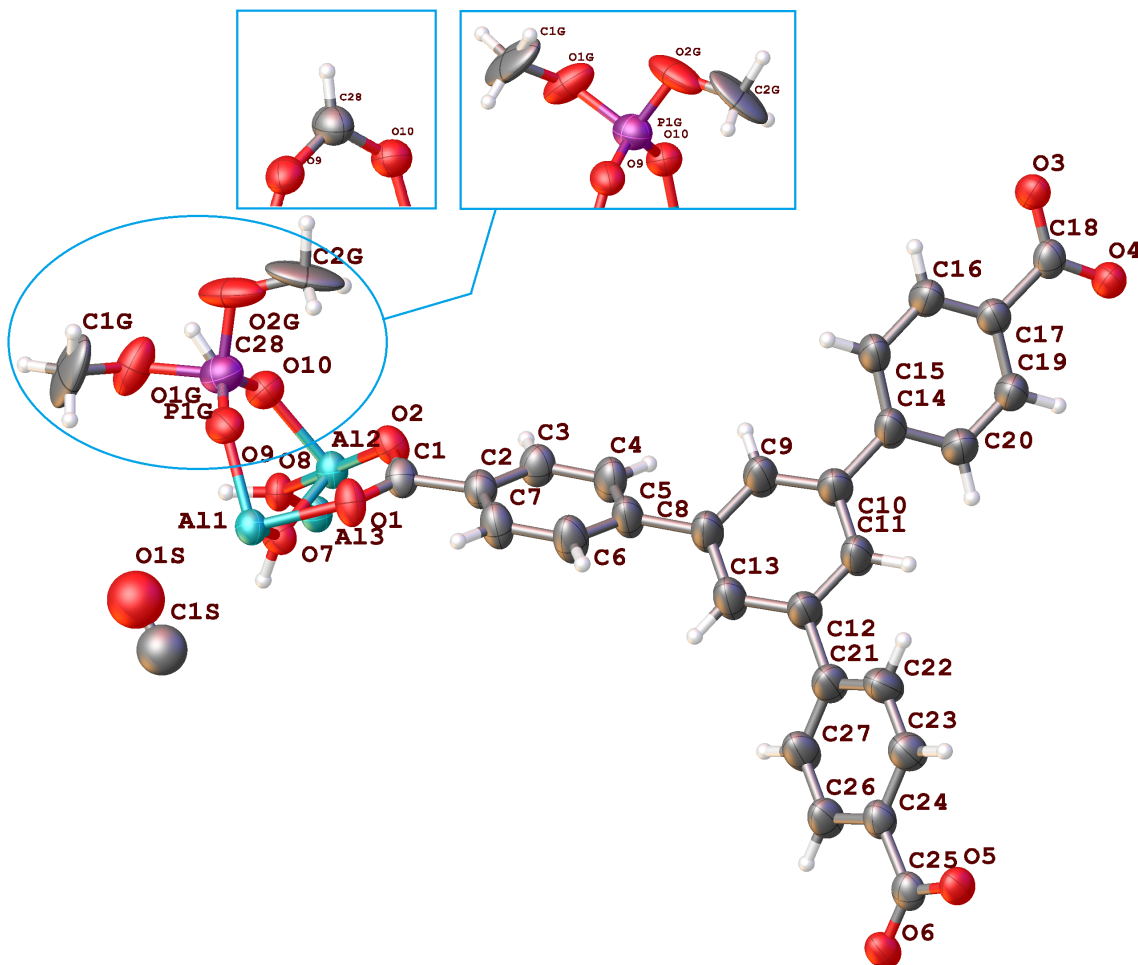


Figure 2.26. Asymmetric unit in the single crystal structure of Δ -MOF-520-10. Thermal ellipsoids are drawn with 50% probability. The positions of P1G and C28 overlap, but are illustrated in separate insets for clarity.

Table 2.21. Crystal data, data collection, and structure refinement parameters for Δ -MOF-520-10.

Name	Δ -MOF-520-10
Empirical formula	$C_{28.3}H_{19.22}Al_2O_{10.76}P_{0.35}$
Formula weight	596.18
Temperature/K	100(2)
Crystal system	tetragonal
Space group	$P4_22_12$
$a/\text{\AA}$	19.1935(11)
$b/\text{\AA}$	19.1935(11)
$c/\text{\AA}$	36.602(2)
$\alpha/^\circ$	90
$\beta/^\circ$	90
$\gamma/^\circ$	90
Volume/ \AA^3	13483.8(17)
Z	2
$\rho_{\text{calc}} (\text{g/cm}^3)$	0.587
μ/mm^{-1}	0.081
F(000)	2451.0
Crystal size/ mm^3	$0.067 \times 0.058 \times 0.047$
Radiation	Synchrotron ($\lambda = 0.7288 \text{ \AA}$)
2θ range for data collection/ $^\circ$	4.352 to 50.834
Index ranges	$-22 \leq h \leq 22, -22 \leq k \leq 22, -43 \leq l \leq 43$
Reflections collected	167679
Independent reflections	11497 [$R_{\text{int}} = 0.0529, R_{\text{sigma}} = 0.0235$]
Data/restraints/parameters	11497/15/402
Goodness-of-fit on F^2	1.076
Final R indexes [$I \geq 2\sigma(I)$]	$R_1 = 0.0668, wR_2 = 0.2000$
Final R indexes [all data]	$R_1 = 0.0731, wR_2 = 0.2053$
Largest diff. peak/hole / $e \text{ \AA}^{-3}$	0.57/-0.41
Flack parameter	0.01(2)

Refinement Details of Δ -MOF-520-11

A colorless crystal of Δ -MOF-520-11 was measured at beamline 12.2.1 at ALS with radiation of $\lambda = 0.7288 \text{ \AA}$. Based on intensity statistics for the whole dataset (PRP file), the resolution was cut off to 0.80 \AA ($R_{\text{merge}} \leq 40\%$ or average $I/\sigma > 2.5$ for the highest resolution shell). The formates were not fully substituted, so that the occupancies of formate and **11** were found via a free variable. Because the carbon atom of formate (C28) and the sulfur atom of **11** (S1G) were too close to be distinguished, they were constrained at same coordinate with EXYZ and EADP. Due to the disorder of **11** caused by the flash-cooling of solvent, SADI and FLAT were used to constrain the geometry of the benzene ring. SIMU was applied to the benzene ring to solve the bad anisotropic refinement caused by the interference of solvent electron density. After the refinement converged, the occupancy of **11** was constrained to 0.3594. All the non-hydrogen atoms were refined anisotropically and hydrogen atoms were placed in calculated positions. Solvent masking was applied: the void volume was estimated to be 8015.9 \AA^3 with 2141.0 electrons removed during masking. Reflections that are affected by the beamstop or having $(I_{\text{obs}} - I_{\text{calc}})/\sigma > 7$ were omitted. The weighting scheme was refined to convergence and the a, b parameters are 0.1194 and 0, respectively.

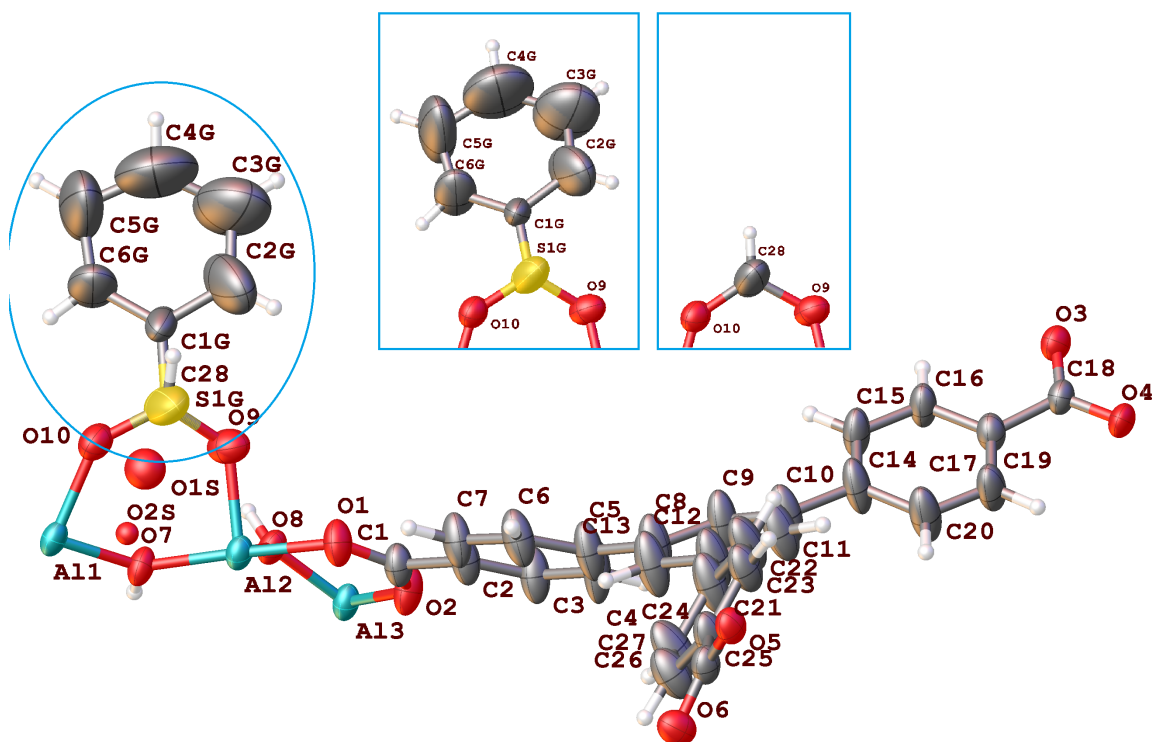


Figure 2.27. Asymmetric unit in the single crystal structure of Δ -MOF-520-11. Thermal ellipsoids are drawn with 50% probability. The positions of S1G and C28 overlap, so they are illustrated in separate insets for clarity.

Table 2.22. Crystal data, data collection, and structure refinement parameters for Δ -MOF-520-11.

	Before Solvent Masking	After Solvent Masking
Empirical formula	$C_{29.8}H_{17.44}Al_2O_{10.15}S_{0.36}$	$C_{29.8}H_{17.44}Al_2O_{10.15}S_{0.36}$
Formula weight	603.31	603.31
Temperature/K	100(2)	100(2)
Crystal system	tetragonal	tetragonal
Space group	$P4_22_12$	$P4_22_12$
$a/\text{\AA}$	18.4641(6)	18.4641(6)
$b/\text{\AA}$	18.4641(6)	18.4641(6)
$c/\text{\AA}$	37.4193(12)	37.4193(12)
$\alpha/^\circ$	90	90
$\beta/^\circ$	90	90
$\gamma/^\circ$	90	90
Volume/ \AA^3	12757.1(9)	12757.1(9)
Z	8	8
ρ_{calc} (g/cm^3)	0.628	0.628
μ/mm^{-1}	0.089	0.089
F(000)	2473.0	2473.0
Crystal size/ mm^3	$0.068 \times 0.064 \times 0.05$	$0.068 \times 0.064 \times 0.05$
Radiation	Synchrotron ($\lambda = 0.7288 \text{\AA}$)	Synchrotron ($\lambda = 0.7288 \text{\AA}$)
2Θ range for data collection/ $^\circ$	3.178 to 54.352	4.04 to 54.352
Index ranges	$-23 \leq h \leq 23,$ $-23 \leq k \leq 23,$ $-43 \leq l \leq 46$	$-23 \leq h \leq 23,$ $-23 \leq k \leq 23,$ $-43 \leq l \leq 46$
Reflections collected	205860	206016
Independent reflections	13110 [$R_{\text{int}} = 0.0608,$ $R_{\text{sigma}} = 0.0226$]	13117 [$R_{\text{int}} = 0.0608,$ $R_{\text{sigma}} = 0.0227$]
Data/restraints/parameters	13110/55/420	13117/55/420
Goodness-of-fit on F^2	1.453	1.060
Final R indexes [$I \geq 2\sigma(I)$]	$R_1 = 0.1121,$ $wR_2 = 0.2941$	$R_1 = 0.0491,$ $wR_2 = 0.1422$
Final R indexes [all data]	$R_1 = 0.1193,$ $wR_2 = 0.3075$	$R_1 = 0.0526,$ $wR_2 = 0.1466$
Largest diff. peak/hole / $e \text{\AA}^{-3}$	1.38/-0.73	0.52/-0.34
Flack parameter	0.03(2)	0.05(2)

Refinement Details of Δ -MOF-520-12

A colorless crystal of Δ -MOF-520-12 was measured at beamline 12.2.1 at ALS with radiation of $\lambda = 0.7288 \text{ \AA}$. Based on intensity statistics for the whole dataset (PRP file), the resolution was cut off to 0.85 \AA ($R_{\text{merge}} \leq 40\%$ or average $I/\sigma > 2.5$ for the highest resolution shell). The formate was not fully substituted and the occupancies of formate and **12** were refined with a free variable. DELU was applied to C3G, N2G, N1G, C1G to stabilize the anisotropic refinement given the close distances between N1G, N2G and O9, O10. Non-hydrogen atoms were refined anisotropically and hydrogen atoms were placed in calculated positions. After refinement converged, the occupancy of **12** was constrained to 0.3821. Reflections that are affected by the beamstop or having $(I_{\text{obs}} - I_{\text{calc}})/\sigma > 7$ were omitted. The weighting scheme was refined to convergence and the a, b parameters are 0.1191 and 1.6976, respectively. Solvent masking was not applied since the solvent in the structure was evacuated before measurement.

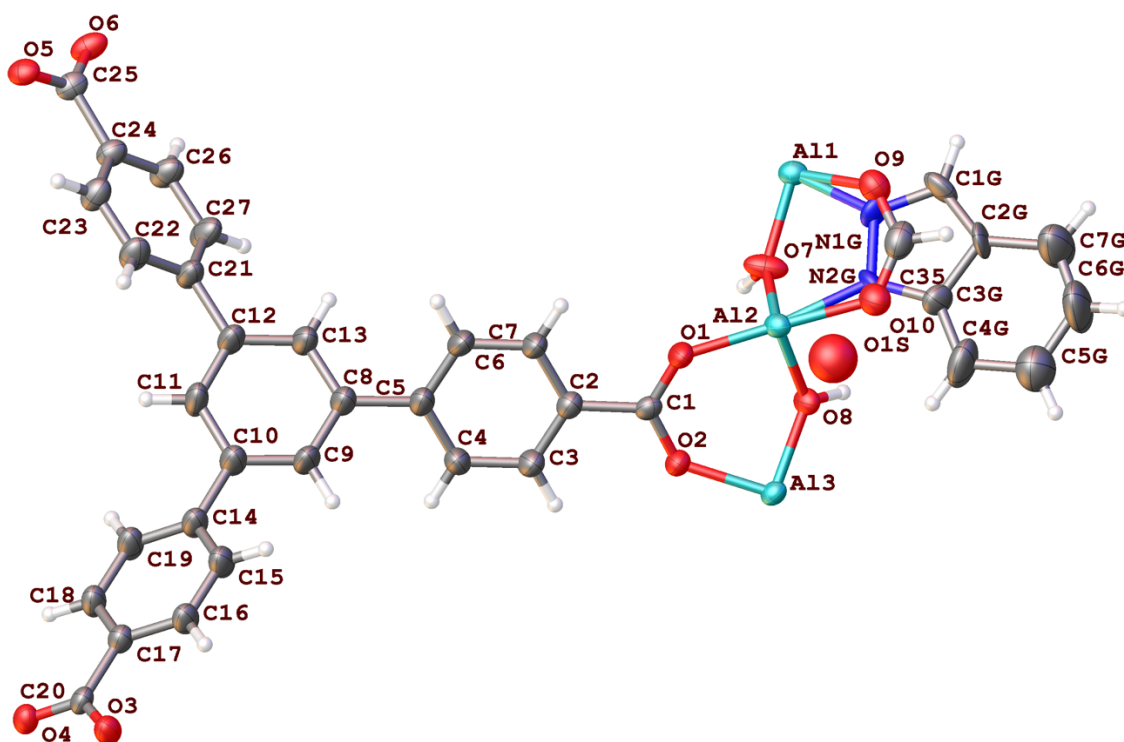


Figure 2.28. Asymmetric unit in the single crystal structure of Δ -MOF-520-12. Thermal ellipsoids are drawn with 50% probability.

Table 2.23. Crystal data, data collection, and structure refinement parameters for Δ -MOF-520-12.

Name	Δ -MOF-520-12
Empirical formula	$C_{30.29}H_{19.53}Al_2N_{0.76}O_{9.35}$
Formula weight	597.74
Temperature/K	100(2)
Crystal system	tetragonal
Space group	$P4_22_12$
$a/\text{\AA}$	19.3331(6)
$b/\text{\AA}$	19.3331(6)
$c/\text{\AA}$	36.2317(12)
$\alpha/^\circ$	90
$\beta/^\circ$	90
$\gamma/^\circ$	90
Volume/ \AA^3	13542.3(10)
Z	8
ρ_{calc} (g/cm^3)	0.586
μ/mm^{-1}	0.071
F(000)	2459.0
Crystal size/ mm^3	$0.071 \times 0.071 \times 0.048$
Radiation	Synchrotron ($\lambda = 0.7288 \text{\AA}$)
2Θ range for data collection/ $^\circ$	4.32 to 50.81
Index ranges	$-22 \leq h \leq 20, -22 \leq k \leq 22, -42 \leq l \leq 42$
Reflections collected	119524
Independent reflections	11559 [$R_{\text{int}} = 0.0732, R_{\text{sigma}} = 0.0371$]
Data/restraints/parameters	11559/5/444
Goodness-of-fit on F^2	1.053
Final R indexes [$I \geq 2\sigma(I)$]	$R_1 = 0.0556, wR_2 = 0.1596$
Final R indexes [all data]	$R_1 = 0.0682, wR_2 = 0.1704$
Largest diff. peak/hole / $e \text{\AA}^{-3}$	1.53/-0.26
Flack parameter	0.03(4)

Refinement Details of Λ -MOF-520-13

A colorless crystal of Λ -MOF-520-13 was measured at beamline 12.2.1 at ALS with radiation of $\lambda = 0.7288 \text{ \AA}$. Based on intensity statistics for the whole dataset (PRP file), the resolution was cut off to 0.90 \AA ($R_{\text{merge}} \leq 40\%$ or average $I/\sigma > 2.5$ for the highest resolution shell). The MOF framework was first assigned and refined anisotropically. Then the electron density peaks of the incorporated molecule were assigned and their occupancies were refined via adding new variables with SUMP (= 1.0000(1)) command. Two disordered positions were found: one points toward the center of the SBU, the other does not. Their occupancies converged and were constrained to 0.2920 and 0.2299, respectively. The molecule in the first disordered position overlaps with the symmetry-related one on the opposite side of the same SBU are overlapped, so that strong constraints and restraints (DFIX, SADI, SIMU, DELU) were applied to separate the overlapped positions. For the other disordered position, SADI and SIMU was applied to constrain the vibrational disorder. Now the whole structure was refined anisotropically and hydrogen atoms were placed in calculated positions. Hydrogens were not added to C4GB and C5GB due to an unresolved problem in the connectivity table. Solvent masking was applied: The void volume was estimated to be 7634.7 \AA^3 with 2946.8 electrons were removed during masking. Reflections that are affected by the beamstop or having $(I_{\text{obs}} - I_{\text{calc}})/\sigma > 7$ were omitted. The weighting scheme was refined to convergence and the a, b parameters are 0.1123 and 0, respectively.

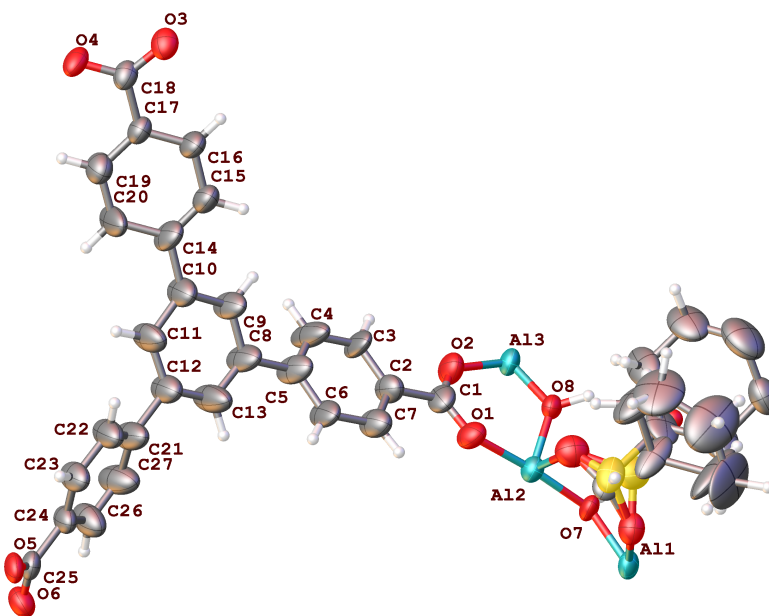


Figure 2.29. Asymmetric unit in the single crystal structure of Λ -MOF-520-13. Thermal ellipsoids are drawn with 50% probability.

Table 2.24. Crystal data, data collection, and structure refinement parameters for Λ -MOF-520-13.

	Before Solvent Masking	After Solvent Masking
Empirical formula	$C_{30.61}H_{21.53}Al_2O_{10.25}S_{0.52}$	$C_{30.61}H_{21.53}Al_2O_{10.25}S_{0.52}$
Formula weight	623.98	623.98
Temperature/K	100(2)	100(2)
Crystal system	tetragonal	tetragonal
Space group	$P4_22_12$	$P4_22_12$
$a/\text{\AA}$	18.6986(11)	18.6986(11)
$b/\text{\AA}$	18.6986(11)	18.6986(11)
$c/\text{\AA}$	37.201(3)	37.201(3)
$\alpha/^\circ$	90	90
$\beta/^\circ$	90	90
$\gamma/^\circ$	90	90
Volume/ \AA^3	13006.8(18)	13006.8(18)
Z	8	8
ρ_{calc} (g/cm^3)	0.624	0.637
μ/mm^{-1}	0.088	0.093
F(000)	2521.0	2572.0
Crystal size/ mm^3	$0.095 \times 0.069 \times 0.043$	$0.095 \times 0.069 \times 0.043$
Radiation	Synchrotron ($\lambda = 0.7288 \text{\AA}$)	Synchrotron ($\lambda = 0.7288 \text{\AA}$)
2Θ range for data collection/ $^\circ$	2.5 to 47.772	4.042 to 47.772
Index ranges	$-20 \leq h \leq 20,$ $-20 \leq k \leq 20,$ $-41 \leq l \leq 41$	$-20 \leq h \leq 20,$ $-20 \leq k \leq 20,$ $-41 \leq l \leq 41$
Reflections collected	132853	132943
Independent reflections	9342 [$R_{\text{int}} = 0.0998,$ $R_{\text{sigma}} = 0.0510$]	9350 [$R_{\text{int}} = 0.0993,$ $R_{\text{sigma}} = 0.0512$]
Data/restraints/parameters	9342/159/489	9350/159/489
Goodness-of-fit on F^2	1.296	1.036
Final R indexes [$I \geq 2\sigma(I)$]	$R_1 = 0.1114,$ $wR_2 = 0.2805$	$R_1 = 0.0541,$ $wR_2 = 0.1465$
Final R indexes [all data]	$R_1 = 0.1304,$ $wR_2 = 0.3013$	$R_1 = 0.0646,$ $wR_2 = 0.1560$
Largest diff. peak/hole / $e \text{\AA}^{-3}$	0.95/-0.69	0.35/-0.37
Flack parameter	0.13(6)	0.14(6)

2.5.4. Structure Models for Hirshfeld Analyses

Table S31. Atom coordinates of *inverse-Λ-MOF-520-2* structural model.

<i>inverse-Λ-MOF-520-2</i>				
Tetragonal, $P4_22_12$				
$a = b = 18.9155 \text{ \AA}, c = 36.6951 \text{ \AA}$				
Atom	x	y	z	Occupancy
Al1	0.3983	0.37598	0.41971	1
O2	0.47585	0.43356	0.4226	1
H3	0.5056	0.4288	0.4435	1
O4	0.36602	0.40197	0.46581	1
H5	0.3645	0.4505	0.472	1
O6	0.47532	0.43912	0.34944	1
O7	0.76382	0.19208	0.03131	1
O8	0.8192	0.18511	0.08596	1
O9	0.42755	0.33778	0.37414	1
N10	0.40756	0.27073	0.47791	1
C11	0.21213	0.047	0.12614	1
C12	0.69881	0.2033	0.08711	1
C13	0.7639	0.1939	0.06678	1
C14	0.4522	0.33807	0.31242	1
C15	0.3286	0.1323	0.14779	1
C16	0.15044	0.0067	0.11431	1
C17	0.5092	0.2093	0.14928	1
C18	0.44516	0.2752	0.2422	1
C19	0.27816	0.0205	0.11999	1
H20	0.2846	-0.0247	0.1093	1
C21	0.5714	0.2091	0.12836	1
C22	0.63328	0.20762	0.06822	1
H23	0.6315	0.2072	0.0421	1
C24	0.45148	0.3727	0.34823	1
C25	0.7012	0.20436	0.12653	1
H26	0.7451	0.2054	0.1391	1
C27	0.47974	0.3734	0.28177	1
H28	0.4987	0.4194	0.2842	1
C29	0.41657	0.27649	0.30723	1
H30	0.3939	0.2547	0.3276	1
C31	0.57108	0.21259	0.08932	1
H32	0.5274	0.2185	0.077	1
C33	0.50599	0.2433	0.18188	1
H34	0.5457	0.2696	0.1897	1
C35	0.3362	0.0624	0.13011	1
H36	0.3823	0.0451	0.1254	1

C37	0.63865	0.2039	0.14604	1
H38	0.6403	0.2	0.1721	1
C39	0.19884	0.1163	0.14301	1
H40	0.1524	0.1332	0.147	1
C41	0.3901	0.1739	0.16022	1
C42	0.2588	0.1566	0.15309	1
H43	0.2519	0.2017	0.1638	1
C44	0.4787	0.3387	0.24677	1
H45	0.5016	0.36	0.2264	1
C46	0.4127	0.2444	0.27207	1
H47	0.3876	0.2015	0.2691	1
C48	0.45125	0.175	0.13776	1
H49	0.4512	0.1517	0.1147	1
C50	0.4461	0.2412	0.2047	1
C51	0.38685	0.20254	0.19294	1
H52	0.3464	0.1975	0.2081	1
O53	0.15845	-0.05607	0.10419	1
O54	0.08941	0.03704	0.11551	1
N55	0.44224	0.29175	0.44578	1
N56	0.43641	0.21006	0.48983	1
C57	0.48641	0.23943	0.43851	1
H58	0.51607	0.23731	0.4175	1
C59	0.48349	0.1903	0.46469	1
H60	0.51049	0.14823	0.46531	1
Al61	0.33671	0.33671	0.5	1
Al62	0.5	0.5	0.38771	1

2.6. Bibliography

- (1) Lee, S.; Kapustin, E. A.; Yaghi, O. M. Coordinative Alignment of Molecules in Chiral Metal-Organic Frameworks. *Science* **2016**, *353*, 808–811.
- (2) Yaghi, O. M.; Kalmutzki, M. J.; Diercks, C. S. *Introduction to Reticular Chemistry: Metal-Organic Frameworks and Covalent Organic Frameworks*; Wiley-VCH: Weinheim, 2019.
- (3) *Crystallography of Supramolecular Compounds*; Tsoucaris, G., Atwood, J. L., Lipkowski, J.; Kluwer Academic Publishers: Dordrecht, the Netherlands, 1996.
- (4) Inokuma, Y.; Yoshioka, S.; Ariyoshi, J.; Arai, T.; Hitora, Y.; Takada, K.; Matsunaga, S.; Rissanen, K.; Fujita, M. X-ray analysis on the Nanogram to Microgram Scale Using Porous Complexes. *Nature* **2013**, *495*, 461–466.
- (5) Yan, K.; Dubey, R.; Arai, T.; Inokuma, Y.; Fujita, M. Chiral Crystalline Sponges for the Absolute Structure Determination of Chiral Guests. *J. Am. Chem. Soc.* **2017**, *139*, 11341–11344.
- (6) Bruker. *APEX3, Version 8.38*; Bruker AXS Inc.: Madison, WI, USA, 2018.
- (7) Bruker. *SADABS, Version 2014/4*; Bruker AXS Inc.: Madison, WI, USA, 2014.
- (8) Sheldrick, G. M. A Short History of *SHELX*. *Acta Cryst. A.* **2008**, *64*, 112–122.
- (9) Sheldrick, G. M. Crystal Structure Refinement with *SHELXL*. *Acta Cryst. C.* **2015**, *71*, 3–8.
- (10) Dolomanov, O. V.; Bourhis, L. J.; Gildea, R. J.; Howard, J. A. K.; Puschmann, H.; OLEX2: A Complete Structure Solution, Refinement and Analysis Program. *J. Appl. Crystallogr.* **2009**, *42*, 339–341.
- (11) Jiang, J.-S.; Brünger, A.; Protein Hydration Observed by X-ray Diffraction Solvation Properties of Penicillopepsin and Neuraminidase Crystal Structures. *J. Mol. Biol.* **1994**, *243*, 100–115.
- (12) Rees, B.; Jenner, L.; Yusupov, M.; Bulk-solvent Correction in Large Macromolecular Structures. *Acta Crystallogr., Sect. D: Biol. Crystallogr.* **2005**, *61*, 1299–1301.
- (13) Frisch, M. J.; Trucks, G. W.; Schlegel, H. B.; Scuseria, G. E.; Robb, M. A.; Cheeseman, J. R.; Scalmani, G.; Barone, V.; Petersson, G. A.; Nakatsuji, H.; Li, X.; Caricato, M.; Marenich, A. V.; Bloino, J.; Janesko, B. G.; Gomperts, R.; Mennucci, B.; Hratchian, H. P.; Ortiz, J. V.; Izmaylov, A. F.; Sonnenberg, J. L.; Williams-Young, D.; Ding, F.; Lipparini, F.; Egidi, F.; Goings, J.; Peng, B.; Petrone, A.; Henderson, T.; Ranasinghe, D.; Zakrzewski, V. G.; Gao, J.; Rega, N.; Zheng, G.; Liang, W.; Hada, M.; Ehara, M.; Toyota, K.; Fukuda, R.; Hasegawa, J.; Ishida, M.; Nakajima, T.; Honda, Y.; Kitao, O.; Nakai, H.; Vreven, T.; Throssell, K.; Montgomery, J. A., Jr.; Peralta, J. E.; Ogliaro, F.; Bearpark, M. J.; Heyd, J. J.; Brothers, E. N.; Kudin, K. N.; Staroverov, V. N.; Keith, T. A.; Kobayashi, R.; Normand, J.; Raghavachari, K.; Rendell, A. P.; Burant, J. C.; Iyengar, S. S.; Tomasi, J.; Cossi, M.; Millam, J. M.; Klene, M.; Adamo, C.; Cammi, R.; Ochterski, J. W.; Martin, R. L.; Morokuma, K.; Farkas, O.; Foresman, J. B.; Fox, D. J. *Gaussian 16*, Revision A.03; Gaussian, Inc., Wallingford CT, 2016.
- (14) Adamo, C.; Barone, V. Toward Reliable Density Functional Methods without Adjustable Parameters: The PBE0 Model. *J. Chem. Phys.* **1999**, *110*, 6158–6170.
- (15) Grimme, S.; Ehrlich, S.; Goerigk, L. Effect of the Damping Function in Dispersion Corrected Density Functional Theory. *J. Comp. Chem.* **2011**, *32*, 1456–1465.

- (16) Weigend, F.; Ahlrichs, R. Balanced Basis Sets of Split Valence, Triple Zeta Valence and Quadruple Zeta Valence Quality for H to Rn: Design and Assessment of Accuracy. *Phys. Chem. Chem. Phys.* **2005**, *7*, 3297–3305.
- (17) Weigend, F. Accurate Coulomb-fitting Basis Sets for H to Rn. *Phys. Chem. Chem. Phys.* **2006**, *8*, 1057–1065.
- (18) Tomasi, J.; Mennucci B.; Cammi, R.; Quantum mechanical continuum solvation models. *Chem. Rev.* **2005**, *105*, 2999–3093.
- (19) Turner, M. J.; McKinnon, J. J.; Wolff, S. K.; Grimwood, D. J.; Spackman, P. R.; Jayatilaka, D.; Spackman, M. A. *CrystalExplorer17*; University of Western Australia, 2017.
- (20) Gándara, F.; Furukawa, H.; Lee, S.; Yaghi, O. M. High Methane Storage Capacity in Aluminum Metal–Organic Frameworks. *J. Am. Chem. Soc.* **2014**, *136*, 5271–5274.
- (21) Parent, R. P.; Nakazono, T.; Lin, S.; Utsunomiya, S.; Sakai, K. Mechanism of Water Oxidation by Non-heme Iron Catalysts When Driven with Sodium Periodate. *Dalton Trans.* **2014**, *43*, 12501–12513.
- (22) Grimvall, S. The Crystal Structure of NaHSO₄H₂O. *Acta Chem. Scand. (1947-1973)* **1971**, *25*, 3213–3219.
- (23) Pauling, L.; *The Nature of the Chemical Bond*, 3rd ed.; Cornell University Press: Ithaca, 1960; pp 320–321.
- (24) Anderson, K. M.; Goeta, A. E.; Martin, J. E.; Mason, S. A.; McIntyre, G. J.; Sansam, B. C. R.; Wilkinson, C.; Steed, J. W. *Cryst. Growth Des.* **2011**, *11*, 4904–4919.
- (25) Vilminot, S.; Philippot, E.; Lehmann, M. Affinement de la structure de NH₄NH₃CH₂COOHSO₄ par diffraction neutronique. *Acta Cryst.* **1976**, *B32*, 1817–1822.
- (26) Broach, R. W.; Williams, J. M.; Felcher, G. P.; Hinks, D. G. A neutron diffraction study of yttrium tris(ethyl sulfate) nonahydrate, Y(C₂H₅SO₄)₃·9H₂O. *Acta Cryst.* **1979**, *B35*, 2317–2321.
- (27) Turner, D. R.; Henry, M.; Wilkinson, C.; McIntyre, G. J.; Mason, S. A.; Goeta, A. E.; Steed, J. W. Cooperative Hydrogen-Bonding Effects in a Water Square: A Single-Crystal Neutron and Partial Atomic Charges and Hardness Analysis Study. *J. Am. Chem. Soc.* **2005**, *127*, 11063–11074.
- (28) Figgis, B. N.; Mason, R.; Smith, A. R. P.; Verghese, J. N.; Williams, G.A. Spin density and structure of aquabis(2,2'-bipyridine)di-μ-hydroxosulphatodicopper(II) tetrahydrate at 4.2 K. *J. Chem. Soc., Dalton Trans.* **1983**, *4*, 703–711.
- (29) Hubbard, C. R.; Quicksall, C. O.; Jacobson, R. A. A neutron-diffraction study of holmium ethylsulfate enneahydrate by the white-radiation method. *Acta Cryst.* **1974**, *B30*, 2613–2619.
- (30) jFortes, A. D.; Howard, C. M.; Wood, I. G.; Gutmann, M. J. Glycine zinc sulfate pentahydrate: redetermination at 10 K from time-of-flight neutron Laue diffraction. *Acta Cryst.* **2016**, *E72*, 1438–1445.
- (31) Kazimirov, V. Yu.; Sarin, V. A.; Ritter, C.; Shuvalov, L. A. Neutron diffraction study of the atomic structure of the ferroelectric phase of (CH₃)₂NH₂Al(SO₄)₂·6(H₂O) ferroelectric-ferroelastic (DMAAS). *Kristallografiya* **1999**, *44*, 61–66.
- (32) Kay, M. I.; Kleinberg, R. The crystal structure of triglycine sulfate. *Ferroelectrics*, **1973**, *5*, 45–52.

- (33) Andreotti, G. D.; Cavalca, L.; Musatti, A. The crystal and molecular structure of tris(thiourea)zinc(II) sulphate. *Acta Cryst.* **1968**, *B24*, 683–690.
- (34) Janesko, B. G.; Fisher, H. C.; Bridle, M. J.; Montchamp, J.-L. P(=O)H to P–OH Tautomerism: A Theoretical and Experimental Study. *J. Org. Chem.* **2015**, *80*, 10025–10032.
- (35) Pietro, W. J.; Hehre, W. J. Tautomerization of Dimethyl Phosphonate. *J. Am. Chem. Soc.* **1982**, *104*, 3594–3595.
- (36) Spackman, M. A.; Jayatilaka, D. Hirshfeld Surface Analysis. *CrystEngComm* **2008**, *11*, 19–32.
- (37) *BIOVIA Materials Studio 2017*; Dassault Systèmes, Waltham, MA, 2016.
- (38) McKinnon, J. J.; Spackman, M. A.; Mitchell, A. S. Novel tools for visualizing and exploring intermolecular interactions in molecular crystals. *Acta Crystallogr., Sect. B: Struct. Sci.* **2004**, *60*, 627–668.

Chapter 3.

Reducing the Disorder of Incorporated Large Biomolecules in MOF-520

The research in this chapter was published as a part of:

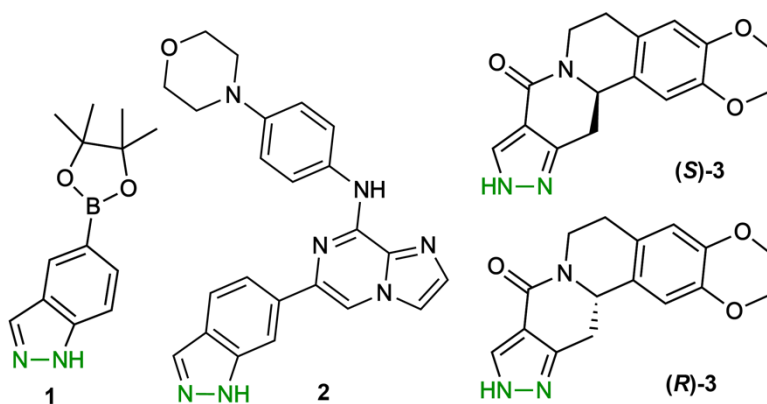
Pei, X.; Bürgi, H.-B.; Kapustin, E. A.; Liu, Y.; Yaghi, O. M. Coordinative Alignment in the Pores of MOFs for the Structural Determination of N-, S-, and P-Containing Organic Compounds Including Complex Chiral Molecules. *J. Am. Chem. Soc.* **2019**, *141* (47), 18862–18869. <https://doi.org/10.1021/jacs.9b10501>.

3.1. Introduction

The golden rule for testing a host-assisted guest structure determination is being able to resolve structures for actual large and complex molecules. This is usually challenged by limited inner volume of host, shape of the interior space of host, and symmetry of the host.¹⁻³ The higher the symmetry, the more energy-equivalent incorporation configurations are, the more likely positional disorders occur. The interior space defines the geometrically similar molecules that can be incorporated. For example, MOF-808 is a popular candidate for guest binding because of its 6-coordinated Zr SBU and large pore size of 18.4 Å.⁴ However, the owned space for each incorporation site in MOF-808 is a cone (triangle) from one sixth of a hexagon with the incorporation site lying on one of the edges: if molecules larger than half of the pore size are incorporated, six molecules will coincide at the center of the hexagon which creates difficult disorder. In addition, there is a mirror plane across the incorporation site, which means that the any guest molecule will incorporate as two mirrored orientations. All of which demonstrates the stringent requirement for a good host candidate.

Luckily, MOF-520 used in the coordinative alignment method has the required features. The incorporation site in MOF-520 has a site symmetry of 1 (identity). The space around the incorporation site is a non-isosceles triangle with the site locating at one of the vertices. Having an open angle of space for guest incorporation lower the chance for molecules coincide closer to the center of pores. In addition, the asymmetric opening angle creates steric selectivity and promoting the molecules to reside in a specific configuration. Given the incorporation conditions of molecules with eight functionalities explored in Chapter 2, it is practical to apply the developed conditions to the incorporation of larger molecules and examine the quality of structure output. Therefore, four molecules with molecular weight ranging from 250 to 500 g·mol⁻¹ were chosen (**Scheme 3.1**): 1*H*-indazole-5-boronic acid pinacol ester **1**, Entospletinib **2**, and 2,3-dimethoxy-5,11,12,12a-tetrahydropyrazolo[3',4':4,5]pyrido[2,1-a]-isoquinolin-8(6*H*)-one [(*S*)-**3** and (*R*)-**3**]. Among them, **2** is an inhibitor of spleen tyrosine kinase, and is an experimental drug for various type of cancers.⁵ These molecules have never had their single-crystal structures determined before.

Scheme 3.1. Target Molecules of Incorporation.



3.2. Experimental

3.2.1. Materials

Al(NO₃)₃·9H₂O, *N,N*-dimethylformamide (DMF) (98%, HPLC) were purchased from Sigma-Aldrich. 1,3,5-benzenetricarboxylic acid (H₃BTB) was purchased from TCI America. Formic acid

(99.8 %) was obtained from EMD Millipore. Molecule **1** were purchased from Sigma-Aldrich. Molecule **2**, **3** were purchased from Key Organics Inc. *N,N*-dimethylformamide (DMF) (98%, HPLC) was purchased from Sigma-Aldrich and was purified in an Inert[®] solvent purification system PureSolv MD7 before use. All other chemicals were used without further purification. Scintillation vials (20 mL) and polypropylene cabs with foil liner were purchased from VWR International, LLC. LC/GC vials (1.5 mL) was purchased from Fischer Scientific.

3.2.2. Syntheses

Synthesis of MOF-520 single crystals.

90 mg $\text{Al}(\text{NO}_3)_3 \cdot 9\text{H}_2\text{O}$ was dissolved in 2 mL anhydrous DMF and 75 mg H_3BTB was dissolved in 2 mL anhydrous DMF. Two solution was mixed and additional 13 mL anhydrous DMF was added, followed by 1.75 mL formic acid and 40 μL deionized water. The mixture was sealed in a 20 mL scintillation vial then heated at 140 °C for 3 to 5 days. Colorless block crystals were obtained and washed with DMF (9×20 mL).

Incorporation of the guest molecules.

MOF-520-1: 1 mg of MOF-520 were immersed in 1 mL of 0.5 mol L⁻¹ DMF solution of **1** and the reaction mixture was heated at 85 °C for 3 days. The crystals were washed with DMF for 3 times then soaked in DMF before further treatment/measurement.

MOF-520-2: 3 mg of **2** was dissolved in 50 μL of DMF. 1 mg of MOF-520 were immersed in the solution and the reaction mixture was heated at 100 °C for 3 days. The crystals were washed with DMF for 3 times then soaked in DMF before further treatment/measurement.

MOF-520-(*S/R*)-3: 5 mg of the racemic mixture of (*S*)-**3** and (*R*)-**3** was dissolved in 50 μL of DMF. 1 mg of MOF-520 were immersed in the solution and the reaction mixture was heated at 100 °C for 3 days. The crystals were washed with DMF for 3 times then soaked in DMF before further treatment/measurement.

Activation of MOF-520-1 and MOF-520-2.

As-synthesized incorporated MOFs were washed with DMF for 10 times in 2 days followed by CH_2Cl_2 for 10 times in 2 days. After removing most of the CH_2Cl_2 liquid, the crystals were dried under a vacuum of ~ 10 Torr for 1 hour then activated under a dynamic vacuum of 20 mTorr for 8 hours. The activated samples were carefully protected from moisture before SXR measurement.

3.2.3. Single-Crystal X-ray Diffraction

Because the chirality of a single crystal could not be distinguished by inspection of the shape of the crystal or by polarized light, the choice of the chirality of the inclusion crystal from the batch was random. Three single crystals from each batch of incorporated samples were analyzed by SXR. The dataset with best R_{int} and resolution was chosen and is reported here. Single crystal datasets were collected at beamlines 12.2.1 at the Advanced Light Source with beam monochromated by Si(111). The crystals were mounted in a 100(2) K nitrogen cold stream. The data up to $\sin(\theta)/\lambda = 2/3$ were collected with combined phi and omega scans to ensure a data multiplicity of at least 8. The raw data were processed with the Bruker APEX3 V8.38 software package.⁶ The data were first integrated using SAINT⁷ and then corrected for absorption with SADABS.⁸ The structures were solved by direct methods (*SHELXS*) and the refinements done by full-matrix least squares on F^2 (*SHELXL*),^{9,10} using the Olex² software package.¹¹ Solvent masking was applied to non-activated structures.¹² The parameters indicating data qualities are summarized in **Table 3.1**.

Table 3.1. Summary of parameters from the reported crystallographic data.

Name	Δ -MOF-520-1-solvent	Δ -MOF-520-1-activated	Δ -MOF-520-2-solvent	Δ -MOF-520-2-activated	Δ -MOF-520-S-3	Δ -MOF-520-R-3	
$a / \text{\AA}$	19.0466(6)	19.2915(5)	18.6944(6)	19.079(3)	19.4248(7)	19.3750(9)	
$c / \text{\AA}$	36.3890(12)	36.0810(11)	37.0688(12)	36.683(5)	35.7345(13)	35.8159(16)	
Occupancy of guest	0.5988	0.50749	0.3612	0.262	0.6	0.5808	
Resolution / \AA	0.91	0.91	0.76	0.74	0.85	0.85	
Solvent evacuation	No	Yes	No	Yes	Yes	Yes	
R_{int}	3.67%	9.42%	6.87%	5.62%	7.33%	8.42%	
R (all data)	14.65%	6.72%	9.95%	5.88%	7.96%	8.93%	
Flack parameter	0.230(11)	-0.06(5)	0.05(3)	0.126(18)	0.04(3)	0.13(2)	
s.u. of C–C bond length / \AA	0.0152	0.0061	0.0088	0.0044	0.0085	0.0097	
Weighting parameters*	a	0.2	0.1026	0.2	0.1135	0.1482	0.1533
	b	0	2.6675	0	0.1333	3.7013	5.5734

*Weighting scheme is given by the follow equation: $w = 1/[\sigma^2 F_o^2 + (aP)^2 + bP]$, where $P = (F_o^2 + 2F_c^2)/3$.

Observed structure factor (F_{obs}) electron density maps were visualized as follows: the finalized structure was first imported into GSAS-II,¹³ then least-square refined against F^2 while fixing atom coordinates, ADPs, occupancies, and unit cell dimensions. The Fourier map of F_{obs} was calculated with a resolution of 0.25 \AA . The map was then exported and visualized in VESTA 3.¹⁴

Table 3.2. Calculation of theoretical electron densities of common solvents.

Solvents	Density (g cm^{-3})	MW (g mol^{-1})	Formula	# of e^-	Theoretical electron density ($e \text{\AA}^{-3}$) *
DMF	0.9445	73.09	$\text{C}_3\text{H}_7\text{NO}$	40	0.3113
acetone	0.7845	58.079	$\text{C}_3\text{H}_6\text{O}$	32	0.2603
dichloromethane	1.325	84.93	CH_2Cl_2	42	0.3946
DMSO	1.092	78.13	$\text{C}_2\text{H}_6\text{OS}$	42	0.3535
diethyl ether	0.713	74.123	$\text{C}_4\text{H}_{10}\text{O}$	42	0.243
THF	0.8833	72.107	$\text{C}_4\text{H}_8\text{O}$	40	0.2951

* Calculated by the following equation (DMF as an example):

$$e^- \text{ density} = \frac{\rho_{\text{DMF}} \times (\# \text{ of } e^-) \times N_A}{MW} = \frac{0.9445 \text{ g} \cdot (10^8 \text{ \AA})^{-3} \times 40 e \times (6.022140857 \times 10^{23}) \text{ mol}^{-1}}{73.09 \text{ g} \cdot \text{mol}^{-1}} = 0.3113 e \text{ \AA}^{-3}$$

3.3. Results and Discussions

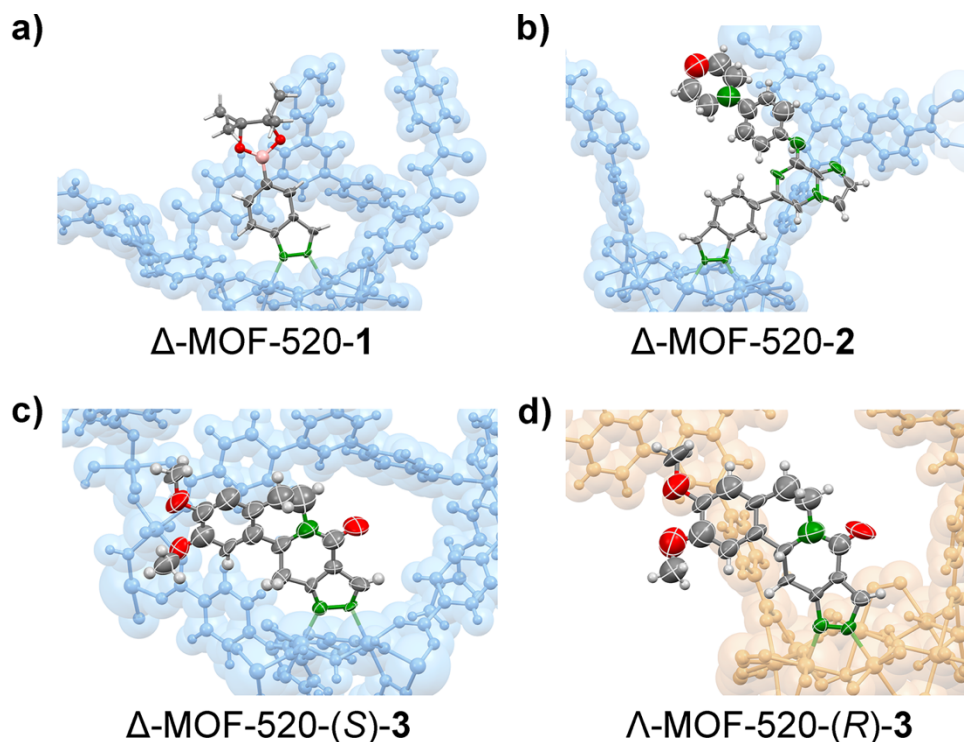


Figure 3.1. Refined structures of **1** to **3** crystallized in Δ - or Λ -MOF-520. The refined structures of the molecules obtained from SXR data are illustrated with 50% probability thermal ellipsoids. In the case of positional disorder, only one conformation of the bound molecules is shown for clarity (c, h, n). Color code: blue, Al; orange, O; green, N; dark gray, C; pink, B; gray, H. The MOF backbone in the figures was drawn as blue (for Δ -MOF-520) or orange (for Λ -MOF-520) space-filling model.

3.3.1. Enantiomeric Discrimination of a Racemic Mixture by Incorporation into MOF-520

Enantiomeric separation was demonstrated for a racemic mixture of (*S*)-**3** and (*R*)-**3**. A racemic batch of MOF-520 crystals was immersed into a 0.2 mol L⁻¹ DMF solution and kept at 85 °C for 3 days, then washed with fresh solvents and activated. Single crystal structures of molecule-incorporated Δ - and Λ -MOF-520 crystals were subsequently determined. In both MOF structures, two disordered, homochiral molecules were modeled (~25% occupancy for each); from which it is concluded that (*S*)-**3** coordinates to Δ -MOF-520 only, while (*R*)-**3** coordinates exclusively to Λ -MOF-520 (**Figure 3.1c, d**). The reliability of the assigned absolute configuration of the molecule structures was confirmed by analyzing the chiral volume of the chiral carbon (C32, **Figure 3.2a**). As a point of reference, the chiral volume of the chiral center in amino acids is $\pm 2.492 \text{ \AA}^3$.¹⁵ The chiral volumes of C32 of the two positions in each framework were measured to be $-2.20 (0.19)$ and $-1.94 (0.20) \text{ \AA}^3$ in Δ -MOF-520-(*S*)-**3**, $+2.07 (0.18)$ and $+1.71 (0.24) \text{ \AA}^3$ in Λ -MOF-520-(*R*)-**3**, three of which are within 3σ of the ideal value. Additionally, enantiopurity of the incorporated molecules in each framework was corroborated by analyzing their conformations. The different chiralities of C32 induce mirrored conformations of the two six-membered rings (B and C, **Figure 3.2b**), resulting in dihedral angles between the benzene ring D and pyrazole ring A of opposite sign (**Figure 3.2b**). In both structures no residual electron density attributable to the other enantiomer was observed, further substantiating that MOF-520 can be highly selective towards

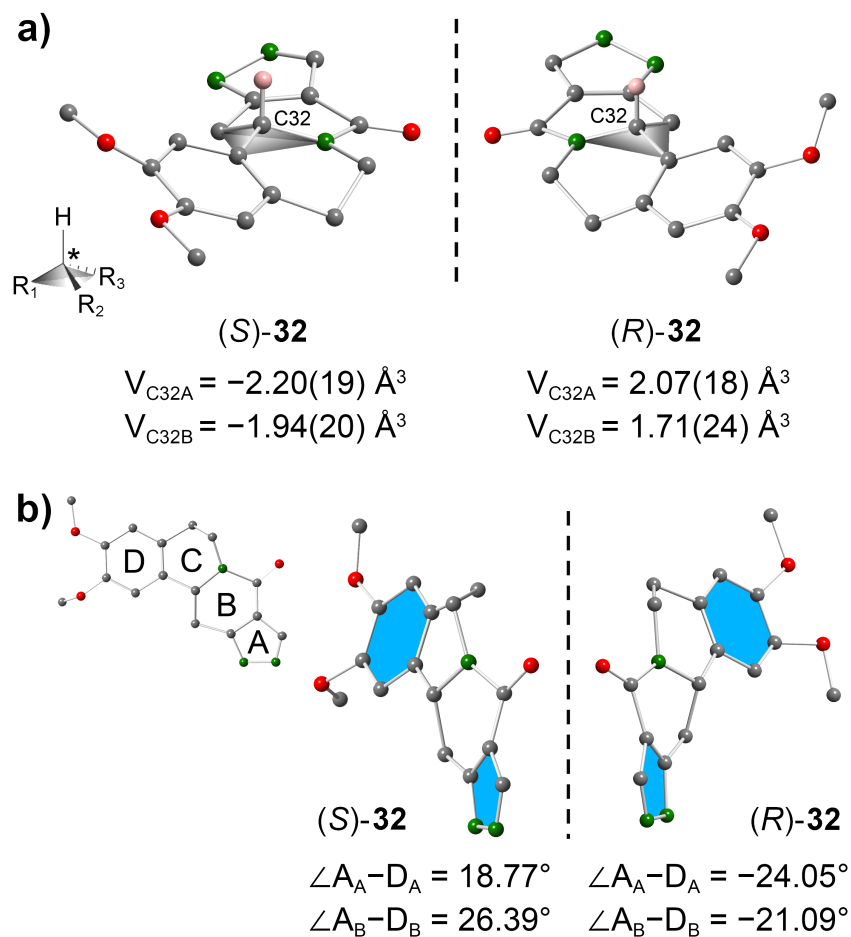


Figure 3.2. (a) Illustration of the chiral volume determined for the structures (*S*)-**3** and (*R*)-**3**. (b) The measured dihedral angle between the planes A and D (filled in blue) in (*S*)-**3** and (*R*)-**3**. Color code for atoms: O, red; N, green; C, gray; and H, pink. Subscript A, B in the angle notations refers to A and B position of **3** in the SXR D structures.

one enantiomer of racemic mixtures.

3.3.2. Incorporated MOF-520 Crystals with and without Solvent

Incorporated MOF-520 crystals with low target molecule occupancy were evacuated prior to SXR D measurements because additional solvent molecules in the pore will (1) tend to form disordered structures due to flash cooling and thus contributing to positional disorder of the target molecules,¹⁶ and (2) increase background electron densities, implying the risk of ambiguous atom assignment of target molecules. The solvent removal becomes possible because of the high architectural stability of MOF-520, which enables full retention of its crystallinity throughout incorporation, activation procedure and the SXR D measurement. Here we compare F_{obs} (observed structure factor) electron density maps before and after activation of MOF-520-**1** and MOF-520-**2**, respectively, and the results illustrate that solvent removal is advantageous for the determination of unknown crystal structures of molecules **1** and **2** (**Figure 3.3**).

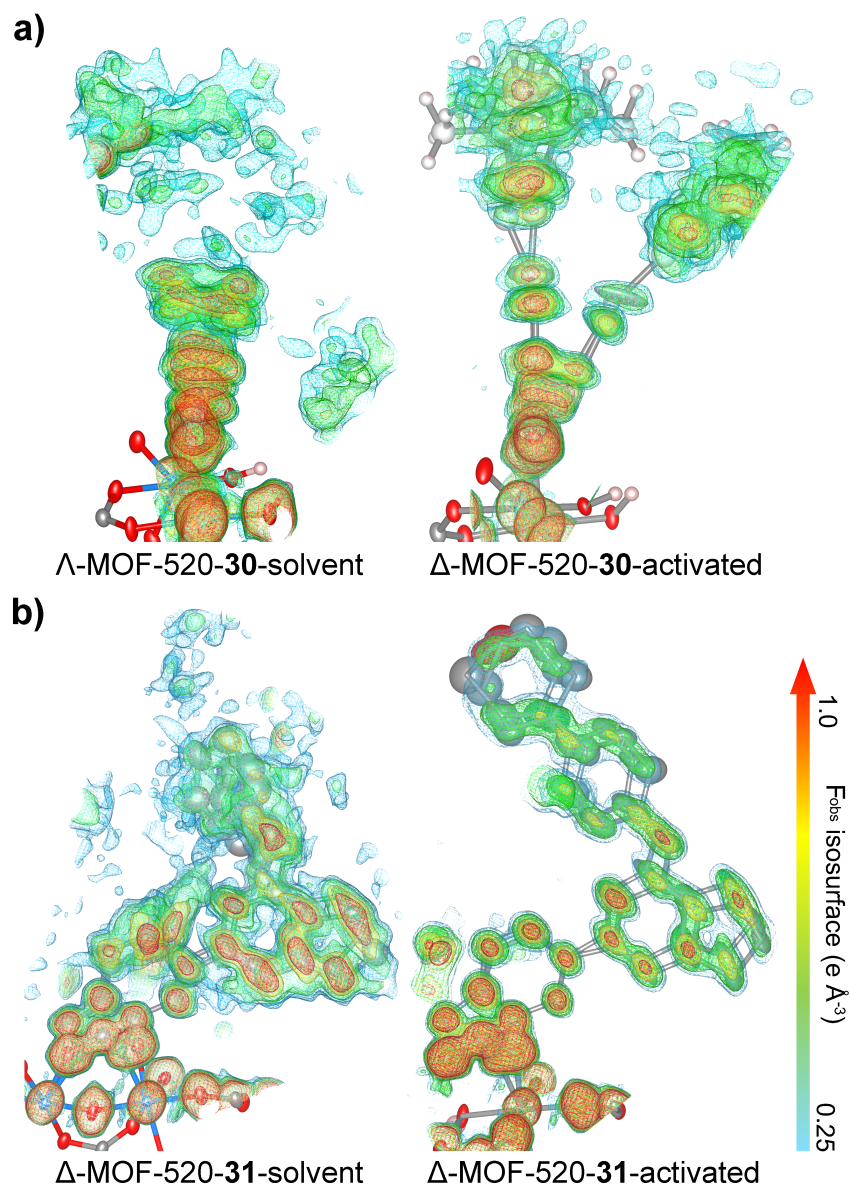


Figure 3.3. F_{obs} electron density isosurface plots for MOF-520-1 and MOF-520-2 before and after solvent evacuation. The plot is overlaid with the structure model. Color code of structure models: Al, blue; O, red; N, green; C, gray; B, purple; and H, pink.

Δ -MOF-520-1 was first measured in the presence of DMF at 100 K. Continuous electron densities representing continuous disordered positions between two modeled positions are observed for this structure (**Figure 3.3a**), posing challenges for the refinement of atomic coordinates and ADPs of the planar indazole fragment. Moreover, the pinacol ester could not be modeled. Upon activation, the positional disorder of the molecule is reduced to only two distinct positions, allowing for unambiguous structure modeling and full structural resolution of **1**.

The solvent molecules which are present in porous structures inevitably form a background of electron densities with average levels of 0.2–0.4 $e \text{ \AA}^{-3}$ (**Table 3.2**),¹⁷ which overlaps with the electron density of low occupancy incorporated molecules. For example, Δ -MOF-520-2-solvated and Δ -MOF-520-2-activated were solved with molecule occupancies of 36% and 26%,

respectively. Comparison of the F_{obs} maps of the two structures reveal that the structure of **2** is obscured in the solvated MOF due to smeared out electron densities contributed by the solvent molecules, but becomes better defined upon activation of the framework (electron density distribution matches the incorporated molecule; **Figure 3.3b**).

3.4. Conclusion

In this section of work, the coordinative alignment method was further expanded to large molecules with sizes ranging from 250 to 500 Daltons. The vibrational disorder of the large molecule was carefully examined, and it was found that the removal of solvent inside MOF-520 greatly reduced the vibrational and static disorder of the incorporated guest molecule. In addition, the removal of background solvent electron densities provided structural solution with better reliability. The F_{obs} electron density plots of guest molecules **1** and **2** showed great matches with their chemical structures, proving that the coordinative alignment method is applicable to solving structures of complex large molecules with high confidence. Furthermore, the enantioselective incorporation is found to be feasible on large molecules containing the newly introduced eight functionalities, providing a tool for chiral structure determination without the need of pre-separation of enantiomers.

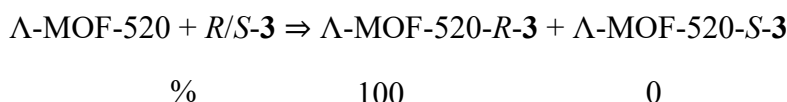
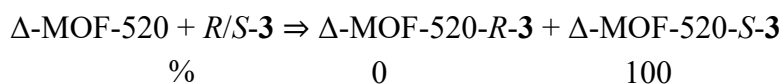
3.5. Appendices and Notes

3.5.1. Terms for Describing Stereoselectivity of MOF-520

The definition from IUPAC on stereoselectivity, enantioselectivity, and diastereoselectivity is:^{18,19}

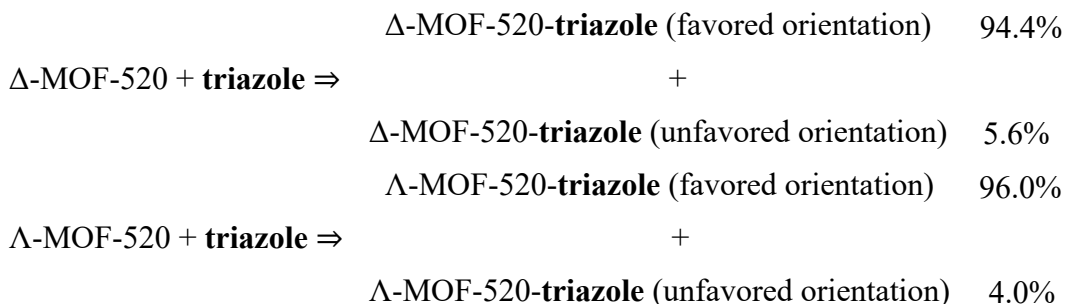
Stereoselectivity is the preferential formation in a chemical reaction of one stereoisomer over another. When the stereoisomers are enantiomers, the phenomenon is called enantioselectivity and is quantitatively expressed by the enantiomer excess: when they are diastereoisomers, it is called diastereoselectivity and is quantitatively expressed by the diastereomer excess.

The definition is based on the stereo relation of the possible products. Consider the ligand exchange reaction of the molecule incorporation into MOF-520, for example, *R/S-3*, a racemic mixture of enantiomers. The reaction for each enantiomorph of MOF can be written as:



The two products in each reaction are diastereomers, and one of them is in excess over the other. So, the selectivity should be considered as diastereoselectivity. Only when considering the both reactions, the two favored products are enantiomer to each other.

Same analysis can be applied to the incorporation of achiral molecule molecules, for example, 1,2,3-triazole and methylphosphonic acid:



The selectivity should also be considered as diastereoselectivity. The relationship between two favored products, and two unfavored products, are enantiomers.

In the main article, the words used for describing the selectivity on chiral and achiral molecules are selected to be different to facilitate a clearer discussion. “Enantiomeric discrimination” or “enantioselective incorporation” are used for the chiral molecules, to emphasize the phenomena that two enantiomers in a racemic mixture selectively goes to different enantiomorph of MOF. “Diastereoselective incorporation” is used for the achiral molecules to be a parallel term of “enantioselective incorporation”. “Stereoselectivity” is used as an inclusive term for the two aspects mentioned above.

3.5.2. Single-crystal X-ray diffraction results

Refinement details of Λ -MOF-520-1-solvated

A colorless crystal of Λ -MOF-520-1-solvated was measured on a Bruker D8 Venture Diffractometer with Cu K α radiation. Based on intensity statistics for the whole dataset (PRP file), the resolution was cut off to 0.91 Å ($R_{\text{merge}} \leq 40\%$ or average $I/\sigma > 2.5$ for the highest resolution shell).

The refinement procedure is as follow: 1) Atoms belonging to the MOF backbone were first assigned and refined anisotropically; 2) The 5-membered pyrazole ring that is directly bonded to the Al atoms was assigned, together with the non-substituted formate. After several atom assignments, it can be concluded from the atomic connectivity that the molecule is disordered over two sites. Their occupancies were refined via free variables and after they converged, they were constrained to 0.31646 and 0.28234.

As described in the main article, there was strong disorder caused by the remaining solvent in the MOF pore, and the observed electron density was very smeared making the anisotropic refinement of **1** was very unstable. To address the problem, constraints and restraints (SADI, SIMU, FLAT, ISOR) were applied to each atom and bond throughout the structure of the incorporated molecule. ISOR and EADP were used to stabilize the anisotropic refinement of the two coordinating nitrogen atoms and the nearby formate. After these efforts, the whole structure could be refined anisotropically and hydrogen atoms were placed in calculated positions. Solvent masking was not applied during structure refinement. Reflections that are affected by the beamstop or having $(I_{\text{obs}} - I_{\text{calc}})/\sigma > 7$ were omitted. The weighting scheme was not refined and the a, b parameters are remained at SHELXL defaults (0.2000 and 0, respectively).

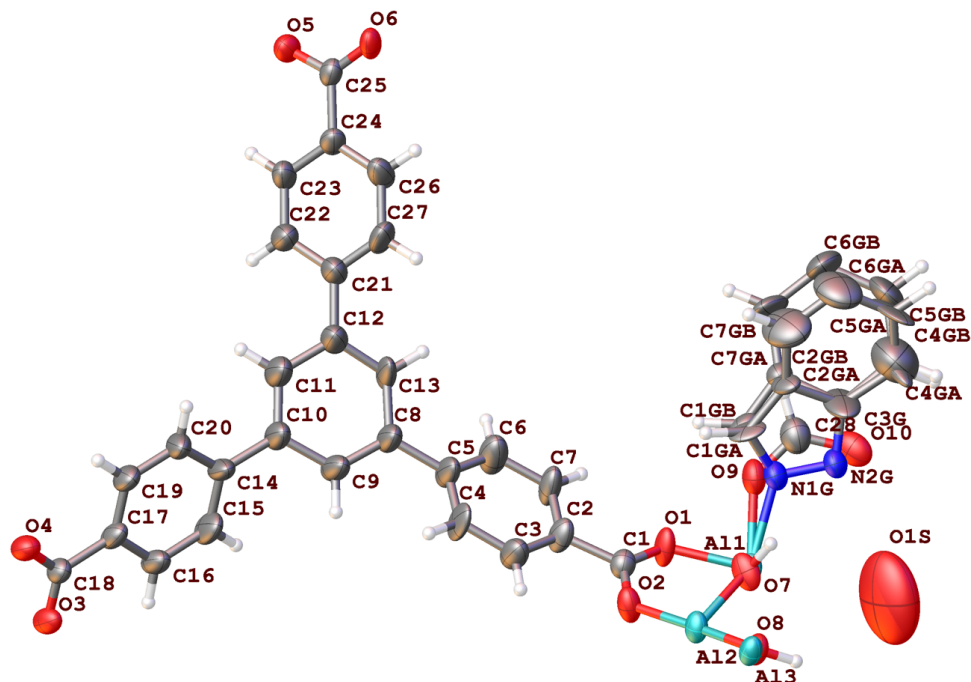


Figure 3.4. Asymmetric unit in the single crystal structure of Λ -MOF-520-1-solvated. Thermal ellipsoids are drawn with 50% probability.

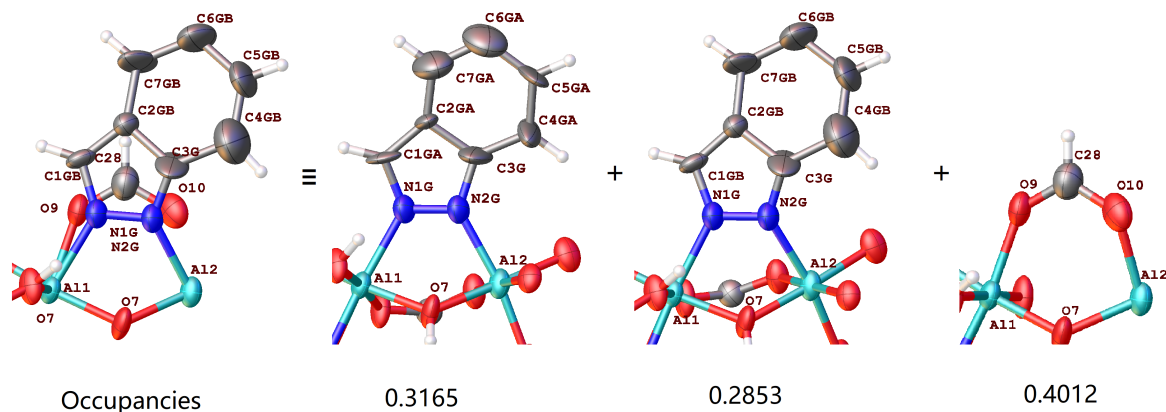


Figure 3.5. Illustration of the disorder at the incorporation site in the single crystal structure of Λ -MOF-520-1-solvated. Thermal ellipsoids are drawn with 50% probability.

Table 3.3. Crystal data, data collection, and structure refinement parameters for Λ -MOF-520-1-solvated.

Name	Λ -MOF-520-1-solvated
Empirical formula	$C_{31.59}H_{19.8}Al_2N_{1.2}O_{9.05}$
Formula weight	614.96
Temperature/K	100
Crystal system	tetragonal
Space group	$P4_22_12$
$a/\text{\AA}$	19.0466(6)
$b/\text{\AA}$	19.0466(6)
$c/\text{\AA}$	36.3890(12)
$\alpha/^\circ$	90
$\beta/^\circ$	90
$\gamma/^\circ$	90
Volume/ \AA^3	13200.9(9)
Z	8
$\rho_{\text{calc}} (\text{g/cm}^3)$	0.619
μ/mm^{-1}	0.621
F(000)	2529.0
Crystal size/ mm^3	$0.1 \times 0.085 \times 0.08$
Radiation	$\text{CuK}\alpha (\lambda = 1.54178 \text{\AA})$
2θ range for data collection/ $^\circ$	6.718 to 116.56
Index ranges	$-20 \leq h \leq 13, -15 \leq k \leq 20, -38 \leq l \leq 16$
Reflections collected	34031
Independent reflections	9065 [$R_{\text{int}} = 0.0367, R_{\text{sigma}} = 0.0493$]
Data/restraints/parameters	9065/134/494
Goodness-of-fit on F^2	1.423
Final R indexes [$I \geq 2\sigma(I)$]	$R_1 = 0.1250, wR_2 = 0.3230$
Final R indexes [all data]	$R_1 = 0.1465, wR_2 = 0.3391$
Largest diff. peak/hole / $e \text{\AA}^{-3}$	1.14/-0.49
Flack parameter	0.230(11)

Refinement details of Δ -MOF-520-1-activated

A colorless crystal of Δ -MOF-520-1-activated was measured at beamline 12.2.1 at ALS with radiation of $\lambda = 0.7288 \text{ \AA}$. Based on intensity statistics for the whole dataset (PRP file), the resolution was cut off to 0.75 \AA ($R_{\text{merge}} \leq 40\%$ or average $I/\sigma > 2.5$ for the highest resolution shell). Considering that the electron densities from this data is going to be compared to Δ -MOF-520-1-solvent of which the resolution was 0.90 \AA , the resolution of Δ -MOF-520-1-activated was further cut off to 0.91 \AA with the SHEL command (SHEL 999 0.91).

The refinement procedure is as follow: 1) Atoms belonging to the MOF backbone were first assigned and refined anisotropically; 2) The 5-membered pyrazole ring that is directly bonded to the Al atoms was assigned, together with the non-substituted formate. After several atom assignments, it can be concluded from the atomic connectivity that the molecule is disordered over two sites. Their occupancies were refined via free variables and after they converged, they were constrained to 0.30759 and 0.1999.

At the boric ester end of **1** the assignment of atoms is complicated for two reasons: first, for one site the molecules overlap with those on the other side of the SBU (related by a twofold rotation). The positions of the pinacol esters were so overlapped that it was hard to assign separate atomic positions. By comparison, atom assignment at the other position was relatively easy. It was found that the 5-membered boric acid ester ring was disordered over two conformations, *i.e.*, split into two positions and for each of them the occupancy was $0.30759/2 = 0.1538$. The refinement of the 5-membered ring could be stabilized with SADI, and the boron atom positions were fixed via FLAT to the indazole fragment. The atoms of the pinacol ester had to be refined isotropically. At this stage, besides the pinacol ester, the whole structure was refined anisotropically and hydrogen atoms were placed into calculated positions. Solvent masking was not applied during structure refinement. Reflections that are affected by the beamstop or having $(I_{\text{obs}} - I_{\text{calc}})/\sigma > 7$ were omitted. The weighting scheme was refined to convergence and the a, b parameters are 0.1026 and 2.6675, respectively.

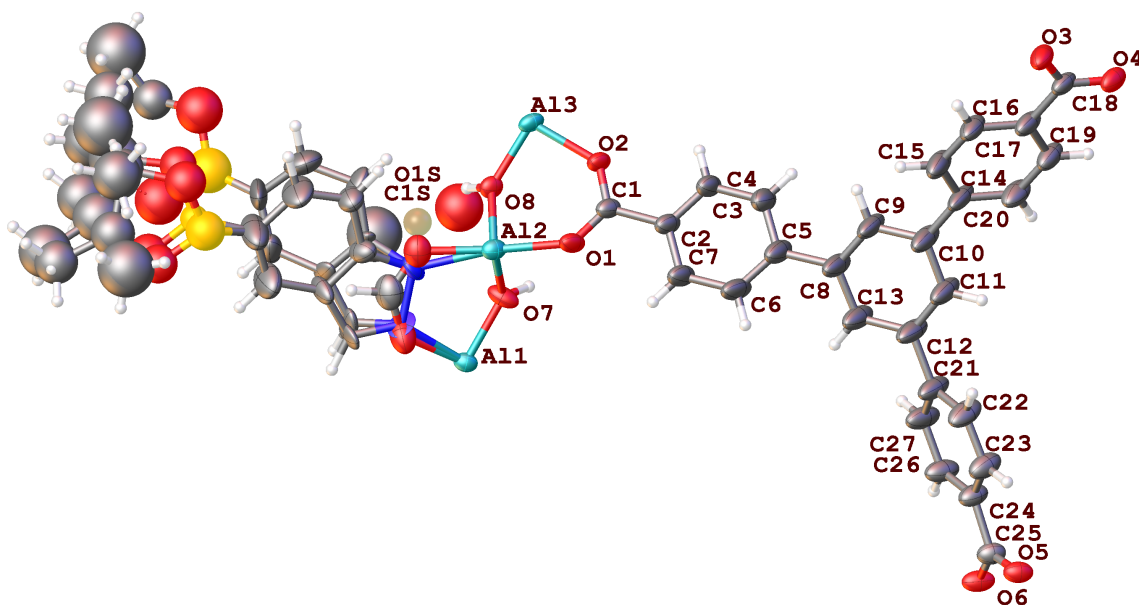


Figure 3.6. Asymmetric unit in the single crystal structure of Δ -MOF-520-1-activated. Thermal ellipsoids are drawn with 50% probability.

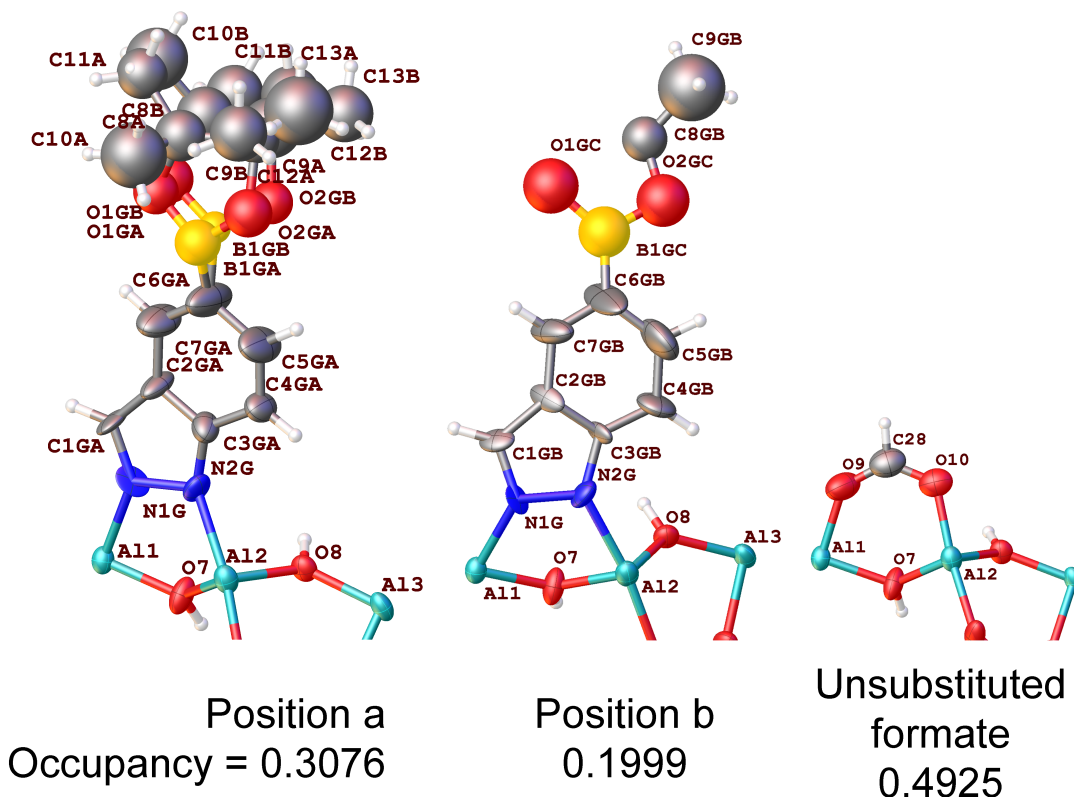


Figure 3.7. Illustration of the disorder at the incorporation site in the single crystal structure of Δ -MOF-520-1-activated. Thermal ellipsoids are drawn with 50% probability.

Table 3.4. Crystal data, data collection, and structure refinement parameters for Δ -MOF-520-1-activated.

Name	Δ -MOF-520-1-activated
Empirical formula	$C_{33.75}H_{23.81}Al_2B_{0.51}N_{1.01}O_{10.22}$
Formula weight	666.40
Temperature/K	100
Crystal system	tetragonal
Space group	$P4_22_12$
$a/\text{\AA}$	19.2915(5)
$b/\text{\AA}$	19.2915(5)
$c/\text{\AA}$	36.0810(11)
$\alpha/^\circ$	90
$\beta/^\circ$	90
$\gamma/^\circ$	90
Volume/ \AA^3	13428.0(8)
Z	8
ρ_{calc} (g/cm ³)	0.659
μ/mm^{-1}	0.077
F(000)	2749.0
Crystal size/mm ³	$0.057 \times 0.057 \times 0.043$
Radiation	Synchrotron ($\lambda = 0.7288 \text{ \AA}$)
2Θ range for data collection/ $^\circ$	3.838 to 47.21
Index ranges	$-21 \leq h \leq 21, -21 \leq k \leq 21, -39 \leq l \leq 39$
Reflections collected	128287
Independent reflections	9297 [$R_{\text{int}} = 0.0942, R_{\text{sigma}} = 0.0471$]
Data/restraints/parameters	9297/64/600
Goodness-of-fit on F^2	1.070
Final R indexes [$I \geq 2\sigma(I)$]	$R_1 = 0.0544, wR_2 = 0.1434$
Final R indexes [all data]	$R_1 = 0.0572, wR_2 = 0.1479$
Largest diff. peak/hole / e \AA^{-3}	0.53/-0.23
Flack parameter	-0.06(5)

Refinement details of Δ -MOF-520-2-solvated

A colorless crystal of Δ -MOF-520-2-solvated was measured at beamline 12.2.1 at ALS with radiation of $\lambda = 0.7288 \text{ \AA}$. Based on intensity statistics for the whole dataset (PRP file), the resolution was cut off to 0.76 \AA ($R_{\text{merge}} \leq 40\%$ or average $I/\sigma > 2.5$ for the highest resolution shell).

The refinement procedure is as follow: 1) Atoms belonging to the MOF backbone were first assigned and refined anisotropically; 2) The 5-membered pyrazole ring that is directly bonded to the Al atoms was assigned, together with the non-substituted formate. The occupancies of them were refined via a free variable and finally the total occupancy of **2** converged and was constrained to 0.36118. 3) Starting from the pyrazole ring, the closest electron densities peaks were found and assigned. The Uiso of them were constrained to 0.06 and the occupancies were refined freely. After several atom assignments, it can be concluded from the atomic connectivity that the molecule is disordered over two sites. The occupation of the atoms of each guest were fixed to 0.18059 and the Uiso were refined freely.

The refinement of the atom positions for benzene ring (C14A-C19A, C14B-C19B) is unstable due to the disorder caused by solvent (see main article); the morpholine ring could not be assigned at all. The anisotropic refinement of **2** was also not stable due to the closely overlapping disordered positions, so that the following constraints/restraints were applied to the bounded molecule: a) SADI was applied to the 6-membered ring of the indazole fragment because the atomic positions of C5A to C7A and C5B to C7B were not stable in the refinement. b) The 6-membered rings of imidazo[1,2-a]pyrazine in position A and B were constrained with AFIX 66. c) The 5-membered rings of imidazo[1,2-a]pyrazine in position A and B were restrained with SADI, and to the same plane with the adjacent 6-membered ring. d) N6GA and N6GB were restrained with FLAT to the two connected planes. SADI was also used to fix the relative position of benzene ring to imidazo[1,2-a]pyrazine. e) The benzene rings (C14A to C19A, C14B to C19B) of **2** were constrained by AFIX 66. f) SIMU and ISOR were applied throughout the structure of **2**. After the constraints/restraints were applied, the whole structure was refined anisotropically and hydrogen atoms were placed into calculated positions.

Solvent masking was not applied because the sample was activated. Reflections that are affected by the beamstop or having $(I_{\text{obs}} - I_{\text{calc}})/\sigma > 7$ were omitted. The weighting scheme was not refined and the a, b parameters are remained at SHELXL defaults (0.2000 and 0, respectively).

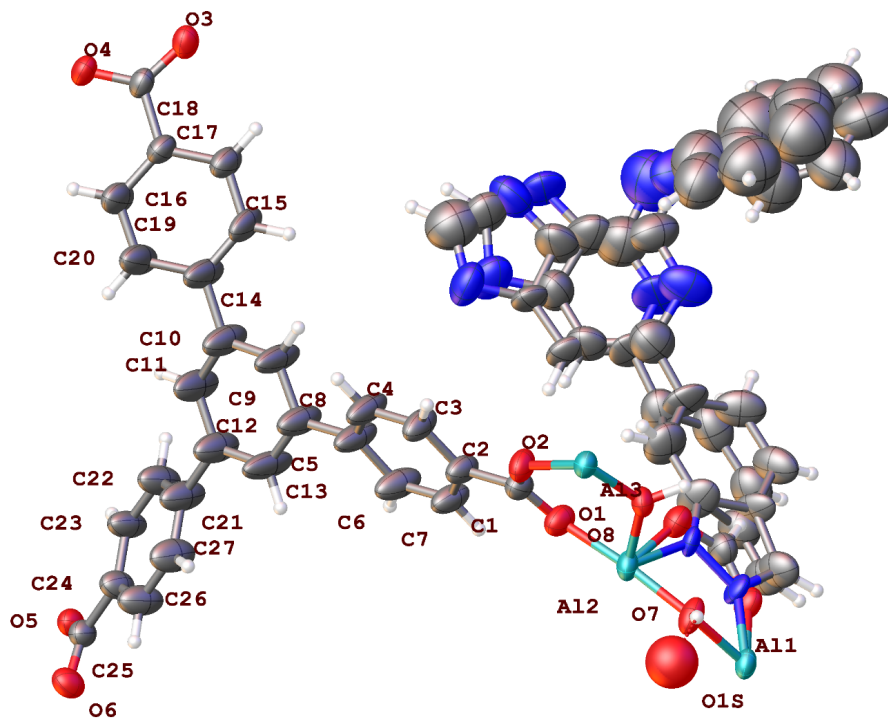


Figure 3.8. Asymmetric unit in the single crystal structure of Δ -MOF-520-2-solvated. Thermal ellipsoids are drawn with 50% probability.

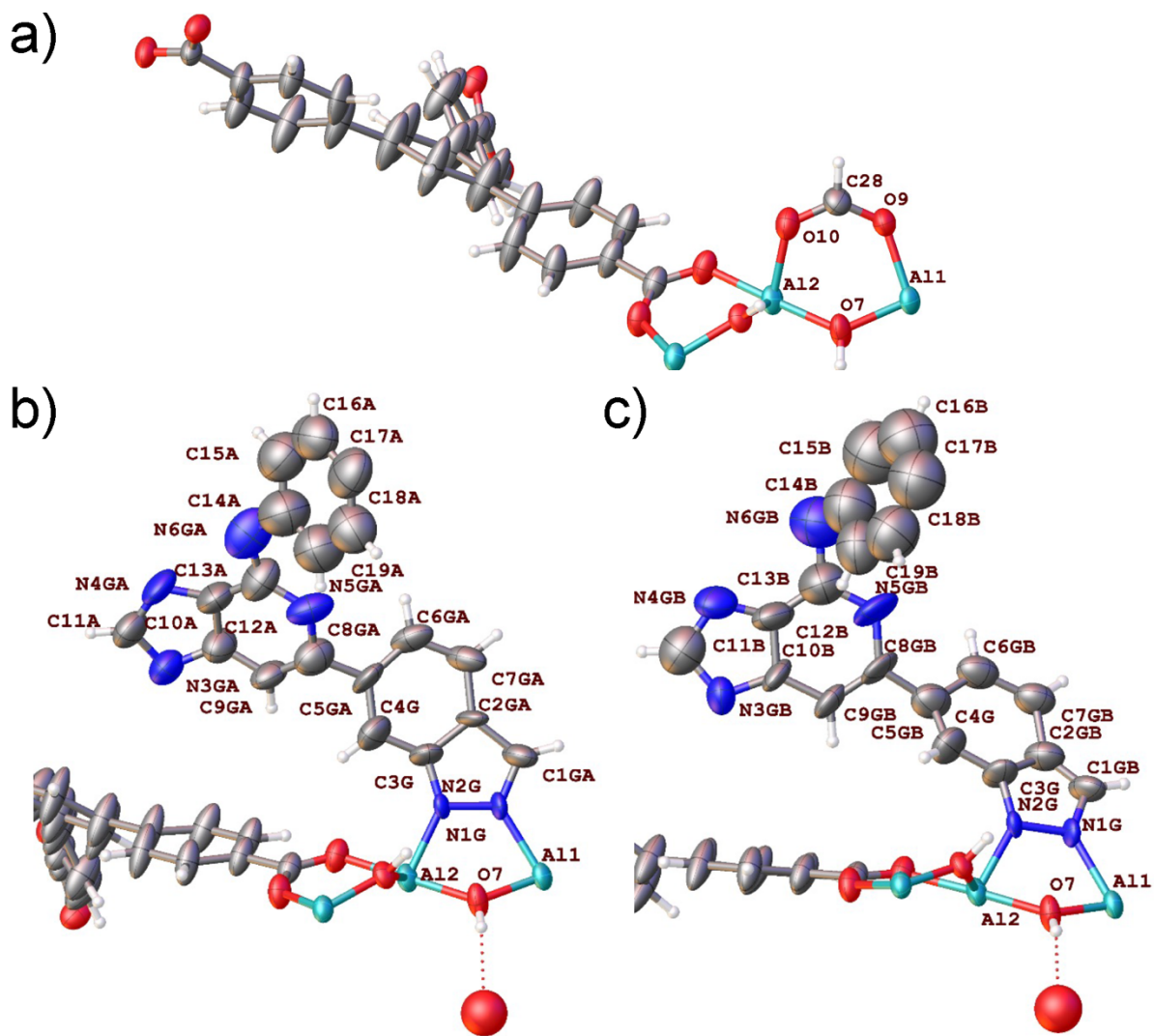


Figure 3.9. Asymmetric unit with a focus on the three disorder positions at the incorporation site in the single crystal structure of Δ -MOF-520-2-solvated. (a) The non-substituted formate. (b) Disordered position A of **2**. (c) Disordered position B of **2**. Thermal ellipsoids are drawn with 50% probability.

Table 3.5. Crystal data, data collection, and structure refinement parameters for Δ -MOF-520-2-solvated.

Name	Δ -MOF-520-2-solvated
Empirical formula	$C_{34.5}H_{21.61}Al_2N_{2.17}O_{9.85}$
Formula weight	678.01
Temperature/K	100(2)
Crystal system	tetragonal
Space group	$P4_22_12$
$a/\text{\AA}$	18.6944(6)
$b/\text{\AA}$	18.6944(6)
$c/\text{\AA}$	37.0688(12)
$\alpha/^\circ$	90
$\beta/^\circ$	90
$\gamma/^\circ$	90
Volume/ \AA^3	12954.8(9)
Z	8
$\rho_{\text{calc}} (\text{g/cm}^3)$	0.695
μ/mm^{-1}	0.080
F(000)	2788.0
Crystal size/ mm^3	$0.087 \times 0.066 \times 0.055$
Radiation	Synchrotron ($\lambda = 0.7288 \text{ \AA}$)
2Θ range for data collection/ $^\circ$	4.996 to 57.3
Index ranges	$-24 \leq h \leq 24, -24 \leq k \leq 23, -45 \leq l \leq 48$
Reflections collected	139633
Independent reflections	15391 [$R_{\text{int}} = 0.0687, R_{\text{sigma}} = 0.0365$]
Data/restraints/parameters	15391/483/727
Goodness-of-fit on F^2	1.135
Final R indexes [$I \geq 2\sigma(I)$]	$R_1 = 0.0995, wR_2 = 0.2600$
Final R indexes [all data]	$R_1 = 0.1202, wR_2 = 0.2812$
Largest diff. peak/hole / $e \text{ \AA}^{-3}$	1.13/-0.46
Flack parameter	0.05(3)

Refinement details of Δ -MOF-520-2-activated

A colorless crystal of Δ -MOF-520-2-activated was measured at beamline 12.2.1 at ALS with radiation of $\lambda = 0.7288 \text{ \AA}$. Based on intensity statistics for the whole dataset (PRP file), the resolution was cut off to 0.74 \AA ($R_{\text{merge}} \leq 40\%$ or average $I/\sigma > 2.5$ for the highest resolution shell).

The refinement procedure is as follow: 1) Atoms belonging to the MOF backbone were first assigned and refined anisotropically; 2) The 5-membered pyrazole ring that directly bonded to the Al atoms was assigned, together with the non-substituted formate. Their occupancies were refined via a free variable and finally the total occupancy of **2** converged and was constrained to 0.2620. 3) Starting from the pyrazole ring, the closest electron densities peaks were found and assigned. Their Uiso were constrained to 0.06 and the occupancies were refined freely. After several atom assignments, it can be concluded from the atomic connectivity that the molecule is disordered over two sites. For each disordered position the atomic occupancies were fixed to 0.1310 and the Uiso were refined freely. 4) After all the atoms from the molecule were assigned and constraints/restraints were applied (listed in next paragraph), the whole structure was refined anisotropically and hydrogen atoms were placed into calculated positions.

The anisotropic refinement of **2** wasn't stable due to the closely overlapping disordered positions, so that the following constraints/restraints were applied **2**: a) the 6-membered ring of imidazo[1,2-*a*]pyrazine in position A was constrained with AFIX 66; the 5-membered ring of imidazo[1,2-*a*]pyrazine in position B was constrained with AFIX 56. b) the benzene rings (C14A to C19A, C14B to C19B) of **2** were constrained with AFIX 66. c) The atoms bonded to the two benzene rings (N6GA, N7GA, N6GB, N7GB) were fixed to be in the same plane as the benzene rings with FLAT. d) The two morpholine rings of **2** were restrained with SADI and DFIX.

Solvent masking was not applied because the sample was activated. Reflections that are affected by the beamstop or having $(I_{\text{obs}} - I_{\text{calc}})/\sigma > 7$ were omitted. The weighting scheme was refined to convergence and the a, b parameters are 0.1135 and 0.1333, respectively.

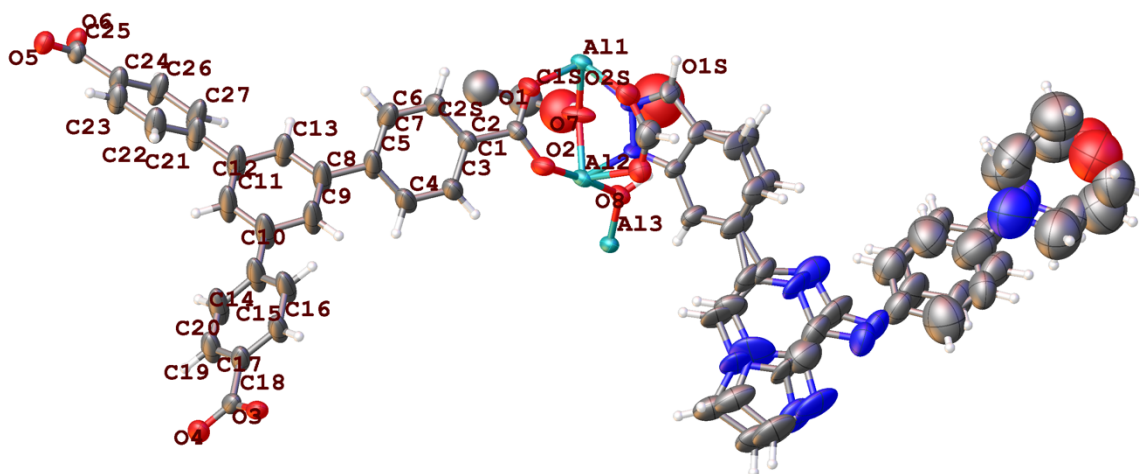


Figure 3.10. Asymmetric unit in the single crystal structure of Δ -MOF-520-2-activated. Thermal ellipsoids are drawn with 50% probability.

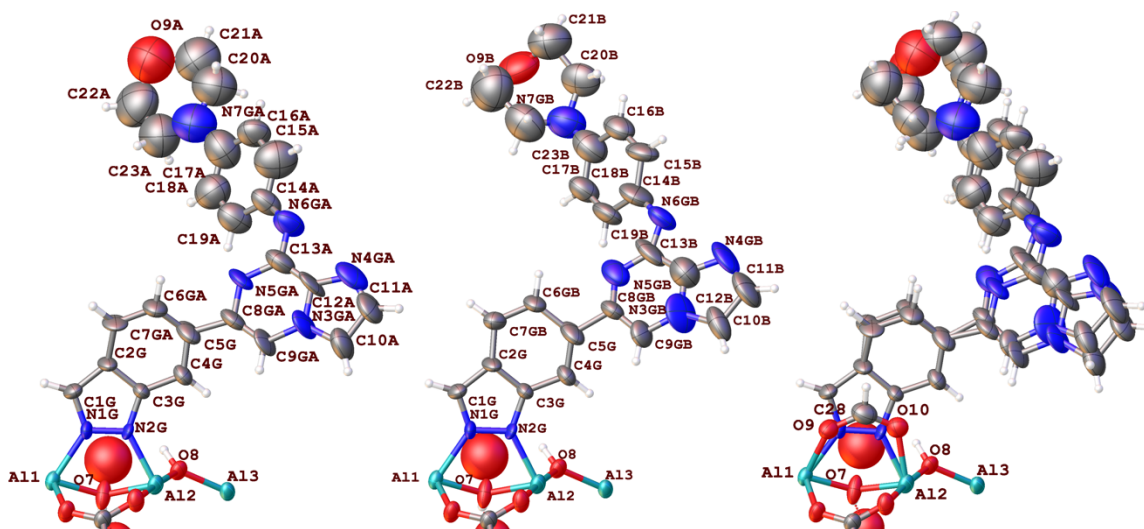


Figure 3.11. Illustration of the disorder at the incorporation site in the single crystal structure of Δ -MOF-520-2-activated. Thermal ellipsoids are drawn with 50% probability.

Table 3.6. Crystal data, data collection, and structure refinement parameters for Δ -MOF-520-2-activated.

Name	Δ -MOF-520-2-activated
Empirical formula	$C_{34.45}H_{22.72}Al_2N_{1.83}O_{10.47}$
Formula weight	683.81
Temperature/K	100
Crystal system	tetragonal
Space group	$P4_22_12$
$a/\text{\AA}$	19.079(3)
$b/\text{\AA}$	19.079(3)
$c/\text{\AA}$	36.683(5)
$\alpha/^\circ$	90
$\beta/^\circ$	90
$\gamma/^\circ$	90
Volume/ \AA^3	13353(4)
Z	8
$\rho_{\text{calc}} (\text{g/cm}^3)$	0.680
μ/mm^{-1}	0.079
$F(000)$	2816.0
Crystal size/ mm^3	$0.143 \times 0.121 \times 0.104$
Radiation	Synchrotron ($\lambda = 0.7288 \text{\AA}$)
2θ range for data collection/ $^\circ$	3.844 to 58.682
Index ranges	$-25 \leq h \leq 25, -25 \leq k \leq 25, -49 \leq l \leq 49$
Reflections collected	146105
Independent reflections	16935 [$R_{\text{int}} = 0.0562, R_{\text{sigma}} = 0.0261$]
Data/restraints/parameters	16935/391/825
Goodness-of-fit on F^2	1.077
Final R indexes [$I \geq 2\sigma(I)$]	$R_1 = 0.0532, wR_2 = 0.1450$
Final R indexes [all data]	$R_1 = 0.0587, wR_2 = 0.1504$
Largest diff. peak/hole / $e \text{\AA}^{-3}$	0.62/-0.29
Flack parameter	0.126(18)

Refinement details of Δ -MOF-520-S-3

A colorless crystal of Δ -MOF-520-S-3 was measured at beamline 12.2.1 at ALS with radiation of $\lambda = 0.7288 \text{ \AA}$. Based on intensity statistics for the whole dataset (PRP file), the resolution was cut off to 0.85 \AA ($R_{\text{merge}} \leq 40\%$ or average $I/\sigma > 2.5$ for the highest resolution shell).

The refinement procedure is as follow: 1) Atoms belonging to the MOF backbone were first assigned and refined anisotropically; 2) The 5-membered pyrazole ring directly bonded to the Al atoms was assigned, together with the non-substituted formate. Their occupancies were refined via a free variable. The occupancy of pyrazole converged and was constrained to 0.6. 3) Starting from the pyrazole ring, the closest electron densities peaks were found and assigned. Their Uiso of them were constrained to 0.06 and the occupancies were refined freely. After several atom assignments, it can be concluded from the atomic connectivity that the molecule is disordered over two sites. For each disordered position the atomic occupancies were fixed to 0.3 and the Uiso were refined freely. 4) After all the atoms from the incoming molecule were assigned, they were refined anisotropically and hydrogen atoms were placed in calculated positions. The ellipsoids of the atoms are elongated along the same direction, increasing so with increasing distance from the binding site, possibly due to the vibrational disordered. The refinement of the methoxy carbon (C15A, C15B, C16A, C16B) wasn't stable due to the rotation of methyl group, so that the C-O bond lengths were fixed.

At this stage, the connectivity of the molecule was determined and found to correspond to expectations. However, the bond lengths are not accurate enough to go for a detailed discussion. Therefore the following constraints were applied: 1) DFIX was applied to the bonds connected to the tertiary nitrogen atoms (N3GA/N3GB) and the chiral carbon atoms (C5GA/C5GB) using distances from previous reported structures.^{20,21} 2) ISOR was applied to all atoms of the incoming molecule for a more accurate refinement of the atom positions, leading to a more accurate dihedral angle between ring A and ring D (see main article).

At the end of the refinement, solvent masking was not applied because the sample was activated. Reflections that are affected by the beamstop or having $(I_{\text{obs}} - I_{\text{calc}})/\sigma > 7$ were omitted. The weighting scheme was refined to convergence and the a, b parameters are 0.1482 and 3.7013, respectively.

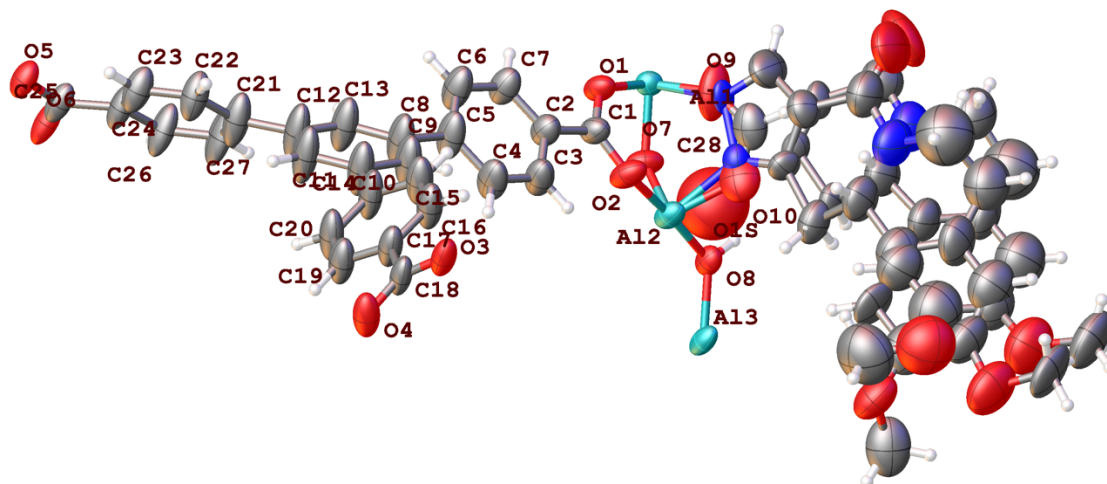


Figure 3.12. Asymmetric unit in the single crystal structure of Δ -MOF-520-S-3. Thermal ellipsoids are drawn with 50% probability.

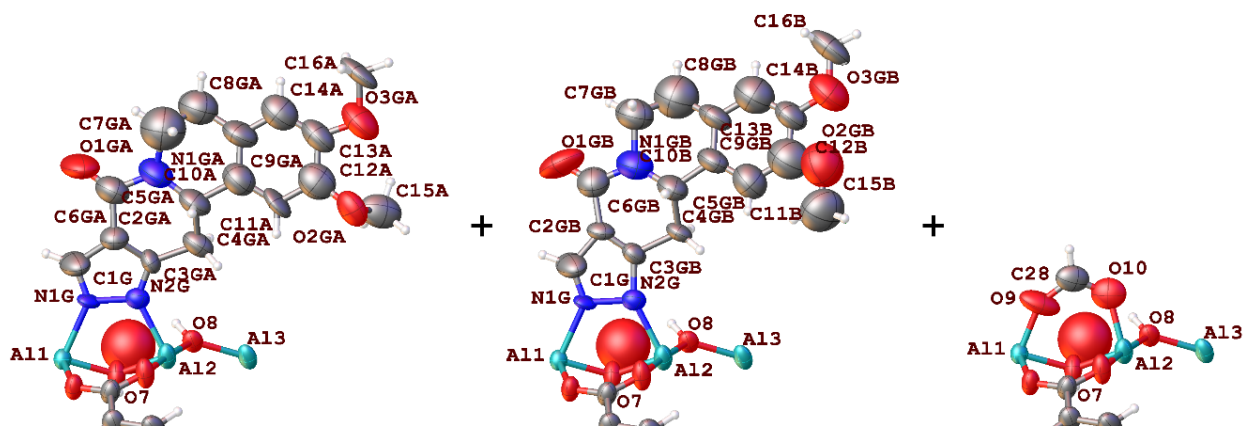


Figure 3.13. Illustration of the disorder at the incorporation site in the single crystal structure of Δ -MOF-520-S-3. Thermal ellipsoids are drawn with 50% probability.

Table 3.7. Crystal data, data collection, and structure refinement parameters for Δ -MOF-520-S-3.

Name	Δ -MOF-520-S-3
Empirical formula	$C_{37}H_{27}Al_2N_{1.8}O_{10.85}$
Formula weight	724.36
Temperature/K	100
Crystal system	tetragonal
Space group	$P4_22_12$
$a/\text{\AA}$	19.4248(7)
$b/\text{\AA}$	19.4248(7)
$c/\text{\AA}$	35.7345(13)
$\alpha/^\circ$	90
$\beta/^\circ$	90
$\gamma/^\circ$	90
Volume/ \AA^3	13483.4(11)
Z	8
ρ_{calc} (g/cm^3)	0.714
μ/mm^{-1}	0.081
F(000)	2995.0
Crystal size/ mm^3	$0.079 \times 0.068 \times 0.048$
Radiation	Synchrotron ($\lambda = 0.7288 \text{\AA}$)
2θ range for data collection/ $^\circ$	4.3 to 50.822
Index ranges	$-22 \leq h \leq 22, -22 \leq k \leq 22, -42 \leq l \leq 42$
Reflections collected	171051
Independent reflections	11493 [$R_{\text{int}} = 0.0733, R_{\text{sigma}} = 0.0307$]
Data/restraints/parameters	11493/272/708
Goodness-of-fit on F^2	1.105
Final R indexes [$I \geq 2\sigma(I)$]	$R_1 = 0.0795, wR_2 = 0.2190$
Final R indexes [all data]	$R_1 = 0.0827, wR_2 = 0.2224$
Largest diff. peak/hole / $e \text{\AA}^{-3}$	0.66/-0.44
Flack parameter	0.04(3)

Refinement details of Δ -MOF-520-*R*-3

A colorless crystal of Δ -MOF-520-*R*-3 was measured at beamline 12.2.1 at ALS with radiation of $\lambda = 0.7288 \text{ \AA}$. Based on intensity statistics for the whole dataset (PRP file), the resolution was cut off to 0.85 \AA ($R_{\text{merge}} \leq 40\%$ or average $I/\sigma > 2.5$ for the highest resolution shell).

The refinement procedure follows that for Δ -MOF-520-*S*-3 (Section S3.2.22). The total occupancy of the two positions of (*S*)-3 was determined to be 0.5808. The refinement of the methoxy carbon (C15A, C15B, C16A, C16B) wasn't stable due to the rotation of the methyl group, so that the C-O bond lengths were fixed. DFIX was applied for the bonds connected to the chiral carbon (C5GA/C5GB) and the tertiary nitrogen (N3GA/N3GB) based on previously reported structures.^{20,21} ISOR was applied to all atoms of the target molecule for a more accurate refinement of the atom positions. At the end of the refinement, solvent masking was not applied because the sample was activated. Reflections that are affected by the beamstop or having $(I_{\text{obs}} - I_{\text{calc}})/\sigma > 7$ were omitted. The weighting scheme was refined to convergence and the a, b parameters are 0.1533 and 5.5734, respectively.

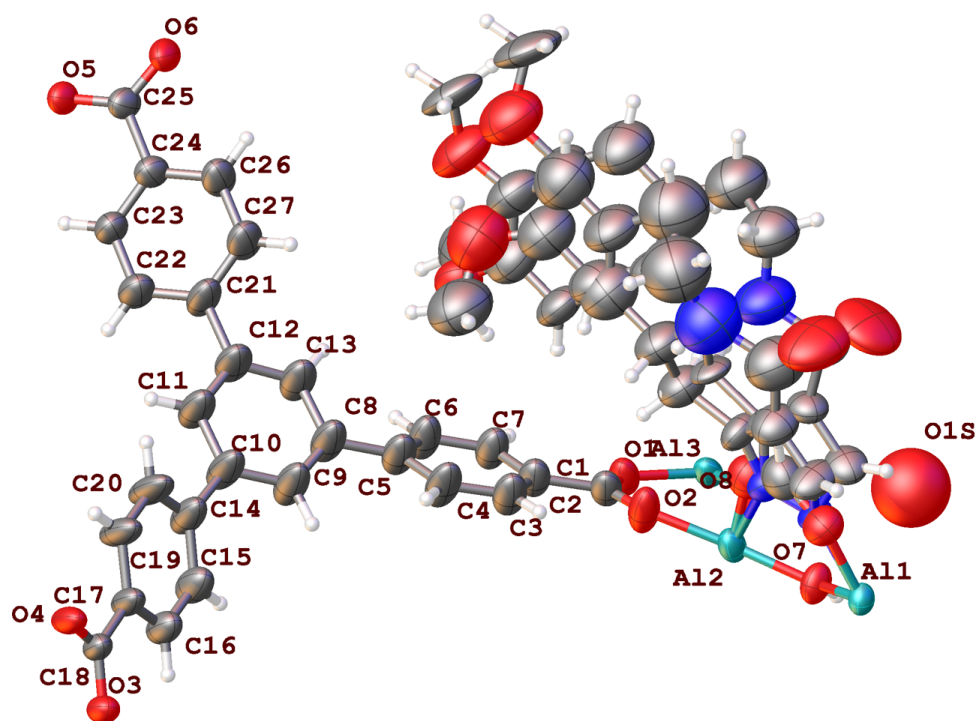


Figure 3.14. Asymmetric unit in the single crystal structure of Δ -MOF-520-*R*-3. Thermal ellipsoids are drawn with 50% probability.

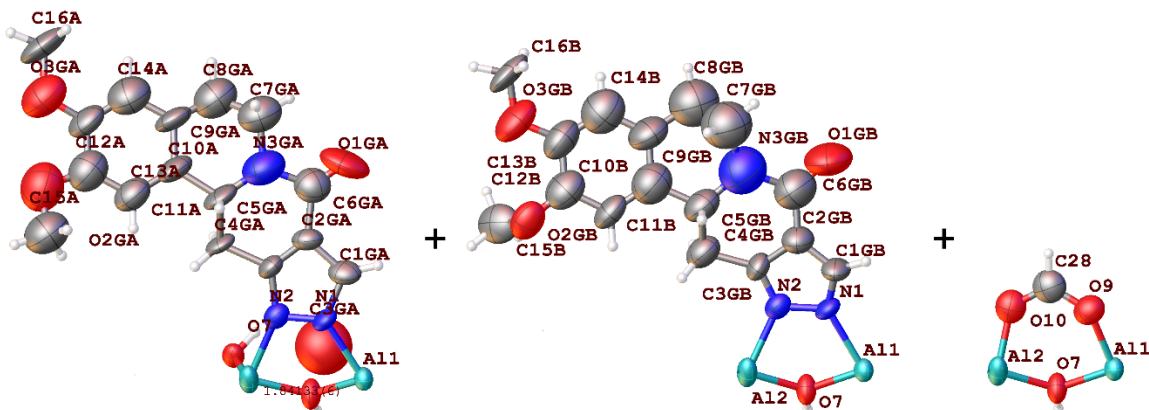


Figure 3.15. Illustration of the disorder at the incorporation site in the single crystal structure of Λ -MOF-520-R-3. Thermal ellipsoids are drawn with 50% probability.

Table 3.8. Crystal data, data collection, and structure refinement parameters for Λ -MOF-520-R-3.

Name	Λ -MOF-520-R-3
Empirical formula	$C_{36.71}H_{26.71}Al_2N_{1.74}O_{10.8}$
Formula weight	718.94
Temperature/K	100
Crystal system	tetragonal
Space group	$P4_22_12$
$a/\text{\AA}$	19.3750(9)
$b/\text{\AA}$	19.3750(9)
$c/\text{\AA}$	35.8159(16)
$\alpha/^\circ$	90
$\beta/^\circ$	90
$\gamma/^\circ$	90
Volume/ \AA^3	13445.0(14)
Z	8
ρ_{calc} (g/cm^3)	0.710
μ/mm^{-1}	0.081
$F(000)$	2972.0
Crystal size/ mm^3	$0.087 \times 0.078 \times 0.052$
Radiation	Synchrotron ($\lambda = 0.7288 \text{ \AA}$)
2θ range for data collection/ $^\circ$	4.312 to 50.77
Index ranges	$-22 \leq h \leq 22, -22 \leq k \leq 22, -42 \leq l \leq 42$
Reflections collected	165225
Independent reflections	11389 [$R_{\text{int}} = 0.0842, R_{\text{sigma}} = 0.0312$]
Data/restraints/parameters	11389/316/717
Goodness-of-fit on F^2	1.099
Final R indexes [$I > 2\sigma(I)$]	$R_1 = 0.0873, wR_2 = 0.2379$
Final R indexes [all data]	$R_1 = 0.0893, wR_2 = 0.2398$
Largest diff. peak/hole / $e \text{ \AA}^{-3}$	0.70/-0.53
Flack parameter	0.13(2)

3.6. Bibliography

- (1) Poel, W.; Tinnemans, P.; Duchateau, A. L. L.; Honing, M.; Rutjes, F. P. J. T.; Vlieg, E.; Gelder, R. The Crystalline Sponge Method in Water. *Chem. - Eur. J.* **2019**, *25* (65), 14999–15003.
- (2) Wang, L.; Moore, C. E.; Cohen, S. M. Coordinative Alignment To Achieve Ordered Guest Molecules in a Versatile Molecular Crystalline Sponge. *Cryst. Growth Des.* **2017**, *17* (12), 6174–6177.
- (3) Baek, J.; Rungtaweevoranit, B.; Pei, X.; Park, M.; Fakra, S. C.; Liu, Y.-S.; Matheu, R.; Alshimri, S. A.; Alshihri, S.; Trickett, C. A.; Somorjai, G. A.; Yaghi, O. M. Bioinspired Metal–Organic Framework Catalysts for Selective Methane Oxidation to Methanol. *J. Am. Chem. Soc.* **2018**, *140* (51), 18208–18216.
- (4) Furukawa, H.; Gándara, F.; Zhang, Y.-B.; Jiang, J.; Queen, W. L.; Hudson, M. R.; Yaghi, O. M. Water Adsorption in Porous Metal–Organic Frameworks and Related Materials. *J. Am. Chem. Soc.* **2014**, *136* (11), 4369–4381.
- (5) Currie, K. S.; Kropf, J. E.; Lee, T.; Blomgren, P.; Xu, J.; Zhao, Z.; Gallion, S.; Whitney, J. A.; Maclin, D.; Lansdon, E. B.; Maciejewski, P.; Rossi, A. M.; Rong, H.; Macaluso, J.; Barbosa, J.; Paolo, J. A. D.; Mitchell, S. A. Discovery of GS-9973, a Selective and Orally Efficacious Inhibitor of Spleen Tyrosine Kinase. *J. Med. Chem.* **2014**, *57* (9), 3856–3873.
- (6) Bruker. *APEX3, Version 8.38*; Bruker AXS Inc.: Madison, WI, USA, 2018.
- (7) Bruker. *SAINTE*; Bruker AXS Inc.: Madison, WI, USA, 2012.
- (8) Bruker. *SADABS, Version 2014/4*; Bruker AXS Inc.: Madison, WI, USA, 2014.
- (9) Sheldrick, G. M. A Short History of SHELX. *Acta Crystallogr., Sect. A: Found. Crystallogr.* **2008**, *64* (1), 112–122.
- (10) Sheldrick, G. M. Crystal Structure Refinement with SHELXL. *Acta Crystallogr., Sect. C: Struct. Chem.* **2015**, *71* (1), 3–8.
- (11) Dolomanov, O. V.; Bourhis, L. J.; Gildea, R. J.; Howard, J. A. K.; Puschmann, H. OLEX2: A Complete Structure Solution, Refinement and Analysis Program. *J. Appl. Crystallogr.* **2009**, *42* (2), 339–341.
- (12) Sluis, P. van der; Spek, A. L. BYPASS: An Effective Method for the Refinement of Crystal Structures Containing Disordered Solvent Regions. *Acta Crystallogr., Sect. A: Found. Crystallogr.* **1990**, *46* (3), 194–201.
- (13) Toby, B. H.; Dreele, R. B. V. GSAS-II: The Genesis of a Modern Open-Source All Purpose Crystallography Software Package. *J. Appl. Crystallogr.* **2013**, *46* (2), 544–549.
- (14) Momma, K.; Izumi, F. VESTA 3 for Three-Dimensional Visualization of Crystal, Volumetric and Morphology Data. *J. Appl. Crystallogr.* **2011**, *44* (6), 1272–1276.
- (15) Prince, E.; Finger, L.; Konnert, J. Constraints and Restraints in Refinement. In *International Tables for Crystallography*; John Wiley & Sons, Inc.: USA; Vol. A, pp 694–701.
- (16) Lee, S.; Bürgi, H.-B.; Alshimri, S. A.; Yaghi, O. M. Impact of Disordered Guest–Framework Interactions on the Crystallography of Metal–Organic Frameworks. *J. Am. Chem. Soc.* **2018**, *140* (28), 8958–8964.

- (17) Rees, B.; Jenner, L.; Yusupov, M. Bulk-Solvent Correction in Large Macromolecular Structures. *Acta Crystallogr. Sect. D: Biol. Crystallogr.* **2005**, *61* (9), 1299–1301.
- (18) Muller, P. Glossary of Terms Used in Physical Organic Chemistry (IUPAC Recommendations 1994). *Pure Appl. Chem.* **1994**, *66* (5), 1077–1184.
- (19) Moss, G. Basic Terminology of Stereochemistry (IUPAC Recommendations 1996). *Pure Appl. Chem.* **1996**, *68* (12), 2193–2222.

Chapter 4.

Accurate Structure Determination and Displacive Phase Transition of ZIF-90

The research in this chapter results from a collaboration with Dr. Stefano Canossa (Delft University of Technology/University of Antwerp) and Prof. Hans-Beat Bürgi (University of Bern/University of Zurich). The complete study on ZIF-90 also includes the diffuse scattering analyses on correlated disorders, which is not included in the thesis.

4.1. Introduction

Zeolitic imidazolate frameworks (ZIFs), as shown in the name, share great similarities with the structures and properties of zeolites. The tetrahedral-coordinating metal ions are structurally equivalent to Si^{4+} and Al^{3+} tetrahedrons in zeolites, while the bridging imidazolates (IMs) form the M-IM-M bond angles identical to Si-O-Si angles in zeolites.^{1,2} The resulting structures of ZIFs and zeolites from these highly symmetrical building units are generally of high space group symmetry as well.^{3,4} However, tilts and distortions of coordination tetrahedrons always occur in zeolites, causing the reduction of symmetry. Such disorders are primarily attributed to the influence of framework-guest (ions and water) interactions onto the total energy of framework and guests, which are widely observed in structures of minerals as well.⁵⁻⁸ While similar phenomena and the caused dynamic process (named displacive phase transition) would have been expected in ZIFs, the reported disorder on ZIFs so far limits to gate-opening effect caused by linker vibration, as discussed in chapter 1.2. Although one might argue that ZIFs are different from zeolites, ZIFs have demonstrated properties that are related to the geometric flexibility of coordination tetrahedrons. For example, ZIFs can be viewed as cages tiling by n -membered rings (n -MRs), and the flexibility of these rings owing to slight geometric changes of tetrahedrons have been both observed in ZIFs and zeolites.^{9,10} Moreover, the metal ions coordinated by four imidazolates in ZIFs showed their ability of undergoing largely distorted transition states at elevated temperatures and forming amorphous ZIF glasses upon cooling.¹¹⁻¹³ The tetrahedron coordination of metal ions were retained in ZIF glasses, indicating the tolerance of this coordination unit toward drastic distortions. Therefore, the disorder in ZIFs is worthwhile to be investigated in order to bridging the observations between static structures, dynamics, and large-scale amorphization.

In this work, we started with finding reported crystal structures of ZIFs that have low refinement qualities or unreasonable molecular geometries. Such features often indicate unaccounted disorders or errors in data processing and refinement. The more disordered the structure is, potentially more flexible the structure is. The search has led us to ZIF-90, a zinc ZIF with sodalite topology, which was originally reported in 2008.¹⁴ Its reported crystal structure was resolved from a good-quality dataset with R_{int} of 2.97%; however, the R factor of refinement was surprisingly high (14.55%). Following this hint, the single crystals of ZIF-90 were reproduced, and the structure of ZIF-90 was reinvestigated.

4.2. Experimental

4.2.1. Materials

$\text{Zn}(\text{NO}_3)_2 \cdot 4\text{H}_2\text{O}$ and 2-imidazolecarboxyaldehyde (Ica) were purchased from Sigma-Aldrich. Methanol (LC-MS Ultra CHROMASOLV™, > 99.9%) was purchased from Honeywell International Inc. *N,N*-dimethylformamide (DMF) (98%, HPLC) was purchased from Sigma-Aldrich and was purified in an Inert® solvent purification system PureSolv MD7 before use. All other chemicals were used without further purification. Scintillation vials (4 mL) and polypropylene cabs with foil liner were purchased from VWR International, LLC. Glass Number 50 capillaries (OD 0.4 mm or 0.1 mm, wall thickness 0.01 mm) were purchased from Hampton Research.

4.2.2. Syntheses of ZIF-90 crystals

0.054 g $\text{Zn}(\text{NO}_3)_2 \cdot 4\text{H}_2\text{O}$ and 0.029 g Ica were dissolved in 3 mL DMF, followed by the addition of 200 μL methanol. The mixed solution was sealed in a 4 mL scintillation vial and heated at

100 °C for 18 hours. Afterwards, the crystals were quickly washed with DMF for three times and were further exchanged with DMF for six times in two days. For the crystals to be activated, the ZIF-90 crystals in DMF were exchanged with methanol for nine times in three days before use.

4.2.3. Instrumentations and Methods

Sample 90AE_1 was measured at beamline 5.2R (XRD1) at Elettra lightsource equipped with a Pilatus 2M detector. All other single-crystal diffraction datasets were collected at beamlines 12.2.1 at the Advanced Light Source equipped with a Bruker D8 diffractometer and a Photon-II CPAD detector. Crystals were mounted in a 100(2) K nitrogen cold stream. The data up to $\sin(\theta)/\lambda = 2/3$ was collected with a phi scan of 180° with a width between frames of 0.4° or 0.5°. The datasets were processed with the Bruker APEX3 V8.38 software package.¹⁵ The frames were first integrated using SAINT¹⁶ and then the diffractions were corrected for absorption with SADABS.¹⁷ The structures were solved by direct methods (*SHELXS*)¹⁸ and the refinements done by full-matrix least squares on F^2 (*SHELXL*)¹⁹, using the Olex2 software package.²⁰ Platon SQUEEZE procedures were applied to non-activated structures.²¹

The activated ZIF-90 crystal was prepared as follow: a crystal immersed in methanol was put inside a glass capillary of 0.4 mm diameter without using glue or oil. A capillary of 0.1 mm diameter was inserted into 0.4 mm capillary to make the crystal stuck in capillary. The capillary was connected to Micromeritics ASAP 2420 system and evacuated to a dynamic vacuum of 2 μmHg for two hours at 100 °C. After the temperature cooled down, the capillary was sealed by a plasma lighter.

4.3. Results and Discussions

4.3.1. The Correct Structure of ZIF-90 Considering Merohedral Twinning

The original single-crystal structure of ZIF-90 was reported in the space group of *I*-43m: in the structure, the Zn ions occupy the Wyckoff position *d* and form square windows in-plane with the faces of the cubic unit cell; the linkers (2-imidazolecarboxyaldehyde; Ica) bridge the Zn ions, and the aldehyde group points to either one of the adjacent Zn ions, resulting in a 50:50 positional disorder. However, the abnormal shape of the imidazole ring (**Figure 4.1**) and unreasonably high

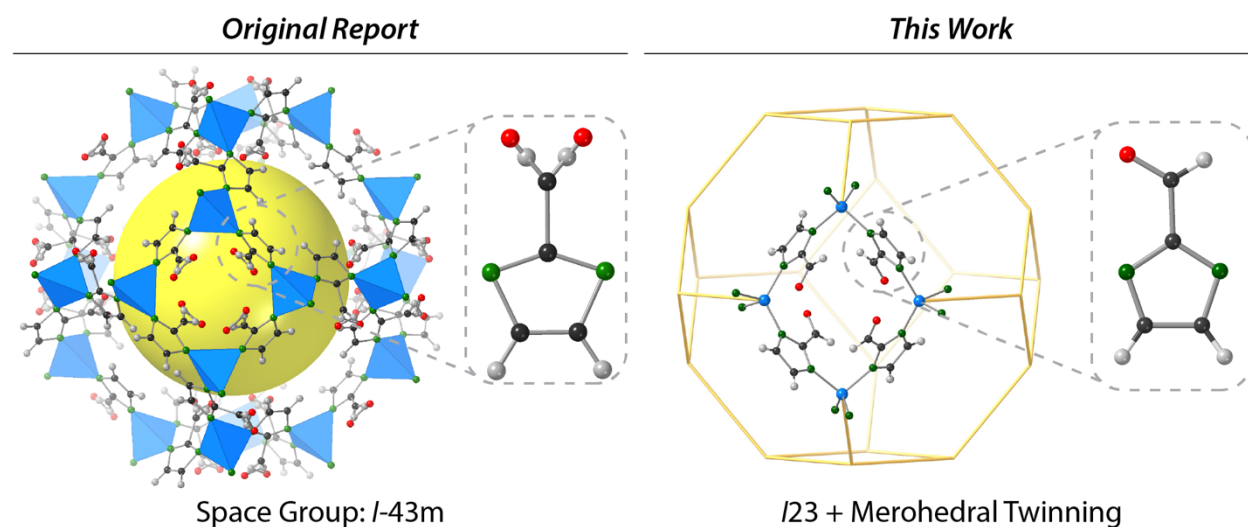


Figure 4.1. Zn coordination geometry and the structure of sodalite cage for the original reported structure (left) and the structural solution reported in this work (right).

R factor (14.55%) indicated the chosen space group might be wrong.

An investigation to the reproduced crystals indicated that the structure lies in a space group with lower symmetry, $I23$. The lower symmetry cleared the disorder imposed by wrongly assigned higher symmetry elements: it is found that the oxygen of the aldehyde group is not positionally disordered but selectively pointing to one of the adjacent Zn ions (**Figure 4.1**). Each Zn ion is weakly coordinated by two aldehyde oxygen in addition to the four imidazole nitrogen atoms, thus forming a pseudo-octahedral geometry. The coordination asymmetry breaks the perfect tetrahedron coordination geometry of Zn, and as a result, the sodalite cage gets distorted and the square pore-opening of the sodalite cage becomes rhombic. Meanwhile, the fractional coordinate of Zn along the direction of movement shifts from 0.25 in the ideal sodalite structure to roughly 0.225/0.275.

The distortion of rhombic pores is not aligned in one direction throughout one crystal: this newly identified structure solution is associated with merohedral twinning. Rigorous analysis was performed to identify the correct twin law. All possible twin operations for the structures in the

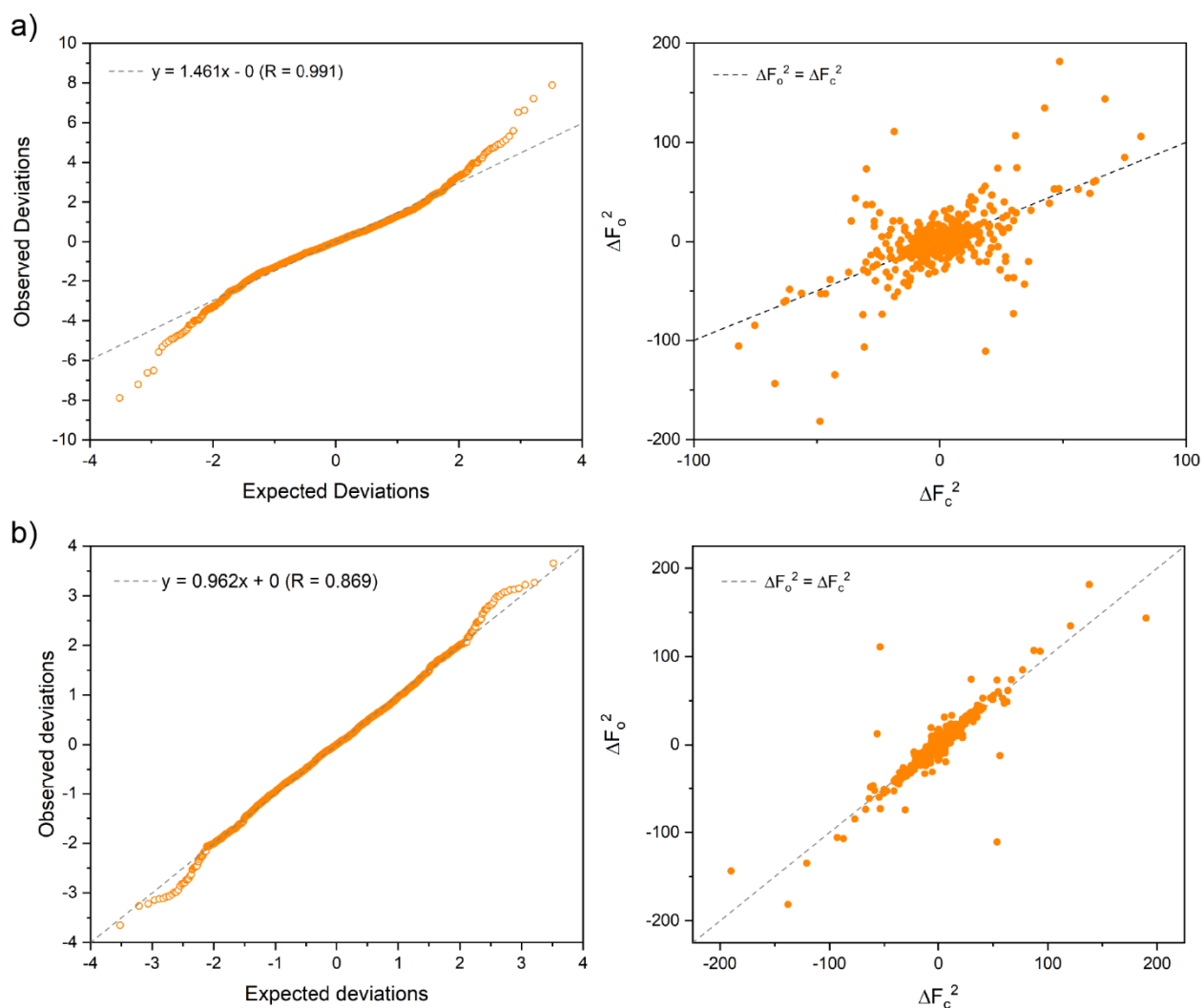


Figure 4.2. Bijvoet pair normal probability plot (left) and scatter plot (right) from the dataset 90AE_1 refined with a) diagonal 2-fold rotation twin law and b) diagonal mirror twin law.

point group 23 are: inversion, diagonal 2-fold rotation, and diagonal mirror.²² The inversion twin law was quickly excluded as it didn't improve the refinement ($R \approx 15\%$), while the latter two could both reduce the R factor to a similar level ($R \approx 5\%$). The difference of two twin laws theoretically lies in the difference of the intensities of observed Friedel pairs: while the diffraction intensities of the primary twin domain is not centrosymmetric, the diagonal mirror twin operation inverses the Friedel differences of the second twin domain, but the diagonal 2-fold rotation preserves them. As a result, the sum of the intensities from the two twin components is different upon choosing different twin laws. Therefore, the normal probability plots of Bijvoet (Friedel) pair difference²³ from the refinement with two twin laws and were examined respectively (**Figure 4.2**, left). The refinement with the diagonal mirror twin law gave a better result, as there is less deviation from the expected linear shape and the slope of the linear fit is closer to 1. The Bijvoet pair scatter plots were examined as well (**Figure 4.2**, right), while the result from the refinement with diagonal mirror twin law had less scattered distribution and is more reliable.

The intensity of anomalous scattering should be maximized to give the best contrast for the Friedel differences. However, the initial dataset was measured at shorter wavelength ($\lambda = 0.6199$ Å; **Table 4.2**), while the Zn absorption edge is at $\lambda = 1.2837$ Å. Aiming at a higher-quality determination of twin law, additional X-ray diffraction experiment was measured with $\lambda = 1.2398$ Å. It was found that the diagonal mirror twin law gave the R factor of 5.88% in the refinement (**Table 4.6**, before SQUEEZE), while the diagonal 2-fold rotation twin law resulted in a R factor of 7.97%. The difference in different twin laws was well reflected in the R factors given a better contrast on the intensities of Bijvoet pairs. Furthermore, a 4-component twin refinement was tested with the diagonal 2-fold twin law, by assuming racemic twinning was presented at the same time. Combination of the two twin laws resulted in 4 domains, and the three domains are related to the primary domain by the following operations: diagonal 2-fold rotation, inversion, and diagonal mirror. The resulting refined fraction of the three components were 0.008(15), 0.003(15), and 0.456(15), respectively, while the R factor dropped to 5.88% again, confirming that the assignment of diagonal mirror twin law is correct.

4.3.2. Structure Variation of Solvated ZIF-90 Crystals Measured at 100 K

Table 4.1. Data collected at 100K for the solvated ZIF-90 crystals synthesized by solvothermal method. Zn shift is defined as the shift of fractional Zn coordinate from the ideal sodalite geometry.

Sample	Radiation / Å	R (after SQUEEZE)	Unit cell a / Å	BASF	Zn shift	Zn-Zn distance / Å
90AE_1	0.61992	3.75%	17.05990(10)	0.507(6)	0.02449(3)	6.06047(8)
463_150	0.71073	5.89%	17.0030(6)	0.456(5)	0.02347(8)	6.0379(2)
450_2_05	0.7288	4.49%	17.0016(8)	0.507(4)	0.01545(11)	6.0224(3)
445_10_02	0.71073	4.73%	17.012(2)	0.488(5)	0.01421(14)	6.0245(6)
450_2_02	0.7288	6.66%	16.9748(7)	0.493(6)	0.01191(16)	6.0083(3)
445_10	0.71073	4.55%	16.957(2)	0.503(7)	0.0038(3)	5.9959(6)
450_2_04	1.2398	2.97%	17.0862(6)	0.536(2)	0.02438(3)	6.06955(71)

During the process of confirming the correct crystal structure of ZIF-90, several as-synthesized ZIF-90 crystals (solvated with DMF) were measured at 100 K. Interestingly, the coordinate fractional coordinate of Zn along the direction of movement is not always close to 0.225/0.275 but distributed from 0.225/0.275 to 0.25. To better identify the distortion of the square pore opening,

we define “Zn shift” as the shift of the fractional Zn coordinate from the ideal sodalite geometry. The Zn shifts in different crystals were plotted against their unit cell parameters and Zn-Zn distances (**Figure 4.3**). Rough trends were observed that the Zn shift increases as unit cell dimension increases, and the distance of the closest Zn-Zn ions also roughly increases as the Zn shift increases.

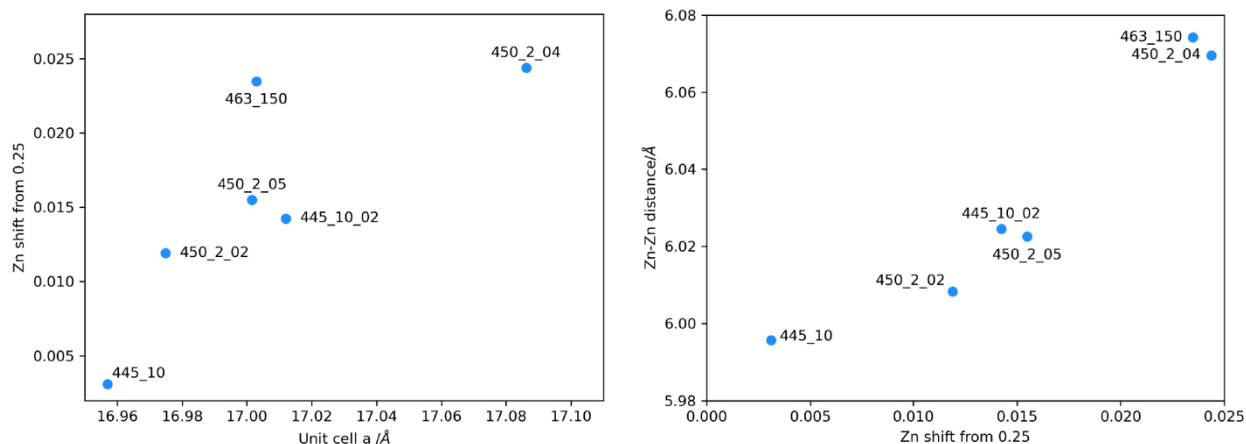


Figure 4.3. The plot of Zn shift against unit cell dimension and Zn-Zn distance against Zn shift for the data from solvothermal-synthesized ZIF-90 collected at 100 K.

4.3.3. Continuous Structure Change of ZIF-90 vs. Temperature

The series of statically disordered structures with various pore openings led us to the hypothesis whether a certain trigger can induce a dynamical change of pore opening. We selected temperature as the first trigger-to-be-tested, and the structure of a ZIF-90 crystal was monitored by SXRD while the temperature was increased from 100 K to 400 K followed by a cooldown to 100 K. The Zn shift decreased as the temperature increased, while the unit cell parameter increased at the same time, which is an inverse trend from the observations among the several crystals measured at 100 K (**Figure 4.4**). At 400 K, the distortion of the pore opening is the least and the structure is quite close to an ideal sodalite structure, with the Zn shift being 0.00078(11). As the temperatures cool down, the unit cell parameter of structure collected at 100 K shrank back, however the atomic displacement parameter (ADP) of Zn atom was significantly higher than the structure before heating up, meaning that additional disorder on the framework was introduced by the variable temperature experiment. Meanwhile, the ADP of Zn atom at 100 K before heating up is also skeptical, as it should be roughly linear to the ADPs at 300 K and 400 K if it’s a simple temperature-dependent process. While the previous report showed that the solvent inside the pores (DMF) can cause disorder to the framework,²⁴ we hypothesize that the trend is disturbed by the contained solvent.

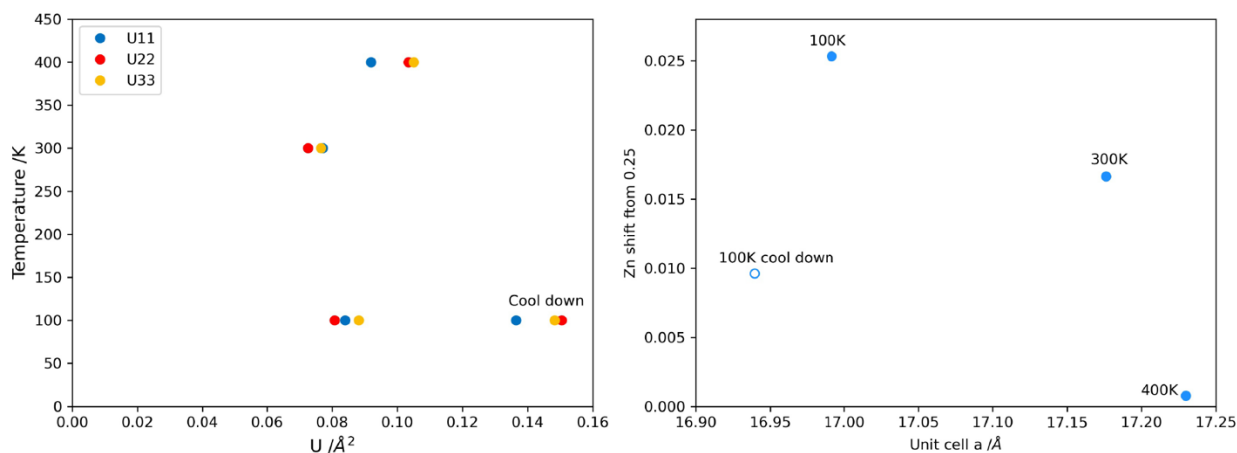


Figure 4.4. The plots of Zn shift vs. unit cell parameter and temperature vs. atomic displacement parameter (ADP) of Zn from the solvated ZIF-90 crystal at different temperatures.

A variable temperature single-crystal X-ray diffraction experiment on an activated crystal was therefore carried out to decouple the possible influence of solvent from the influence of temperature. A crystal of ZIF-90 in methanol was mounted inside a glass capillary, activated to a dynamic vacuum of 2 μmHg followed by the seal of the capillary *in situ*. A series of diffraction data was collected on the crystal in capillary with 50 K interval from 100 K to 500 K, and another cooldown series was collected backward on the same crystal with 100 K interval. Analyses on the crystal structures showed that the maximum residual electron density in each dataset was not higher than $0.1 e/\text{\AA}^3$, indicating the crystal was properly activated.

The structure at 100 K was resolved in space group $I23$ as a merohedral twin, with a pore-opening angle of $79.301(9)^\circ$ (rhombic pore; **Figure 4.6d**) and the Zn–O1 distance of $2.888(2) \text{ \AA}$ (**Figure 4.5**). As the temperature increased to 250 K, both the pore-opening angle and Zn–O1 distance slightly increased to $80.260(9)^\circ$ and $2.898(3)$, respectively. Starting from 300 K, the aldehyde oxygen rotates to its opposite position, with the occupancy of minor oxygen position (O2) increased from $0.022(4)$ to $0.269(12)$ at 400 K. Meanwhile, the Zn–O1 distance and pore-opening angle keep increase until 450 K, where the distance reaches to its maxima of $3.078(6)$. At this distance, the aldehyde oxygen completely loses its coordination from zinc, and as a result, the coordination geometry of zinc changes from pseudo-octahedral geometry to ideal tetrahedral geometry. Accompanied by this change, the space group of the crystal changes to $I-43m$ at 450 K with the disappearance of merohedral twinning. O2 and O1 become symmetry-equivalent in $I-43m$, such that the occupancies of both oxygen positions reach to equal (0.5).



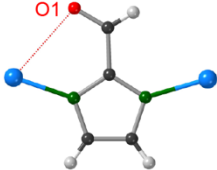
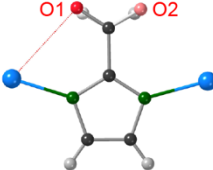

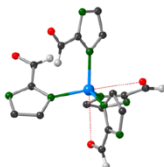
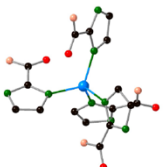
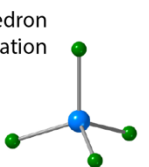
Temperature of Measurement (K)	100	150	200	250	300	350	400	450	500
Space Group	S.G. /23; Merohedral Twin							S.G. /-43m; No Twin	
Shape of Pore Opening	Rhombus 							Square 	
Position of Aldehyde Oxygen									
Oxygen Occupancies	O1 1				O1 0.978(4) O2 0.022(4)			O1 0.5	
Distances	Zn-O1 2.888(2) Zn-O2 2.892(3)				Zn-O1 2.894(3) Zn-O2 2.898(3)			Zn-O1 2.907(3) Zn-O2 2.98(8)	
					Zn-O1 2.935(5) Zn-O2 3.06(3)			Zn-O1 2.993(8) Zn-O2 3.055(17)	
Zn coordination									

Figure 4.5. Summary of the structural change in the variable temperature SXRD series on an activated ZIF-90 crystal.

Quantitative changes in the variable temperature series were further investigated. Specifically, unit cell parameter, Zn shift, the equivalent isotropic atomic displacement parameter of Zn (U_{eq}) and the pore-opening angle were plotted in Figure 6. Among the four plots, it can be clearly observed that the trend can be divided into three regions: from 100 K to 300 K, the data points are in a linear trend; from 300 K to 450 K, the slopes of the correlations are steeper; from 450 K to 500 K, the slopes become smaller. A closer look at the plot of the U_{eq} of Zn against temperature provides more information. The first linear trend shows that the atomic displacement parameter is exclusively related to temperature, indicating there was no disorder introduced by temperature change. The x intercept of this linear trend is not 0, meaning that there was already static disorder existing in the activated crystal at 100 K. Theoretically, the plot should follow the linear trend through all temperatures, however, there is a sharp increase from 300 K to 450 K, indicating the occurrence of a phase transition. The change slows down after 450 K, indicating the phase transition was completed at or before 450 K. The temperature range of phase transition is in accordance with the temperatures that aldehyde rotates, thus indicating the phase transition is driven by the rotation of the aldehyde group. During the cooldown, the structure first went on a different pathway compared to the 400 K structure during heating-up, as all the parameters of two 400 K datasets were rather far from each other. After that, the parameters get closer but not exactly the same, indicating the structure change from 100 K to 300 K is approximately a reversible process.

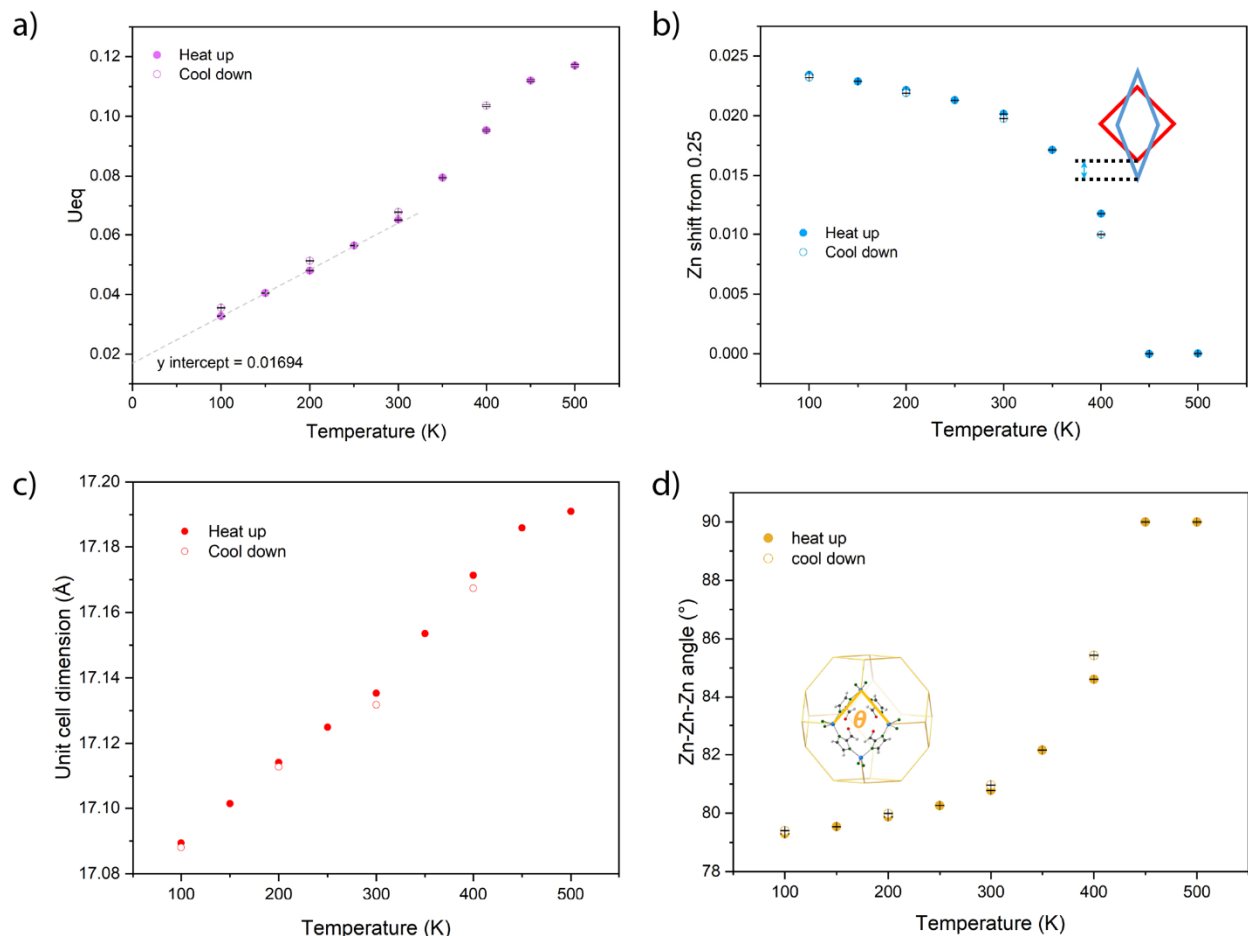


Figure 4.6. Plots of the trends observed in the variable temperature series of the activated ZIF-90 crystal.

4.4. Conclusion

To summarize, firstly, the structural solution of ZIF-90 was revised into space group $I23$ along with the identification of merohedral twinning. The twin law was rigorously analyzed by Bijvoet pair difference analyses and additional measurement at Zn absorption edge, and was confirmed to be diagonal mirror reflection. The prominent feature of the revised structure of ZIF-90 is the distortion from square pore opening in ideal sodalite structures to rhombic pore opening, and the distortion was attributed to the selective coordination of aldehyde oxygen to one of adjacent Zn ions. A dynamic change of the pore opening was observed when increasing temperature from 100 K to 500 K, and this change was driven by the rotation of aldehyde group from one coordinating Zn to another. This phase transition doesn't follow the rules of the most common first-order phase transition that the transition completes at one temperature. Instead, the transition spans in a temperature range around 150 K, starting from a temperature between 250 K and 300 K, and finishing before 450 K. Such transition falls into the common observations of higher order phase transitions. However, the exact order of the phase transition needs to be further determined by the order of heat capacity during phase transition showing in differential scanning calorimetry curve.²⁵ Nevertheless, it is the first time that such displacive phase transition was reported in ZIFs, and the transition driven by the rotational-selective coordination is not reported in any kind of materials.

4.5. Appendices and Notes

4.5.1. SXR D Results of Solvated ZIF-90 Crystals Measured at 100 K

Table 4.2. Crystal data, data collection, and structure refinement parameters for 90AE_1.

Empirical formula	C ₄ H ₃ N ₂ OZn _{0.5}
Formula weight	127.77
Temperature/K	100
Crystal system	cubic
Space group	<i>I</i> 23
a/Å	17.05990(10)
b/Å	17.05990(10)
c/Å	17.05990(10)
α /°	90
β /°	90
γ /°	90
Volume/Å ³	4965.12(9)
Z	24
ρ_{calc} (g/cm ³)	1.026
μ /mm ⁻¹	1.016
F(000)	1536.0
Crystal size/mm ³	0.1 × 0.1 × 0.1
Radiation	synchrotron ($\lambda = 0.61992$ Å)
2 θ range for data collection/°	2.944 to 52.472
Index ranges	-24 ≤ h ≤ 24, -24 ≤ k ≤ 24, -24 ≤ l ≤ 24
Reflections collected	47803
Independent reflections	2521 [R _{int} = 0.0665, R _{sigma} = 0.0244]
Data/restraints/parameters	2521/0/70
Goodness-of-fit on F ²	1.128
Final R indexes [I >= 2 σ (I)]	R ₁ = 0.0366, wR ₂ = 0.0855
Final R indexes [all data]	R ₁ = 0.0375, wR ₂ = 0.0859
Largest diff. peak/hole (e Å ⁻³)	0.68/-0.21

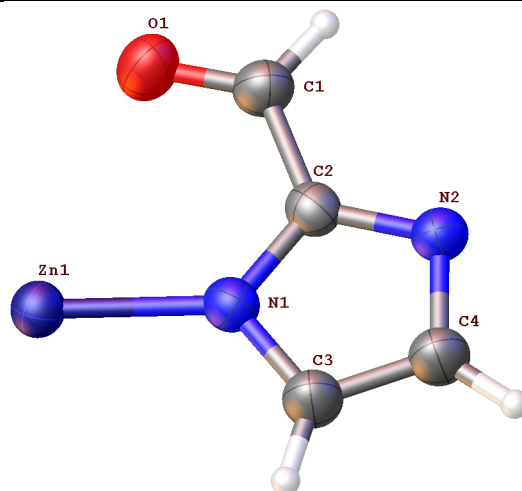


Figure 4.7. Asymmetric unit in the single crystal structure of 90AE_1. Thermal ellipsoids are drawn with 50% probability.

Table 4.3. Crystal data, data collection, and structure refinement parameters for 445_10_02.

Empirical formula	C ₄ H ₃ N ₂ OZn _{0.5}
Formula weight	127.77
Temperature/K	100
Crystal system	cubic
Space group	<i>I</i> 23
<i>a</i> /Å	17.012(2)
<i>b</i> /Å	17.012(2)
<i>c</i> /Å	17.012(2)
α /°	90
β /°	90
γ /°	90
Volume/Å ³	4924(2)
<i>Z</i>	24
ρ_{calc} (g/cm ³)	1.034
μ /mm ⁻¹	1.486
F(000)	1536.0
Crystal size/mm ³	0.4 × 0.3 × 0.3
Radiation	MoK α (λ = 0.71073 Å)
2 Θ range for data collection/°	4.788 to 41.676
Index ranges	-16 ≤ <i>h</i> ≤ 15, -16 ≤ <i>k</i> ≤ 16, -16 ≤ <i>l</i> ≤ 17
Reflections collected	7908
Independent reflections	877 [<i>R</i> _{int} = 0.0482, <i>R</i> _{sigma} = 0.0265]
Data/restraints/parameters	877/45/70
Goodness-of-fit on <i>F</i> ²	1.080
Final <i>R</i> indexes [<i>I</i> ≥ 2 σ (<i>I</i>)]	<i>R</i> ₁ = 0.0422, <i>wR</i> ₂ = 0.1180
Final <i>R</i> indexes [all data]	<i>R</i> ₁ = 0.0473, <i>wR</i> ₂ = 0.1237
Largest diff. peak/hole (e Å ⁻³)	0.15/-0.47

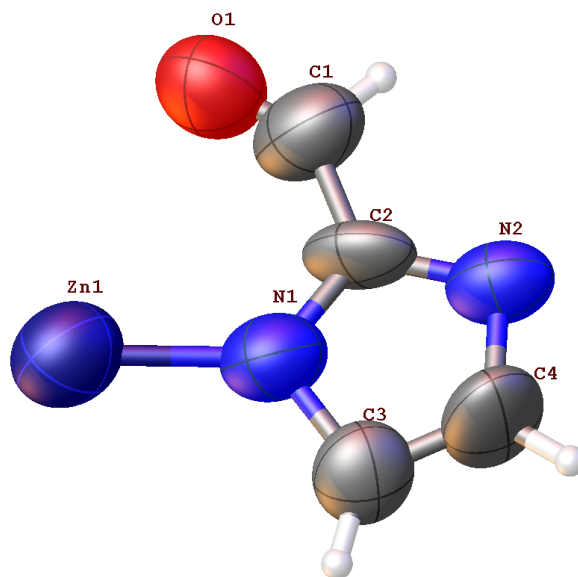
**Figure 4.8.** Asymmetric unit in the single crystal structure of 445_10_02. Thermal ellipsoids are drawn with 50% probability.

Table 4.4. Crystal data, data collection, and structure refinement parameters for 445_10.

Empirical formula	C ₄ H ₃ N ₂ OZn _{0.5}
Formula weight	127.77
Temperature/K	100
Crystal system	cubic
Space group	<i>I</i> 23
<i>a</i> /Å	16.957(2)
<i>b</i> /Å	16.957(2)
<i>c</i> /Å	16.957(2)
α /°	90
β /°	90
γ /°	90
Volume/Å ³	4876(2)
<i>Z</i>	24
ρ_{calc} (g/cm ³)	1.044
μ /mm ⁻¹	1.501
F(000)	1536.0
Crystal size/mm ³	0.4 × 0.36 × 0.35
Radiation	MoK α (λ = 0.71073 Å)
2 Θ range for data collection/°	4.804 to 41.21
Index ranges	-16 ≤ <i>h</i> ≤ 16, -16 ≤ <i>k</i> ≤ 16, -16 ≤ <i>l</i> ≤ 16
Reflections collected	7161
Independent reflections	840 [<i>R</i> _{int} = 0.0394, <i>R</i> _{sigma} = 0.0216]
Data/restraints/parameters	840/0/70
Goodness-of-fit on <i>F</i> ²	1.088
Final <i>R</i> indexes [<i>I</i> ≥ 2 σ (<i>I</i>)]	<i>R</i> ₁ = 0.0398, <i>wR</i> ₂ = 0.1023
Final <i>R</i> indexes [all data]	<i>R</i> ₁ = 0.0455, <i>wR</i> ₂ = 0.1070
Largest diff. peak/hole (e Å ⁻³)	0.14/-0.23

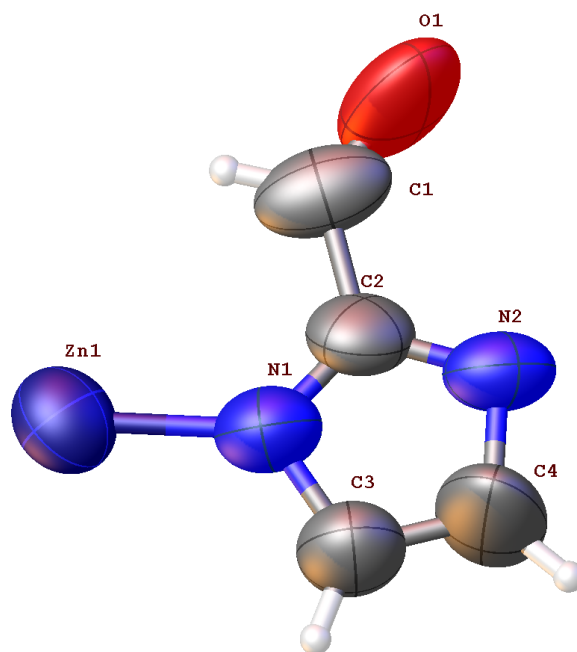
**Figure 4.9.** Asymmetric unit in the single crystal structure of 445_10. Thermal ellipsoids are drawn with 50% probability.

Table 4.5. Crystal data, data collection, and structure refinement parameters for 450_2_02.

Empirical formula	C ₄ H ₃ N ₂ OZn _{0.5}
Formula weight	127.77
Temperature/K	100
Crystal system	cubic
Space group	<i>I</i> 23
<i>a</i> /Å	16.9748(7)
<i>b</i> /Å	16.9748(7)
<i>c</i> /Å	16.9748(7)
α /°	90
β /°	90
γ /°	90
Volume/Å ³	4891.2(6)
<i>Z</i>	24
ρ_{calc} (g/cm ³)	1.041
μ /mm ⁻¹	1.590
F(000)	1536.0
Crystal size/mm ³	0.35 × 0.34 × 0.3
Radiation	Synchrotron ($\lambda = 0.7288$ Å)
2 θ range for data collection/°	3.48 to 46.344
Index ranges	-18 ≤ <i>h</i> ≤ 18, -18 ≤ <i>k</i> ≤ 18, -17 ≤ <i>l</i> ≤ 18
Reflections collected	17600
Independent reflections	1080 [<i>R</i> _{int} = 0.0866, <i>R</i> _{sigma} = 0.0347]
Data/restraints/parameters	1080/0/71
Goodness-of-fit on F ²	1.172
Final <i>R</i> indexes [<i>I</i> ≥ 2 σ (<i>I</i>)]	<i>R</i> ₁ = 0.0657, <i>wR</i> ₂ = 0.1585
Final <i>R</i> indexes [all data]	<i>R</i> ₁ = 0.0666, <i>wR</i> ₂ = 0.1601
Largest diff. peak/hole (e Å ⁻³)	0.27/-0.48

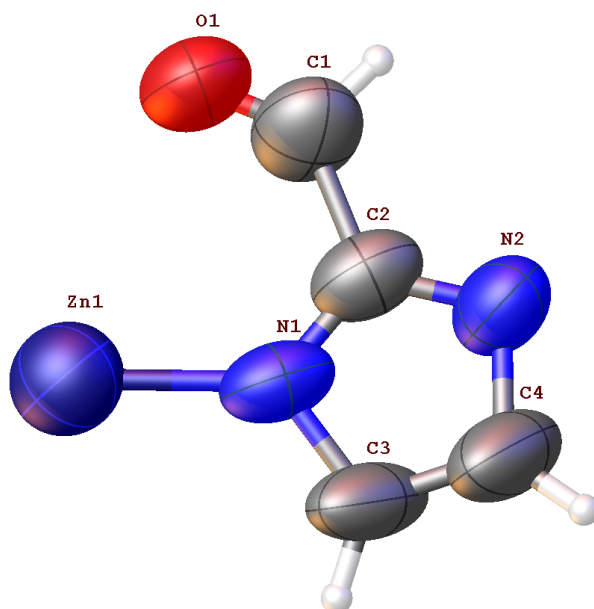
**Figure 4.10.** Asymmetric unit in the single crystal structure of 450_2_02. Thermal ellipsoids are drawn with 50% probability.

Table 4.6. Crystal data, data collection, and structure refinement parameters for 450_2_04.

Empirical formula	C ₄ H ₃ N ₂ OZn _{0.5}
Formula weight	127.77
Temperature/K	100
Crystal system	cubic
Space group	<i>I</i> 23
<i>a</i> /Å	17.0862(6)
<i>b</i> /Å	17.0862(6)
<i>c</i> /Å	17.0862(6)
α /°	90
β /°	90
γ /°	90
Volume/Å ³	4988.1(5)
<i>Z</i>	24
ρ_{calc} (g/cm ³)	1.021
μ /mm ⁻¹	6.344
F(000)	1536.0
Crystal size/mm ³	0.44 × 0.42 × 0.35
Radiation	Synchrotron ($\lambda = 1.2398$ Å)
2 θ range for data collection/°	5.882 to 99.416
Index ranges	-20 ≤ <i>h</i> ≤ 20, -20 ≤ <i>k</i> ≤ 20, -21 ≤ <i>l</i> ≤ 20
Reflections collected	17259
Independent reflections	1629 [R _{int} = 0.0303, R _{sigma} = 0.0138]
Data/restraints/parameters	1629/0/70
Goodness-of-fit on F ²	1.080
Final R indexes [I ≥ 2 σ (I)]	R ₁ = 0.0281, wR ₂ = 0.0773
Final R indexes [all data]	R ₁ = 0.0297, wR ₂ = 0.0789
Largest diff. peak/hole (e Å ⁻³)	0.14/-0.17

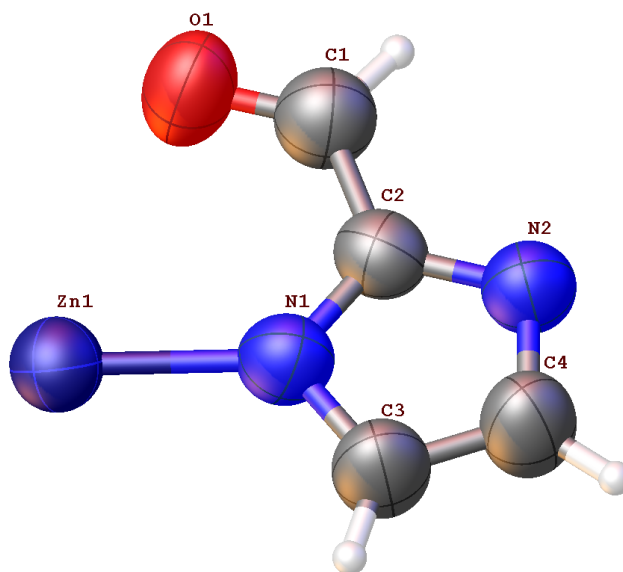
**Figure 4.11.** Asymmetric unit in the single crystal structure of 450_2_04. Thermal ellipsoids are drawn with 50% probability.

Table 4.7. Crystal data, data collection, and structure refinement parameters for 450_2_05.

Empirical formula	C ₄ H ₃ N ₂ OZn _{0.5}
Formula weight	127.77
Temperature/K	100
Crystal system	cubic
Space group	<i>I</i> 23
<i>a</i> /Å	17.0016(8)
<i>b</i> /Å	17.0016(8)
<i>c</i> /Å	17.0016(8)
α /°	90
β /°	90
γ /°	90
Volume/Å ³	4914.4(7)
<i>Z</i>	24
ρ_{calc} (g/cm ³)	1.036
μ /mm ⁻¹	1.583
F(000)	1536.0
Crystal size/mm ³	0.35 × 0.34 × 0.27
Radiation	Synchrotron ($\lambda = 0.7288$ Å)
2 Θ range for data collection/°	3.474 to 47.422
Index ranges	-18 ≤ <i>h</i> ≤ 18, -18 ≤ <i>k</i> ≤ 18, -18 ≤ <i>l</i> ≤ 18
Reflections collected	27961
Independent reflections	1160 [<i>R</i> _{int} = 0.0456, <i>R</i> _{sigma} = 0.0194]
Data/restraints/parameters	1160/0/70
Goodness-of-fit on <i>F</i> ²	1.131
Final <i>R</i> indexes [<i>I</i> ≥ 2 σ (<i>I</i>)]	<i>R</i> ₁ = 0.0438, <i>wR</i> ₂ = 0.1224
Final <i>R</i> indexes [all data]	<i>R</i> ₁ = 0.0449, <i>wR</i> ₂ = 0.1234
Largest diff. peak/hole (e Å ⁻³)	0.18/-0.20

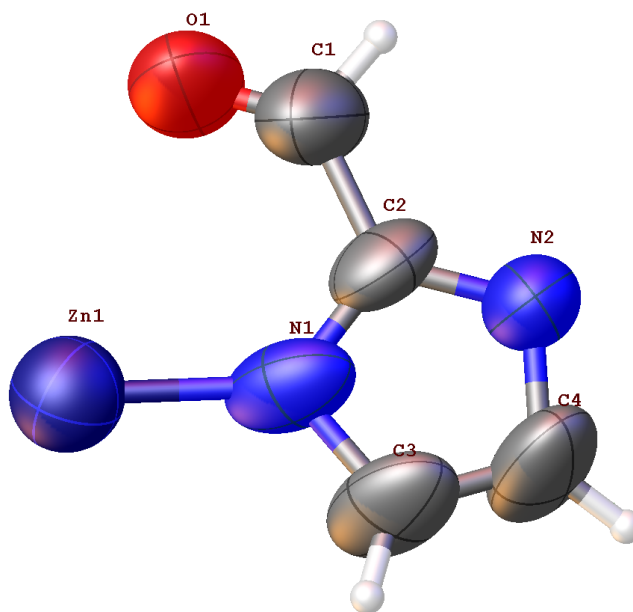
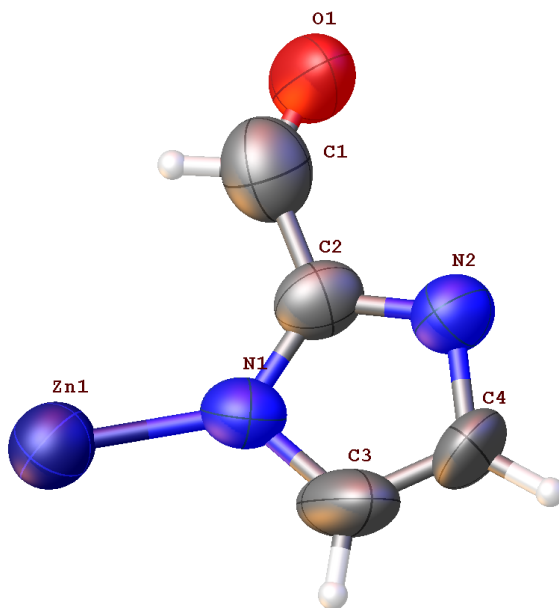
**Figure 4.12.** Asymmetric unit in the single crystal structure of 450_2_05. Thermal ellipsoids are drawn with 50% probability.

Table 4.8. Crystal data, data collection, and structure refinement parameters for 463_150.

Empirical formula	C ₄ H ₃ N ₂ OZn _{0.5}
Formula weight	127.77
Temperature/K	100.00
Crystal system	cubic
Space group	<i>I</i> 23
<i>a</i> /Å	17.0030(6)
<i>b</i> /Å	17.0030(6)
<i>c</i> /Å	17.0030(6)
α /°	90
β /°	90
γ /°	90
Volume/Å ³	4915.6(5)
<i>Z</i>	24
ρ_{calc} (g/cm ³)	1.036
μ /mm ⁻¹	1.489
F(000)	1536.0
Crystal size/mm ³	0.3 × 0.3 × 0.3
Radiation	MoK α (λ = 0.71073 Å)
2 Θ range for data collection/°	4.792 to 49.942
Index ranges	-20 ≤ <i>h</i> ≤ 19, -20 ≤ <i>k</i> ≤ 20, -20 ≤ <i>l</i> ≤ 20
Reflections collected	29358
Independent reflections	1452 [<i>R</i> _{int} = 0.0331, <i>R</i> _{sigma} = 0.0122]
Data/restraints/parameters	1452/0/70
Goodness-of-fit on F ²	1.092
Final <i>R</i> indexes [<i>I</i> ≥ 2 σ (<i>I</i>)]	<i>R</i> ₁ = 0.0572, <i>wR</i> ₂ = 0.1538
Final <i>R</i> indexes [all data]	<i>R</i> ₁ = 0.0589, <i>wR</i> ₂ = 0.1563
Largest diff. peak/hole (e Å ⁻³)	0.65/-0.59

**Figure 4.13.** Asymmetric unit in the single crystal structure of 463_150. Thermal ellipsoids are drawn with 50% probability.

4.5.2. Variable Temperature SXRD Results of Solvated ZIF-90 Crystals

Table 4.9. Crystal data, data collection, and structure refinement parameters for ZIF-90-DMF-VT-100K.

Empirical formula	C ₄ H ₃ N ₂ OZn _{0.5}
Formula weight	127.77
Temperature/K	100
Crystal system	cubic
Space group	<i>I</i> 23
<i>a</i> /Å	16.9915(7)
<i>b</i> /Å	16.9915(7)
<i>c</i> /Å	16.9915(7)
α /°	90
β /°	90
γ /°	90
Volume/Å ³	4905.6(6)
<i>Z</i>	24
ρ_{calc} (g/cm ³)	1.038
μ /mm ⁻¹	1.586
F(000)	1536.0
Crystal size/mm ³	0.4 × 0.39 × 0.37
Radiation	Synchrotron ($\lambda = 0.7288$ Å)
2 θ range for data collection/°	4.916 to 47.452
Index ranges	-18 ≤ <i>h</i> ≤ 18, -18 ≤ <i>k</i> ≤ 18, -18 ≤ <i>l</i> ≤ 18
Reflections collected	38903
Independent reflections	1158 [<i>R</i> _{int} = 0.0926, <i>R</i> _{sigma} = 0.0288]
Data/restraints/parameters	1158/0/70
Goodness-of-fit on F ²	1.114
Final <i>R</i> indexes [<i>I</i> ≥ 2 σ (<i>I</i>)]	<i>R</i> ₁ = 0.0284, <i>wR</i> ₂ = 0.0807
Final <i>R</i> indexes [all data]	<i>R</i> ₁ = 0.0291, <i>wR</i> ₂ = 0.0818
Largest diff. peak/hole (e Å ⁻³)	0.23/-0.24

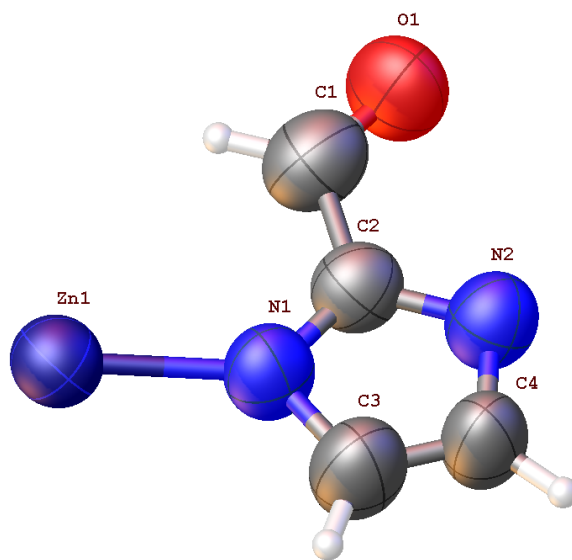


Figure 4.14. Asymmetric unit in the single crystal structure of ZIF-90-DMF-VT-100K. The overlapped atoms (C1 and C1A) mean the same aldehyde carbon separated into two parts to illustrate each aldehyde position. Thermal ellipsoids are drawn with 50% probability.

Table 4.10. Crystal data, data collection, and structure refinement parameters for ZIF-90-DMF-VT-300K.

Empirical formula	C ₄ H ₃ N ₂ OZn _{0.5}
Formula weight	127.77
Temperature/K	300
Crystal system	cubic
Space group	<i>I</i> 23
<i>a</i> /Å	17.1761(5)
<i>b</i> /Å	17.1761(5)
<i>c</i> /Å	17.1761(5)
α /°	90
β /°	90
γ /°	90
Volume/Å ³	5067.3(4)
<i>Z</i>	24
ρ_{calc} (g/cm ³)	1.005
μ /mm ⁻¹	1.535
F(000)	1536.0
Crystal size/mm ³	0.4 × 0.39 × 0.37
Radiation	Synchrotron (λ = 0.7288 Å)
2 Θ range for data collection/°	4.864 to 50.882
Index ranges	-20 ≤ <i>h</i> ≤ 20, -20 ≤ <i>k</i> ≤ 20, -20 ≤ <i>l</i> ≤ 20
Reflections collected	29248
Independent reflections	1467 [<i>R</i> _{int} = 0.0526, <i>R</i> _{sigma} = 0.0187]
Data/restraints/parameters	1467/7/80
Goodness-of-fit on F ²	1.160
Final <i>R</i> indexes [<i>I</i> ≥ 2 σ (<i>I</i>)]	<i>R</i> ₁ = 0.0223, <i>wR</i> ₂ = 0.0647
Final <i>R</i> indexes [all data]	<i>R</i> ₁ = 0.0247, <i>wR</i> ₂ = 0.0666
Largest diff. peak/hole (e Å ⁻³)	0.10/-0.10

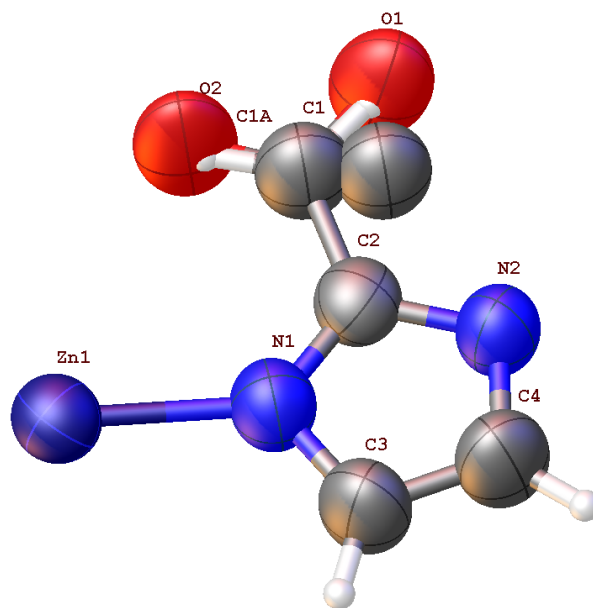
**Figure 4.15.** Asymmetric unit in the single crystal structure of ZIF-90-DMF-VT-300K. The overlapped atoms (C1 and C1A) mean the same aldehyde carbon separated into two parts to illustrate each aldehyde position. Thermal ellipsoids are drawn with 50% probability.

Table 4.11. Crystal data, data collection, and structure refinement parameters for ZIF-90-DMF-VT-400K.

Empirical formula	C ₄ H ₃ N ₂ OZn _{0.5}
Formula weight	127.77
Temperature/K	400
Crystal system	cubic
Space group	<i>I</i> 23
a/Å	17.2298(7)
b/Å	17.2298(7)
c/Å	17.2298(7)
α /°	90
β /°	90
γ /°	90
Volume/Å ³	5114.9(6)
Z	24
ρ_{calc} (g/cm ³)	0.996
μ /mm ⁻¹	1.521
F(000)	1536.0
Crystal size/mm ³	0.4 × 0.39 × 0.37
Radiation	Synchrotron ($\lambda = 0.7288$ Å)
2 Θ range for data collection/°	4.848 to 50.314
Index ranges	-20 ≤ h ≤ 20, -20 ≤ k ≤ 20, -20 ≤ l ≤ 20
Reflections collected	32573
Independent reflections	1423 [R _{int} = 0.0410, R _{sigma} = 0.0150]
Data/restraints/parameters	1423/1/80
Goodness-of-fit on F ²	1.053
Final R indexes [I ≥ 2 σ (I)]	R ₁ = 0.0145, wR ₂ = 0.0372
Final R indexes [all data]	R ₁ = 0.0154, wR ₂ = 0.0377
Largest diff. peak/hole (e Å ⁻³)	0.07/-0.09

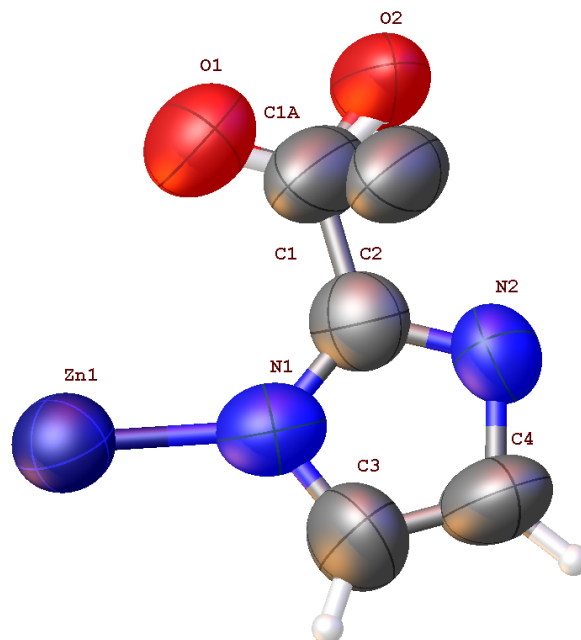
**Figure 4.16.** Asymmetric unit in the single crystal structure of ZIF-90-DMF-VT-400K. The overlapped atoms (C1 and C1A) mean the same aldehyde carbon separated into two parts to illustrate each aldehyde position. Thermal ellipsoids are drawn with 50% probability.

Table 4.12. Crystal data, data collection, and structure refinement parameters for ZIF-90-DMF-VT-100Kcd.

Empirical formula	C ₄ H ₃ N ₂ OZn _{0.5}
Formula weight	127.77
Temperature/K	100
Crystal system	cubic
Space group	<i>I</i> 23
<i>a</i> /Å	16.9395(5)
<i>b</i> /Å	16.9395(5)
<i>c</i> /Å	16.9395(5)
α /°	90
β /°	90
γ /°	90
Volume/Å ³	4860.7(4)
<i>Z</i>	24
ρ_{calc} (g/cm ³)	1.048
μ /mm ⁻¹	1.600
F(000)	1536.0
Crystal size/mm ³	0.4 × 0.39 × 0.37
Radiation	Synchrotron ($\lambda = 0.7288$ Å)
2 Θ range for data collection/°	4.932 to 46.006
Index ranges	-18 ≤ <i>h</i> ≤ 18, -18 ≤ <i>k</i> ≤ 18, -18 ≤ <i>l</i> ≤ 18
Reflections collected	18733
Independent reflections	1056 [<i>R</i> _{int} = 0.0397, <i>R</i> _{sigma} = 0.0187]
Data/restraints/parameters	1056/35/74
Goodness-of-fit on <i>F</i> ²	1.113
Final <i>R</i> indexes [<i>I</i> ≥ 2 σ (<i>I</i>)]	<i>R</i> ₁ = 0.0498, <i>wR</i> ₂ = 0.1378
Final <i>R</i> indexes [all data]	<i>R</i> ₁ = 0.0501, <i>wR</i> ₂ = 0.1385
Largest diff. peak/hole (e Å ⁻³)	0.19/-0.20

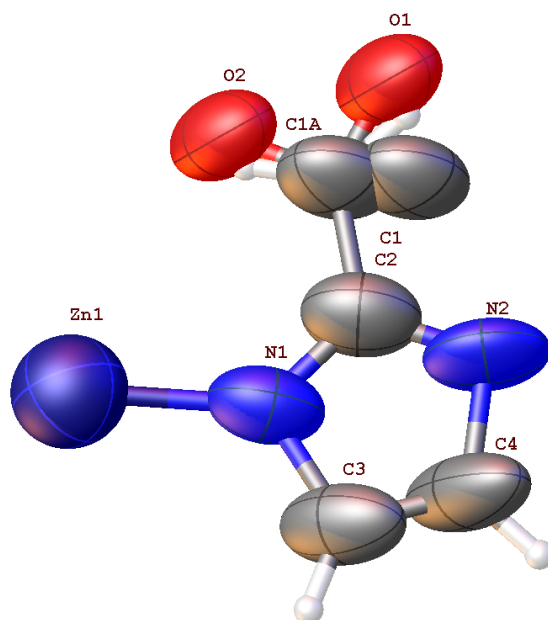


Figure 4.17. Asymmetric unit in the single crystal structure of ZIF-90-DMF-VT-100Kcd. The overlapped atoms (C1 and C1A) mean the same aldehyde carbon separated into two parts to illustrate each aldehyde position. Thermal ellipsoids are drawn with 50% probability.

4.5.3. SXRD Results of Variable Temperature Series of Activated ZIF-90

Table 4.13. Crystal data, data collection, and structure refinement parameters for ZIF-90-VT-100K.

Empirical formula	C ₄ H ₃ N ₂ OZn _{0.5}
Formula weight	127.77
Temperature/K	100
Crystal system	cubic
Space group	<i>I</i> 23
<i>a</i> /Å	17.08940(12)
<i>b</i> /Å	17.08940(12)
<i>c</i> /Å	17.08940(12)
α /°	90
β /°	90
γ /°	90
Volume/Å ³	4990.92(11)
<i>Z</i>	24
ρ_{calc} (g/cm ³)	1.020
μ /mm ⁻¹	1.559
F(000)	1536.0
Crystal size/mm ³	0.300 × 0.300 × 0.300
Radiation	Synchrotron ($\lambda = 0.7288$ Å)
2 θ range for data collection/°	9.152 to 59.768
Index ranges	-21 ≤ <i>h</i> ≤ 21, -21 ≤ <i>k</i> ≤ 20, -18 ≤ <i>l</i> ≤ 19
Reflections collected	14107
Independent reflections	1908 [<i>R</i> _{int} = 0.0283, <i>R</i> _{sigma} = 0.0181]
Data/restraints/parameters	1908/0/70
Goodness-of-fit on F ²	1.195
Final <i>R</i> indexes [<i>I</i> ≥ 2 σ (<i>I</i>)]	<i>R</i> ₁ = 0.0185, <i>wR</i> ₂ = 0.0492
Final <i>R</i> indexes [all data]	<i>R</i> ₁ = 0.0189, <i>wR</i> ₂ = 0.0493
Largest diff. peak/hole / e Å ⁻³	0.17/-0.14

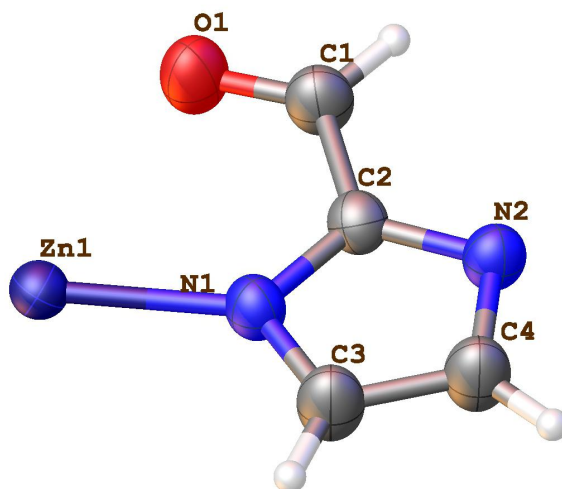


Figure 4.18. Asymmetric unit in the single crystal structure of ZIF-90-VT-100K. Thermal ellipsoids are drawn with 50% probability.

Table 4.14. Crystal data, data collection, and structure refinement parameters for ZIF-90-VT-100Kcd.

Empirical formula	C ₄ H ₃ N ₂ OZn _{0.5}
Formula weight	127.77
Temperature/K	100
Crystal system	cubic
Space group	<i>I</i> 23
<i>a</i> /Å	17.08800(17)
<i>b</i> /Å	17.08800(17)
<i>c</i> /Å	17.08800(17)
α /°	90
β /°	90
γ /°	90
Volume/Å ³	4989.69(15)
<i>Z</i>	24
ρ_{calc} (g/cm ³)	1.020
μ /mm ⁻¹	1.559
F(000)	1536.0
Crystal size/mm ³	0.3 × 0.3 × 0.3
Radiation	Synchrotron ($\lambda = 0.7288$ Å)
2 θ range for data collection/°	9.154 to 59.774
Index ranges	-21 ≤ <i>h</i> ≤ 20, -21 ≤ <i>k</i> ≤ 21, -19 ≤ <i>l</i> ≤ 18
Reflections collected	14556
Independent reflections	1968 [<i>R</i> _{int} = 0.0298, <i>R</i> _{sigma} = 0.0182]
Data/restraints/parameters	1968/0/70
Goodness-of-fit on F ²	1.071
Final <i>R</i> indexes [<i>I</i> ≥ 2 σ (<i>I</i>)]	<i>R</i> ₁ = 0.0194, <i>wR</i> ₂ = 0.0438
Final <i>R</i> indexes [all data]	<i>R</i> ₁ = 0.0208, <i>wR</i> ₂ = 0.0443
Largest diff. peak/hole / e Å ⁻³	0.16/-0.18

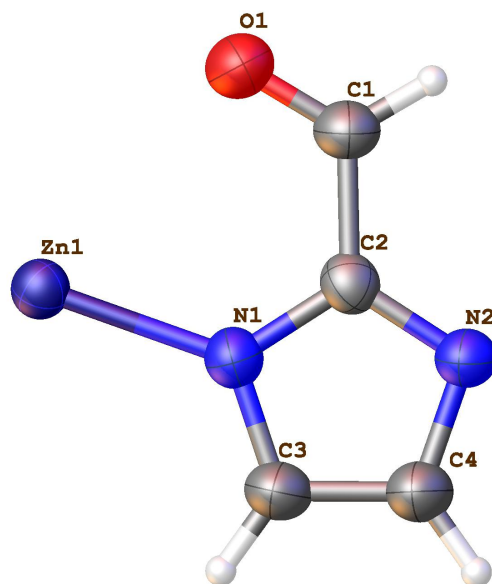
**Figure 4.19.** Asymmetric unit in the single crystal structure of ZIF-90-VT-100Kcd. Thermal ellipsoids are drawn with 50% probability.

Table 4.15. Crystal data, data collection, and structure refinement parameters for ZIF-90-VT-150K.

Empirical formula	C ₄ H ₃ N ₂ OZn _{0.5}
Formula weight	127.77
Temperature/K	150
Crystal system	cubic
Space group	<i>I</i> 23
<i>a</i> /Å	17.10140(12)
<i>b</i> /Å	17.10140(12)
<i>c</i> /Å	17.10140(12)
α /°	90
β /°	90
γ /°	90
Volume/Å ³	5001.44(11)
<i>Z</i>	24
ρ_{calc} (g/cm ³)	1.018
μ /mm ⁻¹	1.555
F(000)	1536.0
Crystal size/mm ³	0.300 × 0.300 × 0.300
Radiation	Synchrotron (λ = 0.7288 Å)
2 θ range for data collection/°	9.146 to 59.722
Index ranges	-19 ≤ <i>h</i> ≤ 18, -21 ≤ <i>k</i> ≤ 21, -21 ≤ <i>l</i> ≤ 20
Reflections collected	14342
Independent reflections	1925 [<i>R</i> _{int} = 0.0291, <i>R</i> _{sigma} = 0.0185]
Data/restraints/parameters	1925/0/70
Goodness-of-fit on F ²	1.154
Final <i>R</i> indexes [<i>I</i> ≥ 2 σ (<i>I</i>)]	<i>R</i> ₁ = 0.0187, <i>wR</i> ₂ = 0.0463
Final <i>R</i> indexes [all data]	<i>R</i> ₁ = 0.0196, <i>wR</i> ₂ = 0.0468
Largest diff. peak/hole / e Å ⁻³	0.12/-0.17

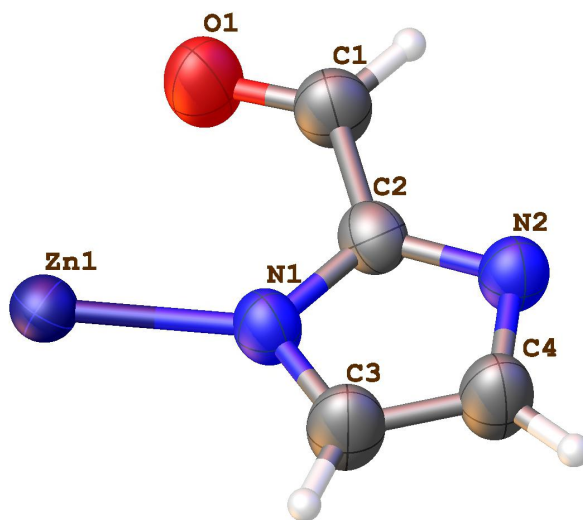
**Figure 4.20.** Asymmetric unit in the single crystal structure of ZIF-90-VT-150K. Thermal ellipsoids are drawn with 50% probability.

Table 4.16. Crystal data, data collection, and structure refinement parameters for ZIF-90-VT-200K.

Empirical formula	C ₄ H ₃ N ₂ OZn _{0.5}
Formula weight	127.77
Temperature/K	200
Crystal system	cubic
Space group	<i>I</i> 23
a/Å	17.11420(12)
b/Å	17.11420(12)
c/Å	17.11420(12)
α /°	90
β /°	90
γ /°	90
Volume/Å ³	5012.68(11)
Z	24
ρ_{calc} (g/cm ³)	1.016
μ /mm ⁻¹	1.552
F(000)	1536.0
Crystal size/mm ³	0.300 × 0.300 × 0.300
Radiation	Synchrotron ($\lambda = 0.7288$ Å)
2 θ range for data collection/°	9.14 to 59.794
Index ranges	-21 ≤ h ≤ 21, -21 ≤ k ≤ 20, -18 ≤ l ≤ 20
Reflections collected	14551
Independent reflections	1942 [R _{int} = 0.0301, R _{sigma} = 0.0181]
Data/restraints/parameters	1942/0/70
Goodness-of-fit on F ²	1.126
Final R indexes [I ≥ 2 σ (I)]	R ₁ = 0.0193, wR ₂ = 0.0472
Final R indexes [all data]	R ₁ = 0.0211, wR ₂ = 0.0478
Largest diff. peak/hole / e Å ⁻³	0.15/-0.17

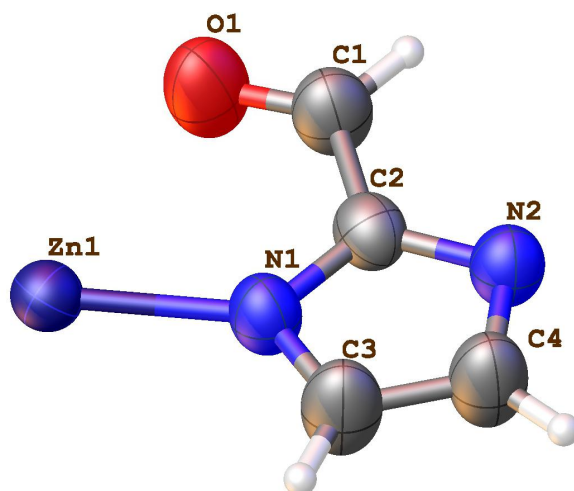
**Figure 4.21.** Asymmetric unit in the single crystal structure of ZIF-90-VT-200K. Thermal ellipsoids are drawn with 50% probability.

Table 4.17. Crystal data, data collection, and structure refinement parameters for ZIF-90-VT-200Kcd.

Empirical formula	C ₄ H ₃ N ₂ OZn _{0.5}
Formula weight	127.77
Temperature/K	200
Crystal system	cubic
Space group	<i>I</i> 23
<i>a</i> /Å	17.11280(17)
<i>b</i> /Å	17.11280(17)
<i>c</i> /Å	17.11280(17)
α /°	90
β /°	90
γ /°	90
Volume/Å ³	5011.45(15)
<i>Z</i>	24
ρ_{calc} (g/cm ³)	1.016
μ /mm ⁻¹	1.552
F(000)	1536.0
Crystal size/mm ³	0.300 × 0.300 × 0.300
Radiation	Synchrotron ($\lambda = 0.7288$ Å)
2 Θ range for data collection/°	9.14 to 57.24
Index ranges	-18 ≤ <i>h</i> ≤ 18, -21 ≤ <i>k</i> ≤ 20, -21 ≤ <i>l</i> ≤ 17
Reflections collected	9721
Independent reflections	1899 [R _{int} = 0.0285, R _{sigma} = 0.0212]
Data/restraints/parameters	1899/0/70
Goodness-of-fit on F ²	1.067
Final R indexes [<i>I</i> ≥ 2 σ (<i>I</i>)]	R ₁ = 0.0203, wR ₂ = 0.0452
Final R indexes [all data]	R ₁ = 0.0229, wR ₂ = 0.0463
Largest diff. peak/hole / e Å ⁻³	0.12/-0.15

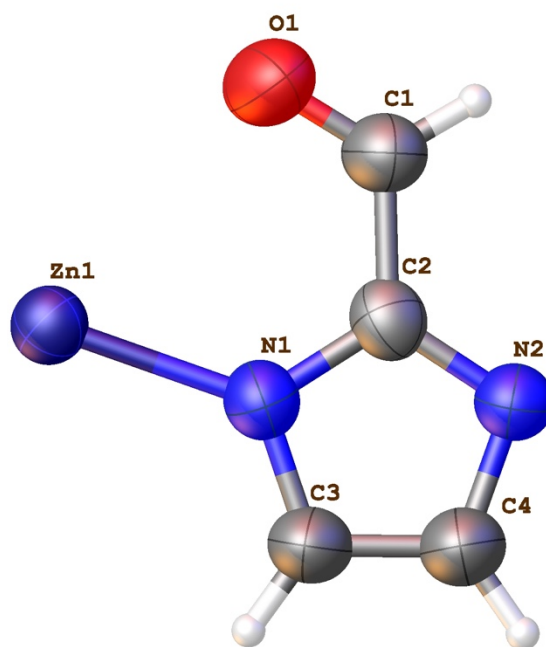
**Figure 4.22.** Asymmetric unit in the single crystal structure of ZIF-90-VT-200Kcd. Thermal ellipsoids are drawn with 50% probability.

Table 4.18. Crystal data, data collection, and structure refinement parameters for ZIF-90-VT-250K.

Empirical formula	C ₄ H ₃ N ₂ OZn _{0.5}
Formula weight	127.77
Temperature/K	250
Crystal system	cubic
Space group	<i>I</i> 23
<i>a</i> /Å	17.12490(10)
<i>b</i> /Å	17.12490(10)
<i>c</i> /Å	17.12490(10)
α /°	90
β /°	90
γ /°	90
Volume/Å ³	5022.09(9)
<i>Z</i>	24
ρ_{calc} (g/cm ³)	1.014
μ /mm ⁻¹	1.549
F(000)	1536.0
Crystal size/mm ³	0.300 × 0.300 × 0.300
Radiation	Synchrotron (λ = 0.7288 Å)
2 θ range for data collection/°	9.134 to 59.752
Index ranges	-21 ≤ <i>h</i> ≤ 20, -21 ≤ <i>k</i> ≤ 21, -20 ≤ <i>l</i> ≤ 19
Reflections collected	14733
Independent reflections	1960 [<i>R</i> _{int} = 0.0315, <i>R</i> _{sigma} = 0.0197]
Data/restraints/parameters	1960/0/70
Goodness-of-fit on F ²	1.091
Final <i>R</i> indexes [<i>I</i> ≥ 2 σ (<i>I</i>)]	<i>R</i> ₁ = 0.0193, <i>wR</i> ₂ = 0.0409
Final <i>R</i> indexes [all data]	<i>R</i> ₁ = 0.0235, <i>wR</i> ₂ = 0.0420
Largest diff. peak/hole / e Å ⁻³	0.11/-0.12

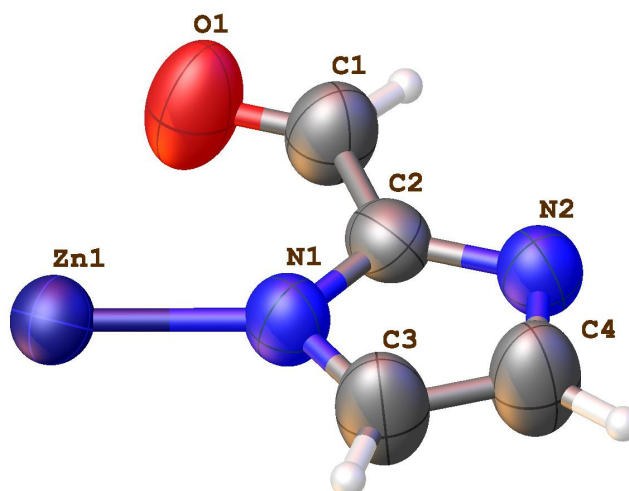
**Figure 4.23.** Asymmetric unit in the single crystal structure of ZIF-90-VT-250K. Thermal ellipsoids are drawn with 50% probability.

Table 4.19. Crystal data, data collection, and structure refinement parameters for ZIF-90-VT-300K.

Empirical formula	C ₄ H ₃ N ₂ OZn _{0.5}
Formula weight	127.77
Temperature/K	300
Crystal system	cubic
Space group	<i>I</i> 23
<i>a</i> /Å	17.13530(17)
<i>b</i> /Å	17.13530(17)
<i>c</i> /Å	17.13530(17)
α /°	90
β /°	90
γ /°	90
Volume/Å ³	5031.24(15)
<i>Z</i>	24
ρ_{calc} (g/cm ³)	1.012
μ /mm ⁻¹	1.546
F(000)	1536.0
Crystal size/mm ³	0.300 × 0.300 × 0.300
Radiation	Synchrotron (λ = 0.7288 Å)
2 θ range for data collection/°	9.128 to 56.414
Index ranges	-20 ≤ <i>h</i> ≤ 21, -18 ≤ <i>k</i> ≤ 19, -21 ≤ <i>l</i> ≤ 21
Reflections collected	14670
Independent reflections	1843 [<i>R</i> _{int} = 0.0336, <i>R</i> _{sigma} = 0.0184]
Data/restraints/parameters	1843/7/75
Goodness-of-fit on F ²	1.074
Final <i>R</i> indexes [<i>I</i> >= 2 σ (<i>I</i>)]	<i>R</i> ₁ = 0.0196, <i>wR</i> ₂ = 0.0463
Final <i>R</i> indexes [all data]	<i>R</i> ₁ = 0.0229, <i>wR</i> ₂ = 0.0476
Largest diff. peak/hole / e Å ⁻³	0.11/-0.11

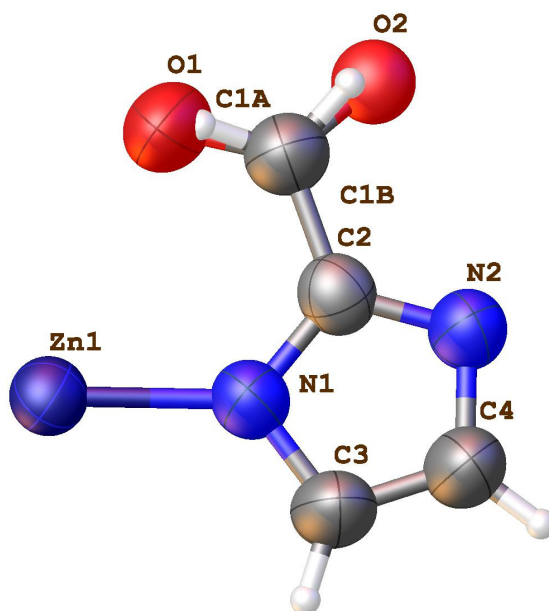
**Figure 4.24.** Asymmetric unit in the single crystal structure of ZIF-90-VT-300K. Thermal ellipsoids are drawn with 50% probability.

Table 4.20. Crystal data, data collection, and structure refinement parameters for ZIF-90-VT-300Kcd.

Empirical formula	C ₄ H ₃ N ₂ OZn _{0.5}
Formula weight	127.77
Temperature/K	300
Crystal system	cubic
Space group	<i>I</i> 23
<i>a</i> /Å	17.13180(17)
<i>b</i> /Å	17.13180(17)
<i>c</i> /Å	17.13180(17)
α /°	90
β /°	90
γ /°	90
Volume/Å ³	5028.16(15)
<i>Z</i>	24
ρ_{calc} (g/cm ³)	1.013
μ /mm ⁻¹	1.547
F(000)	1536.0
Crystal size/mm ³	0.300 × 0.300 × 0.300
Radiation	Synchrotron (λ = 0.7288 Å)
2 θ range for data collection/°	9.13 to 55.678
Index ranges	-18 ≤ <i>h</i> ≤ 19, -21 ≤ <i>k</i> ≤ 21, -20 ≤ <i>l</i> ≤ 21
Reflections collected	14815
Independent reflections	1817 [<i>R</i> _{int} = 0.0370, <i>R</i> _{sigma} = 0.0200]
Data/restraints/parameters	1817/0/70
Goodness-of-fit on F ²	1.056
Final <i>R</i> indexes [<i>I</i> ≥ 2 σ (<i>I</i>)]	<i>R</i> ₁ = 0.0216, <i>wR</i> ₂ = 0.0512
Final <i>R</i> indexes [all data]	<i>R</i> ₁ = 0.0269, <i>wR</i> ₂ = 0.0530
Largest diff. peak/hole / e Å ⁻³	0.13/-0.09

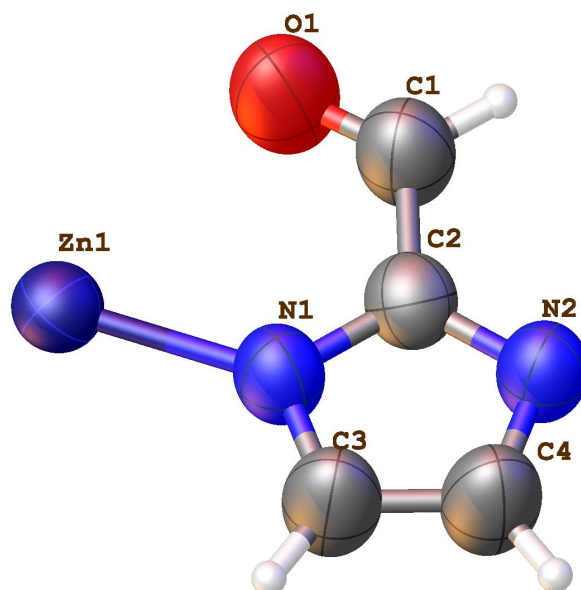
**Figure 4.25.** Asymmetric unit in the single crystal structure of ZIF-90-VT-300Kcd. Thermal ellipsoids are drawn with 50% probability.

Table 4.21. Crystal data, data collection, and structure refinement parameters for ZIF-90-VT-350K.

Empirical formula	C ₄ H ₃ N ₂ OZn _{0.5}
Formula weight	127.77
Temperature/K	350
Crystal system	cubic
Space group	<i>I</i> 23
<i>a</i> /Å	17.15350(17)
<i>b</i> /Å	17.15350(17)
<i>c</i> /Å	17.15350(17)
α /°	90
β /°	90
γ /°	90
Volume/Å ³	5047.29(15)
<i>Z</i>	24
ρ_{calc} (g/cm ³)	1.009
μ /mm ⁻¹	1.541
F(000)	1536.0
Crystal size/mm ³	0.300 × 0.300 × 0.300
Radiation	Synchrotron (λ = 0.7288 Å)
2 θ range for data collection/°	9.118 to 52.534
Index ranges	-19 ≤ <i>h</i> ≤ 20, -18 ≤ <i>k</i> ≤ 18, -20 ≤ <i>l</i> ≤ 20
Reflections collected	13741
Independent reflections	1538 [<i>R</i> _{int} = 0.0361, <i>R</i> _{sigma} = 0.0189]
Data/restraints/parameters	1538/7/80
Goodness-of-fit on F ²	1.077
Final <i>R</i> indexes [<i>I</i> >= 2 σ (<i>I</i>)]	<i>R</i> ₁ = 0.0195, <i>wR</i> ₂ = 0.0462
Final <i>R</i> indexes [all data]	<i>R</i> ₁ = 0.0216, <i>wR</i> ₂ = 0.0470
Largest diff. peak/hole / e Å ⁻³	0.09/-0.10

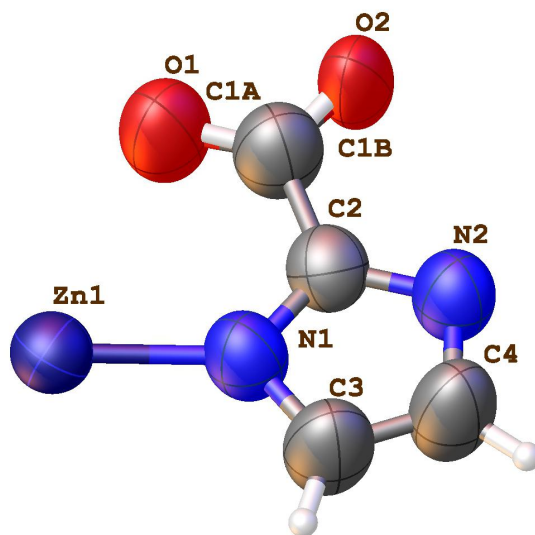
**Figure 4.26.** Asymmetric unit in the single crystal structure of ZIF-90-VT-350K. Thermal ellipsoids are drawn with 50% probability.

Table 4.22. Crystal data, data collection, and structure refinement parameters for ZIF-90-VT-400K.

Empirical formula	C ₄ H ₃ N ₂ OZn _{0.5}
Formula weight	127.77
Temperature/K	400
Crystal system	cubic
Space group	<i>I</i> 23
<i>a</i> /Å	17.1713(2)
<i>b</i> /Å	17.1713(2)
<i>c</i> /Å	17.1713(2)
α /°	90
β /°	90
γ /°	90
Volume/Å ³	5063.0(2)
<i>Z</i>	24
ρ_{calc} (g/cm ³)	1.006
μ /mm ⁻¹	1.536
F(000)	1536.0
Crystal size/mm ³	0.300 × 0.300 × 0.300
Radiation	Synchrotron (λ = 0.7288 Å)
2 θ range for data collection/°	9.108 to 49.96
Index ranges	-19 ≤ <i>h</i> ≤ 19, -18 ≤ <i>k</i> ≤ 18, -18 ≤ <i>l</i> ≤ 19
Reflections collected	10687
Independent reflections	1327 [R _{int} = 0.0379, R _{sigma} = 0.0198]
Data/restraints/parameters	1327/6/80
Goodness-of-fit on F ²	1.104
Final R indexes [<i>I</i> ≥ 2 σ (<i>I</i>)]	R ₁ = 0.0213, wR ₂ = 0.0533
Final R indexes [all data]	R ₁ = 0.0241, wR ₂ = 0.0547
Largest diff. peak/hole / e Å ⁻³	0.10/-0.15

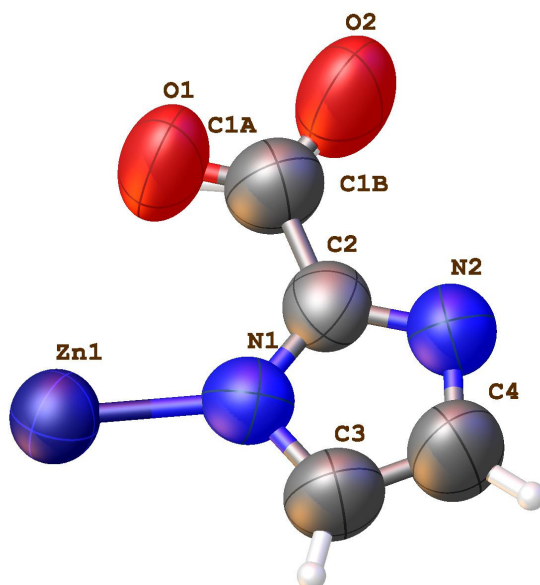
**Figure 4.27.** Asymmetric unit in the single crystal structure of ZIF-90-VT-400K. Thermal ellipsoids are drawn with 50% probability.

Table 4.23. Crystal data, data collection, and structure refinement parameters for ZIF-90-VT-400Kcd.

Empirical formula	C ₄ H ₃ N ₂ OZn _{0.5}
Formula weight	127.77
Temperature/K	400
Crystal system	cubic
Space group	<i>I</i> 23
<i>a</i> /Å	17.1674(2)
<i>b</i> /Å	17.1674(2)
<i>c</i> /Å	17.1674(2)
α /°	90
β /°	90
γ /°	90
Volume/Å ³	5059.6(2)
<i>Z</i>	24
ρ_{calc} (g/cm ³)	1.006
μ /mm ⁻¹	1.537
F(000)	1536.0
Crystal size/mm ³	0.300 × 0.300 × 0.300
Radiation	Synchrotron ($\lambda = 0.7288$ Å)
2 Θ range for data collection/°	9.11 to 48.472
Index ranges	-18 ≤ <i>h</i> ≤ 18, -19 ≤ <i>k</i> ≤ 19, -17 ≤ <i>l</i> ≤ 19
Reflections collected	12171
Independent reflections	1241 [<i>R</i> _{int} = 0.0438, <i>R</i> _{sigma} = 0.0235]
Data/restraints/parameters	1241/0/80
Goodness-of-fit on F ²	1.131
Final <i>R</i> indexes [<i>I</i> ≥ 2 σ (<i>I</i>)]	<i>R</i> ₁ = 0.0216, <i>wR</i> ₂ = 0.0476
Final <i>R</i> indexes [all data]	<i>R</i> ₁ = 0.0245, <i>wR</i> ₂ = 0.0487
Largest diff. peak/hole / e Å ⁻³	0.05/-0.07

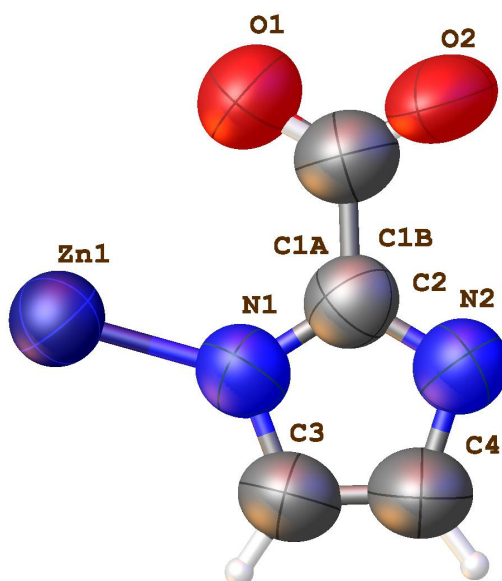
**Figure 4.28.** Asymmetric unit in the single crystal structure of ZIF-90-VT-400Kcd. Thermal ellipsoids are drawn with 50% probability.

Table 4.24. Crystal data, data collection, and structure refinement parameters for ZIF-90-VT-450K.

Empirical formula	C ₂ HNO _{0.5} Zn _{0.25}
Formula weight	63.38
Temperature/K	450
Crystal system	cubic
Space group	<i>I</i> -43m
a/Å	17.1860(2)
b/Å	17.1860(2)
c/Å	17.1860(2)
α /°	90
β /°	90
γ /°	90
Volume/Å ³	5076.0(2)
Z	48
ρ_{calc} (g/cm ³)	0.995
μ /mm ⁻¹	1.532
F(000)	1512.0
Crystal size/mm ³	0.300 × 0.300 × 0.300
Radiation	Synchrotron ($\lambda = 0.7288$ Å)
2 Θ range for data collection/°	9.1 to 47.862
Index ranges	-17 ≤ h ≤ 19, -18 ≤ k ≤ 18, -19 ≤ l ≤ 19
Reflections collected	11912
Independent reflections	684 [R _{int} = 0.0371, R _{sigma} = 0.0138]
Data/restraints/parameters	684/0/42
Goodness-of-fit on F ²	1.073
Final R indexes [I ≥ 2 σ (I)]	R ₁ = 0.0218, wR ₂ = 0.0568
Final R indexes [all data]	R ₁ = 0.0230, wR ₂ = 0.0578
Largest diff. peak/hole / e Å ⁻³	0.06/-0.06

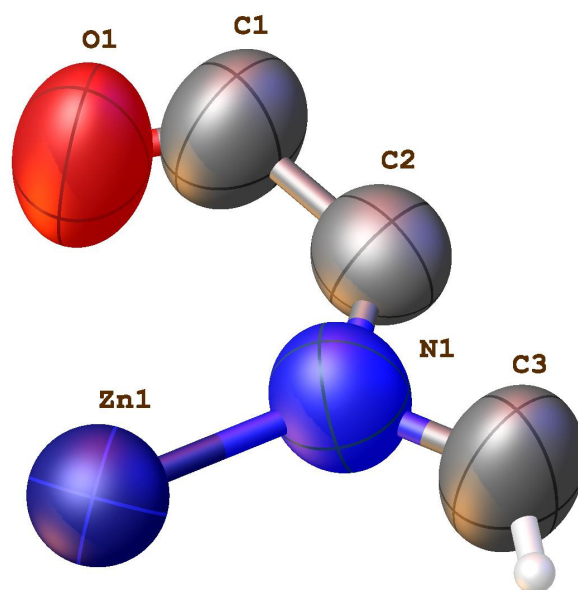
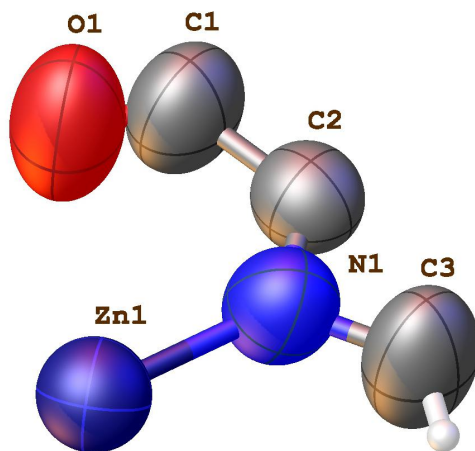
**Figure 4.29.** Asymmetric unit in the single crystal structure of ZIF-90-VT-450K. Thermal ellipsoids are drawn with 50% probability.

Table 4.25. Crystal data, data collection, and structure refinement parameters for ZIF-90-VT-500K.

Empirical formula	C ₂ HNO _{0.5} Zn _{0.25}
Formula weight	63.38
Temperature/K	500
Crystal system	cubic
Space group	<i>I</i> -43m
<i>a</i> /Å	17.1910(2)
<i>b</i> /Å	17.1910(2)
<i>c</i> /Å	17.1910(2)
α /°	90
β /°	90
γ /°	90
Volume/Å ³	5080.46(18)
<i>Z</i>	48
ρ_{calc} (g/cm ³)	0.994
μ /mm ⁻¹	1.531
F(000)	1512.0
Crystal size/mm ³	0.300 × 0.300 × 0.300
Radiation	Synchrotron (λ = 0.7288 Å)
2 θ range for data collection/°	9.098 to 46.158
Index ranges	-18 ≤ <i>h</i> ≤ 18, -18 ≤ <i>k</i> ≤ 18, -17 ≤ <i>l</i> ≤ 18
Reflections collected	10948
Independent reflections	621 [R _{int} = 0.0349, R _{sigma} = 0.0128]
Data/restraints/parameters	621/0/42
Goodness-of-fit on F ²	1.054
Final R indexes [<i>I</i> ≥ 2 σ (<i>I</i>)]	R ₁ = 0.0209, wR ₂ = 0.0578
Final R indexes [all data]	R ₁ = 0.0213, wR ₂ = 0.0583
Largest diff. peak/hole / e Å ⁻³	0.07/-0.06

**Figure 4.30.** Asymmetric unit in the single crystal structure of ZIF-90-VT-500K. Thermal ellipsoids are drawn with 50% probability.

4.6. Bibliography

- (1) Smith, J. V.; Blackwell, C. S. Nuclear Magnetic Resonance of Silica Polymorphs. *Nature* **1983**, *303* (5914), 223–225.
- (2) Park, K. S.; Ni, Z.; Côté, A. P.; Choi, J. Y.; Huang, R.; Uribe-Romo, F. J.; Chae, H. K.; O’Keeffe, M.; Yaghi, O. M. Exceptional Chemical and Thermal Stability of Zeolitic Imidazolate Frameworks. *Proc. Natl. Acad. Sci. U. S. A.* **2006**, *103* (27), 10186–10191.
- (3) Atlas of Prospective Zeolite Structures. <http://www.hypotheticalzeolites.net>. (accessed 2021-09-27).
- (4) Banerjee, R.; Phan, A.; Wang, B.; Knobler, C.; Furukawa, H.; O’Keeffe, M.; Yaghi, O. M. High-Throughput Synthesis of Zeolitic Imidazolate Frameworks and Application to CO₂ Capture. *Science* **2008**, *319* (5865), 939–943.
- (5) Depmeier, W. Tilt and Tetrahedra Distortions in the Zeolite A Framework. *Acta Crystallogr., Sect. B: Struct. Sci.* **1985**, *41* (2), 101–108.
- (6) Armbruster, T.; Gunter, M. E. Crystal Structures of Natural Zeolites. *Rev. Mineral. Geochem.* **2001**, *45* (1), 1–67.
- (7) Bish, D. L.; Wang, H.-W. Phase Transitions in Natural Zeolites and the Importance of P H₂O. *Philos. Mag.* **2010**, *90* (17–18), 2425–2441.
- (8) Dove, M. T. Review: Theory of Displacive Phase Transitions in Minerals. *Am. Mineral.* **1997**, *82* (3–4), 213–244.
- (9) Corbin, D. R.; Abrams, L.; Jones, G. A.; Eddy, M. M.; Stucky, G. D.; Cox, D. E. Flexibility of the Zeolite Rho Framework. Neutron Powder Structural Characterization of Ca-Exchanged Zeolite Rho. *J. Chem. Soc. Chem. Commun.* **1989**, *0* (1), 42–43.
- (10) Ryder, M. R.; Civalleri, B.; Bennett, T. D.; Henke, S.; Rudić, S.; Cinque, G.; Fernandez-Alonso, F.; Tan, J.-C. Identifying the Role of Terahertz Vibrations in Metal-Organic Frameworks: From Gate-Opening Phenomenon to Shear-Driven Structural Destabilization. *Phys. Rev. Lett.* **2014**, *113* (21), 215502.
- (11) Bennett, T. D.; Goodwin, A. L.; Dove, M. T.; Keen, D. A.; Tucker, M. G.; Barney, E. R.; Soper, A. K.; Bithell, E. G.; Tan, J.-C.; Cheetham, A. K. Structure and Properties of an Amorphous Metal-Organic Framework. *Phys. Rev. Lett.* **2010**, *104* (11), 115503.
- (12) Bennett, T. D.; Cheetham, A. K. Amorphous Metal–Organic Frameworks. *Acc. Chem. Res.* **2014**, *47* (5), 1555–1562.
- (13) Gaillac, R.; Pullumbi, P.; Beyer, K. A.; Chapman, K. W.; Keen, D. A.; Bennett, T. D.; Coudert, F.-X. Liquid Metal–Organic Frameworks. *Nat. Mater.* **2017**, *16* (11), 1149–1154.
- (14) Morris, W.; Doonan, C. J.; Furukawa, H.; Banerjee, R.; Yaghi, O. M. Crystals as Molecules: Postsynthesis Covalent Functionalization of Zeolitic Imidazolate Frameworks. *J. Am. Chem. Soc.* **2008**, *130* (38), 12626–12627.
- (15) Bruker. *APEX3, Version 8.38*; Bruker AXS Inc.: Madison, WI, USA, 2018.
- (16) Bruker. *SAINTE*; Bruker AXS Inc.: Madison, WI, USA, 2012.
- (17) Bruker. *SADABS, Version 2014/4*; Bruker AXS Inc.: Madison, WI, USA, 2014.

- (18) Sheldrick, G. M. A Short History of SHELX. *Acta Crystallogr., Sect. A: Found. Crystallogr.* **2008**, *64* (1), 112–122.
- (19) Sheldrick, G. M. Crystal Structure Refinement with SHELXL. *Acta Crystallogr., Sect. C: Struct. Chem.* **2015**, *71* (1), 3–8.
- (20) Dolomanov, O. V.; Bourhis, L. J.; Gildea, R. J.; Howard, J. A. K.; Puschmann, H. OLEX2: A Complete Structure Solution, Refinement and Analysis Program. *J. Appl. Crystallogr.* **2009**, *42* (2), 339–341.
- (21) Spek, A. L. PLATON SQUEEZE: A Tool for the Calculation of the Disordered Solvent Contribution to the Calculated Structure Factors. *Acta Crystallogr., Sect. C: Struct. Chem.* **2015**, *71* (1), 9–18.
- (22) Koch, E. Twinning by Merohedry. In *International Tables for Crystallography*; Prince, E., **2006**; Vol. C, pp 12–14.
- (23) Hooft, R. W. W.; Straver, L. H.; Spek, A. L. Determination of Absolute Structure Using Bayesian Statistics on Bijvoet Differences. *J. Appl. Crystallogr.* **2008**, *41* (1), 96–103.
- (24) Lee, S.; Bürgi, H.-B.; Alshimmri, S. A.; Yaghi, O. M. Impact of Disordered Guest–Framework Interactions on the Crystallography of Metal–Organic Frameworks. *J. Am. Chem. Soc.* **2018**, *140* (28), 8958–8964.
- (25) Blundell, S. J.; Blundell, K. M. Classification of Phase Transitions. In *Concepts in Thermal Physics*; Oxford University Press Inc.: New York, USA, **2006**; pp 320–322.

Chapter 5.
Synthesis and Characterization Toward a Woven Covalent Organic
Framework

5.1. Introduction

Topological entanglement in chemical compounds is of interest to chemists for decades.¹ Starting from 1960s, the development of such compounds focuses on catenanes,² rotaxanes,³ and molecular knots,⁴⁻⁶ which are all molecular species with finite dimensions. Polyrotaxanes are infinite chain of rotaxanes in one dimension,⁷ however, their synthetic method is based on polymer chemistry which makes them difficult to form higher dimensions of topological entanglements. In 2015, our group introduced a reticular chemistry approach toward three-dimensionally covalent-organic framework (COF) composed of woven threads (**Figure 5.1a, c**),⁸ which shed light on strategies toward topologically entangled structures (interlocking and interpenetration) in higher dimensions.⁹ Following that, in 2018, one-dimensional ribbons that are topologically interlocked in three dimensions was reported (**Figure 5.1b, d**),¹⁰ proving the feasibility of the strategy for a broader scope of structures.

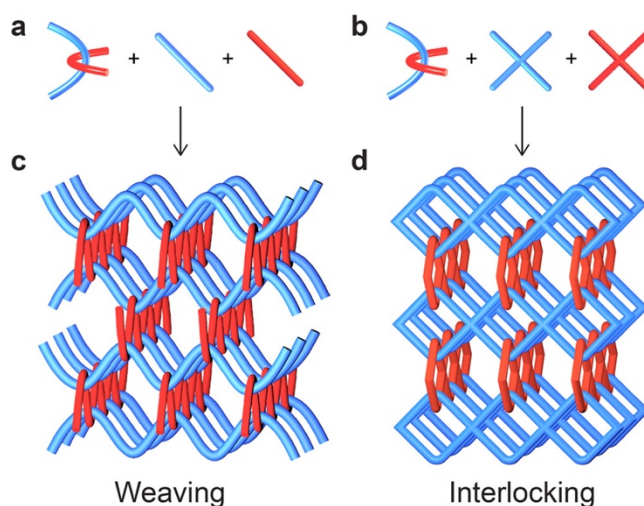


Figure 5.1. Illustration on how reticular chemistry approach builds mechanically or topologically entangled structures starting from pre-assembled molecular crossing. Reproduced with permission (American Chemical Society, 2019).¹⁰

Among the interlocking structures, those formed by rings are of particular interest, as they are of highest degree of freedom compared to those formed by one-dimensional or two-dimensional interlocking units. Such structures, sometimes referred as polycatenanes, are highly synthetically challenging. Though one-dimensional polycatenanes with finite and infinite number of catenations has been reported,¹¹⁻¹³ two dimensional polycatenanes are even rare as the catenation is difficult to control if stitches ring by ring.¹⁴

Herein, we provide a reticular chemistry approach toward a structure of two-dimensional interlocking rings, or to say, a two-dimensional polycatenane network. The structure is retrosynthetically deconstructed into the same periodically repeating entanglement units and the linkers connecting in between (**Figure 5.2**). Thus, the forward synthetic route is to first synthesize a woven COF from a pre-entangled molecular complex whose geometries are fixed by coordination of metal ions, and ditopic linkers. Afterwards, the desired interlocking ring structure will be obtained upon the removal of templating metal ions. The synthesis of the complex with designed entanglement is feasible because its topology of entanglement is identical to a molecular knot reported by Leigh *et al.* in 2017.¹⁵ By modifying the terminating group of the knot into aldehyde groups (**Scheme 5.2**), the thus obtained complex can be linked with diamine linkers *via* imine condensation reaction, which is well-developed in COF chemistry.

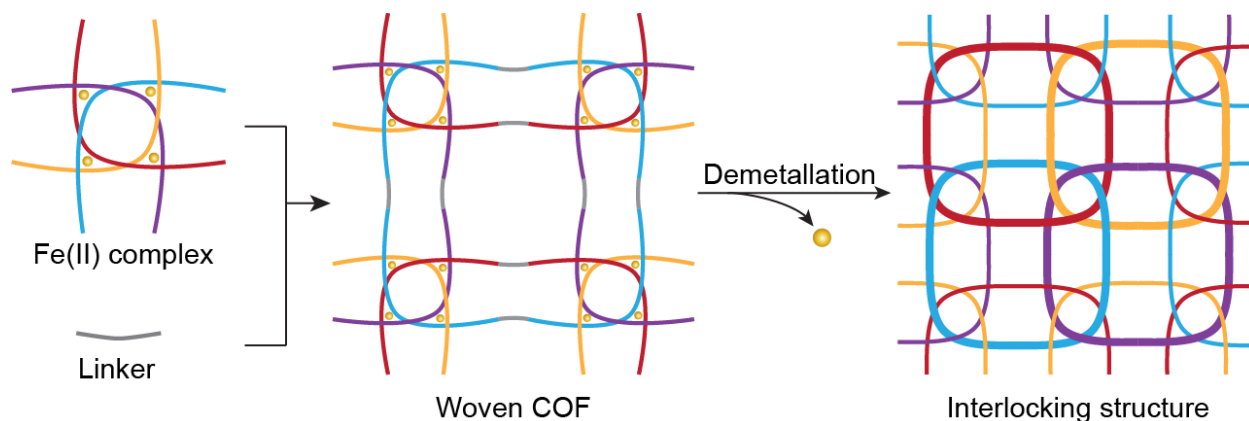


Figure 5.2. Design of the structure composed 2D interlocking rings *via* a reticular chemistry approach.

5.2. Experimental

5.2.1. Materials and Methods

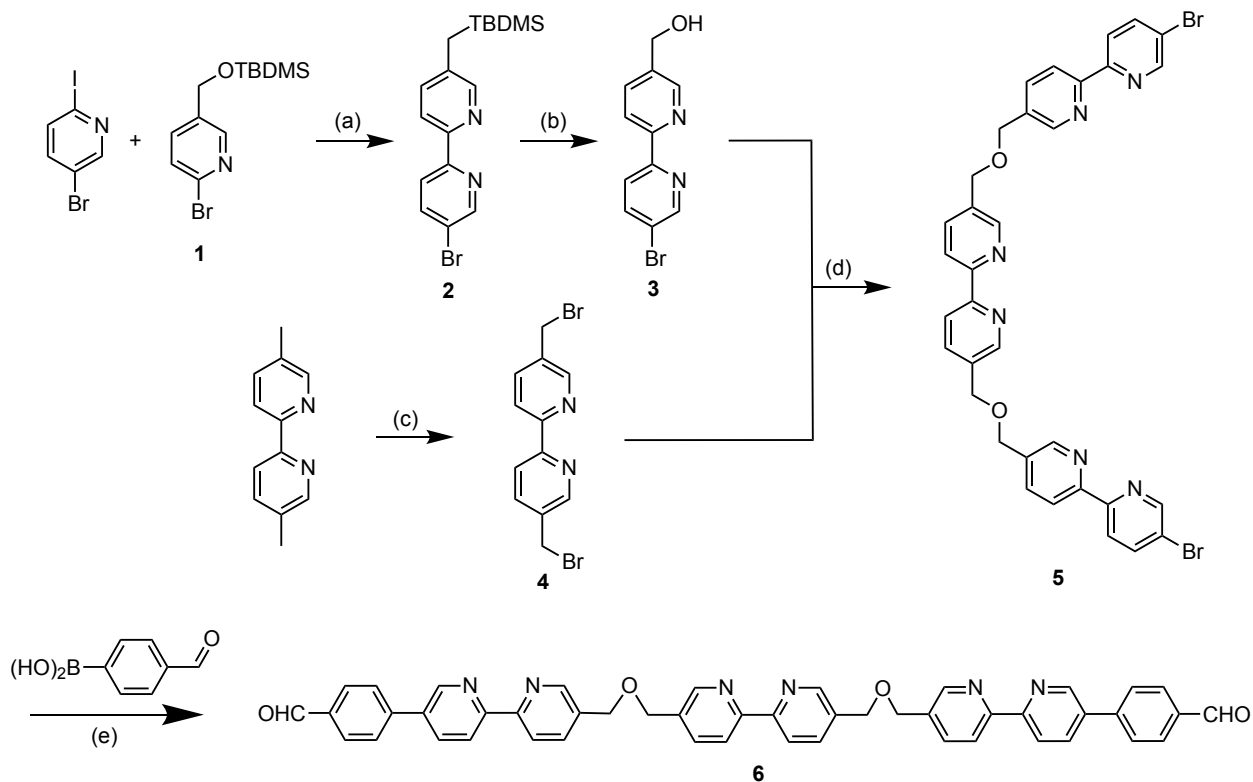
5-bromo-2-iodopyridine, benzene-1,4-diamine, benzidine, *tert*-butyllithium (1.7 M in pentane), Pd(PPh₃)₄, Tetrabutylammonium fluoride solution (1.0 M in THF), CCl₄, NaH (60% dispersion in mineral oil), and CsF were purchased from Sigma-Aldrich. Cyclohexane-1,4-diamine was purchased from TCI America. (6-bromopyridin-3-yl)methanol, (*E*)-1,2-bis(4-bromophenyl)ethene, (4-aminophenyl)boronic acid, and (4-formylphenyl)boronic acid were purchased from AK Scientific. Anhydrous ZnCl₂, KPF₆, K₂CO₃, *tert*-butylchlorodimethylsilane (TBDMS-Cl), N-bromosuccinimide (NBS), and Azobisisobutyronitrile (AIBN) were purchased from Fisher Scientific. THF, dioxane, toluene and ethanol are HPLC grade solvents purified in an Inert® solvent purification system PureSolv MD7.

¹H nuclear magnetic resonance (NMR) spectra were collected on a Bruker Avance III 600 and a Bruker AVANCE NEO 500 spectrometers. Attenuated total reflectance Fourier-transform infrared spectroscopy (ATR-FT-IR) was performed on a Bruker ALPHA Platinum ATR- FT-IR spectrometer equipped with a single reflection diamond ATR module in ambient atmosphere. Powder X-ray diffraction measurements were performed on a Rigaku MiniFlex diffractometer in Bragg-Brentano geometry with CuK α source ($\lambda = 1.54178 \text{ \AA}$). Single-crystal X-ray diffraction was collected at beamlines 12.2.1 at the Advanced Light Source equipped with a Bruker D8 diffractometer, a Bruker PHOTON-II CPAD detector, and the Oxford Cryosystem 800.

Structure of the proposed woven COF was modeled in Materials Studio.¹⁶ The structure of the complex was taken and modified from the single-crystal structure of the previous reported molecular knot. The linkers and linkages between the complexes were drawn by the provided structure sketch tool. Geometries of the sketched woven COF and unit cell of the modeled crystal structure were optimized by Forcite module, during which the iron-tris(bipyridine) units and their linked ether bonds were kept as rigid groups. Universal force field and smart algorithm were selected for the optimization. The models were obtained after the optimizations converged.

5.2.2. Syntheses and Characterizations

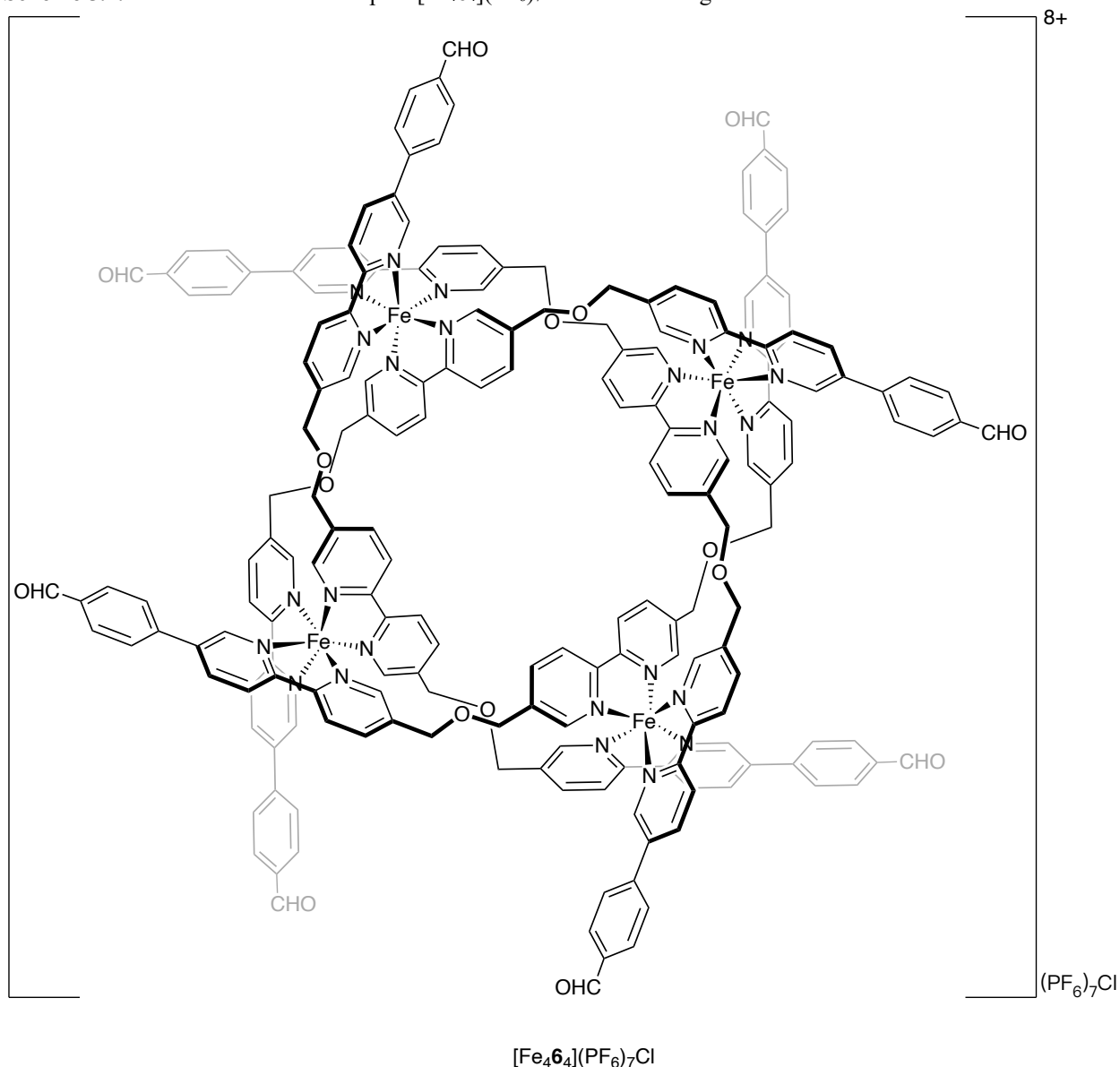
Scheme 5.1. Synthetic procedure of the ligand of Fe₄ complex. The compounds **1** – **5** were synthesized based on a previous report.



Synthesis of compound 6

Compound **5** (710 mg, 1 mmol), (4-formylphenyl)boronic acid (600 mg, 4 mmol, 4 equiv.) and CsF (1 g, 6.6 mmol, 6.6 equiv.) were added to a mixture of 30 mL anhydrous dioxane and 20 mL anhydrous ethanol. The solution was bubbled with nitrogen for 15 minutes, followed by the addition of 100 mg Pd(PPh₃)₄ (0.08 mmol). The reaction was stirred and heated at 75 °C for 24 hours. The suspension was subjected to air-free filtration setup and washed with mixtures of N₂ purged mixture of dioxane and ethanol (v/v = 3:2) for 5 times. The obtained white solid was redispersed in 50 mL methanol and refluxed for 24 hours, and this procedure was repeated twice to yield 656 mg (86 %) of white solids. ¹H NMR [500 MHz, CF₃COOD : Chloroform-*d* = 1:5 (v/v)] δ 10.07 (s, 1H), 9.16 (d, *J* = 2.2 Hz, 1H), 9.01 (d, *J* = 3.9 Hz, 2H), 8.63 (d, *J* = 8.4 Hz, 1H), 8.57 – 8.49 (m, 3H), 8.44 (t, *J* = 6.8 Hz, 2H), 8.20 (dd, *J* = 8.4, 1.7 Hz, 2H), 7.95 – 7.89 (m, 2H), 5.03 (s, 4H).

Scheme 5.2. Structure of the iron complex $[\text{Fe}_4\mathbf{6}_4](\text{PF}_6)_7\text{Cl}$ as the building unit of the woven COF.



Synthesis of $[\text{Fe}_4\mathbf{6}_4](\text{PF}_6)_7\text{Cl}$

50.0 mg FeCl_2 and 300.1 mg of **6** were added to a 200 mL pressure tube followed by the addition of 50 mL of anhydrous DMF under argon atmosphere. The pressure tube was sealed, the mixture was stirred and heated at 140 °C for 3 days. After the reaction cooled to room temperature, 150 mL of saturated KPF_6 in methanol was added. The mixture was stirred for 1 hour, filtrated on celite, and the purple solid was washed with 10 mL water for 3 times. The solids on celite were transferred into a Soxhlet extractor and extracted by acetone for 24 hours. The obtained solution was concentrated to ~ 5 mL and was added 5 mL of hexanes. The pink-purple powder was dried to yield 215 mg (49%) of product.

Single crystal of $[\text{Fe}_4\mathbf{6}_4](\text{BPh}_4)_7\text{Cl}$: the as-synthesized 50 mL DMF solution of the complex was added 1 gram of NaBPh_4 . The solid was filtered off, and additional 50 mg of NaBPh_4 was added.

The solution was kept for three months until plate-like crystals formed at the bottom of the container.

Synthesis of (*E*)-4',4'''-(ethene-1,2-diyl)bis([1,1'-biphenyl]-4-amine) (EDDBA)

(*E*)-1,2-bis(4-bromophenyl)ethene (1 g, 3.0 mmol), (4-aminophenyl)boronic acid (2 g, 14.6 mmol, 4.9 equiv.), K₂CO₃ (2.1 g, 15.2 mmol, 5.14 equiv.) and a mixed solvent of toluene/ethanol/water (180 mL, 5:1:1) were charged into a 250 mL round-bottom flask. The mixture was purged with N₂ for 20 minutes, followed by the addition of Pd(PPh₃)₄ (400 mg, 0.35 mmol, 0.11 equiv.). The reaction was stirred and refluxed for 18 hours. After cooling to room temperature, all solvents were removed by rotary evaporation. The resulting solid was washed with methanol, water and methanol/acetone mixture (v/v = 10:1) to give the product as a pale brown solid (0.86 g, 58%). ¹H NMR (400 MHz, DMSO-*d*₆): δ 7.58 (q, *J* = 8.3 Hz, 8H), 7.41 (d, *J* = 8.5 Hz, 4H), 7.23 (s, 2H), 6.64 (d, *J* = 8.5 Hz, 4H), 5.27 (s, 4H). ¹³C NMR (151 MHz, DMSO-*d*₆): δ 148.48, 139.65, 134.58, 131.57, 127.21, 126.96, 126.84, 125.38, 114.22.

Synthetic trials of COF

[Fe₄6₄](PF₆)₇Cl complex, diamine linker, solvent and acid catalyst were charged into a glass tube (OD = 10 mm, ID = 8 mm) of 15 cm long. The mixture went through freeze-pump-thaw cycle for one time, then the glass tube was flame-sealed and shorten to 12 cm. The tubes were place in isothermal ovens for three days. The obtained product was washed with DMF for three times *via* centrifuge, then washed in Soxhlet with acetone overnight followed by drying under vacuum. The specific choices of the parameters during synthetic screening are listed in **Table 5.1**.

Table 5.1. Choices of parameters in synthetic condition screenings.

[Fe ₄ 6 ₄](PF ₆) ₇ Cl	Diamine linker	Solvent (0.5 mL)	Catalyst (50 μL)	Temperature
1.34 mmol	4 equiv.	Dioxane	6M HAc(aq)	120 °C
2.08 mmol	6 equiv.	Dioxane : mesitylene = 1:1	3M HAc(aq)	150 °C
	8 equiv.	Dichlorobenzene : <i>n</i> -butanol = 1:1		180 °C

5.3. Results and Discussions

The complex, upon formation, has the molecular formula of [Fe₄6₄]Cl₈ because the only anion presented in the reaction media was chloride. The further precipitation of the complex with KPF₆ solution, theoretically, exchanged all anions in the final product into PF₆⁻. However, electrospray ionization mass spectrometry (ESI-MS) spectrum of the complex dissolved in methanol showed a series of *m/z* signals around 1295.8 (**Figure 5.6**), which was attributed to {[Fe₄6₄](PF₆)₄Cl}³⁺, indicating the existence of unexchanged chloride in the product. Single-crystal structure measurement of the crystallized product confirmed formation of the desired complex; furthermore, a preferred binding of chloride was observed also in the single-crystal structure of the complex, where a chloride anion was observed at the center of the that the complex contains chloride (**Figure 5.10**). Eight aromatic C–H bonds point to the chloride, indicating that the preferred binding could be attributed to a high number of C–H⋯Cl interactions. Based on the evidences above, the formula of the synthesized complex was determined to be [Fe₄6₄](PF₆)₇Cl.

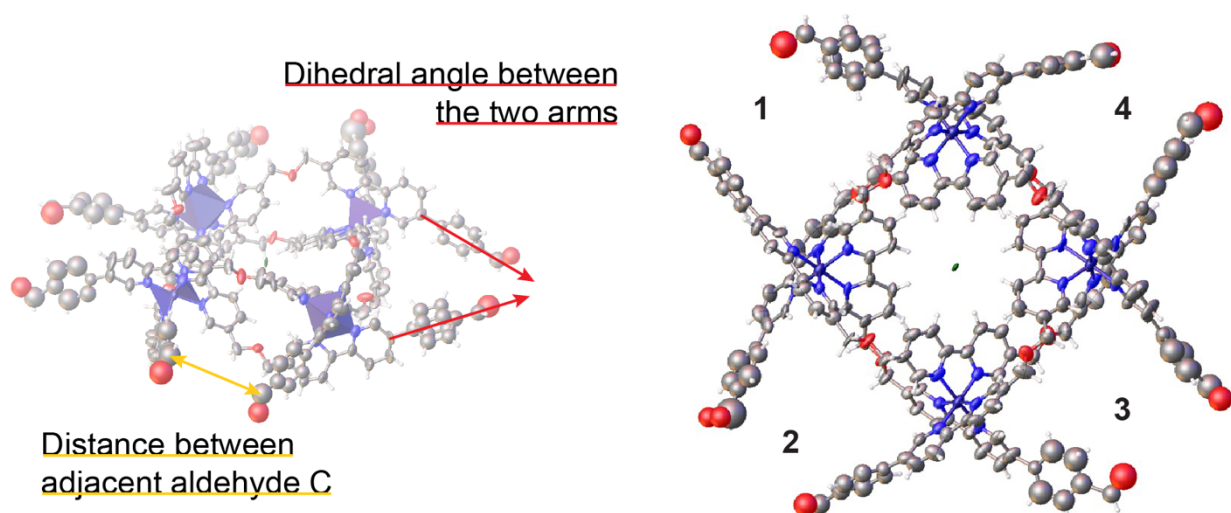


Figure 5.3. Illustration on the geometric parameters being analyzed (left) and the observed aldehyde pairs (right). Color code: Fe, dark purple; Cl, dark green; O, red; N, purple; C, gray; B, yellow; H, white. Thermal ellipsoids are shown with 50% probability.

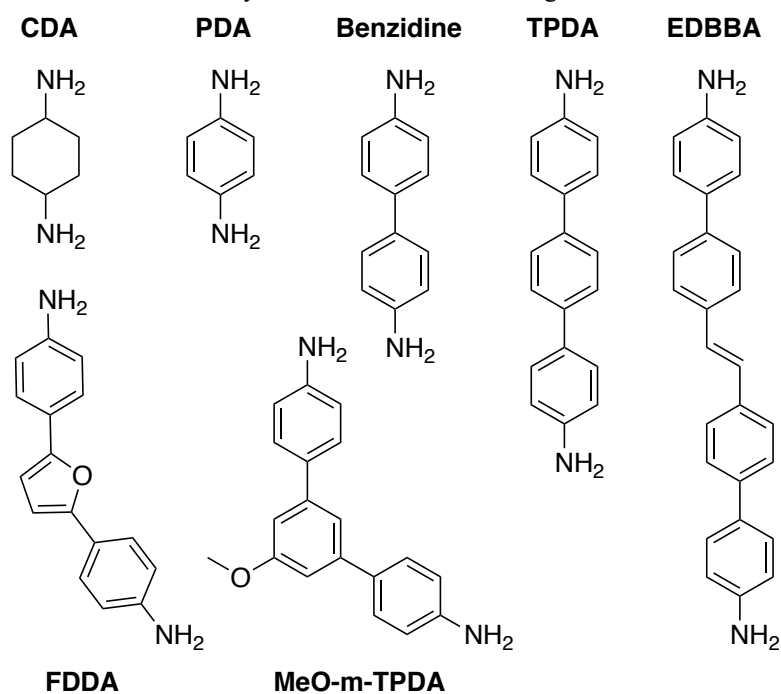
The highest possible point group among all possible conformations of the complex is 4 (Schönflies: D_4), and such conformation was found in the similar molecular knot which crystallized in a tetragonal space group $I4/m$. However, the complex synthesized in this work, $\{[\text{Fe}_4\mathbf{6}_4]\text{Cl}\}^{7+}$, was reported in space group $P-1$. The complex didn't exhibit a local symmetry higher than 1 (Schönflies: C_1). This gives a chance to observe the degrees of freedom that possibly cause the deviation of structure from its ideal geometry. A quick look at the crystal structure of $\{[\text{Fe}_4\mathbf{6}_4]\text{Cl}\}^{7+}$ shows that the terminating 4-formylphenyl groups has a significant labile motion (**Figure 5.3**). The distance between pairs of aldehyde carbons on the same side of square ranges from 6.65 Å to 8.84 Å (**Table 5.2**), indicating the bending motion of 4-formylphenyl groups in the square plane. Furthermore, the 4-formylphenyl groups bend out of plane, causing changes to the dihedral angles between the adjacent two (**Table 5.2**).

Table 5.2. Distances between the adjacent pairs of aldehyde carbons, and the dihedral angles between pairs of phenylaldehyde arms. Illustrations corresponding to the listed geometric parameters are in **Figure 5.3**.

Pair of aldehydes	1	2	3	4
C···C distance (Å)	8.84(4)	7.38(9)	8.12(5)	6.65(7)
Dihedral angle (°)	37.8(5)	41.1(9)	34.3(5)	30.6(6)

The dihedral angles of around 35° bring challenge to the formation of COF. The design of COFs usually favors building units with canonical geometries of organic species such as regular cubes, regular tetrahedrons, equilateral triangles and straight lines. Such geometries, like tiles, are likely to form periodic structures with least strains, so that the structures are prone to be thermodynamically preferred. In the case of the designed 2D interlocking COF, one needs to connect two square tiles in an in-plane fashion, but the connection points bend $17.5^\circ (= 35^\circ/2)$ out of plane. A bent two-end connector will be desired; however, the bending angle of the connector needs to be $180^\circ - 35^\circ = 145^\circ$, which is not common in organic compounds.

Scheme 5.3. Ditopic amine linkers used in synthetic trials toward the targeted COF.



Luckily, the 4-formylphenyl group demonstrated its flexibility of motion. Therefore, it is reasonable to screen the diamine linkers as the second building unit in the COF synthesis other than the complex $[\text{Fe}_4\text{6}_4](\text{PF}_6)_7\text{Cl}$ with aldehyde groups. The linkers with different length, bending angles, and flexibilities were selected (**Scheme 5.3**): cyclohexane-1,4-diamine (CDA), benzene-1,4-diamine (BDA), benzidine, [1,1':4',1''-terphenyl]-4,4''-diamine (TPDA), (*E*)-4',4'''-(ethene-1,2-diyl)bis([1,1'-biphenyl]-4-amine) (EDBBA), 4,4'-(furan-2,5-diyl)dianiline (FDDA), and 5'-methoxy-[1,1':3',1''-terphenyl]-4,4''-diamine (MeO-*m*-TPDA). Generally, the longer the linker, the better it allows strains in structures. A C=C double bond was additionally introduced into the EDBBA, which is expected to increase its possible conformations and help the formation of COF.

Synthetic screenings were performed for each of the selected diamine linker. Eventually, compound **7** that was synthesized from the complex and EDBBA was obtained (**Figure 5.4**). The IR spectrum of **7** (**Figure 5.5d**) showed the diminish of the IR signal corresponding to the stretch of aldehyde C=O group, indicating the successful reaction between $[\text{Fe}_4\text{6}_4](\text{PF}_6)_7\text{Cl}$ and EDDBA.¹⁷ The signal corresponding to imine –C=N– stretching vibration at $\sim 1616\text{ cm}^{-1}$ is not significant, and it might be attributed to the reason that the imine stretching signal is submerged under the signals from aromatic C=N stretch in 2,2'-bipyridyl ligands.¹⁸

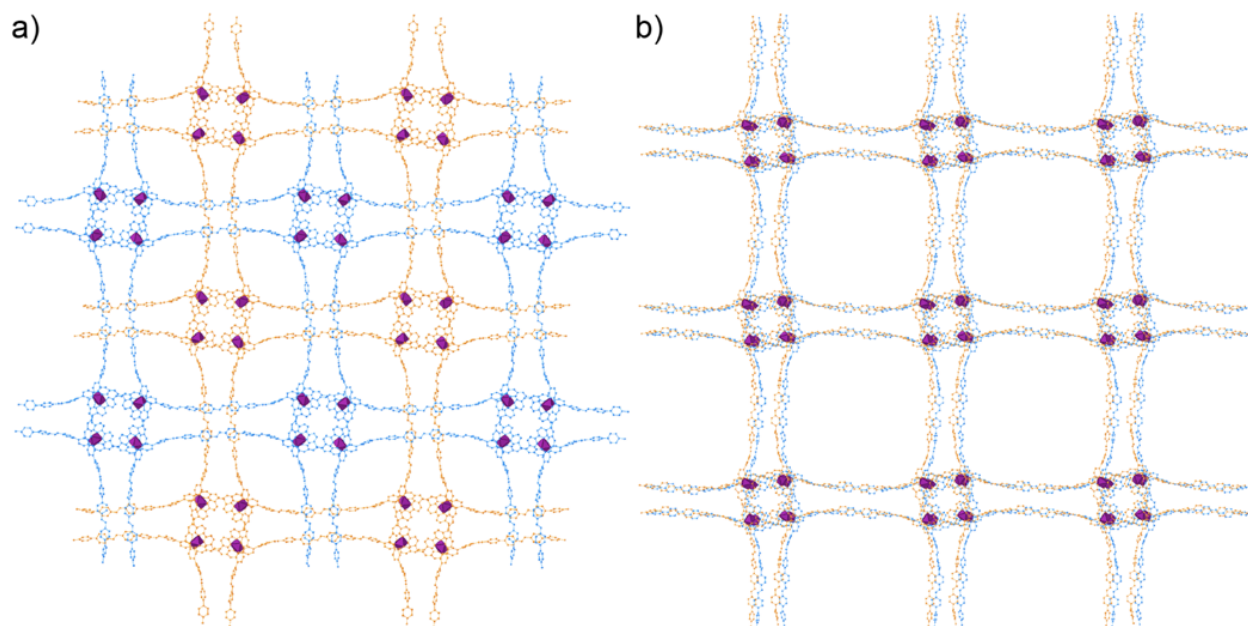


Figure 5.4. Synthesis of compound **7**, and the proposed eclipsed (a) and staggered (b) model of **7**. Two layers of COFs are shown in each figure and are colored as blue and yellow respectively. The purple polyhedral illustrates the iron coordination octahedra.

Two structural models were built for the expected woven COF between $[\text{Fe}_4\mathbf{6}_4](\text{PF}_6)_7\text{Cl}$ and EDBBA that differs by the stacking mode of adjacent 2D layers, eclipsed and staggered (**Figure 5.4**). The powder X-ray diffraction (PXRD) patterns of the two models have been simulated and compared with the measured PXRD pattern of **7** (**Figure 5.5a**). The diffractions at $2\theta = 2.45^\circ$ and 3.46° match with the predicted PXRD patterns of both models (**Figure 5.5b**). However, it is not possible to definitively assign the structure of **7** to a specific model because the first diffraction at 1.74° from the eclipsed model is not in the allowed 2θ range of an in-house powder X-ray diffractometer. Other diffractions observed in the PXRD of **7** were found to be identical to a part of the PXRD pattern of a reaction product between $[\text{Fe}_4\mathbf{6}_4](\text{PF}_6)_7\text{Cl}$ and 4,4',4'',4'''-(ethene-1,1,2,2-tetrayl)tetraaniline (**Figure 5.5c**), indicating these signals are only related to the common reactants of the two products (*i.e.*, $[\text{Fe}_4\mathbf{6}_4](\text{PF}_6)_7\text{Cl}$ and acetic acid). Interestingly, the compound **7** was washed thoroughly with common organic solvents before the PXRD measurement, which should have washed away $[\text{Fe}_4\mathbf{6}_4](\text{PF}_6)_7\text{Cl}$ if there was any left. Therefore, it is concluded that the current reaction yields an insoluble side product that is a derivative of $[\text{Fe}_4\mathbf{6}_4](\text{PF}_6)_7\text{Cl}$. The synthetic condition of **7** needs to be optimized to have the formation of **7** surpasses side reactions and to improve the crystallinity of **7**.

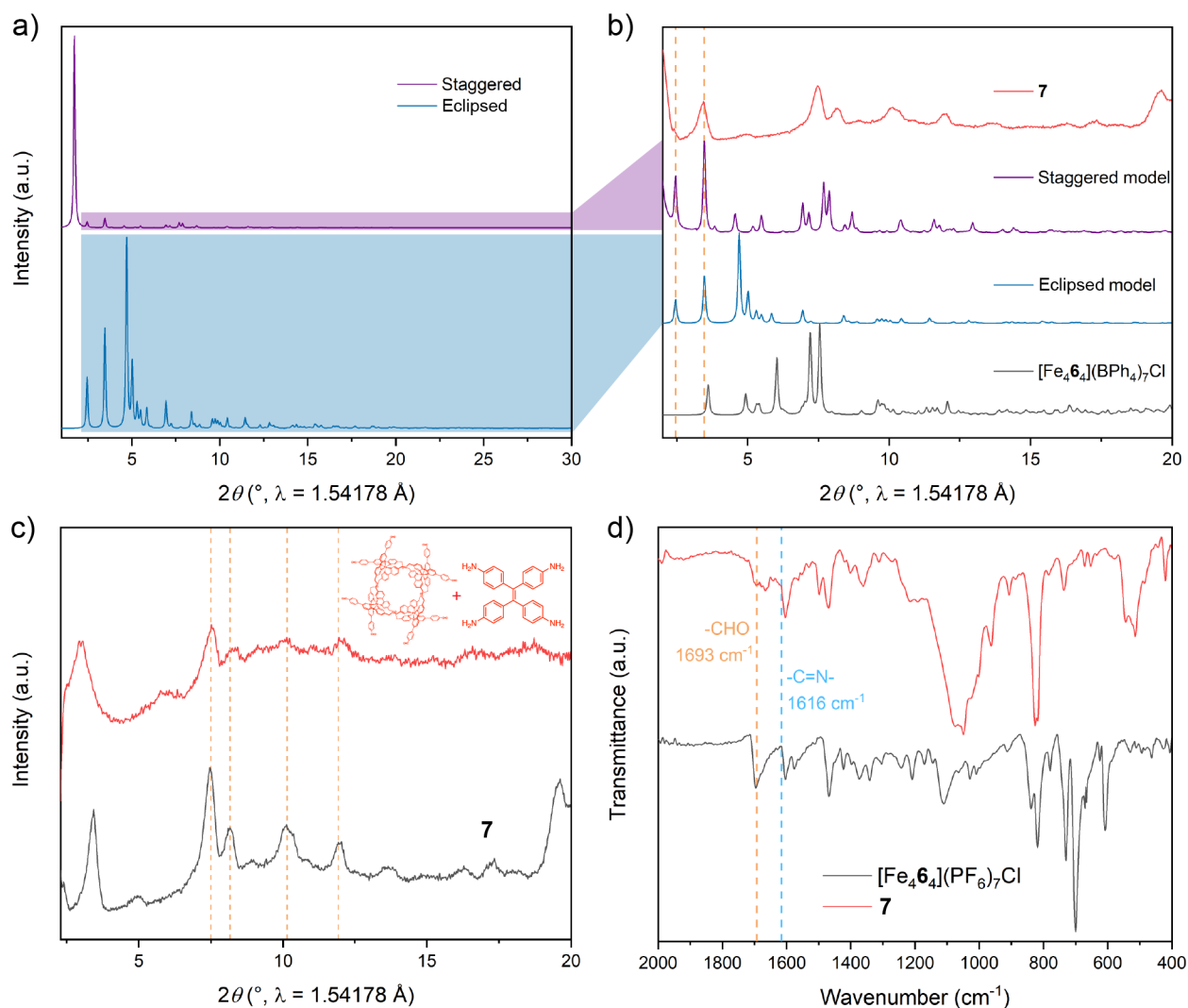


Figure 5.5. (a) Simulated PXRD patterns of the eclipsed and staggered model of the desired interlocking COF. 2θ ranges from 1° to 30° . (b) Comparison between the simulated PXRD patterns, the experimental PXRD of **7**, and the simulated PXRD of $[\text{Fe}_4\mathbf{6}_4](\text{BPh}_4)_7\text{Cl}$. 2θ ranges from 2° to 30° . (c) The PXRD pattern of **7** in comparison with the PXRD of a reaction product between $[\text{Fe}_4\mathbf{6}_4](\text{PF}_6)_7\text{Cl}$ and 4,4',4'',4'''-(ethene-1,1,2,2-tetrayl)tetraaniline. (d) IR spectra of **7** and $[\text{Fe}_4\mathbf{6}_4](\text{PF}_6)_7\text{Cl}$.

5.4. Conclusion

To conclude, we designed a reticular chemistry approach toward the structure of 2D interlocking rings *via* the synthesis of a woven COF. The building unit of the COF, a complicated iron complex, was successfully synthesized; and a preliminary product matching the predicted structure of the woven COF was obtained. Further optimizations in the synthetic conditions of the woven COF are required to eliminate the side product and improve the crystallinity of the desired product. Additionally, small-angle X-ray scattering measurement will be in need to confirm the staggered or eclipsed stacking mode of the final product. Once the woven COF with good quality is obtained, the demetallation condition will be determined and then the structure of 2D interlocking rings will be characterized.

5.5. Appendices and Notes

5.5.1. Acknowledgments

The author acknowledges Dr. Yuzhong Liu, Dr. Tianqiong Ma, Dr. Xing Han, Hao Lyu for their helpful discussions on COF synthesis. The linkers TPDA and MeO-*m*-TPDA used in initial synthetic screenings were generously provided by Dr. Tianqiong Ma and Hao Lyu. The single-crystal data collection was completed at beamline 12.2.1, the Advanced Light Source, which is a DOE Office of Science User Facility under contract no. DE-AC02-05CH11231. We thank Drs. Hasan Celik, Alicia Lund, and UC Berkeley's NMR facility in the College of Chemistry (CoC-NMR) for spectroscopic assistance. Instruments in the CoC-NMR are supported in part by NIH S10OD024998.

5.5.2. Mass Spectrometry

ESI-MS was performed on the methanol and acetonitrile solution of the synthesized iron complex. Analysis on the spectrum in methanol indicated that the complex contains chloride, which means that the precipitation of the complex with KPF₆ solution didn't fully transfer all the anions into PF₆⁻. The complex forms additives with methanol in its solution, as the *m/z* signals corresponding to complex adding 1 – 4 methanol molecules were observed (**Figure 5.6**). Such behavior was not observed for the acetonitrile solution of the complex as indicated by the ESI-MS spectrum (**Figure 5.7**). The formation of the complex was proved by high-resolution ESI-MS performed on the acetonitrile solution, and the simulated spectrum matched the observed spectrum (**Figure 5.9, Figure 5.9**).

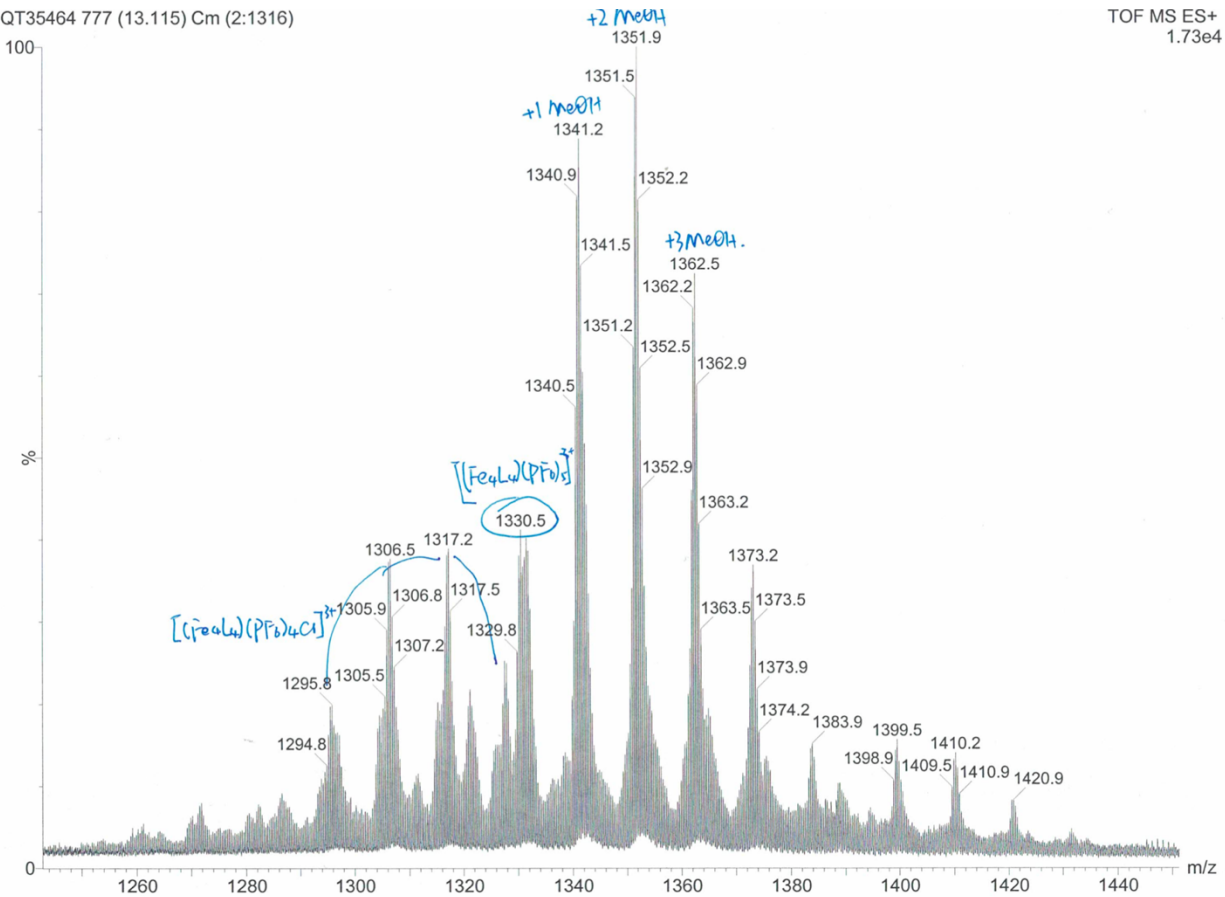


Figure 5.6. ESI-MS spectrum of $[\text{Fe}_{464}](\text{PF}_6)_7\text{Cl}$ in methanol.

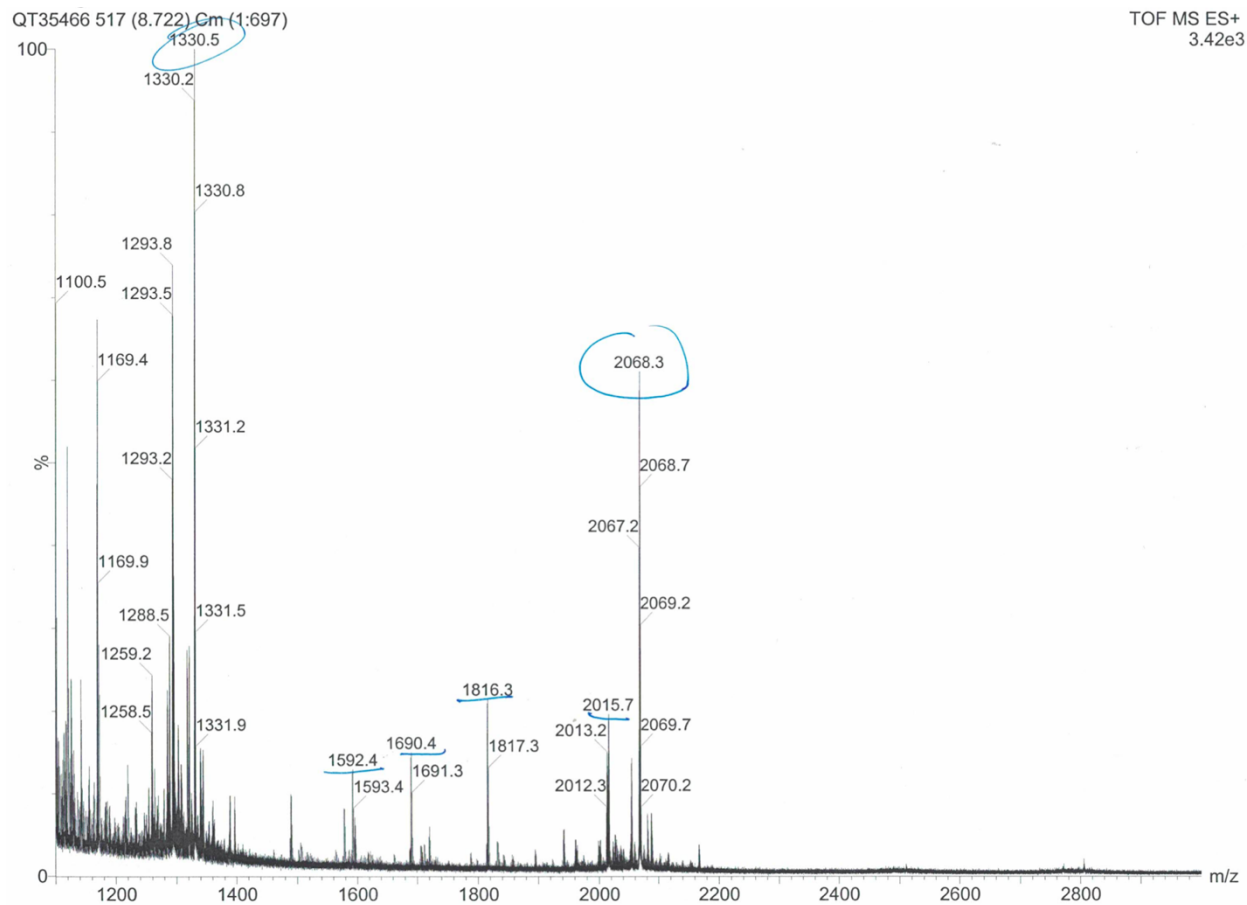


Figure 5.7. ESI-MS spectrum of $[\text{Fe}_{464}](\text{PF}_6)_7\text{Cl}$ in acetonitrile.

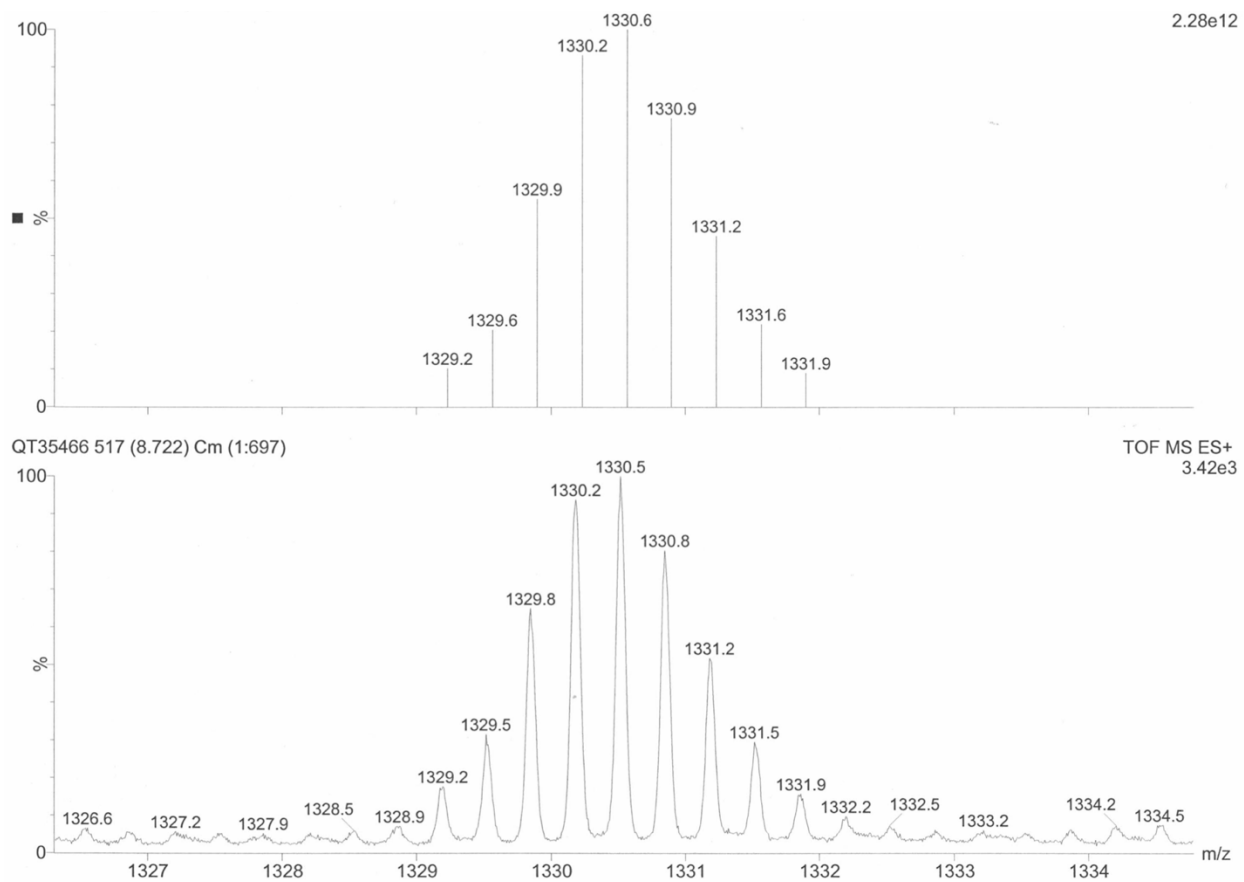


Figure 5.8. High-resolution electrospray ionization mass spectrum (HRESI-MS) of $[\text{Fe}_4\text{6}_4](\text{PF}_6)_7\text{Cl}$ in acetonitrile. The found formula was $\{[\text{Fe}_4(\text{C}_{48}\text{H}_{36}\text{N}_6\text{O}_3)_4](\text{PF}_6)_5\}^{3+}$.

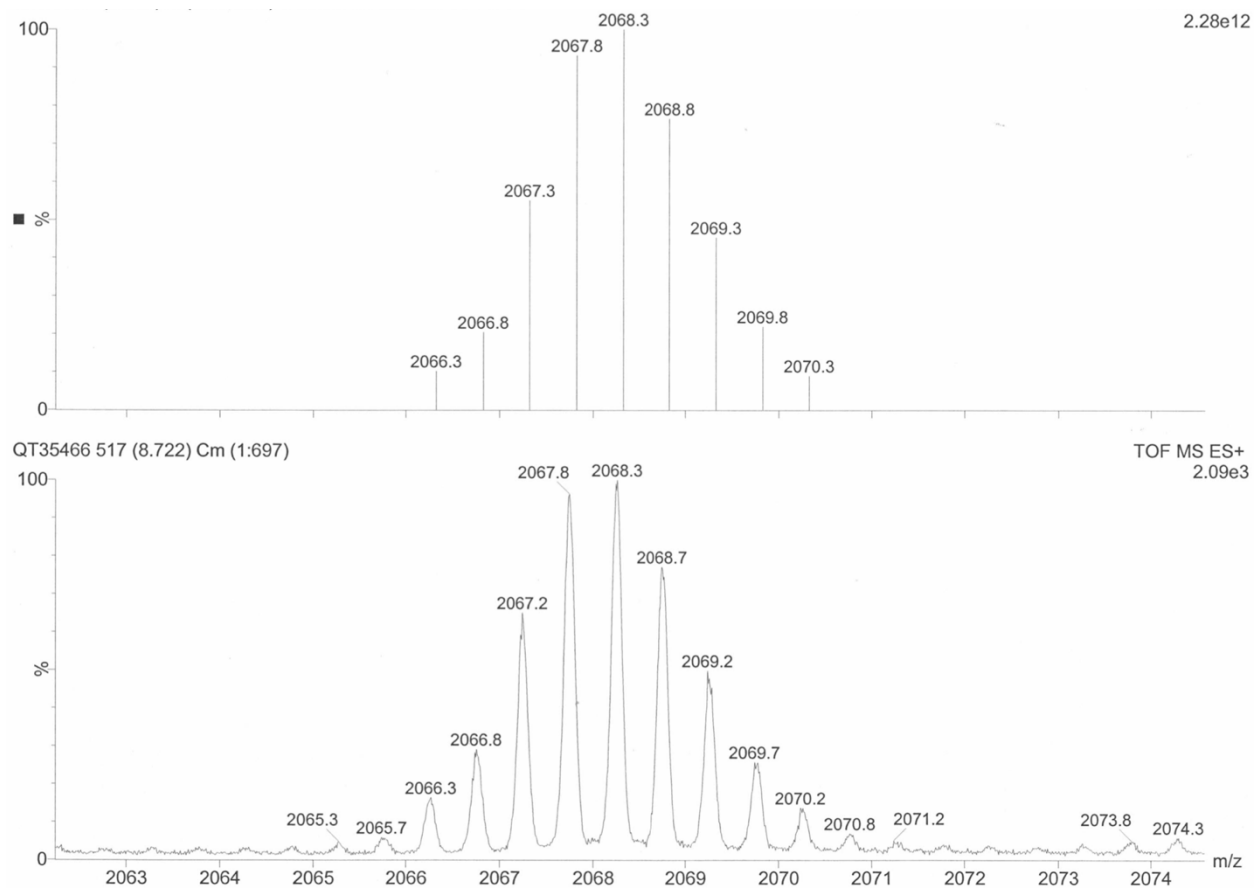


Figure 5.9. High-resolution electrospray ionization mass spectrum (HRESI-MS) of $[\text{Fe}_{46}](\text{PF}_6)_7\text{Cl}$ in acetonitrile. The found formula was $\{[\text{Fe}_4(\text{C}_{48}\text{H}_{36}\text{N}_6\text{O}_3)_4](\text{PF}_6)_6\}^{2+}$.

5.5.3. Single-crystal X-ray diffraction results

A membrane-like crystal of $[\text{Fe}_4\mathbf{6}_4](\text{BPh}_4)_7\text{Cl}$ was mounted onto a MiTeGen pin and measured at beamline 12.2.1 at ALS with radiation of $\lambda = 0.7288 \text{ \AA}$. The raw data was integrated using SAINT¹⁹ and scaled with SADABS²⁰, which are both integrated executables of Bruker APEX3 software suite.²¹ Based on intensity statistics for the whole dataset (PRP file), the resolution was cut off to 1.15 \AA ($R_{\text{merge}} \leq 40\%$ or average $I/\sigma > 2.5$ for the highest resolution shell). The completeness of the dataset was 77.7% due to the limited diffraction ability of the thinnest dimension of the crystal. The structure was phased with SHELXT and the least-square refinement on F^2 was performed by SHELXL,^{22,23} in a graphical user interface provided by Olex2.²⁴ A chloride ion was found at the center of the complex, which is in agreement with the previous report that the central void of the complex has a high affinity to halides because of C–H \cdots Cl interactions. The data-to-parameter ratio of refinement was limited by the low resolution of the dataset, low completeness, and a large number (387) of non-hydrogen atoms in the asymmetric unit. Therefore, the two found DMF molecules and six BPh_4^- anions were refined isotropically to reduce the number of parameters, and the complex was refined anisotropically besides the eight terminal 4-formylphenyl groups. The final number of parameters was 2382 and the data-to-parameter ratio was controlled to 7.62. Seven BPh_4^- anions were originally found in the asymmetric unit of the structure, however, one of them was too disordered to have its atomic structure refined and was eliminated. RIGU was applied to all other six BPh_4^- anions, as well as the ether (–C–O–C–) unit in the complex. Solvent mask procedure was applied at the end of refinement.²⁵ The total masked volume and the masked number of electrons were 2268 \AA^3 and $540 e^-$, respectively.

Table 5.3. Crystal data, data collection, and structure refinement parameters for $[\text{Fe}_4\mathbf{6}_4](\text{BPh}_4)_7\text{Cl}$.

Empirical formula	$[\text{Fe}_4\text{C}_{184}\text{H}_{148}\text{N}_{24}\text{O}_{16}](\text{BC}_2\text{H}_2\text{O})_6\text{Cl}(\text{C}_3\text{NH}_7\text{O})_2$
Formula weight	5367.63
Temperature/K	100
Crystal system	triclinic
Space group	$P-1$
$a/\text{\AA}$	18.657(2)
$b/\text{\AA}$	18.968(2)
$c/\text{\AA}$	49.372(6)
$\alpha/^\circ$	95.818(3)
$\beta/^\circ$	92.557(3)
$\gamma/^\circ$	102.399(3)
Volume/ \AA^3	16937(4)
Z	2
$\rho_{\text{calc}} (\text{g}/\text{cm}^3)$	1.053
μ/mm^{-1}	0.249
$F(000)$	5622.0
Crystal size/ mm^3	$0.1 \times 0.1 \times 0.001$
Radiation	Synchrotron ($\lambda = 0.7288 \text{ \AA}$)
2Θ range for data collection/ $^\circ$	2.678 to 36.946

Index ranges	$-16 \leq h \leq 16, -16 \leq k \leq 16, -40 \leq l \leq 42$
Reflections collected	33077
Independent reflections	18148 [$R_{\text{int}} = 0.0645, R_{\text{sigma}} = 0.1110$]
Data/restraints/parameters	18148/1474/2382
Goodness-of-fit on F^2	2.077
Final R indexes [$I \geq 2\sigma(I)$]	$R_1 = 0.1428, wR_2 = 0.3504$
Final R indexes [all data]	$R_1 = 0.1908, wR_2 = 0.3760$
Largest diff. peak/hole / ($e \text{ \AA}^{-3}$)	0.98/-0.61

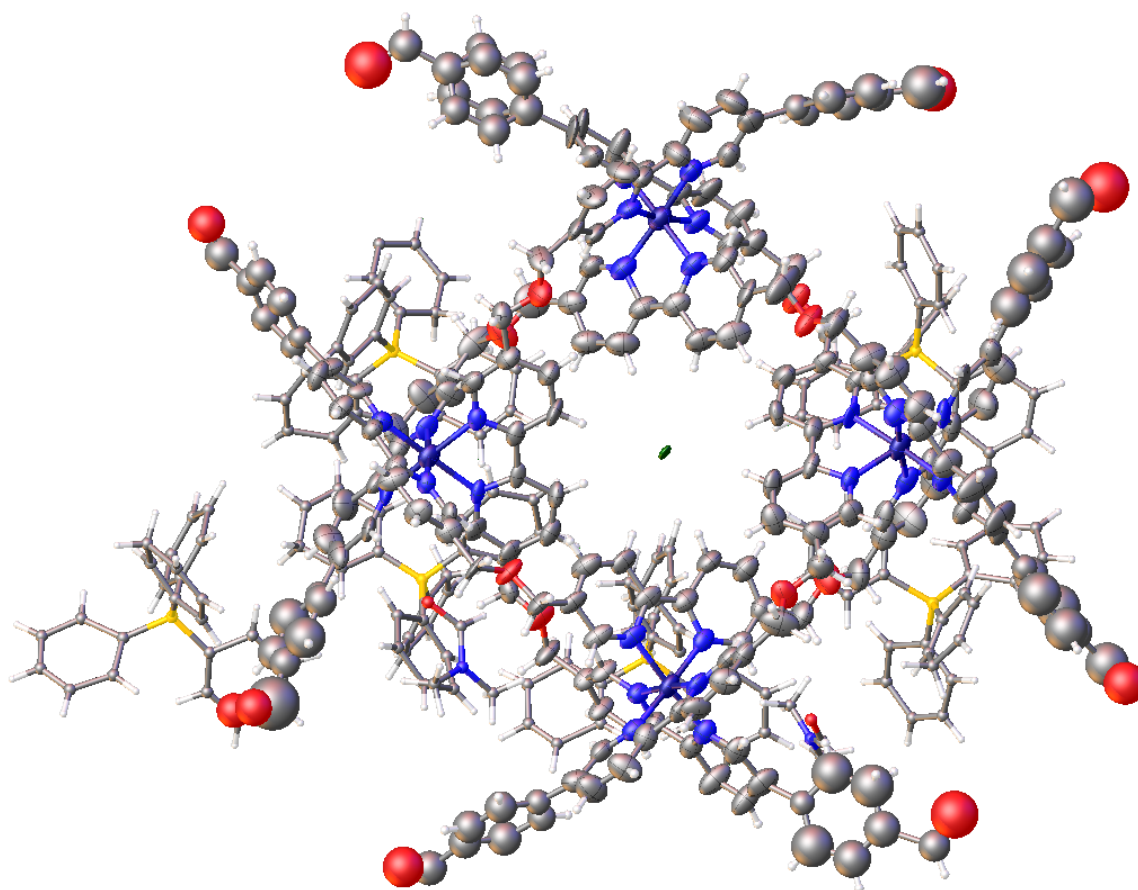


Figure 5.10. The plot of asymmetric unit of $[\text{Fe}_{464}](\text{BPh}_4)_7\text{Cl}$. The solvent molecules and BPh_4^- anions were shown as ball-and-stick model. Color code: Fe, dark purple; Cl, dark green; O, red; N, purple; C, gray; B, yellow; H, white. Thermal ellipsoids are shown with 50% probability.

5.5.4. Structural Model of the Proposed Woven COFs

Table 5.4. Atomic coordinates of the proposed staggered model of the woven COF.

Model: staggered layers									
$P4/m$; $a = 50.8875 \text{ \AA}$, $c = 23.0000 \text{ \AA}$									
Atom	Fractional coordinates			Occupancy	Atom	Fractional coordinates			Occupancy
	x	y	z			x	y	z	
N1	0.08979	0.07538	0.77885	1	C71	0.443	0.05333	0.82368	1
C2	0.06612	0.0636	0.76385	1	C72	0.4159	0.05296	0.81369	1
C3	0.0598	0.03891	0.78574	1	C73	0.48681	0.07776	0.82063	1
H4	0.04034	0.02928	0.77351	1	C74	0.50247	0.05745	0.83581	1
C5	0.07722	0.02599	0.82253	1	C75	0.5315	0.05975	0.84136	1
H6	0.07208	0.00574	0.84037	1	C76	0.54572	0.04029	0.87212	1
C7	0.10089	0.03778	0.83753	1	C77	0.5733	0.04096	0.87561	1
C8	0.10722	0.06247	0.81564	1	C78	0.58724	0.06098	0.84779	1
H9	0.12667	0.07211	0.82785	1	C79	0.57244	0.08131	0.816	1
N10	0.12292	-0.12129	0.78355	1	C80	0.54523	0.07984	0.8127	1
C11	0.13986	-0.12031	0.82864	1	C81	0.61578	0.05964	0.83825	1
C12	0.14852	-0.14327	0.85697	1	C82	0.63384	0.06867	0.88025	1
H13	0.16257	-0.14234	0.89551	1	C83	0.66055	0.07114	0.86599	1
C14	0.13983	-0.16741	0.83651	1	C84	0.66921	0.06679	0.80883	1
H15	0.1468	-0.18632	0.85816	1	C85	0.65059	0.05922	0.76641	1
C16	0.12261	-0.16855	0.78952	1	C86	0.62461	0.0535	0.78226	1
C17	0.11415	-0.14549	0.76309	1	N87	0.6967	0.07074	0.79519	1
H18	0.10004	-0.14639	0.72465	1	H88	0.32364	0.06555	0.69128	1
O19	0.131	0.00133	0.85175	1	H89	0.37154	0.061	0.6958	1
C20	0.02281	0.10915	0.64821	1	H90	0.37098	0.09034	0.87214	1
C21	0.01239	0.08471	0.66247	1	H91	0.3232	0.09363	0.86881	1
H22	-0.00689	0.07798	0.64211	1	H92	0.40882	0.11367	0.7536	1
C23	0.02552	0.06854	0.70156	1	H93	0.45602	0.11478	0.771	1
H24	0.01701	0.0485	0.71327	1	H94	0.45162	0.03641	0.84415	1
C25	0.04898	0.07674	0.72639	1	H95	0.4044	0.03631	0.82777	1
N26	0.0594	0.10118	0.71213	1	H96	0.49509	0.09708	0.81486	1
C27	0.04627	0.11736	0.67294	1	H97	0.49432	0.03798	0.84291	1
H28	0.05482	0.13737	0.66118	1	H98	0.53537	0.02446	0.89353	1
N29	0.13047	-0.07674	0.81	1	H99	0.58383	0.02553	0.89783	1
C30	0.14539	-0.09389	0.84352	1	H100	0.58283	0.09695	0.79351	1
C31	0.16162	-0.08421	0.88708	1	H101	0.53527	0.09475	0.78758	1
H32	0.17382	-0.09831	0.91453	1	H102	0.62721	0.07443	0.92327	1

C33	0.16296	-0.0573	0.89711	1	H103	0.67448	0.07768	0.89889	1
H34	0.17628	-0.04931	0.93284	1	H104	0.65474	0.06053	0.71968	1
C35	0.14806	-0.04008	0.86359	1	H105	0.61066	0.04698	0.74915	1
C36	0.13181	-0.04984	0.82004	1	Fe10	0.89485	0.09179	0.7418	1
H37	0.11959	-0.03576	0.79256	1	C107	0.83641	0.08675	0.71633	1
C38	0.09169	-0.23509	0.80592	1	H108	0.83549	0.07229	0.75413	1
H39	0.08555	-0.24733	0.84205	1	N109	0.86037	0.09738	0.6995	1
C40	0.10057	-0.2099	0.81808	1	C110	0.86152	0.11499	0.65343	1
H41	0.10053	-0.20306	0.8628	1	C111	0.8387	0.12196	0.6242	1
C42	0.11068	-0.19403	0.7738	1	H112	0.83963	0.13639	0.58635	1
C43	0.10994	-0.20298	0.71597	1	C113	0.81467	0.11134	0.64102	1
H44	0.11728	-0.19078	0.68097	1	H114	0.79594	0.11709	0.61699	1
C45	0.10028	-0.22812	0.70342	1	C115	0.81352	0.09373	0.68709	1
H46	0.10007	-0.23482	0.65891	1	C116	0.96346	0.13737	0.59421	1
C47	0.09196	-0.24466	0.74855	1	H117	0.96812	0.15924	0.59704	1
C48	0.14882	-0.01378	0.88362	1	H118	0.96435	0.13073	0.54691	1
H49	0.14175	-0.01319	0.93064	1	C119	0.93405	0.11539	0.65964	1
H50	0.17009	-0.00681	0.88187	1	H120	0.95073	0.10578	0.68502	1
C51	0.00822	0.12564	0.61681	1	N121	0.90808	0.10953	0.67328	1
H52	0.01153	0.12051	0.56912	1	C122	0.8878	0.12131	0.64244	1
H53	0.01558	0.14659	0.62346	1	C123	0.8934	0.1389	0.59787	1
C54	0.08594	-0.27246	0.73684	1	H124	0.87671	0.14853	0.5726	1
C55	0.12588	0.02653	0.87697	1	C125	0.91935	0.14469	0.58423	1
H56	0.12123	0.02706	0.92544	1	H126	0.924	0.15908	0.54768	1
H57	0.14434	0.03829	0.86644	1	C127	0.93972	0.13296	0.61508	1
H58	0.30693	-0.04865	0.71544	1	O128	0.98172	0.12407	0.63167	1
H59	0.28299	0.08463	0.69257	1	C129	0.70833	0.06235	0.74802	1
N60	0.29201	0.08388	0.78049	1	C130	0.75374	0.07836	0.7784	1
C61	0.3199	0.08037	0.77987	1	H131	0.74775	0.08057	0.82357	1
C62	0.33375	0.07099	0.731	1	C132	0.73616	0.0689	0.73557	1
C63	0.36111	0.06829	0.73359	1	C133	0.74496	0.06601	0.67827	1
C64	0.37474	0.07545	0.78439	1	H134	0.73216	0.05848	0.64443	1
C65	0.3608	0.08463	0.83286	1	C135	0.77027	0.0737	0.66266	1
C66	0.33363	0.08667	0.8308	1	H136	0.77571	0.07248	0.61703	1
C67	0.40351	0.07447	0.78775	1	C137	0.78785	0.08346	0.70494	1
C68	0.41828	0.09656	0.77224	1	C138	0.77952	0.08534	0.76286	1
C69	0.44531	0.09716	0.78287	1	H139	0.79258	0.09347	0.79546	1
C70	0.45813	0.07561	0.80882	1					

Table 5.5. Atomic coordinates of the proposed eclipsed model of the woven COF.

Model: eclipsed layers									
<i>P4/m</i> ; a = 50.8875 Å, c = 18.7760 Å									
Atom	Fractional coordinates			Occupancy	Atom	Fractional coordinates			Occupancy
	x	y	z			x	y	z	
Fe1	-0.1072	0.59037	1.57852	1	C71	0.14677	0.4848	1.75225	1
N2	0.08775	0.57397	1.62391	1	H72	0.1397	0.48539	1.80984	1
C3	0.06407	0.56218	1.60553	1	H73	0.16805	0.49177	1.7501	1
C4	0.05775	0.53749	1.63234	1	C74	0.00618	0.62422	1.42542	1
H5	0.03829	0.52786	1.61736	1	H75	0.00948	0.61909	1.367	1
C6	0.07517	0.52458	1.67741	1	H76	0.01353	0.64517	1.43356	1
H7	0.07003	0.50432	1.69927	1	C77	0.08389	0.22612	1.57245	1
C8	0.09885	0.53637	1.69578	1	C78	-0.29371	0.56094	1.58614	1
C9	0.10517	0.56105	1.66898	1	C79	0.12383	0.52511	1.7441	1
H10	0.12462	0.5707	1.68393	1	H80	0.11918	0.52564	1.80347	1
N11	0.12088	0.37729	1.62966	1	H81	0.14229	0.53687	1.7312	1
C12	0.13781	0.37827	1.6849	1	C82	-0.24831	0.57694	1.62335	1
C13	0.14647	0.35531	1.7196	1	H83	-0.25429	0.57916	1.67869	1
H14	0.16053	0.35625	1.76681	1	C84	-0.26589	0.56748	1.57089	1
C15	0.13779	0.33117	1.69454	1	C85	-0.25708	0.5646	1.5007	1
H16	0.14475	0.31226	1.72106	1	H86	-0.26989	0.55706	1.45924	1
C17	0.12056	0.33003	1.63698	1	C87	-0.23177	0.57228	1.48158	1
C18	0.11211	0.35309	1.6046	1	H88	-0.22633	0.57106	1.42568	1
H19	0.09799	0.35219	1.55752	1	C89	-0.2142	0.58204	1.53337	1
C20	-0.16564	0.58533	1.54732	1	C90	-0.22253	0.58392	1.60432	1
H21	-0.16656	0.57087	1.59362	1	H91	-0.20946	0.59205	1.64426	1
N22	-0.14168	0.59597	1.5267	1	H92	0.30488	0.44994	1.54623	1
C23	-0.14053	0.61357	1.47027	1	H93	0.28094	0.58321	1.51821	1
C24	-0.16334	0.62054	1.43446	1	N94	0.28996	0.58247	1.62592	1
H25	-0.16242	0.63498	1.3881	1	C95	0.31785	0.57896	1.62516	1
C26	-0.18738	0.60992	1.45507	1	C96	0.3317	0.56957	1.56529	1
H27	-0.20611	0.61568	1.42564	1	C97	0.35906	0.56687	1.56846	1
C28	-0.18853	0.59232	1.5115	1	C98	0.37269	0.57403	1.63069	1
C29	-0.03859	0.63595	1.39773	1	C99	0.35875	0.58322	1.69007	1
H30	-0.03393	0.65782	1.4012	1	C100	0.33158	0.58525	1.68754	1
H31	-0.0377	0.62931	1.33979	1	C101	0.40146	0.57306	1.63481	1
C32	-0.068	0.61397	1.47788	1	C102	0.41623	0.59515	1.61581	1
H33	-0.05132	0.60437	1.50897	1	C103	0.44327	0.59575	1.62882	1
N34	-0.09397	0.60811	1.49459	1	C104	0.45608	0.57419	1.66062	1

C35	-0.11425	0.61989	1.45681	1	C105	0.44095	0.55192	1.67882	1
C36	-0.10865	0.63748	1.40221	1	C106	0.41386	0.55155	1.66659	1
H37	-0.12534	0.64711	1.37126	1	C107	0.48476	0.57634	1.67508	1
C38	-0.0827	0.64327	1.38551	1	C108	0.50043	0.55603	1.69368	1
H39	-0.07805	0.65767	1.34073	1	C109	0.52946	0.55833	1.70048	1
C40	-0.06232	0.63154	1.42329	1	C110	0.54367	0.53887	1.73815	1
O41	0.12895	0.49991	1.71321	1	C111	0.57125	0.53955	1.74244	1
C42	0.02076	0.60773	1.46387	1	C112	0.5852	0.55956	1.70836	1
C43	0.01034	0.5833	1.48135	1	C113	0.5704	0.57989	1.66941	1
H44	-0.00894	0.57656	1.4564	1	C114	0.54318	0.57843	1.66537	1
C45	0.02347	0.56712	1.52923	1	C115	0.61373	0.55822	1.69667	1
H46	0.01497	0.54708	1.54357	1	C116	0.63179	0.56726	1.74812	1
C47	0.04693	0.57533	1.55965	1	C117	0.65851	0.56972	1.73065	1
N48	0.05735	0.59977	1.54218	1	C118	0.66717	0.56537	1.66063	1
C49	0.04422	0.61594	1.49417	1	C119	0.64855	0.5578	1.60867	1
H50	0.05277	0.63595	1.47976	1	C120	0.62256	0.55208	1.62808	1
N51	0.12843	0.42184	1.66206	1	N121	0.69466	0.56932	1.64393	1
C52	0.14334	0.40469	1.70312	1	H122	0.32159	0.56413	1.51664	1
C53	0.15957	0.41438	1.75648	1	H123	0.3695	0.55958	1.52218	1
H54	0.17177	0.40027	1.79011	1	H124	0.36893	0.58892	1.73819	1
C55	0.16091	0.44128	1.76878	1	H125	0.32116	0.59222	1.7341	1
H56	0.17423	0.44927	1.81254	1	H126	0.40677	0.61226	1.59297	1
C57	0.14602	0.4585	1.72771	1	H127	0.45398	0.61336	1.61429	1
C58	0.12976	0.44875	1.67436	1	H128	0.44957	0.535	1.7039	1
H59	0.11754	0.46282	1.6407	1	H129	0.40235	0.5349	1.68383	1
C60	0.08964	0.26349	1.65707	1	H130	0.49304	0.59567	1.66802	1
H61	0.08351	0.25126	1.70133	1	H131	0.49228	0.53656	1.70237	1
C62	0.09852	0.28868	1.67196	1	H132	0.53333	0.52304	1.76439	1
H63	0.09848	0.29552	1.72674	1	H133	0.58178	0.52411	1.76965	1
C64	0.10863	0.30455	1.61772	1	H134	0.58078	0.59553	1.64186	1
C65	0.10789	0.29561	1.54687	1	H135	0.53323	0.59333	1.6346	1
H66	0.11524	0.3078	1.50401	1	H136	0.62516	0.57302	1.80082	1
C67	0.09823	0.27046	1.53151	1	H137	0.67243	0.57626	1.77095	1
H68	0.09802	0.26376	1.47698	1	H138	0.65269	0.55911	1.55143	1
C69	0.08992	0.25392	1.58679	1	H139	0.60861	0.54556	1.58752	1
O70	-0.02033	0.62266	1.44362	1					

5.6. Bibliography

- (1) Forgan, R. S.; Sauvage, J.-P.; Stoddart, J. F. Chemical Topology: Complex Molecular Knots, Links, and Entanglements. *Chem. Rev.* **2011**, *111* (9), 5434–5464.
- (2) Evans, N. H.; Beer, P. D. Supramolecular Chemistry: From Molecules to Nanomaterials. **2012**.
- (3) Xue, M.; Yang, Y.; Chi, X.; Yan, X.; Huang, F. Development of Pseudorotaxanes and Rotaxanes: From Synthesis to Stimuli-Responsive Motions to Applications. *Chem. Rev.* **2015**, *115* (15), 7398–7501.
- (4) Sauvage, J.; Amabilino, D. B. Supramolecular Chemistry: From Molecules to Nanomaterials. **2012**.
- (5) Fielden, S. D. P.; Leigh, D. A.; Woltering, S. L. Molecular Knots. *Angew. Chem. Int. Ed.* **2017**, *56* (37), 11166–11194.
- (6) Segawa, Y.; Levine, D. R.; Itami, K. Topologically Unique Molecular Nanocarbons. *Acc. Chem. Res.* **2019**, *52* (10), 2760–2767.
- (7) Harada, A.; Hashidzume, A.; Yamaguchi, H.; Takashima, Y. Polymeric Rotaxanes. *Chem. Rev.* **2009**, *109* (11), 5974–6023.
- (8) Liu, Y.; Ma, Y.; Zhao, Y.; Sun, X.; Gándara, F.; Furukawa, H.; Liu, Z.; Zhu, H.; Zhu, C.; Suenaga, K.; Oleynikov, P.; Alshammari, A. S.; Zhang, X.; Terasaki, O.; Yaghi, O. M. Weaving of Organic Threads into a Crystalline Covalent Organic Framework. *Science* **2016**, *351* (6271), 365–369.
- (9) Diercks, C. S.; Yaghi, O. M. The Atom, the Molecule, and the Covalent Organic Framework. *Science* **2017**, *355* (6328), eaal1585.
- (10) Liu, Y.; Diercks, C. S.; Ma, Y.; Lyu, H.; Zhu, C.; Alshimmri, S. A.; Alshihri, S.; Yaghi, O. M. 3D Covalent Organic Frameworks of Interlocking 1D Square Ribbons. *J. Am. Chem. Soc.* **2019**, *141* (1), 677–683.
- (11) Watanabe, N.; Ikari, Y.; Kihara, N.; Takata, T. Bridged Polycatenane. *Macromolecules* **2004**, *37* (18), 6663–6666.
- (12) Wu, Q.; Rauscher, P. M.; Lang, X.; Wojtecki, R. J.; Pablo, J. J. de; Hore, M. J. A.; Rowan, S. J. Poly[n]Catenanes: Synthesis of Molecular Interlocked Chains. *Science* **2017**, *358* (6369), 1434–1439.
- (13) Datta, S.; Kato, Y.; Higashiharaguchi, S.; Aratsu, K.; Isobe, A.; Saito, T.; Prabhu, D. D.; Kitamoto, Y.; Hollamby, M. J.; Smith, A. J.; Dalgliesh, R.; Mahmoudi, N.; Pesce, L.; Perego, C.; Pavan, G. M.; Yagai, S. Self-Assembled Poly-Catenanes from Supramolecular Toroidal Building Blocks. *Nature* **2020**, *583* (7816), 400–405.
- (14) Amabilino, D. B.; Ashton, P. R.; Reder, A. S.; Spencer, N.; Stoddart, J. F. Olympiadane. *Angew. Chem. Int. Ed.* **1994**, *33* (12), 1286–1290.
- (15) Danon, J. J.; Krüger, A.; Leigh, D. A.; Lemonnier, J.-F.; Stephens, A. J.; Vitorica-Yrezabal, I. J.; Woltering, S. L. Braiding a Molecular Knot with Eight Crossings. *Science* **2017**, *355* (6321), 159–162.
- (16) BIOVIA; Systèmes, D. *Materials Studio*; Dassault Systèmes: San Diego, USA, 2019.

- (17) Ma, T.; Kapustin, E. A.; Yin, S. X.; Liang, L.; Zhou, Z.; Niu, J.; Li, L.-H.; Wang, Y.; Su, J.; Li, J.; Wang, X.; Wang, W. D.; Wang, W.; Sun, J.; Yaghi, O. M. Single-Crystal X-Ray Diffraction Structures of Covalent Organic Frameworks. *Science* **2018**, *361* (6397), 48–52.
- (18) Sinha, S. P. 2,2'-Dipyridyl Complexes of Rare Earths I: Preparation, Infra-Red and Some Other Spectroscopic Data. *Spectrochim. Acta* **1964**, *20* (5), 879–886.
- (19) Bruker. *SAINT*; Bruker AXS Inc.: Madison, WI, USA, 2012.
- (20) Bruker. *SADABS, Version 2014/4*; Bruker AXS Inc.: Madison, WI, USA, 2014.
- (21) Bruker. *APEX3, Version 8.38*; Bruker AXS Inc.: Madison, WI, USA, 2018.
- (22) Sheldrick, G. M. A Short History of SHELX. *Acta Crystallogr., Sect. A: Found. Crystallogr.* **2008**, *64* (1), 112–122.
- (23) Sheldrick, G. M. Crystal Structure Refinement with SHELXL. *Acta Crystallogr., Sect. C: Struct. Chem.* **2015**, *71* (Pt 1), 3–8.
- (24) Dolomanov, O. V.; Bourhis, L. J.; Gildea, R. J.; Howard, J. A. K.; Puschmann, H. OLEX2: A Complete Structure Solution, Refinement and Analysis Program. *J. Appl. Crystallogr.* **2009**, *42* (2), 339–341.
- (25) Sluis, P. van der; Spek, A. L. BYPASS: An Effective Method for the Refinement of Crystal Structures Containing Disordered Solvent Regions. *Acta Crystallogr., Sect. A: Found. Crystallogr.* **1990**, *46* (3), 194–201.

Chapter 6.
Conclusion and Outlook

Although the field of reticular materials has been developed for more than 20 years, the structural studies of MOFs, ZIFs, and COFs largely remained at a relatively basic level of knowing their skeleton. The studies of the complex structural behaviors of MOFs, ZIFs, and COFs demonstrated here have shown that deeper crystallographic research is a gold mine for accurately understanding their properties and advancing fundamental scientific knowledge. From a basic science aspect, chapter 2 analyzed the intrinsic stereoselectivity of the coordinative alignment method supported by asymmetric coordination bond. The result found its meaning in the application that the method can fundamentally avoid a primary source of disorder caused by alternating orientation of incorporation, allowing it to assist structure determination of small molecules better. The thorough look at the solvent-induced guest disorder in chapter 3 provided an insight into solvent-guest interactions that generally exist in porous crystals, and in addition, introduced a method for the better quality of structural solutions by solvent removal. Chapter 4 is a particular example on how many questions remain unexplored in the previously reported crystal structures. A revisit to ZIF-90 structure revealed a new form of disorder in ZIFs and an unprecedented cause of displacive phase transition among any materials.

However, the existing research is far from enough considering the vast applications of the reticular materials and the small number of well-characterized mechanisms being reported. For instance, COFs are widely used in gas separation, gas storage, and loading of catalysts, but the interpretations of corresponding characterizations merely consider the significant population of defects and disorders that can potentially alter the behavior of COFs. Indeed, it is challenging to fully characterize the nonideal structures, especially when the materials are functioning in their applications. Nevertheless, it is such knowledge that promotes the discovery of new materials and the optimization of existing materials. The emerging synchrotron techniques and *in operando* setups connecting multiple characterizations meet the challenge of research and provide platforms for better mechanism studies, such as the environmental gas cell for single-crystal gas sorption studies and SXRDX-EXAFS setup for capturing catalytic cycle in single crystals.

Chapter 5 present a more crucial question to the structural characterization of reticular materials because the woven COFs, upon demetallation, produce a topologically ordered but spatially amorphous material. Such material still possesses long-range order to a certain extent while short-range order diminishes. It forms an interesting contrast with another class of amorphous material, glass, that the long-range order disappears but the short-range order is preserved. How to characterize the structures and motions of such states between crystalline and non-crystalline? The boundary between crystalline and non-crystalline materials is becoming vague with the development of the materials field. It urges the combination of diffraction and scattering techniques for understanding the new materials at the boundary. While the above question might be too far, a realistic question is how to resolve the structures of low-resolution crystalline materials. For example, the diffraction ability of most COFs has their limit of diffraction ability before $\sim 2 \text{ \AA}$. To address this, one can borrow knowledge from the field of protein crystallography, which is the expert in getting structure from low-resolution, weakly diffracting samples. The successful grafting of techniques from protein to reticular materials will advance the field with respect to better structural determinations of many materials.

Overall, there are numerous questions buried in the structures of reticular material and numerous opportunities for multi-disciplinary research. Resolving the questions will not only benefit reticular chemistry, but also deepen the knowledge in solid-state chemistry.